**Title**
Fundamental Research and Applications of Conducting Polyaniline and Oligoanilines



**Author**
Lin, Cheng-Wei

**Publication Date**
2019

Peer reviewed|Thesis/dissertation

UNIVERSITY OF CALIFORNIA

Los Angeles

# Fundamental Research and Applications of Conducting Polyaniline and Oligoanilines

A dissertation submitted in partial satisfaction of the requirements for the degree Doctor of Philosophy in Chemistry

by

Cheng-Wei Lin

2019

ABSTRACT OF THE DISSERTATION

Fundamental Research and Applications of
Conducting Polyaniline and Oligoanilines

by

Cheng-Wei Lin
Doctor of Philosophy in Chemistry
University of California, Los Angeles
Professor Richard B. Kaner, Chair

Conjugated polyaniline, as one of the earliest developed conducting polymers, has been extensively studied during the past few decades and applied to gas sensors, mechanical actuators, energy storage devices, electrochromics, gas and water separation membranes, anti-corrosive coatings, *etc*. However, the long and entangled polymer chain conformations with uncertain numbers of aniline units (*i.e.* polydispersity) has limited its processability and also covered up some important information regarding the conjugated aniline-based system. Therefore, conjugated aniline oligomers, with defined chain lengths and a specific number of aniline units, are ideal small molecules for deciphering polyaniline. Previous studies have shown that tetraaniline is able to form distinct crystalline morphologies by introducing different acidic dopants and vertically aligned crystals with high electrical conductivities based on the nature of small molecules. These reports not only revealed the interactions between dopants and

tetraaniline molecules, but also provided some insights into self-assembly and charge transport in organic semiconductors.

The goals of this dissertation are to investigate fundamental properties of oligoanilines in order to further our understanding of the conjugated aniline system/derivatives, and to introduce tetraaniline to applications where polyaniline finds processing difficulties that are hard to deal with. Chapter 1 provides an introduction, while Chapter 2 compiles detailed performance data and separation mechanisms of conjugated polymer-based membranes for gas separation, water filtration and capacitive deionization. The advantages and evolution of using conjugated polymers for separation membranes are also explained. On the basis of polyaniline-based gas separation membranes, Chapter 3 briefly describes a project for turning carbon dioxide enriched from power plants into cement using membranes. Chapter 4 lays down the foundation for achieving high power density supercapacitors by freeze-casting as-filtered reduced graphene oxide films. In Chapter 5, aniline tetramers are combined with reduced graphene oxides in order to avoid chain scission and enhance the cycle stability of supercapacitors. In Chapter 6 tetraaniline, which can be dissolved in common organic solvents, is grafted onto different materials, creating hydrophilic and low bio-adhesion surfaces. Chapter 7 reveals the sequence of doping of the conjugated aniline system due to the defined amount of doping sites of tetraaniline and the insufficient amount of dopants added in. In the final chapter, quantified rate constants measured for oligoanilines in aniline electrochemical polymerization systems show different levels of catalytic effects depending on the chain length, capped functional groups, and redox properties of linear aniline derivatives.

The dissertation of Cheng-Wei Lin is approved.

Anastassia Alexandrova

Yang Yang

Richard B. Kaner, Committee Chair

University of California, Los Angeles

2019

*Dedicated in loving memory of*

*my late grandfather, Liao Huo-Jie*

TABLE OF CONTENTS

LIST OF FIGURES

Figure S4-7 X-ray photoelectron spectra C1s profiles for different GO samples……. 145

Figure S4-8 Raman spectra for GO, pre-reduced GO and 3D porous RGO films…… 146

Figure S4-9 Conductivities of different GO films………………………………………. 147

Figure S4-10 A strain-stress curve for the 3D porous RGO film……………………… 148

Figure S4-11 Schematic illustration of the structure of the fabricated symmetric two-electrode supercapacitor………………………………………………… 148

Figure S4-12 Cyclic voltammetry profiles of a 3D porous RGO film supercapacitor in 1.0 M $H_2SO_4$ aqueous electrolyte………………………………………. 149

Figure S4-13 Cyclic voltammetry profiles of a RGO film supercapacitor…………….. 150

Figure S4-14 Comparison of galvanostatic charge/discharge profiles for RGO and 3D porous RGO films at the same current density of 100 A $g^{-1}$……………. 151

Figure S4-15 Illustration of specific elements in the Nyquist spectra…………………. 152

Figure S4-16 Capability of an all solid-state 3D porous RGO supercapacitor under bending conditions………………………………………………………. 153

Figure S4-17 Schematic diagrams showing cross-section structure of different elements of a supercapacitor with their thicknesses. …………………… 154

Figure 5-1 Molecular structures showing the redox chemistry and doping properties, and the cyclic voltammetry measurement of aniline tetramer.. ………………………………………………………………... 177

Figure 5-2 UV-vis spectra and measured zeta potential versus pH of both polyaniline and aniline tetramer……………………………………… 177

Figure 5-3 Cyclic voltammetries and Matrix-Assisted Laser Desorption Ionization Time-of-Flight spectra of electropolymerization of aniline tetramer in solutions……………………………….……….…….….…….……... 178

Figure 5-4 Scanning electron microscope images of fabricated aniline tetramer/graphene oxidee composite electrode………….……………………… 179

LIST OF TABLES

ACKNOWLEDGEMENT

Studying abroad is exciting but very challenging, same as switching my major from materials science and engineering to chemistry. For the first few years in graduate school, I struggled in organic synthesis and learned how to view the world as a chemist. The proposal writings seemed endless and new ideas are always well hidden. I am glad that my passion toward seeking the beauty of pure science and my thick skin (and liver) back me up strongly. Here, I would like to acknowledge people who helped me reach my goals, supported me through difficulties, and whom I shared my good times and bad times with.

First, I would like to thank my advisor, Prof. Ric Kaner, for being such a hands-off and supportive P.I., and for being so nice and considerate so that we can simply focus on research. I would like to show my sincere gratitude to Dr. Michael T. Yeung who showed me around during the time I visited UCLA, shared news, papers, and ideas with me, and encouraged me whenever I feel desperate. I will always remember the times when only two of us were in lab discussing research, especially on the Jan. 1st when Ric came in and said "I should give you two promotions". I would also like to thank Dr. Georgiy Akopov for sitting next to me for four years and be so informative. I do miss the Thursday game nights, trips to New Orleans, San Francisco, Universal Studio and many other places with you. A special acknowledgment goes to Prof. Jessica (Yue) Wang, for being a good role model and laying down good foundations on the aniline tetramer.

Additionally, I would like to thank the guidance and collaboration of Prof. Yves Rubin, Prof. Anastassia Alexandrova, Prof. William Gelbart, Prof. Yang Yang, Prof. Gaurav Sant, Prof. Chong Liu, Prof. Thomas Mason, Prof. Shu-Chuan Huang, and Dr. Johnny Pang. My research won't be able to be done without the help from labmates and students in other labs, including Dr.

Sergey Dubin, Dr. Kan Wang, Dr. Lisa Wang, Dr. Brian T. McVerry, Dr. Wanmei Sun, Dr. Miao Xie, Dr. Jee Youn Hwang, Dr. Yuanlong Shao, Dr. Christopher Turner, Dr. Kris L. Marsh, Dr. Xinwei (William) Huang, Dr. Mengping Li, Dr. Haosen Wang, Dr. Jialin Lei, Dr. Emily P. Nguyen, Dr. Robert Jordan, Dr. Bu Wang, Dr. Shauna Robbennolt, Dr. Duk Woo Jun, Dr. Dayong Chen, Dr. Reza Rizvi, Dr. Dandan Zhang, Dr. Zhaoyang Lin, Dr. Volker Strauss, Dr. Arie Borenstein, Dr. Hyukmin Kwon, Daniel Maung, Wai H. Mak, Stephanie Aguilar, Mit Muni, Lisa Pangilinan, Chenhao Ji, Shaungmei Xue, Mackenzie Anderson, Chenxiang Wang, Shanlin Hu, Ethan Rao, Na He, Paige Curson, Matthew D. Kowal, Zach Sobell, Nanetta Pon, Jesus Lopez Baltazar, Guanzhou Zhu, Lindsay Chaney, Logan Steward, and Rebecca L. Li. Furthermore, my sincere gratitude goes to the hardworking staff in the department: Dr. Ignacio Martini, Dr. Robert Taylor, Dr. Xin Gong, Dr. Ivo Atanasov, Ricky Ruiz, and Hans Schieder.

For my fruitful off-work life, I appreciate people whom I shared wonderful memories with, Wai H. Mak, Dr. Po-Yen Chien, Dr. Pei-Hui (Susan) Hsu, Dr. Ming Zhang, Dr. Lei Meng, Ya-An (Chris) Yang, Mumu Tseng, Cheng-Yen (Charles) Lee, Tien-Shu Chang, Tzu-Chi (Brian) Chuang, Yi-Hsuan (Sharon) Hsiao, Wilson Li, Peng Lu, Wei Chen, Chi-An (Annie) Cheng, and my best friends in Taiwan, Chun-Gang Liu and Miao-Hsiang (Zephyr) Lin.

My gratitude also goes to Prof. Jiaxing Huang at Northwestern University who supported me strongly and inspired me a lot, and people who helped me in the freezing city of Chicago, Dr. Jaemyung Kim, Dr. Che-Ning Yeh, Prof. Vincent C. Tung, Dr. Lingxuan Peng, Dr. Yi-Kai Huang, Prof. Jiayan Luo, Dr. Xuan Dou, Dr. Bor-Rong Chen, Dr. Zeng Li, Dr. Zhibo Zhao, Dr. Yeechan Wu, Dr. Lucio Liao, Kai-Wen (Kevin) Pai, Tracy Huang, Sheng-Bo Shia, Zhengyu Liu, and Ran Zhang.

I especially thank my undergraduate advisor, Prof. Jwo-Huei Jou, for leading me into research, and Dr. Wei-Ben Wang, Dr. Shih-Ming Shen, and Dr. Chi-Ping Liu, for guiding me. Also, good peers can make you better, and I am grateful that I have wonderful classmates who always inspire me and play with me, Dr. Chun-Hao Lin, Dr. Yi-Chung Wang, Dr. Hung-Wei Tsai, Dr. Yu-Po Peng, Dr. Guan-Yu Wang, Chao-Kuei Su, Yao-Ching Hsieh, Howhow Hong, Cheng-Yen Ho, Wei-Cheng Li, Guan-Ting (NexTo) Chen, Wei-Ing Hsieh, and Ke-Hao Chen. I would also like to mention my advisor during my intern at AU Optronics, Mrs. Mei-Chiao Lin.

Finally, I would like to thank my parents for supporting me and make me dream big, and my fiancée for supporting and caring.

Chapter 2 is reprinted (adapted) with permission from (Lin, C.-W.; Mak, W.H.; McVerry, B.T.; Kaner, R.B. "Separation Techniques Using Conjugated Polymers" *Handbook of the Conducting Polymers, 4th Edition, Volume 2 Properties, Processing and Applications*, Edited by Skotheim T.A., Reynolds, J.R. and Thompson B.C., CRC Press Taylor and Francis Group, Chapter 21, pp. 629-677, 2019." Handbook of Conducting Polymers: Conjugated Polymers: Perspective, Theory, and New Materials by CRC Press. Reproduced with permission of CRC Press in the format Thesis/Dissertation via Copyright Clearance Center). Co-author contributions: Lin C.-W, Mak W.H., and McVerry B.T. wrote the paper, Richard B. Kaner was the P.I.

Chapter 3 is reprinted (adapted) with permission from (Lin, C.-W.; Wang, B.; Kaner, R.B.; Sant G.N. "Green $CO_2$ncrete™ for Sustainable Construction" *Green Chemistry: The Nexus Blog*, 2017). Co-author contributions: Lin C.-W. and Wang B. wrote the paper, Sant G.N. and Richard B. Kaner were the P.Is.

Chapter 4 is reprinted (adapted) with permission from (Shao, Y.; El-Kady, M.F.; Lin, C.-W.; Zhu, G.; Marsh, K.L.; Hwang, J.Y.; Zhang, Q.; Li, Y.; Wang, H.; Kaner, R.B. "3D Freeze-Casting of Cellular Graphene Films for Ultrahigh-Power-Density Supercapacitors" *Adv. Mater.* 2016, 28, 6719-6726 DOI: 10.1002/adma.201506157). Copyright (2016) John Wiley and Sons. Co-author contributions: Shao Y., El-Kady M.F., Lin C.-W., Zhu G., Hwang J.Y. performed the experiments, Marsh K.L. performed XPS, Zhang, Q., Li Y., Wang H., and Richard B. Kaner were the P.Is.

Chapter 5 is reprinted (adapted) with permission from (Li, R.; Lin, C.-W.; Shao, Y.; Chang C.W.; Yao, F.-K.; Kowal, M.D.; Wang, H.; Yeung, M.T.; Huang S.-C.; Kaner, R.B. "Characterization of Aniline Tetramer by MALDI TOF Mass Spectrometry upon Oxidative and Reductive Cycling" *Polymers*, 2016, 8, 401. DOI: 10.3390/polym8110401). Co-author contribution: Rebecca L. Li and Cheng-Wei Lin performed the experiments. Yuanlong Shao helped assemble devices and guided data analysis related to electrochemistry. Che Wei Chang and Fu-Kai Yao performed zeta potential testing. Matthew D. Kowal synthesized graphene oxide. Haosen Wang performed the CV testing. Michael T. Yeung acquired SEM images. Shu-Chuan Haung and Richard B. Kaner supervised the experiments and data analysis.

Chapter 6 is reprinted (adapted) with permission from (Lin, C.-W.; Aguilar, S.; Rao, E.; Mak, W.H.; Huang, X.; Jun, D.; He, N.; Chen, D.; Curson, P.; McVerry, B.T.; Hoek, E.M.V.; Huang, S.-C.; Kaner, R.B. "Direct Grafting of Tetraaniline via Perfluorophenylazide Photochemistry to Create Antifouling, Low Bio-Adhesion Surfaces" *Chemical Science*, 2019, 10, 4445-4457. DOI: 10.1039/C8SC04832K). Co-author contributions: C.-W.L. and S.A. synthesized TANI, ATFB-TANI and measured the cross-flow membrane performances, BSA rejection, contact angles, transmittances, electrical performance and performed modifications. E.R. tested BSA, *E. coli* and

*S. epidermidis* adhesions and analyzed them with ImageJ. W.H.M. made the AFM and XPS measurements. X.H. conceived the idea and obtained preliminary antifouling experiments and *E. coli* adhesion tests. N.H. helped measure the membrane fouling before and after modification. D.C. helped design the ATFB-TANI molecule. D.J. built the cross-flow system and the BSA rejection setup. P.C. helped make and modify the membranes. B.T.M. helped modify membranes and guide this work. Huang S.C. was the co-P.I., Richard B. Kaner was the P.I.

Chapter 7 is reprinted (adapted) with permission from (Lin, C.-W.; Li, R.L.; Robbennolt, S.; Yeung, M.T.; Akopov, G.; Kaner, R.B. "Furthering our Understanding of the Doping Mechanism in Conjugated Polymers Using Tetraaniline" *Macromolecules*, 2017, 50, 15, 5892-5897 DOI: 10.1021/acs.macromol.7b00633).Copyright (2017) American Chemical Society. Co-author contributions: Lin C.-W., Li R.L. and Robbennolt S. performed UV-vis, EPR and optical images, Yeung M.T. and Akopov G. performed XRD, Richard B. Kaner was the P.I.

Chapter 8 is a manuscript written by Lin C.-W., Mak W.H., Chen D., Wang H., Aguilar S., and Kaner, R.B. Co-author contributions: Lin C.-W. and Mak W.H. performed cyclic voltammograms, Chen D., Wang H., and Aguilar S. prepared samples, Richard B. Kaner was the P.I.

I would like to thank the NSF-CBET 1337065, Grant DMR-1506860, the USA/China Clean Energy Research Center for Water-Energy Technologies (CERC-WET), the UC Grand Challenge Program, and UCLA Dissertation Year Fellowship (DYF) for financial support.

# VITA

| | |
|---|---|
| 2013 - 2019 | Graduate Student with Prof. Richard B. Kaner<br>University of California, Los Angeles<br>Los Angeles, California |
| 2018 - 2019 | Dissertation Year Fellowship (DYF)<br>University of California, Los Angeles<br>Los Angeles, California |
| 2018 | Division of Physical Sciences Mautner Graduate Award<br>University of California, Los Angeles<br>Los Angeles, California |
| 2018 | Hanson-Dow Excellence in Teaching Award<br>University of California, Los Angeles<br>Los Angeles, California |
| 2015 - 2018 | Final Round in the Contest of NRG COSIA Carbon XPrize<br>University of California, Los Angeles<br>Los Angeles, California |
| 2017 | Research Showcase Travel Award for the 253$^{rd}$ ACS National Meeting<br>University of California, Los Angeles<br>Los Angeles, California |
| 2016 | Finalist in the Contest of UC Carbon Slam<br>Xerox<br>Palo Alto, California |
| 2015 | Excellence in Second Year Academic and Research Award<br>University of California, Los Angeles<br>Los Angeles, California |
| 2011 - 2013 | Master Student with Prof. Jiaxing Huang<br>Northwestern University<br>Evanston, Illinois |
| 2010 - 2011 | Corporal<br>Taiwan |
| 2006 - 2010 | Bachelor of Science with Prof. Jwo-Huei Jou<br>National Tsing-Hua Univeristy<br>Hsinchu, Taiwan |

| | |
|---|---|
| 2010 | Bachelor of Science with Prof. Jwo-Huei Jou<br>National Tsing-Hua Univeristy<br>Hsinchu, Taiwan |
| 2010 | Tien-Hsing Ho Memorial Scholarship<br>National Tsing-Hua Univeristy<br>Hsinchu, Taiwan |
| 2010 | Outstanding Award of Department of Materials Science and Engineering Undergraduate Research Competition<br>National Tsing-Hua Univeristy<br>Hsinchu, Taiwan |
| 2010 | International Access Award for International Conference Presentation<br>National Tsing-Hua Univeristy<br>Hsinchu, Taiwan |
| 2009 | Excellent Award of Department of Materials Science and Engineering Undergraduate Research Competition<br>National Tsing-Hua Univeristy<br>Hsinchu, Taiwan |
| 2008 | Excellent Project Award<br>AU Optronics<br>Hsinchu, Taiwan |
| 2007 | Academic Achievement Award<br>National Tsing-Hua Univeristy<br>Hsinchu, Taiwan |

# CHAPTER 1. INTRODUCTION

In 1834, Ferdinand Runge discovered polyaniline as a blue dye from coal tar.[1,2] In 1862, Henry Letheby performed the first electrochemical polymerization reaction of aniline with platinum electrodes, and found that the dark green precipitate was polyaniline.[3] However, electrically conducting polyaniline was not revealed until the 1970s when MacDiarmid, Heeger, and Shirakawa created the field of conducting polymers by doping polyacetylene with iodine.[4–6] Fundamental properties, such as mechanical strength, equilibrium between polarons and bipolarons and polymerization mechanisms, were mainly explored in the 1980's and 1990's.[7–9] Applications that benefit from large surface area including gas sensors, actuators, supercapacitors, *etc*. have burgeoned after 2003 due to the discovery of nanofibers formed via simple chemical reactions.[10–14] Compared to other conjugated polymers, polyaniline is especially known for its doping and de-doping chemistry by protonating and deprotonating the imine nitrogens, along with its transitions between oxidation states of leucoemeraldine, emeraldine, and pernigraniline.[9,15,16] Therefore, conjugated polyaniline has been a useful and multi-functional material for the past few decades.

In Chapter 2, a comprehensive review of conducting polymer-based membranes for gas separation, water filtration and capacitive deionization is presented.[17] This chapter starts with the first conjugated polymer-based gas separation membrane which was reported by Anderson *et al.* in 1991,[18] followed by polyaniline-composite membranes, dopable polyimide membranes and sparsely reported polypyrrole- and polythiophene-based membranes. The second part of this chapter focuses on conducting polymer-based water filtration membranes where the first polyaniline-based ultrafiltration membrane was reported in 2008.[19] The third section describes the emerging field of capacitive deionization in which conducting polymers are often mixed with

carbon materials in order to obtain high surface areas for the removal of metal ions. On the basis of polyaniline-based gas separation membranes, a collaborative project with Prof. Sant's group in the UCLA Department of Civil Engineering to turn the greenhouse gas, carbon dioxide, from power plants into cement mainly aimed at the NRG COSIA Carbon XPrize is briefly discussed in Chapter 3.

Apart from polyaniline, aniline oligomers have re-gained people's attention lately even though aniline tetramers and octamers were synthesized and considered as models of polyaniline in the early 1990s.[20–23] With the nature of being a small molecule instead of a long chain polymer, tetraaniline is not only considered as the smallest representative unit of polyaniline, but also shown to be able to form various morphologies with different acidic dopants due to its ability to crystallize.[24,25] The intrachain and interchain conductivities of tetraaniline were also tested by grafting tetraaniline molecules onto a gold surface forming a self-assembled monolayer, and crystallizing vertical tetraaniline single crystals on top of graphene, respectively.[26,27] Since tetraaniline is intrinsically similar to polyaniline, but can be readily dissolved in common organic solvents, some fundamental properties and certain processing issues related to polyaniline can be unraveled by investigating this smallest repeating unit.

In Chapter 4, a porous reduced graphene oxide film was fabricated by rapidly freezing the as-filtered reduced graphene oxide film. The expansion and crystallization of the embedded water molecules result in a beehive-like porous structure, boosting the power density of conventional supercapacitors.[28] It is known that polyaniline mixed with reduced graphene oxide is able to increase the capacitance due to the redox properties of polyaniline; however, long chain conjugated polymer-based supercapacitors often suffer through rapid performance decays.[29] Therefore, short chain tetraaniline was mixed with reduced graphene oxide as the electrode

material in order to investigate the mechanisms involved in device stability; this work was enhanced using matrix-assisted laser desorption/ionization-time of flight mass spectroscopy as described in Chapter 5.[30]

In Chapter 6, tetraaniline is reacted with pentafluorophenylazide and grafted onto different materials by exposing them to UV light. Therefore, we report the first conjugated tetraaniline-modified ultrafiltration membranes.[31] Unlike traditional polyaniline-based membranes fabricated by blending polyaniline with poly(ether)sulfone, the grafted tetraaniline can be readily applied on any commercially available membrane and may serve as seeds for further polymerization. In a similar vein, tetraaniline, with its defined number of amines and imines, when exposed to insufficient amount of dopants, is able to shed light on the doping mechanism in polyaniline. Chapter 7 reveals that the dopants tend to fill the two doping sites of an individual tetraaniline over one doping site on each of two separate tetraanilines.[32] In the final chapter, linear oligoanilines with different chain lengths and end functional groups are introduced into the aniline electrochemical polymerization system. As the formation of polyaniline is known to be autocatalytic, linear oligoanilines as additives serve as initiators for the polymerization process.[33,34] The quantified rate constants for various oligoanilines at different voltage sweeping ranges indicate that the polymerization reaction is likely to reach its rate maximum when forming aniline dimers and trimers, and starts to cease speeding up when tetramers are formed.

**REFERENCES**


(1) Runge, F. F.Ueber Einige Produkte Der Steinkohlendestillation. *Ann. der Phys. und Chemie* **1834**, 65–78.

(2) Rasmussen, S. C.The Early History of Polyaniline: Discovery and Origins. *Substantia* **2017**, *1*.

(3) Letheby, H.XXIX.—On the Production of a Blue Substance by the Electrolysis of Sulphate of Aniline. *J. Chem. Soc.* **1862**, *15*, 161–163.

(4) Shirakawa, H.The Discovery of Polyacetylene Film: The Dawning of an Era of Conducting Polymers (Nobel Lecture)**. *Angew. Chemie Int. Ed.* **2000**, *40*, 2574–2580.

(5) Macdiarmid, A. G."Synthetic Metals": A Novel Role for Organic Polymers ( Nobel Lecture )**. *Angew. Chemie Int. Ed.* **2001**, *40*, 2581–2590.

(6) Heeger, A. J.Semiconducting and Metallic Polymers: The Fourth Generation of Polymeric Materials ( Nobel Lecture )**. *Angew. Chemie Int. Ed.* **2001**, *40*, 2591–2611.

(7) J.L., B.; G.B., S.Polarons , Bipolarons , and Solitons in Conducting Polymers. *Acc. Chem. Res.* **1985**, *18*, 309–315.

(8) Sasaki, K.; Kaya, M.; Yano, J.; Kitani, A.; Kunai, A.Growth Mechanism in the Electropolymerization of Aniline and P-Aminodiphenylamine. *J. Electroanal. Chem. Interfacial Electrochem.* **1986**, *215*, 401–407.

(9) Jin-Chih, J.; Macdiarmid, A. G."Polyaniline": Protonic Acid Doping of the Emeraldine Form to the Metallic Regime. *Synth. Met.* **1986**, *13*, 193–205.

(10) Huang, J.; Virji, S.; Weiller, B. H.; Kaner, R. B.Polyaniline Nanofibers: Facile Synthesis and Chemical Sensors. *J. Am. Chem. Soc.* **2003**, *125*, 314–315.

(11) Huang, J.; Kaner, R. B.A General Chemical Route to Polyaniline Nanofibers. *J. Am.*

*Chem. Soc.* **2004**, *126*, 851–855.

(12) Pan, L.; Yu, G.; Zhai, D.; Lee, H. R.; Zhao, W.; Liu, N.; Wang, H.; Tee, B. C.-K.; Shi, Y.; Cui, Y.; et al.Hierarchical Nanostructured Conducting Polymer Hydrogel with High Electrochemical Activity. *Proc. Natl. Acad. Sci.* **2012**, *109*, 9287–9292.

(13) Baker, B. C. O.; Shedd, B.; Innis, P. C.; Whitten, P. G.; Spinks, G. M.; Wallace, G. G.; Kaner, R. B.Monolithic Actuators from Flash-Welded Polyaniline Nanofibers. *Adv. Mater.* **2008**, *20*, 155–158.

(14) Baker, C. O.; Huang, X.; Nelson, W.; Kaner, R. B.Polyaniline Nanofibers: Broadening Applications for Conducting Polymers. *Chem. Soc. Rev.* **2017**, *46*, 1510–1525.

(15) Libert, J.; Bredas, J. L.; Epstein, A. J.Theoretical Study of P- and n-Type Doping of the Leucoemeraldine Base Form of Polyaniline: Evolution of the Geometric and Electronic Structure. *Phys. Rev. B* **1995**, *51*, 5711–5724.

(16) MacDiarmid, A. G.; Manohar, S. K.; Masters, J. G.; Sun, Y.; Weiss, H.; Epstein, A. J.Polyaniline: Synthesis and Properties of Pernigraniline Base. *Synth. Met.* **1991**, *41*, 621–626.

(17) Lin, Cheng-Wei; Mak, Wai; McVerry, Brian; Kaner, R.Separations Using Conjugated Polymers. In *Handbook of the Conducting Polymers, 4th Edition,*; Skotheim, T.A.; Reynolds, J.R.; Thompson, B. C. ., Ed.; CRC Press Taylor and Francis Group, 2019; pp 629–677.

(18) Anderson, M. R.; Mattes, B. R.; Reiss, H.; Kaner, R. B.Conjugated Polymer Films for Gas Separations. *Science (80-. ).* **1991**, *252*, 1412–1415.

(19) Fan, Z.; Wang, Z.; Sun, N.; Wang, J.; Wang, S.Performance Improvement of Polysulfone Ultrafiltration Membrane by Blending with Polyaniline Nanofibers. *J. Memb. Sci.* **2008**,

*320*, 363–371.

(20) Javadi, H. H. S.; Treat, S. P.; Ginder, J. M.; Wolf, J. F.; Epstein, A. J.Aniline Tetramers: Comparison with Aniline Octamer and Polyaniline. *J. Phys. Chem. Solids* **1990**, *51*, 107–112.

(21) Vaschetto, M. E.; Retamal, B. A.; Contreras, M. L.; Zagal, J. H.; Bulhõ es, L. O. S.Theoretical Studies of Physicochemical Properties of Aniline Oligomers: Analysis of Counterion Influence. *Struct. Chem.* **1995**, *6*, 131–140.

(22) Cao, Y.; Li, S.; Xue, Z.; Guo, D.Spectroscopic and Electrical Characterization of Some Aniline Oligomers and Polyaniline. *Synth. Met.* **1986**, *16*, 305–315.

(23) Zhang, W. J.; Fen, J.; Macdiarmida, A. G.Synthesis of Oligomeric Anilines. *Synth. Met.* **1997**, *84*, 119–120.

(24) Wang, Y.; Tran, H. D.; Liao, L.; Duan, X.; Kaner, R. B.Nanoscale Morphology, Dimensional Control, and Electrical Properties of Oligoanilines. *J. Am. Chem. Soc.* **2010**, *132*, 10365–10373.

(25) Wang, Y.; Tran, H. D.; Kaner, R. B.Applications of Oligomers for Nanostructured Conducting Polymers. *Macromol. Rapid Commun.* **2011**, *32*, 35–49.

(26) Ford, W. E.; Gao, D.; Scholz, F.; Nelles, G.; VonWrochem, F.Resistive Switching of Tetraaniline Films: From Ultrathin Monolayers to Robust Polymeric Blends. *Chem. Mater.* **2013**, *25*, 3603–3613.

(27) Wang, Y.; Torres, J. A.; Stieg, A. Z.; Jiang, S.; Yeung, M. T.; Rubin, Y.; Chaudhuri, S.; Duan, X.; Kaner, R. B.; Al, W. E. T.Graphene-Assisted Solution Growth of Vertically Oriented Organic Semiconducting Single Crystals. **2015**, No. Xx.

(28) Shao, Y.; El-Kady, M. F.; Lin, C. W.; Zhu, G.; Marsh, K. L.; Hwang, J. Y.; Zhang, Q.; Li,

Y.; Wang, H.; Kaner, R. B.3D Freeze-Casting of Cellular Graphene Films for Ultrahigh-Power-Density Supercapacitors. *Adv. Mater.* **2016**, 6719–6726.

(29) Yan, J.; Yang, L.; Cui, M.; Wang, X.; Chee, K. J.; Nguyen, V. C.; Kumar, V.; Sumboja, A.; Wang, M.; Lee, P. S.Aniline Tetramer-Graphene Oxide Composites for High Performance Supercapacitors. *Adv. Energy Mater.* **2014**, *4*, 1–7.

(30) Li, R. L.; Lin, C. W.; Shao, Y.; Chang, C. W.; Yao, F. K.; Kowal, M. D.; Wang, H.; Yeung, M. T.; Huang, S. C.; Kaner, R. B.Characterization of Aniline Tetramer by MALDI TOF Mass Spectrometry upon Oxidative and Reductive Cycling. *Polymers (Basel).* **2016**, *8*, DOI:10.3390/polym8110401.

(31) Lin, C.-W.; Aguilar, S.; Rao, E.; Mak, W. H.; Huang, X.; He, N.; Chen, D.; Jun, D.; Curson, P. A.; McVerry, B. T.; et al.Direct Grafting of Tetraaniline via Perfluorophenylazide Photochemistry to Create Antifouling, Low Bio-Adhesion Surfaces. *Chem. Sci.* **2019**, 4445–4457.

(32) Lin, C.; Li, R. L.; Robbennolt, S.; Yeung, M. T.; Akopov, G.; Kaner, R. B.Furthering Our Understanding of the Doping Mechanism in Conjugated Polymers Using Tetraaniline. *Macromolecules* **2017**, *50*, 5892–5897.

(33) Li, W.; Wang, H. L.Oligomer-Assisted Synthesis of Chiral Polyaniline Nanofibers. *J. Am. Chem. Soc.* **2004**, *126*, 2278–2279.

(34) Shim, Y.-B.; Park, S.-M.Electrochemistry of Conductive Polymers VII. Autocatalytic Rate Constant for Polyaniline Growth. *Synth. Met.* **1989**, *29*, 169–174.

# CHAPTER 2. SEPARATION TECHNIQUES USING CONJUGATED POLYMERS



## 2.1 Gas Separation Membranes Using Conjugated Polymers

### 2.1.1 Outline of the Review

Membranes are widely used in many fields, including wastewater treatment, gas purification/enrichment, fuel cells, dialysis, forward/reverse osmosis (RO), batteries, food technology, electro-deionization, pharmaceuticals, *etc*.[1-4] Membranes for separation can be categorized based on their pore size for different applications, for example: 10-100 μm for conventional filtration, 0.1-10 μm for microfiltration (MF), 50-1000 Å for ultrafiltration (UF), and smaller than 50 Å for RO and gas separation.[5] The driving forces for separation can be the gradients of concentration, temperature, pressure, and/or external/internal electric potential. Materials for fabricating membranes include organic, inorganic, ceramic, polymeric, and mixtures of these. Most commercial membranes are polymeric due to their advantages of low cost and the ability to use roll-to-roll processing. Here we focus on applications of conjugated polymers for selected separations. First, conjugated polymer-based gas separation membranes using polyaniline will be introduced, followed by the use of other conjugated polymers and then composite membranes (Section 2.1). Second, conjugated polymer-based membranes for water purification will be discussed (Section 2.2), followed by the emerging field of capacitive

deionization (Section 2.3). This review highlights the synthesis, mechanisms and performances of membrane technologies that specifically use conjugated polymers.

### 2.1.2 Overview

#### 2.1.2.1 Gas Separation Membranes

The technology of gas separation using membranes has been applied industrially for decades. The most common gas separations include the partitioning of nitrogen and oxygen from air, the recovery of hydrogen from ammonia in the Haber-Bösch process, the recovery of hydrogen in oil refinery processes, gas purification from coal or natural gas power plants, the removal of volatile organic liquids or water vapor from exhaust gases, gas enrichment, and many others.[6,7] The materials used for fabricating membranes can be briefly categorized into polymeric, inorganic, and mixed matrix. Polymeric membranes are the most commonly used materials due to their advantages, including relatively low cost, facile processing, and extraordinary flexibility. On the other hand, silica, zeolite and perovskite are the most used inorganic materials for gas separation membranes. Inorganic membranes are considered more durable, and thermally and chemically more stable than organic membranes; however, these materials are harder to fabricate on a large scale and are brittle and more expensive.[7] Recently, graphene, graphene oxide, metal-organic-frameworks (MOFs), and covalent-organic-frameworks (COFs) have attracted a great deal of attention with the potential to be used for gas separations.[8-14] Mixed matrix membranes generally contain two or more materials in order to enhance certain properties, such as permeability, mechanical properties, or thermal stability.

Polymeric membranes used for gas separations can be categorized into two types: rubbery polymers and glassy polymers. Common rubbery polymers include

polydimethylsiloxane (PDMS), ethylene oxide and polyamides; while glassy polymers include cellulose acetate (CA), polycarbonates, polyimides, poly(phenylene oxides) (PPOs), perfluoropolymers, and polysulfone (PSF). When the glass transition temperature ($T_g$) of a polymer is lower than the operating temperature, the polymer is in its rubbery state. Rubbery polymer chains are more mobile (*i.e.* greater freedom of movement) and often possess higher permeabilities due to the presence of voids, but offer lower selectivity and poor mechanical properties. Therefore, glassy polymers with their stiffer polymer chains and higher selectivity are more commonly used industrially.[15,16] A general method for solving the lower permeability problem inherent in glassy polymers is by adding bulky functional groups to enlarge the size of pores.

The chemical structures of most common commercial polymers are shown in **Figure 2-1**. The top part shows PDMS and two polyamide polymers, all of which are in their rubbery state at ambient temperature. The bottom part of **Figure 2-1** displays polymers that exist in their glassy state at room temperature, including cellulose, polycarbonate, PPO, polyimides, and polysulfones. In the next section, we introduce polyaniline-based gas separation membranes, the first gas separation membranes to employ conjugated polymers, followed by a discussion of the separation mechanism. Other conjugated polymer-based membranes and composite membranes are discussed at the end of this section.

#### 2.1.2.2 Mechanism of Gas Separation

In a laboratory-scale test, membranes are loaded into a well-sealed cell, as illustrated in **Figure 2-2a**. The feed gas is first adsorbed at the interface of the membrane. Second, the gas molecules diffuse across the membrane. Third, the gas molecules desorb at the interface of the membrane to

create the permeant gas at the downstream side. The entire gas transport process is known as *permeation.*[17,18] Industrially, membranes are scrolled individually and bundled together, or scrolled in stacks in a cartridge in order to increase efficiency (**Figure 2-2b,c**).[19] In theory, the permeation of a gas through a membrane is attributed to both kinetic and thermodynamic interactions between the membranes and the permeant gas molecules. The permeability (P) is expressed as the product of the diffusion coefficient or diffusivity (D), and the solubility coefficient (S) as given in **Equation 2-1**.[1,20]

$$P = D \times S \tag{2-1}$$

The diffusion coefficient is well known from Fick's Laws of Diffusion and is typically expressed in units of $cm^2$/sec. The diffusion coefficient is mainly affected by the kinetic diameter of the gas molecules versus the pore sizes in the membrane material. When the pore size is significantly larger than the size of gas molecules and the gas pressure is relatively low, Knudsen diffusion occurs so that lighter gas molecules travel faster across a membrane than heavier molecules at a rate inversely proportional to the square root of their masses. For example, the permeation of nitrogen ($M_w$ = 28 g/mol) is faster than oxygen ($M_w$ = 32 g/mol) (Graham's Law) by a factor of 1.07. Size exclusion, also known as *molecular sieving*, plays an important role in the diffusion process when the gas molecules are comparable to the size of the membrane's pores.[21] However, the pore size of gas separation membranes is very hard to control. On the other hand, the solubility coefficient measures the rate at which gas molecules dissolve into a material at steady-state, generally expressed in $cm^3$ (STP)/$cm^3 \cdot$ cmHg, where 1 $cm^3$ (STP)/$cm^3 \cdot$ cmHg $= 10^{10}$ Barrers as given in **Equation 2-2**.

$$1 \text{ Barrer} = 10^{-10} \frac{cm^3 \text{ (STP)} \cdot cm}{cm^2 \cdot s \cdot cmHg} \tag{2-2}$$

During the experiment, the permeability and diffusion coefficients can be acquired by plotting the penetrant gas concentration versus time, as shown in **Figure 2-3**. Before a time lag, $\tau$, the membrane is still in the unsteady state where the membrane has not yet saturated with the sorbing gas. After time $\tau$, the slope of the curve is taken as the diffusion rate, also known as the permeability (P). The extrapolation from the steady state diffusion rate through the time axis, $\tau$, is related to the diffusion coefficient (D) by the equation: $\tau = l^2/6D$, where $l$ is the thickness of the membrane. Thus, the solubility coefficient can be calculated from **Equation 2-1**. The solubility can be altered by adding functional groups and/or branches onto the backbone of the polymer in order to create more favorable interactions with gas molecules.[16] For example, **Table 2-1** shows the measured permeability and solubility coefficients for $N_2$, $O_2$, $CO_2$, and $CH_4$ in poly[1-(trimethylsilyl)-1propyne] (PTMSP) and PDMS under different temperatures.[22] The diffusivities are derived from the relation D = P/S. The diffusion coefficients for both PTMSP and PDMS are similar; however, the relative high solubility numbers in PTMSP compared to PDMS result in the higher permeabilities for all gases listed.

In order to achieve separations, an enormous difference between the permeabilities is desired. Hence, permeability selectivity or permselectivity, $\alpha$, is defined as the ratio between the two gas permeabilities:

$$\alpha_{ij} = \frac{P_i}{P_j} = \frac{D_i}{D_j} \times \frac{S_i}{S_j} \qquad (2\text{-}3)$$

An ideal separator should therefore possess both high permeability and high selectivity. However, after testing many membranes, researchers found a trade-off between the selectivity and the permeability coefficient. In 1991, Robeson proposed an empirical upper-bound for selectivity-permeability plotted on a log scale (**Figure 2-4a,b**).[19,23,24] In 1999, Freeman predicted the upper-

bound by theoretical calculations based on gas kinetic diameters.[25] Thereafter, the upper-bound has become the indicator for evaluating membrane separations. As shown in **Figure 2-4b**,**c**, scientists have been trying to push the upper-bounds further, *i.e.* higher permeability with higher selectivity, by using more advanced materials.

### 2.1.3 Polyaniline Films for Gas Separation

#### 2.1.3.1 Polyaniline Freestanding Membranes

Gas molecules are small in size; hence, making a sufficiently dense polymeric membrane with angstrom size pores for gas separation is crucial. However, making dense films makes using conjugated polymers problematic since most of them possess quite rigid backbones. The rigid π bonded backbones often lead to fibrillar morphologies, which then form larger pores.[26] For example, chemically synthesized polyacetylene (PA) and electrochemically synthesized polyaniline both possess a fibrillar morphology.[27] Here, we introduce tuning the pore size of chemically produced polyaniline membranes through doping, de-doping and partial re-doping in order to achieve the first reported gas separation by using conjugated polymer-based membranes.[28]

The fabrication process for polyaniline membranes is quite straightforward. Polyaniline powder in the emeraldine base form made from chemical synthesis ($M_w$ ~17 kDa) or purchased from a company (e.g. Sigma Aldrich, $M_w$ ~20 kDa) is dispersed in N-methyl-2-pyrrolidone (NMP) with a concentration of around 5.0 % w/v. Low molecular weight polyaniline, *i.e.* 5 or 10 kDa, results in brittle films that leads to severe cracking during the drying process due to the poor mechanical properties resulting from insufficient chain entanglement. High molecular weight polyaniline, *i.e.* 50 kDa and above, does not form homogeneous solutions due to

gelation.[29] When 17-20 kDa polyaniline is dispersed in NMP, a dark blue viscous solution is produced. Stirring with a magnetic stir bar for 1-2 hours results in a homogeneous solution after filtering. The filtering process is used to prevent the presence of small particles in the membrane, which can accumulate strain leading to cracks. The solution is then gently transferred onto glass plates. The polymer-coated glass substrates are cured in an oven (without vacuum) at 120℃ - 135℃ for 3 hours to remove most of the NMP. After the heat treatment, the polymer-coated glass plates are dried under dynamic vacuum for >24 hours in order to further dry the membranes. The polymer-coated glass plates are immersed into a water bath, and after soaking for 20 min to 1 hour, the pristine, free-standing polyaniline membranes can be peeled off from the edges with the help of a razor blade.[28] A good pristine polyaniline film should show a smooth, shiny surface (**Figure 2-5a**).

In order to make sufficiently dense polyaniline membranes for gas separation, a reasonably high concentration of polyaniline in NMP (5% w/v) is needed. The thickness of the film can be tuned by altering the volume of solution put onto a glass plate. For example, 0.3 mL of the 5% w/v solution placed onto a 1 inch$^2$ plate results in a membrane with a thickness of around 20 µm, as shown in **Figure 2-5b**. Polyaniline films with thicknesses between 3 and 100 µm are desired. Thicker films decrease the permeability too much, while thinner films are usually too fragile. The film shown in **Figure 2-5b** possesses some flexibility, as shown in **Figure 2-5c**.

#### 2.1.3.2 Mechanism of Gas Separation

Polyaniline is one of the most common conducting polymers that was re-discovered in the early 1980s.[30] Its facile synthesis[31,32] and its thermal and chemical stability[33,34] make polyaniline an

interesting and much studied material for many applications, including gas sensors,[35] batteries,[36] supercapacitors,[37,38] anti-corrosion coatings,[39] electrochromic devices,[40] actuators,[41,42] *etc.*[43,44] Polyaniline has three main oxidation states: leucoemeraldine, emeraldine, and pernigraniline.[45,46] These three oxidation states are interchangeable by oxidizing/reducing amine/imine nitrogens to imine/amine nitrogens (**Figure 2-6a**). The electrically insulating emeraldine base form (blue in color) ($\sigma \leqq 10^{-10}$ S/cm) can be doped/protonated by acids, forming conducting emeraldine salts (green in color) ($\sigma \geqq 1$ S/cm), as shown in **Figure 2-6b**.[31] The doping/de-doping process can be carried out either chemically and electrochemically. The dopants, *i.e.* acids, can protonate the imine nitrogens as the anions form counterions around the polyaniline chains. The counterions that associate with polymer chains can be considered as functional groups that can be easily removed by de-doping or washing with water or other solvents. The loss of counter-anions then leaves pores behind, with the pore size dependent on the size of the counterions. Recently, this concept has been applied to make electrodes for batteries and supercapacitors where researchers use fatty acids, ex: phytic acids, as dopants and form 3D porous polyaniline hydrogels with larger pores that serve as ion channels after removal of the dopants.[47]

As can be seen in the schematic in **Figure 2-7**, an as-cast polyaniline membrane has a number of pores (**Figure 2-7a**). Initially, the dopants fill parts of the pores and reduce the permeability for a heavily doped membrane (**Figure 2-7b**). These dopants can be removed by neutralizing and removing the acid groups with aqueous base. The fully de-doped membrane possesses even larger pores due to the removal of the counterions surrounding the polyaniline chains (**Figure 2-7c**). Since the angstrom-size pores in the membranes can serve as molecular sieves and affect the gas permeability, the permeability for the fully de-doped membrane increases, while the selectivity decreases. Finally, the membrane is partially re-doped in order to

tune the permeability and selectivity (**Figure 2-7d**). The dopants are believed to partially re-fill the pores left from the de-doping process. Based on experiments, the level of doping and the type of the dopants can profoundly affect the performance of the membrane.[28]

#### 2.1.3.3 Membrane Performance and the Effect of Dopants

For an as-cast membrane, the permeability of gases mainly depends on the kinetic diameter of the gas molecules due to the effect of molecular sieving (**Figure 2-8**). This also suggests that for an as-cast polyaniline membrane, the permeability is primarily influenced by diffusion instead of solubility. Note, however, that the permeability of oxygen is higher than argon even though oxygen is slightly larger in size; this may be attributed to the higher solubility of oxygen in polyaniline membranes.[28] For an as-cast membrane, hydrogen has a permeability of 3.08 Barrers, while nitrogen has a permeability of only 0.014 Barrers; hence, the selectivity of $H_2/N_2$ is 207. We performed tests on hydrochloric acid (HCl)-doped membranes, de-doped membranes, and partially re-doped membranes. As shown in **Figure 2-9**, these doped membranes possess slightly lower permeabilities for both nitrogen and hydrogen, with a selectivity equal to 260. When the dopants are removed by base, voids form increasing the permeability of nitrogen by around two orders of magnitude, and of hydrogen by more than one order of magnitude. The higher permeabilities result in a decrease in selectivity. In order to perform the partial re-doping of the membranes, a dilute acid solution was used to treat the de-doped membranes. The measured selectivity of $H_2/N_2$ then increased dramatically to 3590 as both the permeability of hydrogen and nitrogen decrease.

As previously mentioned, the level of doping can affect the performance of the membrane. The doping level of the polyaniline membrane protonated with $HCl_{(aq)}$ can be

examined by the ratio between nitrogen and chlorine anions. The freestanding un-doped polyaniline film showed a selectivity of 9.5 for $O_2/N_2$, with the selectivity increasing to 14.9 for 36% doping and 15.2 for fully (50%) doped membranes. Measurements of $O_2/N_2$ selectivity with various dopants were also tested under the same doping level (36%) with the following results: 13.4 for sulfuric acid, 14.9 for *p*-toluenesulfonic acid, and 14.8 for nitric acid.

For systematically investigating how the dopants affect the permeability of membranes, a series of halogen acids were used as dopants. The as-cast membranes were first doped with $HF_{(aq)}$, $HCl_{(aq)}$, $HBr_{(aq)}$, and $HI_{(aq)}$, then neutralized and removed by adding $NH_4OH_{(aq)}$ followed by rinsing with deionized water, to obtain membranes with different pore sizes. Based on the measured permeabilities of gases: He, $H_2$, $CO_2$, Ar, $O_2$, and $N_2$, the HF-doped/de-doped membrane had the highest permeability of all gases tested followed by HCl, HBr, HI doped/de-doped membranes, as shown in **Figure 2-10**. Because all of the halogen acid-removed membranes possess greater permeabilities than an as-cast one, this verifies the mechanism that the removal of the dopants leaves voids in the membranes so that the permeability increases compared to pristine dense membranes. The counterintuitive trend for all the permeant gases, *i.e.* the decreasing permeabilities from HF, HCl, HBr, to HI de-doped membranes is due to the hydrated radii of the dopants where hydrated HF is actually the largest dopant.[48,49] When we performed the same experiments with anhydrous halogen acid gases, followed by de-doping with anhydrous ammonia, the trend in permeability was reversed.[28,48] This is consistent with the crystal radii of the non-hydrated halides where $I^- > Br^- > Cl^- > F^-$. Thus the pore size of the membranes is directly correlated to the size of the dopants removed (**Figure 2-11**).

### 2.1.4 Other Conjugated Polymers and Composite Membranes

As illustrated in **Figure 2-12**, the most common conducting polymers are polyaniline, PA, polyphenylene vinylene, polypyrrole, and polythiophene. PA, the first conducting polymer discovered, is not suitable for making gas separation membranes because it slowly degrades in air.[50,51] Polyaniline- and polypyrrole-based membranes are more widely studied, likely due to their facile synthesis and ability to form dense membranes.[52]

### 2.1.4.1 Polyaniline-Based Membranes

After our publication of the first polyaniline gas separation membrane, other researchers observed similar doping effects on polyaniline membranes, but with lower selectivities. For example, Illing *et al.* tested dense polyaniline film but ended up with 151, 17, 5, for the selectivity of $H_2/N_2$, $CO_2/N_2$, and $O_2/N_2$, respectively.[53,54] The lower selectivity may be attributed to the forming of micro defects in the membrane during the fabrication process. The membranes fabricated by Illing *et al.* were dried at 80 ℃ for 12 hours, followed by annealing under 125 ℃ for 1 hour; however, membranes reported by Anderson *et al.* were cured under 135 ℃ for 1-3 hours. The higher temperature may cause cross-linking between polyaniline chains,[55,56] forming even more dense membranes. Scientists have also attempted to fabricate ultrathin films in order to increase the permeation of gases.[57] In 1994, Kuwabata *et al.* reported both polyaniline freestanding films (thickness = 10-25 μm) and ultrathin polyaniline films on an aluminum supporting layer (thickness = 1.5-4 μm). The freestanding membranes showed an increase in the selectivity of $O_2/N_2$ as the thickness of the film increased; the reported values are very similar to what Anderson *et al.* reported for films thicker than 20 μm.[58] However, the 1.5 μm thick film with the supporting layer showed 0.93 for the selectivity of $O_2/N_2$. This is close to the value of 0.935 expected for Knudsen diffusion where the gases permeate inversely proportional to the square root of their mass.[58] Kuwabata *et al.* claimed that the loss of the selectivity may be

attributed to micro defects in the ultrathin membrane, and concluded the critical thickness for polyaniline film should be at least 3 μm in order to achieve good selectivity. **Table 2-2** lists several reported values for different thicknesses of polyaniline films. Note that for thicknesses over 20 μm, the selectivity of $O_2/N_2$ is always greater than 9, which is consistent with our original report from 1994.

One of the ways to improve the permeation flux is to reinforce the mechanical strength of the membrane by adding a strong supporting layer. The supporting layer has to be macroporous so that it does not hinder gas permeation, but the enhanced strength is needed so that the membranes can survive under relatively high pressure. Typical materials applied as the supporting layer are nylon, polystyrene (PS), polyvinylidene fluoride (PVDF), and polyethylene (PE). Polyaniline, when put onto supporting layers, possesses moderate selectivities but much higher permeabilities compared to those without supporting layers.[59]

Another approach is to form a polyblend. In general, mixing polymers wit physical properties in between the parent polymers forms a composite known as a polyblend. Hence, the selectivity and permeability of a polyblend can be readily tuned by blending different polymers and altering their ratios. A typical example of a polyaniline/polyimide polyblend was reported by Su, *et al.*, where equal amounts of polyimide were mixed with polyaniline. The selectivity of $H_2/N_2$, $CO_2/CH_4$, and $O_2/N_2$ is roughly equal to or in between those of the parent polymers; while the permeability of gases is superior to both polyaniline and polyimide, as shown in **Table 2-3**.[60] Orlov, *et al.* blended polyvinyltrimethylsilane (PVTMS), a polymer with very high permeability, with polyaniline, resulting in decreases in permeability of all gases compared to intrinsic PVTMS, but with three and fourfold increases in the selectivity of $He/N_2$ and $He/CH_4$, respectively.[61] Zhao *et al.* incorporated polyaniline nanoparticles into a matrix of polyvinylamine,

achieving a high selectivity for $CO_2$ and $N_2$ separation.[62] Giel, *et al.* reported polyaniline/polybenzimidazole blends with 0-20 wt% of polyaniline added. The composite exhibited high selectivities, especially for $CO_2/O_2$, $O_2/N_2$, and $CO_2/N_2$.[63]

Instead of blending, Weng, *et al.* reported a synthetic polymer that grafted amine-capped aniline trimer onto polyimide, forming a dopable polyimide (PDI), as shown in **Figure 2-13a**. This material is similar to polyaniline, which can be oxidized/reduced and doped/de-doped. The membrane possessed polyaniline-like color and surfaces; however, the PDI offered better mechanical properties compared to polyaniline and conventional non-PDI. Membranes cast with this mechanically strong and flexible material (**Figure 2-13b**) had much higher oxygen permeability compared to polyaniline and polyaniline/polyimide blends. Amazingly, the selectivity of $O_2/N_2$ of this membrane is nearly the highest among all reported polyaniline/polyimide blends and non-DPI. The selectivity of $O_2/N_2$ even increases from 13.5 to 16.6 when the membrane is doped (**Table 2-5**).[64] Recently, the first work on surface polymerization has been carried out by Ghalei, *et al.* who used a facile interfacial polymerization of polyaniline on a "polymer of intrinsic microporosity" (PIM-1) (**Figure 2-14**), and examined the membranes thoroughly. The formation of a dense polyaniline film on top of PIM-1 achieved high $H_2$ selectivities without significant decreases in permeabilities (**Table 2-5**). When halogen acids (HCl, HBr, and HI) were used to dope the PIM-1 membranes, the resulting trends in permeabilities again agree with the trend of the hydrated radii of anions ($Cl^- > Br^- > I^-$) (**Table 2-4**).[65]

### 2.1.4.2 Polypyrrole and Polythiophene-Based Membranes

The first polypyrrole-based gas separation membrane was reported by Liang and Martin in 1991.[66] They performed interfacial polymerization of polypyrrole on an alumina support membrane with iron nitrate as the oxidant. However, the doped polypyrrole membrane was observed to have a selectivity for $O_2/N_2$ of only 0.94, indicating Knudsen diffusion likely due to the porous structure of their polypyrrole. Thereafter, Liang and Martin used poly(N-methylpyrrole) (PMPy) as a membrane material and acquired 6.2 and 31.9 for the selectivity of $O_2/N_2$ and $CO_2/CH_4$, respectively. They also doped the PMPy membrane with nitric acid and still maintained good selectivities. Most of the polypyrrole-based membranes were studied around the year 2000, when researchers carried out either chemical or electrochemical synthesis on support membranes due to the poor mechanical properties of pristine polypyrrole membranes.[67-69] In 2003, Hacarlioglu, *et al.* compared the performances of a chemically synthesized polypyrrole/polycarbonate composite (CPPY-PC) and an electrochemically synthesized polypyrrole/polycarbonate composite (ECPPY-PC). As shown in **Table 2-6**, ECPPY-PC possessed higher permeability for all gases tested compared to CPPY-PC; while the CPPY-PC had much higher selectivities.[70]

The literature on polythiophene-based gas separation membranes is sparse. Musselman, *et al.* reported the permeability of poly(3-dodecylthiophene) (PDDT) membranes with different oxidation levels. Originally, pristine PDDT membranes suffered from low selectivities; Musselman, *et al.* doped/oxidized them with $SbCl_5$, achieving higher selectivities with lower permeabilities caused by the more rigid polymer chains, as shown in **Table 2-6**. Based on their experiments on different oxidized PDDT and hydrazine treated PDDT membranes, the level of oxidation was found to be directly proportional to the selectivity.[71]

### 2.1.5 Conclusions

Conjugated polymer-based membranes for gas separations are mostly comprised of polyaniline or aniline derivatives. Polyaniline, as a promising material for gas separation membranes, can be easily synthesized and forms sufficiently dense membranes so that Knudsen diffusion, which indicates pinholes, is avoided. On the other hand, polypyrrole and polythiophene membranes are usually made by chemical or electrochemical deposition onto supporting membranes due to the poor mechanical properties of these polymers by themselves. The lower permeability of polypyrrole and polythiophene-based membranes may be due to the tendency of forming micro-defects during membrane fabrication.

The strategy of adding and removing dopants from these conjugated polymer membranes enables the tuning of both permeability and selectivity. Permeability can be enhanced by doping and de-doping the polymers to increase the void space in the membranes. Selectivity can be enhanced by doping or re-doping to select levels with appropriate dopants. Another common way of altering membrane performance is to physically blend parent polymers, for example, polyaniline is often mixed with polyimides that usually possess higher permeability to all gases compared to polyaniline. Thus, the resulting polyblends typically have both permeability and selectivity in between that of polyaniline and polyimides. Chemically synthesizing co-polymers of conjugated polymers with polyimides or other polymers is also feasible, but more studies are needed in order to further elucidate the mechanism(s) and design rules.

## 2.2 Conjugated Polymer – Based Membranes for Water Purification

### 2.2.1 Introduction

Membranes for liquid separations can be categorized into RO, nanofiltration (NF), UF, MF, and conventional filtration, as mentioned in the introduction to Section 2.1. These membranes are widely used in various industries, including fertilizer production, petroleum refining, sterilization, biotechnology, dairy processing, wastewater treatment, *etc*. The separation process strongly depends on the size of the unwanted material being removed due to a sieving effect. For example, conventional filtration deals with contaminants with sizes larger than 10 μm, such as human hair and oil emulsions. UF membranes sieve out micro-pollutants, including proteins, bacteria, and viruses. RO membranes mainly focus on the removal of pollutants with sizes smaller than 5 nm, such as metal ions, dyes, and salts (**Figure 2-15**). Recently, scientists and engineers have focused a great deal of effort on membrane technologies for water purification because of the urgent need for clean drinking water due to population growth.[72,73]

For water purification, conjugated polymers have mainly been explored in two areas: heavy metal ion removal,[74] and antifouling UF membranes.[75,76] The mechanism of heavy metal ion removal, including Hg(II), Cr(VI), Cd(II), Cu(II), Eu(III), *etc*., is attributed to the adsorption of porous conjugated polymers and the chelating effect of functional groups, *e.g.* amines and imines on polyaniline, and amino groups on polypyrrole.[74] Researchers have mixed conjugated polymers with organic or inorganic materials, such as silica, graphene, inorganic salts, carbon nanotubes (CNTs), sawdust, *etc*., in order to tune the morphology of the polymers and enhance their surface areas, leading to higher adsorption capabilities.[77-80] On the other hand, UF is often used as a treatment after conventional filtration, and before entering an RO system. General

commercial UF membranes are made of polymers such as PSF, PVDF, polypropylene (PP), polyacrylonitrile (PAN), polyether ether ketone (PEEK), and polyurethane (PU), whose chemical structures are shown in **Figure 2-16**. However, the accumulation and proliferation of proteins and microorganisms on the abovementioned hydrophobic membranes over time, *i.e.* fouling, can severely block the pores and drastically reduce the permeation flux. Therefore, fabricating intrinsic low fouling or antifouling UF membranes is crucial for water treatment. In this section, we summarize studies on conjugated polymer-based UF membranes, emphasizing their unique characteristics, especially the antibacterial and hydrophilic properties of the membrane surfaces.

### 2.2.2 Fouling and Antifouling Membranes

#### 2.2.2.1 Fouling

Fouling is the process of pollutants accumulating and depositing onto membrane surfaces over time; these pollutants are named *foulants*. Typically, foulants can be classified into three categories: inorganic, organic, and biofoulants. Inorganic foulants include micro/nanoparticles of silica, metal oxides/hydroxides, and mixed organic/inorganic colloids. Organic foulants include protein macromolecules, *e.g.* oil, bovine serum albumin (BSA), humic acid (HA), and sodium alginate (SA). Different from inorganic and organic foulants, which adhere and form stable cake layers on the surfaces of membranes,[81,82] biofoulants are generally bacteria and algae that can proliferate once attached to a surface.[83,84] Commonly found biofoulants include Gram negative *Escherichia coli (E. coli)* and Gram positive *Staphylococcus aureus (S. aureus)*. Fouling may occur during all types of membrane filtrations, and involves the accumulation, spreading, and proliferation of foulants that clog the membrane pores, decrease the permeation flux,

contaminate the filtrate, and can even cause damage to the membrane (**Figure 2-17**).[85] Therefore, fouling continues to be a key issue in the field of membrane science and technology.

The fouling process involves both chemical and physical interactions between the foulants and the surfaces of the membranes. The main factors influencing fouling are roughness, charge, and hydrophilicity of the membrane surfaces. A rough membrane surface usually leads to more severe fouling due to: (1) the increased membrane surface area interacting with the foulants; and (2) the higher probability of foulants accumulating in the valleys of the membrane topology. **Figure 2-18a** shows that the percentage of permeant flux decline is directly related to the RO membrane surface roughness.[86] The surface charges of the membranes influence the adsorption of foulants simply due to electrostatic attractions and repulsions. Membranes are often designed to have negatively charged surfaces because most proteins are negatively charged. However, there are always positively charged foulants. Hence, zwitterionic polymers, *i.e.* polymers with both positively and negatively charged functional groups, have recently been shown to be most effective when grafted onto membranes.[87,88]

Hydrophilicity is also a significant factor affecting fouling as most biomacromolecules and oils are hydrophobic, especially at their iso-electric point.[89-91] Furthermore, studies have shown that the formation of a few-nanometer-thick water layer on top of a hydrophilic or superhydrophilic membrane can effectively resist the adhesion of foulants. **Figure 2-18b** indicates that the permeated flux is close to the original flux when the membrane contact angle is less than 55°, *i.e.* a hydrophilic surface.[92] Other minor factors that may influence fouling include the pH of the feed solution, the temperature of both the feed solution and the membrane, the trans-membrane pressure (TMP), and the concentration of foulants.[93-95]

#### 2.2.2.2 Membrane Characterization

To characterize a membrane, many surface techniques can be used, including atomic force microscopy (AFM), scanning electron microscopy (SEM), transmission electron microscopy (TEM), Fourier transform infrared spectroscopy (FTIR), X-ray photoelectron spectroscopy (XPS), energy dispersive X-ray analysis (EDX), and electron energy loss spectroscopy (EELS). The surface roughness of membranes can be measured using an AFM. With a relatively soft tip in either tapping mode or contact mode, AFM can be used to plot the topology of a specific area, then the average roughness can be calculated based on the topological readings. SEM and TEM are powerful instruments that can image the morphology of a membrane at both surfaces and through cross-sections. EDX and EELS are used to label certain elements in order to confirm the existence and distribution of specific materials. FTIR and XPS are particularly useful in confirming grafting, where FTIR measures the absorbance from functional groups, while XPS detects different binding energies indicative of specific chemical bonds.

Contact angle measurements are generally used in membrane studies because of the importance of hydrophilicity, as previously mentioned. Traditionally, the contact angle is evaluated by placing a water droplet onto the membrane surface (**Figure 2-19a**). The contact angle, $\theta$, is defined via Young's equation:

$$\gamma_{LS} + \gamma_{AL} \cos \theta = \gamma_{AS} \qquad (2\text{-}4)$$

where $\gamma_{LS}$, $\gamma_{AL}$, $\gamma_{AS}$ are the surface energies between liquid-solid, air-liquid, and air-solid, respectively (**Figure 2-19b**).[96-98] However, since membranes for water filtration are water permeable, the water droplet may permeate through the membrane before the image can be captured. Therefore, the captive bubble technique is often used. In this experiment, as shown in

**Figure 2-19c**,[99] the membrane is clamped facedown in a water tank, so that a U-shaped syringe tip can place an air bubble onto the membrane surface in order to measure the contact angle, as labeled in **Figure 2-19d**.

For testing the general fouling/antifouling properties of a membrane, a schematic of a typical lab scale cross-flow system is presented in **Figure 2-20**. A fresh membrane is put inside of the cell, and after about 1 hour of compaction with deionized water, the solution containing foulants is added to the feed tank and the TMP recorded as the permeant flux versus time. The TMP is defined as:

$$TMP = (P_{feed} + P_{retentate})/2 - P_{permeate} \quad (2\text{-}5)$$

As a membrane begins to foul, the permeate pressure and flux start to decrease; hence, the TMP begins to increase. The percentage of TMP increase and permeate flux decrease are indicators of the fouling propensity of a membrane. After a certain period of time fouling, the foulants on the membrane can be physically or chemically removed. The recovered value is another way of evaluating the membrane performance.

In order to test biofouling, bacteria or viruses need to be cultured in broths for use with the membranes. In the case of *E. Coli*, the most common biofoulant tested, *E. Coli* cells were first cultured in a Luria-Bertani (LB) broth and then diluted to the desired concentration. Membranes with a measured surface area were incubated in the *E. Coli* LB broth at room temperature for several days, followed by rinsing with a saline solution. The membranes were then stained with dye solutions in order to be able to observe cells under a florescent microscopy. Typically, live *E. Coli* cells are green in color, while the dead cells appear red. The total amount

of cells and the percentage of dead cells can be quantified, leading to the evaluation of the level of biofouling and the antibacterial properties of the membrane.

#### 2.2.2.3 Antifouling Strategies

Researchers use various strategies to enhance antifouling performance, such as physically blending the base polymer with other polymers and/or inorganic fillers, and/or coating or chemically grafting functional materials onto the base membrane. The strategies can be roughly categorized into passive ways of preventing the adhesion of foulants, and active methods for removing the adhered foulants from the membrane using responsive materials.[75]

##### 2.2.2.3.1 Fouling Resistance

In order to prevent the adhesion of foulants, the most common method used today is to enhance the hydrophilicity of the membrane surfaces.[76,100-110] Hydrophilic materials pick up water molecules and form a water layer on the membrane surfaces. The formation of the hydration layer can effectively resist the adhesion of foulants, as illustrated in **Figure 2-21a**.[75] Therefore, metal oxides, CNTs, and graphene oxides have been widely incorporated into polymers for achieving more hydrophilic membranes. Huang, *et al.* reported that UF polyethersulfone membranes with 4 wt% embedded mesoporous silica nanoparticles, have a decrease in contact angle of 10°. Moreover, the flux recovery was almost two times higher than the intrinsic membrane, and the concentration of adsorbed BSA decreased from 45 to 20 $\mu g/cm^2$, indicating enhancement of both hydrophilicity and antifouling properties.[111] CNTs are flexible and mechanically strong, but a low-density material, thus, they may be ideal for use in a composite. Vatanpour, *et al.* studied a composite of functionalized CNTs and polyethersulfone, successfully

enhancing the contact angle by 5°, while increasing the percentage of sodium sulfate rejection almost threefold, along with a dramatic increase in flux recovery.[112]

Graphene oxide has drawn a lot of attention because of its hydrophilic basal plane and reported antibacterial properties.[113,114] Xu, *et al.* blended graphene oxide with PVDF, showing an improved antifouling performance.[115] Choi, *et al.* coated graphene oxide layers onto polyamide membranes, achieving enhanced hydrophilicity with smoother surfaces showing improved rejection of BSA and higher chlorine tolerance.[116] Graphene oxide can also be grafted onto membranes. Huang, *et al.* demonstrated an azidation reaction followed by freeze-drying graphene oxide to create UV-grafted polyamide RO membranes. The contact angle decreased from 85° to 45°, resulting in a higher flux recovery and about 10 times less coverage of *E. Coli.*[117]

Hydrophilic polymers are popular because of their resistance to biofouling. Polymers grafted onto membrane surfaces are compressed by foulants, thereby constraining the freedom of the polymer chains, which is entropically unfavorable. In short, extended polymer chains are more thermodynamically stable compared to compressed polymer chains caused by fouling, as shown in **Figure 2-21b**. Hence, hydrophilic polymers, such as poly(ethylene glycol) (PEG), and zwitterionic polymers are often used. For example, McVerry, *et al.* reported PEG-perfluorophenyl azide grafted onto polyamide RO membranes. The modified membranes showed a decrease in contact angle from 63° to 35°, and an extremely low coverage of *E. Coli.*[118] The improvement of zwitterionic polymers over neutral PEGs is due to the stronger electrostatic interactions between the zwitterionic polymers and water molecules.[119,120]

#### 2.2.2.3.2 Fouling Release by Responsive Materials

Another strategy for removing foulants is to use the reversible swelling/de-swelling of polymers. Polymers are known to have transitions between globular and coiled states, a concept widely applied to polymer actuators that can mimic muscles by performing certain motions.[41,121,122] The swelling and contraction of a polymer is determined by several factors, including pH, temperature, ionic concentration, light, magnetic field, *etc*. For antifouling, responsive polymer chains have been grafted in the coiled state so that the foulants accumulate on top. When treated with a specific stimulus, the polymer chains tend to expand from the coiled state to the globular state in order to favor entropy. Therefore, the loosening of the polymer chains "pushes" the foulants away, successfully removing the foulants.[123-129] For instance, Zhu, *et al*. reported a pH responsive membrane by grafting polyethyleneimine onto PVDF/polyacrylic acid. The membrane exhibited low oil adhesion under an acidic environment (**Figure 2-22**).[130] Schacher, *et al.* reported a responsive block co-polymer, polystyrene-block-poly(N,N-dimethylaminoethyl methacrylate) (PS-b-PDMAEMA), that switched between states based on different temperatures and pH (**Figure 2-23**).[131] However, similar concepts have not been used with conducting polymers, probably because of the difficulty in processing and solvent limitations.

### 2.2.3 Polyaniline-Based Membranes

#### 2.2.3.1 Polyaniline Composite Membranes

Most conducting polymers are known to be hydrophilic and antibacterial, so conjugated polymers should be suitable for making antifouling membranes. Since polyaniline has been well studied and widely applied for various applications, many UF-related researchers have explored polyaniline and its composites. First, polyaniline was simply blended with PES or PSF, common

polymers for UF membranes, in different proportions and cast into polyblend membranes. In 2008, Fan, *et al.* made composite membranes with PSF and <15 wt% of polyaniline. The contact angles of the polyaniline/PSF membranes are 10°-15° lower than pristine PSF membranes, indicating enhanced hydrophilicity. The composite membranes also showed increases in BSA and albumin egg (AE) rejection and higher permeation fluxes (**Figure 2-24a**) compared to a pristine PSF membrane. However, there was little difference between the 5, 10, and 15 wt% polyaniline-blended membranes.[132] Guillen, *et al.* later reported polyaniline/PSF membranes with ratios of 0%, 25%, 50%, 75%, and 100% polyaniline. A pure polyaniline membrane showed much higher permeability due to the larger porosity, as shown in **Figure 2-24b**. As expected, the contact angle exhibited a trend of decreasing with higher proportions of polyaniline added. Note that the contact angle of a pure polyaniline membrane (24.2°) makes it nearly superhydrophilic.[133] Based on many studies of polyaniline blended with different base polymers, around 10 wt% polyaniline composite membranes appear to exhibit improved performance with contact angles of 50°-70°. These membranes exhibited decent foulant rejection rates, but less than 70% flux recoveries (**Table 2-7**). A few studies on mixing polyaniline with inorganic fillers, such as silver[134] or titanium oxide nanoparticles,[135,136] indicated better foulant rejection percentages and higher flux recoveries.

Liao, *et al.* first reported membranes of pristine polyaniline blended with single-walled carbon nanotubes (SWCNTs), followed by flash welding.[137] The functionalized SWCNTs make the membranes more hydrophilic due to the functional groups, while aromatic rings can still interact with the polyaniline. The preparation procedure is illustrated in **Figure 2-25a**, where the functionalized SWCNTs are wrapped with polyaniline in NMP. The solution is then blade-cast into membranes, and the dried membranes are flash welded with different intensities of light.

The performances of the membranes versus the flash intensity are presented in **Figure 2-25b**. The dramatic increase in permeability and in rejection of BSA as a function of the flash welding intensity are likely due to the formation of larger holes caused by the "melting" of polyaniline, with more hydrophobic surfaces created by flash welding. This is consistent with a previous report by Huang, *et al.*[138] Note that (1) the rejection of silica nanoparticles is kept essentially constant, indicating that the pores after welding are not larger than the size of the silica particles; and (2) the intrinsic polyaniline/SWCNT membrane has a relatively low permeability that may be attributed to the formation of relatively dense polyaniline membranes. Hence, Liao, *et al.* blended 10 to 50 wt% of polyaniline and SWCNTs with a base polymer, PSF, and then performed similar tests.[139].With a lower percentage of polyaniline and SWCNTs, the intrinsic characteristics of PSF membranes for BSA rejection were improved by almost a factor of four (**Figure 2-25c**). The differences in permeability under different flash intensities are shown in **Figure 2-25d**.

Recently, Duan, *et al.* reported an *in situ* cleaning process for polyaniline-CNT membranes by applying different voltages. The electrically conductive membranes (**Figure 2-26a**) showed a good flux recovery compared to the non-conductive PVA/CNT membranes after BSA fouling (**Figure 2-26b**). In **Figure 2-26c**, SEM images showed that (1) the membranes were covered with BSA; (2) some BSA residue still adhered to the membrane surfaces after back washing; and (3) the membranes were cleaned by applying a voltage.[140] The proposed mechanism was related to the electro-oxidation of organic-metal compounds, but further studies are needed.

#### 2.2.3.2 Polyaniline Derivative-Based Membranes

In order to further optimize the performances of polyaniline-based membranes for UF, research has focused on further enhancements to hydrophilicity and to reduce the gelation effect caused by hydrogen bonding between polyaniline chains (**Figure 2-27a**) for easier processing. McVerry, *et al.* first reported on sulfonated polyaniline (SPANI) blended with PSF to make UF membranes.[141] The self-doped polyaniline was synthesized by reacting polyaniline with highly concentrated sulfuric acid, as shown in **Figure 2-27b**. While the sulfonic acid groups make SPANI more hydrophilic, SPANI is also considered a zwitterionic polymer since the backbone of the polymer is charged both negatively and positively.[141,142] The sulfonic acid groups not only prevent gelation, but also create a bulkier backbone that may lead to higher permeability. The superhydrophilic SPANI membrane, with a contact angle of 22°, showed excellent antifouling properties against BSA. The low fouling propensity is directly proportional to the amount of added SPANI, as shown in the flux decline plot in **Figure 2-28a**. Later on, Zhao, *et al.* compared SPANI/PVDF membranes with both un-doped and doped PANI/PVDF membranes. The extraordinary high flux for the SPANI composite membrane may be attributed to the extra bulky benzene rings coupled with sulfonic acid groups, as shown in **Figure 2-28b**. Moreover, the SPANI/PVDF membranes showed extremely high flux recovery, indicating low adhesion of foulants.[142]

Huang, *et al.* polymerized N-(2-hydroxyethyl) aniline monomers, resulting in a non-self-doped, but slightly branched polyaniline derivative, nPANI (**Figure 2-27c**). The branched functional groups again make nPANI more hydrophilic than pristine PANI, while also preventing gelation. The nPANI membrane showed an 11% flux decline after fouling with BSA solutions (**Figure 2-28d**). The authors also reported a relatively low adhesion of *E. Coli* cells

compared to a pristine PANI membrane. The nPANI membrane also showed higher chlorine tolerance compared to PANI membranes.[143] Note that all of the abovementioned techniques successfully enhanced the hydrophilicity of the membranes as the contact angles were reported around 30°, which is very close to the superhydrophilic regime (20°). Therefore, functionalizing polyaniline with hydrophilic functional groups can result in even more hydrophilic membranes, thus improving antifouling properties.

### 2.2.4 Other Conjugated Polymer-Based Membranes

The use of other conjugated polymers as water filtration membranes has not yet been widely reported.[144-147] Polythiophene and polypyrrole are two other common conjugated polymers, but they do not yet appear to be suitable for filtration membranes, as stated in Section 2.1. The reason might, again, be due to the relative difficulty in synthesis and processing with other materials. However, Liao, *et al.* reported dispersible polypyrrole nanospheres embedded in PSF. The membrane had reasonable hydrophilicity with a contact angle of 42°. However, the percentage of recovered permeability dropped to 54.6% when 20% polypyrrole was incorporated. Even though the permeation is 10 times higher than pristine PSF membranes, the BSA rejection decreased from 94.3% to 83.2% with a 65.1% flux decline.[148] Saf, *et al.* made PSF/rGO composite films with polythiophene, as can be seen in the optical images shown in **Figure 2-29a**. Using the antibacterial rGO, the highest value for BSA rejection was around 90% with around 90% flux recovery.[149] Notably, Cao, *et al.* recently designed an electroactive thiophene-based block co-polymer, with the synthesis procedure illustrated in **Figure 2-29b**. The electroactive material showed excellent rejection and low adhesion of *E. Coli* under either the oxidized or the reduced state.[150]

### 2.2.5 Conclusions

Polyaniline is a promising conjugated polymer that can be applied to membrane engineering due to its hydrophilic and antibacterial nature. Blending polyaniline with base polymers can result in membranes with reasonable performances. Flash welded membranes made by combining CNTs with polyaniline exhibited high flux permeation, but lose their BSA rejection ability due to the more hydrophobic welded surfaces. This problem can be solved by blending in a base polymer with a relatively low percentage of polyaniline and other additives. Molecular engineering with polyaniline may turn polyaniline derivatives into superhydrophilic membranes. In addition, bulky side groups can be used to tune the permeation rate as mentioned in Section 2.1. So far, most conjugated polymer membranes studied are simply physical blends with base polymers. Research on stimuli-responsive conjugated polymers should be further investigated to develop membranes that can actively repel foulants.

## 2.3 Capacitive Deionization Using Conjugated Polymers

### 2.3.1 Introduction

Different from removing heavy metal ions by thermodynamic adsorption and chelating of conjugated polymers, capacitive deionization (CDI) is a burgeoning technique for the removal of charged ions or salts from brackish water. Although still a relatively new desalination technology compared to other techniques such as RO, CDI is becoming more prominent with the advent of novel electrode materials and cell designs. The key premise behind CDI technology is that through an applied potential, an electric double layer (EDL) is created, thereby adsorbing ions onto the electrode surfaces. Two porous electrode plates with an applied potential separates the cations and anions from the bulk saltwater solution. Under low salinity, the energy expenditure of CDI is projected to be considerably more energy efficient compared to other desalination techniques because of the low potentials required for electrosorption.[151] Unlike RO, which uses high pressure to separate fresh water from a salt solution using a semipermeable membrane, less energy is spent on separating and removing salt (the minor component) from water (the major component). Furthermore, the energy spent on separating the ion species stored on the electrode plates can be recovered upon discharge to further reduce the energy footprint.[152] In other words, *it is much easier to remove salt from water than water from salt*.

Operational parameters such as the feed flow rate, cell design, pH, and initial salt concentration can affect the performance of CDI.[153] One major component of CDI is the electrode materials as these can drastically affect the salt adsorption capacity. When deciding on an optimum electrode active material, properties such as high specific surface area,[154] well defined pore size and distribution,[155,156] and high electrical conductivity are desirable.

Carbon materials, such as activated carbon,[157,158] carbon aerogels,[159,160] carbide-derived carbon (CDC)[161] and graphene[162] have been well studied due to their highly porous nature and high specific surface areas. Carbon-based electrode materials for CDI have been previously reviewed.[153,163] Recently, a binder-free 3D graphene with an integrated holey graphene oxide electrode has been fabricated. This architecture enhanced the electrosorption capacity to 29.6 mg/g at an applied potential of 2.0 V due to high specific surface area and ideal pore size distribution.[164]

Electrode materials for CDI are increasingly focused on composite materials with the idea of combining the best properties of individual materials in hopes of creating a novel superior material. Polymers, carbon materials, and transition metal oxides have been used as additives to be combined with carbon-based electrode materials, thereby taking advantage of both the conductive and porous nature of carbon materials along with additives that can enhance ion transport properties, capacitance, and mechanical properties.

In the field of supercapacitor electrode design, conducting polymers have been extensively studied to make polymer-carbon based composites due to their high pseudo-capacitance and good electrical conductivity. **Figure 2-30** shows the relative range of specific capacitances for conducting polymers.[165] Carbon materials have a specific capacitance much lower than that of conducting polymers, with conducting polymers approaching the range of the more expensive ruthenium oxide. Although electrode materials for energy storage applications have been extensively studied, the study of composite materials for CDI has only begun to gain traction. Supercapacitor electrode fabrication can act as a good starting point for making CDI electrodes since both use a similar electric double layer mechanism for charge storage, but there

are several key differences that must be studied in order to develop CDI technology into a viable alternative to conventional desalinization techniques.

In this section, we will first introduce a brief overview of CDI. We will then summarize the use of conducting polymer composites for CDI applications and how these polymers play a synergistic effect towards the overall active component in electrosorption properties. Finally, we will provide possible future directions for CDI and the role conducting polymers can play in this process.

### 2.3.2 The History of Capacitive Deionization

CDI marked its start in the 1960's when Murphy and Caudle first introduced it by using porous activated carbon for water desalination.[166] In the 1970s, Johnson and Newman provided a theoretical adsorption model on the use of porous electrodes.[167] This model relied on the EDL for the basis of electrosorption. The 1990s marked an increasing number of studies on optimizing electrode materials with the exploration of carbon aerogels by Farmer, *et al.*[159] Since then, researchers have been studying a variety of electrode materials such as CNTs,[168] carbon fibers,[158] ordered mesoporous carbons,[169] and graphene[170]. In 2006, membrane capacitive deionization (MCDI) was introduced which has been shown to have enhanced electrochemical performance compared to conventional CDI.[171]

In MCDI, anion and cation exchange membranes are placed on top of the electrodes to diminish co-ion effects. When a potential is applied during the CDI process, counterions are adsorbed onto the electrode of opposite polarity, while at the same time, ions of the same charge are discharged from the electrode. This is called the *co-ion effect*. It has been shown that the co-ion effect negatively impacts electrosorption capacity of the electrode. To combat this problem, Lee, *et al.* introduced MCDI to prevent co-ions from diffusing into the solution. **Figure 2-31**

shows the typical configuration of CDI and MCDI. Using a flow-by mode, water passes between two electrode plates, thereby desalting as a potential is applied.[172] To better understand how ions are adsorbed onto the electrodes, the process can be described using the EDL model.

### 2.3.3 Capacitive Deionization Mechanism

An EDL can be defined as the interface between an electrode and an electrolyte solution. To maintain a net neutral charge on the interface, the charged electrode will attract counterions near the surface of the interface due to Coulombic forces. Such interfaces occur in many electrochemical processes and can be understood through models such as the Gouy-Chapman-Stern theory.[173,174] According to this model, there are two layers: the inner Helmholtz layer (**Figure 2-32a**),[175] where the ions directly cover the surface of the electrode, and the Gouy-Chapman layer (**Figure 2-32b**), the diffuse region further away from the charged surface and into the electrolyte.[176]

By combining the two theories together (**Figure 2-32c**), we can consider the total capacity of the system to be that of the two capacitors in series (**Equation 2-6**):

$$\frac{1}{C_d} = \frac{1}{C_H} + \frac{1}{C_D} \tag{2-6}$$

where $C_H$ is the capacitance of the inner Helmholtz layer, $C_D$ is the capacitance of the diffuse layer, and $C_d$ is the capacitance of the double layer. Considering the system as a parallel plate capacitor, the capacity can be calculated using **Equation 2-7**:

$$C = \frac{Q}{V} = \frac{\varepsilon_0 A}{d} \tag{2-7}$$

where Q is the charge on the plate, V is the voltage, $\varepsilon_0$ is the absolute permittivity, A is the area of the plate, and d is the distance between the plates. Based on this equation, to increase specific electrical capacity, the distance between the electrodes must decrease due to the inverse proportionality between distance and total capacitance. Also, the electrostatic permittivity of the

dielectric material between the plates can be increased along with the specific surface area of the electrode materials. However, the surface area of the electrode is of utmost importance when designing a system for CDI because the other two variables cannot be easily controlled due to the need for maintaining effective distances between electrode interfaces and having sufficient ionic conductivity in the electrolyte.

Although electrode materials for energy storage applications have been extensively studied, the same electrode may not produce the same results when translated to CDI applications because of several key differences between the two. Instead of storing energy from electrolyte charges, CDI uses the EDL to remove ions from solution. Supercapacitors generally have electrolytes that are soaked into the separator, while in CDI, the electrolyte is a low salinity aqueous solution that flows between the two electrodes. One must consider the materials used for CDI and determine whether or not toxic molecules could leach out into the aqueous water solution under different temperatures, pH's or solution conditions. An ideal supercapacitor device may perform well with an organic electrolyte, but may fall short under an aqueous salt solution. In terms of structural design, more emphasis is placed on the hierarchal porous nature of the electrode material since ion adsorption is due to the EDLs generated.[177,178]

Pore size also plays a significant role in the CDI process because it determines accessible ion sites and ion mobility within a porous network.[172] The International Union of Pure and Applied Chemistry defines macropores to be pore sizes larger than 50 nm, mesopores to be pore sizes between 2 to 50 nm, and micropores to be of a size smaller than 2 nm.[179] Pores must be large enough for ions to pass through, and there must be a balance between the number of the different-sized pores. Large amounts of micropores increase capacitance by increasing surface area, but macro-sized pores have shorter ion diffusion distances so ions can readily move into the

interior of the electrode material. Mesopores can provide access to micropores within a bulk material equating to high capacitance and faster adsorption. Porada, *et al.* studied the effects of pores for desalinization, and were able to predict electro-sorption capacity based on pore size distribution. They observed that carbon electrodes with high micropore content had higher electro-sorption capacity than predominantly mesoporous structures even though mesopores are predicted to have less EDL overlap.[156] Pore size distribution and pore volume are better indicators than surface area to assess CDI electrode performance.

So far, electrode materials for CDI have been mainly carbon-based materials.[163] Recently, in supercapacitor applications, conducting polymers and transition metal oxides have been incorporated with carbon based materials to enhance capacitance. The two most widely used conjugated polymers for CDI applications are polyaniline and polypyrrole due to their ease of fabrication and stability. These conductive polymers are combined with well-studied carbon materials to enhance salt adsorption capacity. In the next section, conducting polymer-based composite materials used for CDI will be summarized.

### 2.3.4 Conjugated Polymers Composite with Carbon-Based Materials

#### 2.3.4.1 Polyaniline/Polypyrrole Composites with Carbon Nanotubes

For electrode fabrication, there are several advantages of compositing that include improved specific capacitance, improved mechanical properties and stability, and higher conductivity. As a composite material, polypyrrole/CNTs can be synthesized through *in situ* polymerization. Using this synthetic method, a polypyrrole/CNT composite exhibited an increase in conductivity to 16 S/cm compared to that of pure polypyrrole (~3 S/cm).[180] CNTs can also be used as dopants.[181] Through electropolymerization, polypyrrole was uniformly coated onto CNTs with polypyrrole

acting as an electrolyte.[182] CNTs and polypyrrole can form charge-transfer complexes due to covalent bonding that can occur between the nitrogen of the imine group on polypyrrole and carbon in the conjugated bonds of CNTs. This sharing of electrons can increase charge transfer and prevent polypyrrole chains from agglomerating.[183] In many cases, one of the disadvantages of conducting polymers is the swelling and shrinkage that occurs upon charging and discharging, thereby decreasing cycle-life. CNTs have been combined with conducting polymers to resist volume changes, hence increasing the cycle life of the device. For example, Benson, *et al*. used electrodeposition of polyaniline onto a CNT fabric to demonstrate its practical use as a flexible supercapacitor and CDI electrode material. PANI-CNT had a 10-fold capacitance increase compared to that of the initial CNT fabric using an $H_2SO_4$ electrolyte with a high specific capacitance of 200 F/g with a NaCl electrolyte. The high capacitance with NaCl aqueous electrolytes is promising for its use as CDI electrodes. The PANI-CNT fabric showed minimal degradation even after 30,000 cycles demonstrating CNTs' effectiveness in maintaining a stable structure.[184]

Yan, *et al.* incorporated polyaniline and SWCNTs into a composite CDI electrode.[185] The composite was synthesized by *in situ* polymerization. Varying concentrations of SWCNTs were dispersed in HCl under ultrasonication. Ammonium persulfate solution was added to the aniline monomer and SWCNT dispersion to initiate polymerization. PANI was shown to coat and polymerize on the SWCNTs (**Figure 2-33**). By increasing the concentration of SWCNTs, the total Brunauer-Emmett-Teller surface area increased along with the mesopore volume. The PANI coated on the CNTs promoted π-π stacking, which induced high surface area, while controlling the pore size distribution. These composites showed higher capacitance than that of SWCNTs or PANI alone. For CDI performance, SWCNT/PANI had an improved salt removal

efficiency of 12% greater than that of the original SWCNTs. The improved CDI performance was attributed to the increase in mesopores and favorable π-π interactions between SWCNTs and PANI. Similar effects were observed for *in situ* polymerized polypyrrole (PPy) composites with CNTs.[186]

The PPy/CNT composite was also studied for its fouling properties. Wang, *et al.* utilized a half cycling running mode to observe the effects of inorganic and organic foulants while using doped PPy/CNT electrodes made in a previous study.[187,188] The introduction of inorganic foulants, $Ca^{2+}$ and $Fe^{3+}$, caused the feed solution to become basic which, in turn, triggered calcium hydroxide and ferric hydroxide precipitates to form on the electrode's surfaces, thereby decreasing CDI performance. HA, the organic foulant used in this study, caused doping onto PPy from the surface of the electrode, which resulted in damage to the electrode surfaces.

#### 2.3.4.2 Polyaniline/Polypyrrole Composites with Graphitic Materials

The 2010 Nobel Prize in Physics spurred increasing interest in graphene,[189] which has the advantages of being flexible, highly electrically conductive, mechanically strong, and possessing high surface area. For instance, graphene/polyaniline composites have been synthesized through *in situ* polymerization and their electrochemical properties have been assessed.[77] The interaction between PANI and graphene nanosheets reduces the diffusion distances and can enhance electron transfer. Graphene can be mechanically exfoliated from its bulk counterpart, graphite, which can also serve as an effective component in composites.

Zhang, *et al.* prepared polypyrrole nanowire modified graphite (PPy/graphite) to use as an anode.[190] Reaction conditions were optimized by varying the concentration of polypyrrole, the concentration of electrolyte, the pH, the polymerization time, and testing various dopants including chloride ($Cl^-$), *p*-toluene sulfonate (*p*-$TS^-$), and dodecyl benzene sulfonate ($DBS^-$).

The PPy/graphite composite had a much lower surface area compared to other carbon-based materials because of the high amount of PPy deposited during the polymerization process. To overcome this problem, the 2D-layered material, graphene, can be used due to its high theoretical specific surface area of 2630 $m^2/g$ resulting in a much higher capacitance compared to that of graphite.[191,192]

Graphene/polyaniline nanocomposites for MCDI electrodes were reported by Yan, *et al*.[193] The composite was synthesized through chemical polymerization of aniline in the presence of graphene flakes prepared by the reduction of graphite oxide. TEM of the reduced graphene oxide (**Figure 2-34a**) showed a sheet-like morphology. For the graphene/PANI composite (**Figure 2-34b**), polyaniline appears mostly at the edges of the graphene sheets. Due to the use of hydrazine as the reducing agent for the graphene synthesis, amide groups were functionalized on the graphene sheets, which acted as anchoring points for polyaniline to easily attach onto the graphene sheets. The enhanced electrochemical stability of the graphene/PANI composite can be attributed to these connections. Elongation of the π-π conjugated network between graphene and PANI resulted in faster charge transfer as shown by electrochemical impedance spectroscopy.[194] The CDI performance was assessed by flowing a NaCl solution through two electrodes in parallel at a potential of 1.2 V. At an initial conductivity of 500 µS/cm, 94% salt removal was achieved for the graphene/PANI electrode compared to 86% salt removal for the graphene only electrode. At a higher initial conductivity of 1000 µS/cm, the graphene/PANI electrode achieved a 65% salt removal and the graphene electrode only achieved 52% salt removal. The graphene/PANI electrode also had a faster regeneration time compared to the graphene-only electrode (**Figure 2-35**).[165] The interfacial interactions between PANI and graphene led to

favorable electrochemical properties for this layered composite. To further increase capacitance, other strategies for electrode design include the addition of transition metal oxides.

Transition metal oxides, like conducting polymers, have high specific capacitance and are commonly used in composites to enhance overall performance of electrochemical devices. $MnO_2$ by itself has poor conductivity and is highly dense, but it has a high specific capacitance. Because of this, $MnO_2$ have been incorporated into graphene foam/PPy to take advantage of the mechanical support from the graphene material to produce a ternary composite.[195] The 3D structure of the graphene foam prevents the sheets from restacking onto each other. PPy can be added to increase conductivity and capacitance. The resulting graphene foam/PPy/$MnO_2$ composite had a specific capacitance of 601 F/g at a current density of 1 A/g in 1.0 M $Na_2SO_4$ electrolyte. This capacitance was much higher than that of graphene foam with $MnO_2$ only. A similar strategy has been adopted for CDI device fabrication.

To assess the electrochemical performance of this type of composite for CDI, Gu, *et al*. fabricated ternary electrode materials consisting of reduced graphene oxide as the carbon source, polypyrrole as the conducting polymer, and $MnO_2$ as the transition metal oxide (rGO-PPy-$MnO_2$).[196] rGO-PPy-$MnO_2$ hydrogels were prepared through a hydrothermal route to obtain three-dimensional porous structures. Polypyrrole can interact with GO through hydrogen bonding and π-π interactions to prevent GO from restacking. Confirmed through contact angle measurements, $MnO_2$ and polypyrrole can also increase the wettability of the electrodes thereby promoting more accessible ion sites into the porous structure of the electrodes. To test CDI performance, an applied potential of 2.0 V at an initial conductivity of 1000 µS was carried out. RGO-PPy-$MnO_2$ had an electrosorptive capacity of 18.4 mg/g compared to 4.8 mg/g for RGO by

itself. The high electrosorptive capacity is due to high surface area from the graphene and the increase in active sites for ion storage.

### 2.3.5 Other Conducting Polymer-Based Composites

Polyaniline and polypyrrole are the most studied conducting polymers for electrochemical assays because they are relatively inexpensive and easy to process. It has been suggested that by combining the two materials into a composite, the strengths of both materials can be realized. Wang, *et al.* fabricated PANI/PPy composites and tested their desalinization performance.[197] The PPy/PANI composites were assembled through *in situ* polymerization. The PPy/PANI composites were used as the anode materials, while CNT electrodes were used as the cathode materials under an initial NaCl concentration of 500 mg/L at an applied potential of 1.4 V. The salt adsorption capacity of these electrodes was calculated to be 197.8 mg/g, which is much higher than either of the conducting polymers alone.

Recently, a poly(3,4-ethylenedioxythiophene) (PEDOT)-based composite was introduced for desalinization applications. Aldalbahi, *et al.* combined PEDOT with reticulated vitreous carbon (RVC) and the composite was evaluated for CDI.[198] RVC has high surface area and can be easily surface modified. The team studied the effects of different operational parameters such as applied voltage, flow rate, and PEDOT loading. They showed that increasing the voltage and the PEDOT loading increased ion removal. The best parameters for electrode fabrication with RVC was 120 min electrodeposition of PEDOT resulting in an electrosorption capacity of 16.15 mg/g starting at an initial salt concentration of 500 mg/L.

### 2.3.6 Conclusions

CDI technology, especially in regard to the electrode design, is only beginning to be developed. Carbon-based materials continue to dominate the field of electrode materials used for CDI, but there has been a growing trend toward the use of pseudo-capacitive materials such as conducting polymers to improve performance. A list of CDI electrodes containing conducting polymers are summarized in **Table 2-8**. In particular, conducting polymers can be combined with other carbon materials to enhance the capacitance of the resulting composites. In most cases, additives affect the overall porous structure of the electrode material. Carbon-based materials such as CNTs can act as mechanically stable substrates for conducting polymers, thus improving the cycling stability. Conducting polymers have conjugated backbones that can interact effectively with carbon materials like graphene and CNTs through their $\pi$ networks. In addition, additives can prevent graphene sheets from agglomerating, thus increasing surface area for ion adsorption.

Composite materials for CDI are a promising transition toward the use of non-carbonaceous materials as electrodes. The use of non-carbon materials for CDI is still rather rare. Future work within this field calls for further studies on conducting polymers especially in mitigating fouling. There are more and more examples of using redox active materials for CDI electrodes because they could overcome limitations imposed on carbon-based active materials that rely solely on the electric double layer mechanism for adsorption. This could broaden the field towards the goal of seawater desalinization. All in all, conducting polymers can play a significant role in enhanced water desalinization due to the synergistic effects exhibited in composite materials.

**Acknowledgements**

The authors would like to thank the National Science Foundation CBET Grant 1337065, the U.S./China Clean Energy Research Center for Water-Energy Technologies (CERC-WET) and the Sustainable LA Grand Challenge for financial support. R.B.K. would like to thank Dr. Myung Ki Hong Endowed Chair in Materials Innovation; C.-W.L. would like to acknowledge the UCLA Dissertation Year Fellowship; W.H.M. would like to thank the Eugene V. Cota-Robles Fellowship.

**TABLE 2-1** Permeability, Diffusion, and Solubility Coefficients for $N_2$, $O_2$, $CO_2$, and $CH_4$ in PTMSP and PDMS Membranes*

| Penetrant gas | $P \times 10^8$ | $D \times 10^5$ | $S \times 10^2$ |
|---|---|---|---|
| Glassy PTMSP, [-$CH_3C$=$CSi(CH_3)_3$-]; temperature: 30℃ | | | |
| $N_2$ | 49.7 | 3.50 | 1.42 |
| $O_2$ | 77.3 | 4.66 | 1.66 |
| $CO_2$ | 280 | 2.64 | 10.59 |
| $CH_4$ | 130 | 2.64 | 4.92 |
| Rubbery PDMS, [-$(CH_3)_2SiO]_x$; temperature: 35℃ | | | |
| $N_2$ | 4.7 | 4.00 | 0.118 |
| $O_2$ | 9.6 | 3.97 | 0.242 |
| $CO_2$ | 45.5 | 2.63 | 1.74 |
| $CH_4$ | 14.3 | 2.45 | 0.591 |

*PTMSP = poly[1-(trimethylsilyl)-1propyne]; PDMS = polydimethylsiloxane; Units: P [$cm^3$ (STP) cm/s · $cm^2$ · cmHg]; D [$cm^2$/s]; S [$cm^3$ (STP)/$cm^3$ · cmHg] Reprinted with permission from reference 22.

**TABLE 2-2** Film Thickness and Selectivity Reported for Polyaniline Membranes*

| Year | Researcher | thickness (μm) | Selectivity | | | | | |
|---|---|---|---|---|---|---|---|---|
| | | | $H_2/CO_2$ | $H_2/O_2$ | $H_2/N_2$ | $CO_2/O_2$ | $CO_2/N_2$ | $O_2/N_2$ |
| 1991 | Anderson *et al.* | 10 | 7.3 | 21.8 | 207 | 3 | 28.3 | 9.5 |
| 1995 | Rebattet *et al.* | 10 — 15 | 7.8 | 30.7 | 195 | 3.9 | 25.1 | 6.4 |
| 1999 | Wang *et al.* | 43 — 51 | 6.1 | 29.0 | 265 | 4.8 | 38.7 | 9.1 |
| 2001 | Illing *et al.* | 9 — 29 | 5.1 | 16.8 | 164 | 3.3 | 32.3 | 9.8 |
| 2006 | Gupta *et al.* | 4.0 | 8.6 | 69.5 | 348 | 8.1 | 40.4 | 7.1 |

* Adapted from reference 57, Copyright (2006), with permission from Elsevier.

**TABLE 2-3** Permeability and Selectivity of Gases through Polyaniline, Polyimide, and a 50/50 Blend*

| | Gas | Polyimide | 50/50 Blend | PANI (EB) |
|---|---|---|---|---|
| Permeability | $H_2$ | 3.33 | 7.4 | 4.59 |
| | $O_2$ | 0.174 | 0.282 | 0.174 |
| | $N_2$ | 0.028 | 0.027 | 0.019 |
| | $CO_2$ | 0.979 | 1.281 | 0.828 |
| | $CH_4$ | 0.017 | 0.015 | 0.004 |
| Selectivity | $CO_2/CH_4$ | 59 | 85 | 180 |
| | $H_2/N_2$ | 120 | 270 | 240 |
| | $O_2/N_2$ | 6.2 | 10 | 9.1 |

***** Adapted from reference 60 with permission from Elsevier.

**TABLE 2-4** Effect of Doping PIM-1/Polyaniline Composites on Gas Permeability and Selectivity

| Dopant | Permeability (Barrers) | | | | | Selectivity | | | | |
|---|---|---|---|---|---|---|---|---|---|---|
| | $H_2$ | $CO_2$ | $O_2$ | $N_2$ | $CH_4$ | $O_2/N_2$ | $CO_2/N_2$ | $H_2/CO_2$ | $H_2/N_2$ | $H_2/CH_4$ |
| HCl | 519.3 | 224.4 | 80.8 | 9.9 | 6.9 | 8.1 | 22.6 | 2.3 | 52.2 | 75.2 |
| HBr | 531 | 247.7 | 83.7 | 17.8 | 16.1 | 4.7 | 13.9 | 2.1 | 29.8 | 33 |
| HI | 540.7 | 291.2 | 94 | 18.1 | 17.3 | 5.2 | 16.1 | 1.9 | 29.8 | 31.3 |

***** Adapted from reference 65 with permission of the Royal Society of Chemistry.

**TABLE 2-5** Performances of Polyaniline-based Gas Separation Membranes*

| Membrane material | Permeability (Barrers) | | | | | Selectivity | | | | | | | Reference |
|---|---|---|---|---|---|---|---|---|---|---|---|---|---|
| | $P(H_2)$ | $P(O_2)$ | $P(N_2)$ | $P(CH_4)$ | $P(CO_2)$ | $H_2/N_2$ | $CO_2/CH_4$ | $H_2/CO_2$ | $H_2/O_2$ | $CO_2/O_2$ | $O_2/N_2$ | $CO_2/N_2$ | |
| PANI on alumina | — | 0.164 | 0.0112 | 0.0092 | 0.505 | — | 54.9 | — | — | 3.08 | 14.8 | 45.09 | 58 |
| PANI | 3.7 | 0.13 | 0.026 | 0.016 | 0.75 | 142.31 | 46.88 | 4.93 | 28.46 | 5.77 | 5.0 | 28.85 | 199 |
| PANI doped | 0.4 | 0.01 | 0.006 | 0.005 | 0.06 | 66.67 | 12.0 | 6.67 | 40.0 | 6.0 | 1.67 | 10.0 | 199 |
| PANI/PI 50/50 | 7.4 | 0.282 | 0.027 | 0.015 | 1.282 | 270 | 85 | 5.77 | 26.24 | 4.55 | 10.4 | 47.48 | 60 |
| PMANI | 6.04 | 0.202 | 0.047 | — | 1.06 | 126 | — | 5.7 | 29.9 | 5.25 | 4.3 | 22.6 | 200 |
| PEANI | 8.1 | 0.62 | 0.107 | — | 2.22 | 75.7 | — | 3.65 | 13.1 | 3.58 | 5.79 | 20.8 | 200 |
| PANI on nylon | — | 0.49 | 0.068 | — | — | — | — | — | — | — | 7.2 | — | 201 |
| PANI on PS | 2.76 | 0.24 | 0.57 | — | — | 4.84 | — | — | 11.5 | — | 0.41 | — | 202 |
| PANI/PVTMS doped | — | 8 | 2 | 2.6 | 27.7 | — | 10.7 | — | — | 3.5 | 4 | 13.9 | 61 |
| PANI on PVDF | 1.197 | 0.053 | 0.01 | — | 0.247 | 119.7 | — | 4.85 | 22.58 | 4.66 | 5.3 | 24.7 | 54 |
| PANI/P84 | 76.06 | 26.44 | 28.61 | 29.28 | 19.64 | 2.66 | 0.746 | 3.87 | 2.88 | 0.743 | 0.924 | 0.685 | 203 |
| PANI-PI | — | 1.06 | — | — | — | — | — | — | — | — | 13.54 | — | 64 |
| PANI-PI doped | — | 0.93 | — | — | — | — | — | — | — | — | 16.63 | — | 64 |
| PANI/PVAm | — | — | — | — | 0.06 | — | — | — | — | — | — | 71 | 62 |
| PANI on PE | — | 0.63 | 0.04 | — | — | — | — | — | — | — | 15.75 | — | 204 |
| PSN3 | — | 0.1892 | 0.0293 | — | — | — | — | — | — | — | 6.457 | — | 205 |
| PSM1 | — | 0.3696 | 0.0602 | — | — | — | — | — | — | — | 6.140 | — | 205 |
| PANI/PBI 20/80 | 3.79 | 0.129 | 0.012 | 0.01 | 1.07 | 306 | 104 | 3.6 | 29.38 | 8.29 | 10.4 | 86 | 59 |
| PANI/PBI 20/80 doped | 0.841 | 0.05 | — | — | 0.32 | — | — | 2.6 | 16.8 | 6.4 | — | — | 59 |
| PANI/PIM-1 | 348.2 | 165 | 2.2 | 2.2 | 53.6 | 158.3 | 24.36 | 6.5 | 2.15 | 0.325 | 7.5 | 24.4 | 65 |
| PANI/F-aniline/PIM | 1065.9 | 151.8 | 25.8 | 15.8 | 547.7 | 41.4 | 34.66 | 2 | 7.02 | 3.608 | 5.9 | 21.3 | 65 |

* PANI = polyaniline; PI = polyimide; PMANI = polymethoxyaniline; PEANI = polyethoxyaniline; PS = polysulfone; P84 = 3,3'4,4'-benzophenone tetracarboxylic dianhydride and methylphenylene-diamine (80%) + methylene diamine (20%); PVAm = polyvinylamine; PSN1 = polyaniine-silica nanocomposite 1; PSM1 = polyaniline-silica mesocomposite 1; PBI = polybenzimidazole. Modified from reference 64 with permission from the American Chemical Society

**TABLE 2-6** Performances of Polypyrrole- and Polythiophene-based Gas Separation Membranes*

| Membrane material | Permeability (Barrers) | | | | | Selectivity | | | | | | | Reference |
|---|---|---|---|---|---|---|---|---|---|---|---|---|---|
| | $P(H_2)$ | $P(O_2)$ | $P(N_2)$ | $P(CH_4)$ | $P(CO_2)$ | $H_2/N_2$ | $CO_2/CH_4$ | $H_2/CO_2$ | $H_2/O_2$ | $CO_2/O_2$ | $O_2/N_2$ | $CO_2/N_2$ | |
| Polypyrrole-based | | | | | | | | | | | | | |
| PMPy | — | 1.26 | 0.16 | 0.17 | 2.82 | — | 16.2 | — | — | 2.24 | 7.9 | 17.63 | [66] |
| PMPy-$NO_3$ | — | 2.04 | 0.33 | 0.22 | 6.9 | — | 31.9 | — | — | 3.38 | 6.2 | 20.91 | [66] |
| PPY on Vycor | — | — | — | — | — | — | — | — | — | — | 5.2 | — | [67] |
| PPY/PC | — | — | — | — | — | — | — | — | — | — | 17 — 92 | — | [68] |
| PPY-PC | 5.84 | 4.88 | 1.39 | 1.37 | 3.8 | 4.20 | 2.77 | 1.54 | 1.20 | 0.78 | 3.7 — 5.5 | 19 — 27.5 | [69] |
| SPPO-PPY 80/20 | 13.5 | 0.75 | 0.18 | — | — | 75 | — | — | 18.0 | — | 4.2 | — | [206] |
| CPPY-PC-7-10 | 9.98 | 1.35 | 0.2 | 0.25 | 4.1 | 49.9 | 16.4 | 2.43 | 7.39 | 3.04 | 6.75 | 20.5 | [70] |
| ECPPY-PC-7-10 | 19.19 | 6.03 | 2.67 | 3.18 | 7.65 | 7.19 | 6.03 | 2.51 | 3.18 | 1.27 | 2.26 | 2.87 | [70] |
| CM-500 | 51.2 | 20.3 | 17.1 | 21.3 | 15.5 | 2.99 | 0.728 | 3.3 | 2.55 | 0.764 | 1.19 | 0.906 | [207] |
| Polythiophene-based | | | | | | | | | | | | | |
| PDDT | — | 21.8 | 9.4 | — | 88.2 | — | — | — | — | — | 2.2 | 9.4 | [71] |
| 23% oxidized PDDT | — | 10.5 | 3.5 | — | 48.5 | — | — | — | — | — | 3 | 14 | [71] |
| hydrazine PDDT | — | 15.1 | 5.4 | — | 62.9 | — | — | — | — | — | 2.8 | 11.6 | [71] |
| P3HET/P3AcET | — | 111 | 22 | 36 | 668 | — | 18.5 | — | — | — | 5.1 | 30.4 | [208] |

*PMPy = poly(N-methylpyrrole); PPY = polypyrrole; PC = polycarbonate; SPPO = sulfonated poly(phenylene oxide); CPPY = chemically synthesized polypyrrole-polycarbonate; ECPPY = electrochemically synthesized polypyrrole-polycarbonate; CM = carbon membrane; PDDT = poly(3-dodecylthiophene); P3HET = poly(3-(2-hydroxyethyl)thiophene); P3AcET = poly(3-(2-acetoxyethyl)thiophene).

**TABLE 2-7** Performances of Polyaniline-Based Ultrafiltration Membranes

| Lead Author | Membrane materials | Contact angle (°) | Foulant rejection (%) | Flux recovery ratio (%) | Note | Ref. |
|---|---|---|---|---|---|---|
| Fan | PSF/PANI | 55-70 | BSA (96.3); AE (97.6) | 68.3 | The blended membrane has higher porosity and hydrophilicity. Pure water flux increased 1.6 to 2.4 times higher than a pure PSF membrane. | 132 |
| Fan | PSF/PANI | 27 | BSA (99.2) | – | The percentage of flux decline is two times better than a pure PSF membrane. | 209 |
| Guillen | PSF/PANI | 25 - 43 | BSA (0-38); Silica (97-99) | – | The increasing proportion of polyaniline leads to higher permeability, but lower BSA rejection. | 133 |
| Zhao | PSF/PANI | 70 | BSA (98); AE (97-98); Trypsine (65-68) | 62 - 72 | Higher percentage of polyaniline added results in higher flux and flux recovery. The contact angle decreased by 15° compared to a pristine PSF membrane. | 210 |
| Zhao | PSF/PANI/PVP | 54 - 70 | BSA (98); AE (93-95); Trypsine (40-48) | 69.2 - 84.1 | The added polyaniline increases the hydrophilicity, flux, and percentage of flux recovery, with little or no change in both BSA and AE rejection. | 211 |
| Teli | PES-PANI/PMA | 70.8 - 73.2 | BSA (96.3-99.0) | 68.9 - 77.2 | The proposed composite membrane exhibited better antifouling and higher flux compared to the original PES membrane. | 212 |
| Teli | PSF-PANI/$TiO_2$ | 47.3 - 64.3 | BSA (90-99) | 65 - 75 | $TiO_2$ nanoparticles modified with *in situ* polymerized polyaniline, then blended with PSF. The nanocomposite membranes have higher flux and improved antifouling properties. | 135 |
| McVerry | SPANI/PSF | 25 - 50 | BSA (95.2-97.0) | 75 - 95 | Sulfonated polyaniline can be well dispersed in water for better processability. The composite with PSF showed a superhydrophilic membrane surface with very low flux decline. | 141 |
| Liao | PSF/PANI/ functionalized CNT | 35.1 - 56.1 | BSA (39.8-73.7) | – | Flash welding increased the permeability, but reduced the BSA rejection. | 139 |
| Liao | PANI/oxidized SWCNT | – | BSA (0-20); Silica (93-97) | – | Flash welding enhanced the permeability and the silica rejection was kept constant, while BSA rejection decreased. | 137 |
| Zhao | PES/PANI | 60 - 70 | BSA (95.5-96.3) | 65.9 - 66.8 | The size of the polyaniline nanoparticles significantly influenced the membrane properties. | 213 |

| | | | | | | |
|---|---|---|---|---|---|---|
| Huang | nPANI | 36 | *E. Coli* | 91 | The polyaniline derivative-based membrane is more hydrophilic and less biofouling against *E. Coli*. The membrane has a much higher flux recovery and higher chlorine resistance compared to a neat polyaniline membrane. | 143 |
| Zhu | PES/PANI | 43.2 - 46.9 | $MgSO_4$ (88-95); NaCl (35-40) | – | The composite membrane exhibited enhanced permeability and salt rejection. | 214 |
| Zhao | PVDF/SPANI | 30 | BSA (80) | 99 | The sulfonated polyaniline composite membrane when compared with both an undoped and a doped polyaniline composite membrane, showed much better hydrophilicity, BSA rejection, BSA adsorption, and flux recovery. | 142 |
| Pereira | PANI/$TiO_2$ | 64.3 - 66.4 | $Pb^{2+}$ (68); $Cd^{2+}$ (53.78) | 70 - 80 | The composite membrane showed better hydrophilicity, permeability, porosity and better antifouling to heavy metal ions. | 136 |
| Duan | PSF/PANI coated CNT | 19.4 - 27.1 | BSA (70-90) | – | A polyaniline composite with CNTs and doped with acids showed superhydrophilicity. This electrically conducting membrane showed a self-cleaning process with an applied voltage. | 140 |
| Jiang | PANI/PLLA | 65 - 70 | HA (55-70); BSA (50-65) | 51.6 - 65.2 | The addition of polyaniline nanoparticles enhanced the hydrophilicity and antifouling properties. | 215 |
| Zhao | PES/PANI/Ag | 60 - 67 | BSA (81-84); AE (80) | 89.7 - 91.2 | The composite membranes showed much higher hydrophilicity and flux, with about the same BSA and AE rejection, compared to the neat membrane. | 134 |
| Hudaib | PANI/MWCNT/PVDF | 55 - 80 | HA (55-79) | 85 | Higher porosity, hydrophilicity, and positive charged membrane surfaces are attributed to the modification with polyaniline and CNTs. | 216 |

AE = Albumin from egg

PVP = polyvinylpyrrolidone

PMA = phosphomolybdic acid

SPANI = sulfonated polyaniline

nPANI = n-acryl polyaniline

PLLA = poly(L-lactic acid)

**Table 2-8** Conducting Polymer-based Electrodes for CDI

| Electrode material | Specific surface area ($m^2$/g) | Initial conductivity | Initial salt concentration (mg/L) | Specific capacitance (F/g) | Applied voltage (V) | Salt adsorption capacity (mg/g) | Salt removal efficiency (%) | Ref. |
|---|---|---|---|---|---|---|---|---|
| SWCNTs/PANI | 330.1 | 100 µS/cm | – | – | 1.2 | – | 78.4 | [185] |
| PANI coated CNT fabric | – | – | – | 240 | – | – | – | [184] |
| PANI modified Activated Carbon | 618.4 | – | 250 | 101 | 1.2 | 3.15 | – | [217] |
| Graphene/PANI | 394 | 500 µS/cm | – | – | 1.2 | – | 94 | [193] |
| Graphene/PANI | 394 | 1000 µS/cm | – | – | 1.2 | – | 65 | [193] |
| *p*-TS-doped PAC | 1484 | – | 600 | – | 1.2 | 14.3 | – | [218] |
| *p*-TS-doped PAC | 1484 | – | 600 | – | 1.4 | 14.9 | – | [218] |
| PPy/Graphite | 0.015 | – | 500 | – | 1.4 | – | – | [190] |
| PPy/Graphite/*p*-TS | 0.1407 | – | 1000 | – | 1.4 | – | – | [219] |
| PPy/CNT | 185.21 | 6.37 S/cm | – | 106 | 1.4 | 43.99 | – | [186] |
| rGO-PPy-$MnO_2$ | 331 | 24 S/cm | – | 356 | 2 | 18.4 | – | [196] |
| PPy/PANI acid doped $HClO_4$ | – | – | 500 | – | 1.4 | 197.8 | – | [197] |
| PEDOT/RVC | – | – | 500 | – | 0.8 | 16.15 | – | [198] |

SWCNT = single walled carbon nanotubes; PANI = polyaniline; *p*-TS = para-toluene sulfonate; PAC = polyaniline activated carbon; PPy = polypyrrole; rGO = reduced graphene oxide; PEDOT = poly(3,4-ethylenedioxythiophene); RVC = reticulated vitreous carbon

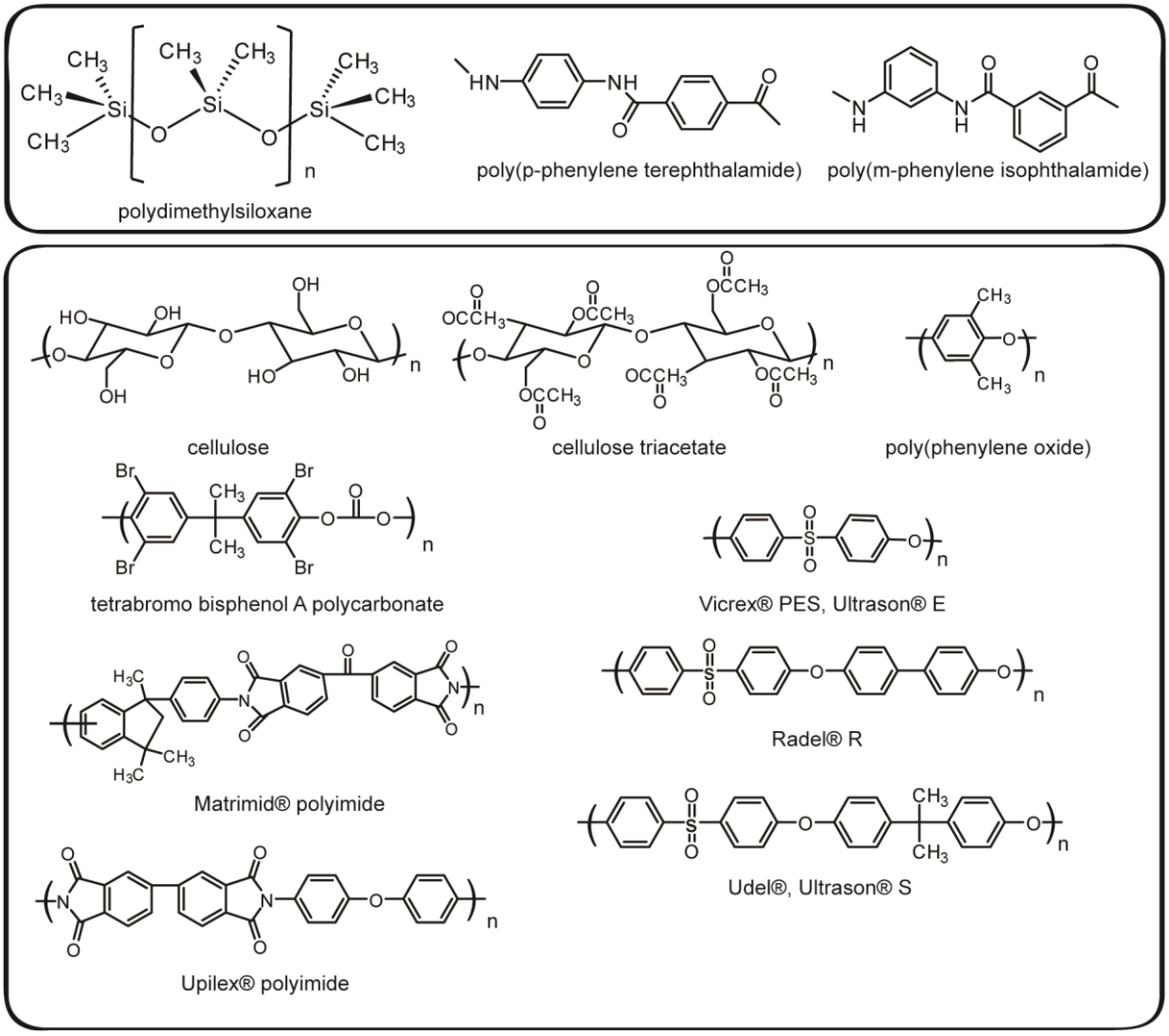


**FIGURE 2-1** Chemical structures of commercial rubbery (top) and glassy (bottom) polymers used for gas separation membranes.

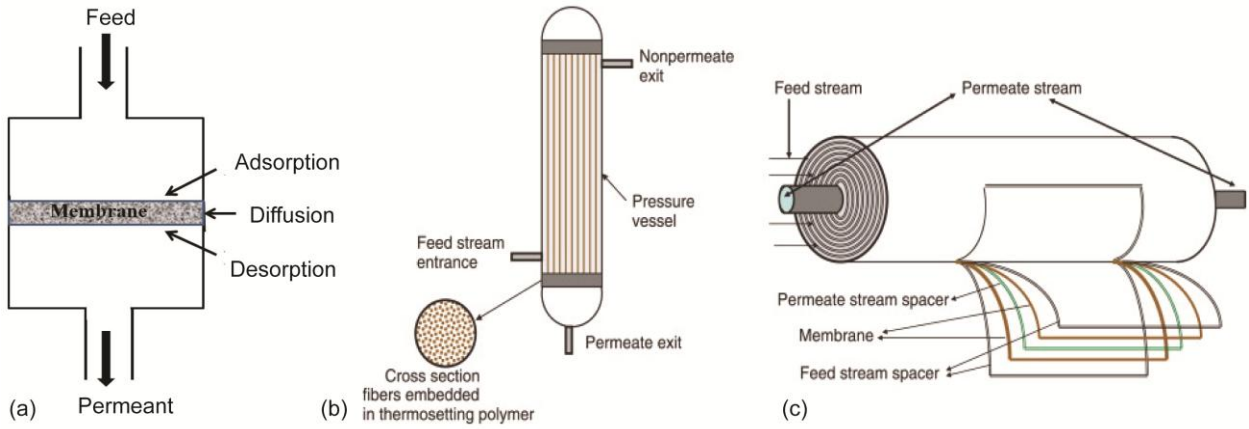


**FIGURE 2-2** Illustration of (a) lab scale; (b) hollow fiber and (c) spiral wound gas separation membrane modules. Reprinted from Ref.19 with permission from Elsevier.

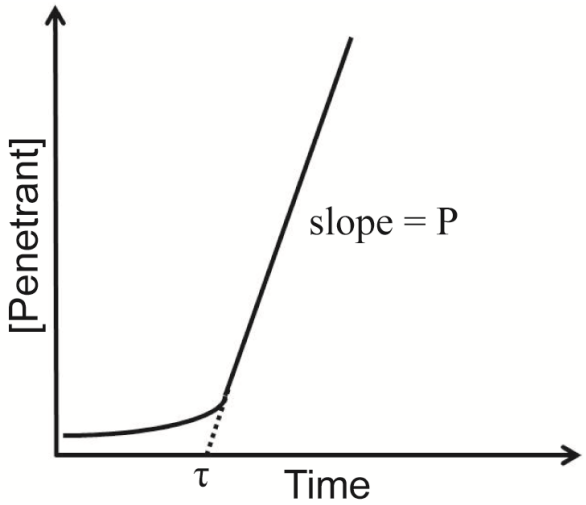


**FIGURE 2-3** A typical plot of the measured concentration of gas permeant versus time.

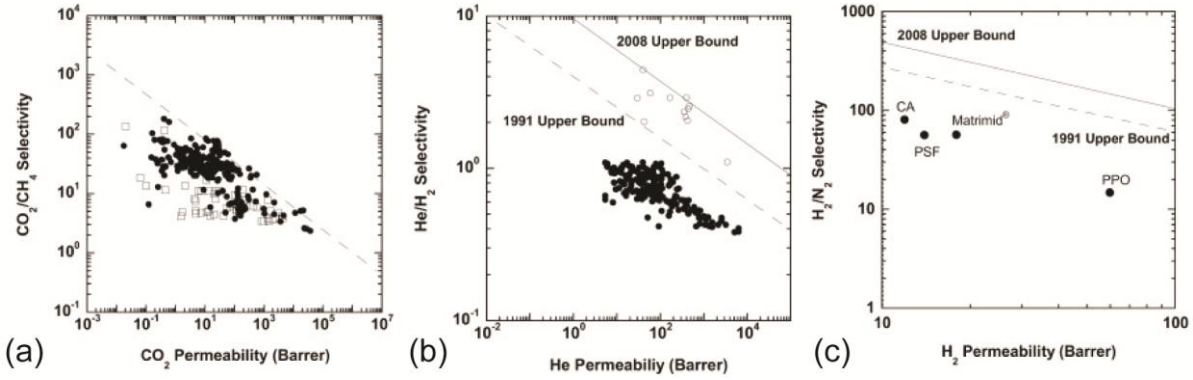


**FIGURE 2-4** Experimental data for (a) $CO_2/CH_4$ separation for glassy (●) and rubbery (□) polymers; (b) $He/H_2$ separation for perfluoropolymers (○) and other polymers (●); (c) $H_2/N_2$ separation for commercial polymers. (Reprinted from Ref. 19 with permission from Elsevier.)

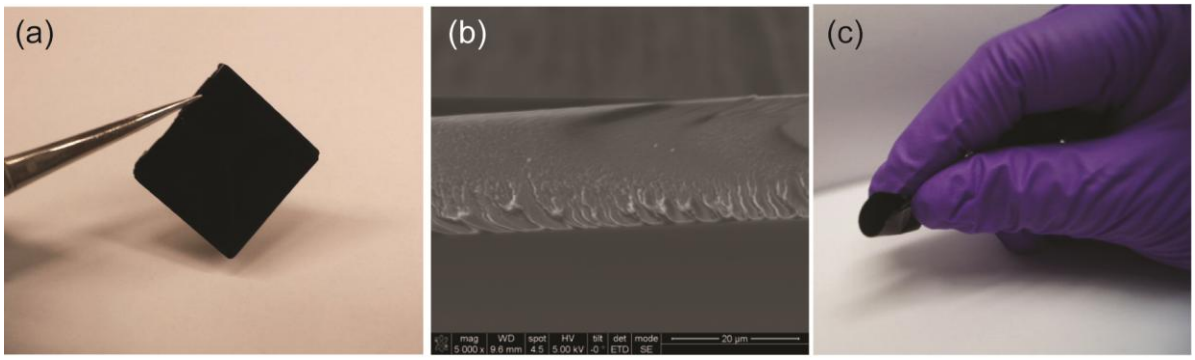


**FIGURE 2-5** Images showing (a) an as-cast polyaniline freestanding film, (b) scanning electron microscopy (SEM) cross-sectional area of the freestanding film and (c) demonstration of the flexibility of the freestanding film.

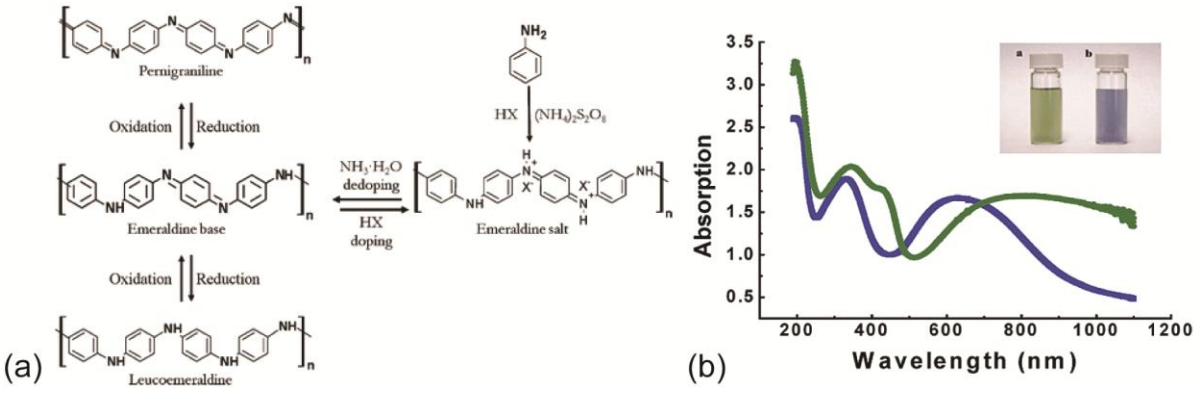


**FIGURE 2-6** (a) Chemical structures showing the three major oxidation states of polyaniline, and the doping and de-doping process between the emeraldine base and the emeraldine salt forms. (Adapted with permission from Ref. 44. Copyright (2009) American Chemical Society); (b) UV-vis spectra and optical images of polyaniline aqueous dispersions in the emeraldine base (blue) and the emeraldine salt (green) forms. (Adapted with permission from Ref. 31. Copyright (2003) American Chemical Society)

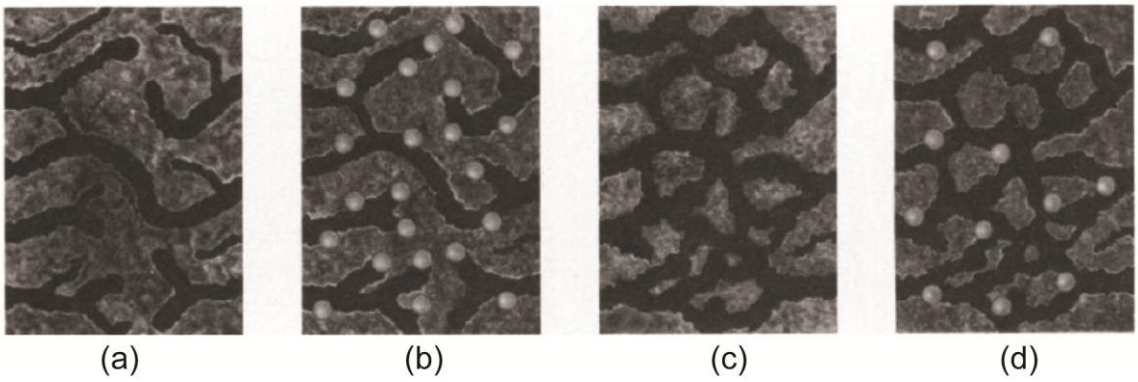


**FIGURE 2-7** A schematic illustration showing that (a) an as-cast polyaniline membrane possesses some pores; (b) the membrane can be doped with dopants (depicted as spheres); (c) the removal of dopants enlarges the pores and leads to higher permeabilities; and (d) partially re-doping the polyaniline membrane partially blocks the pores resulting in improved selectivities. (Reprinted from Ref. 28 with permission from AAAS.)

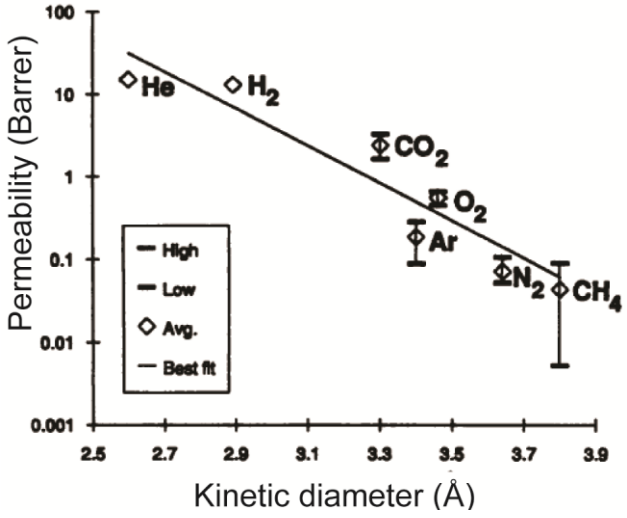


**FIGURE 2-8** The relationship between the permeability of gases through a polyaniline membrane and their kinetic diameters. (Reprinted from Ref. 28 with permission from AAAS.)

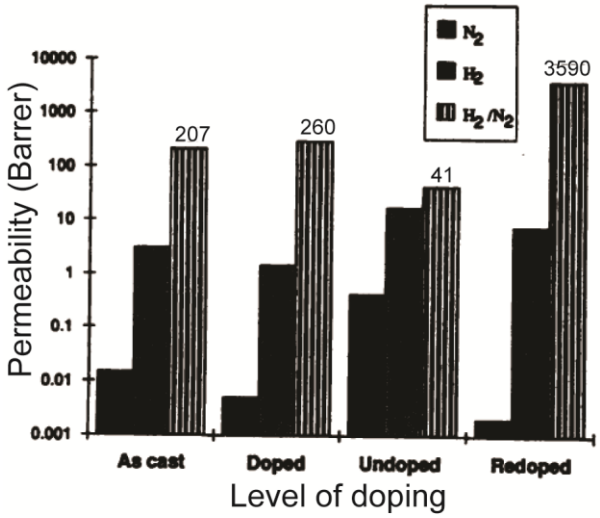


**FIGURE 2-9** The permeability of $N_2$ and $H_2$ gases through different polyaniline membranes. The doped membrane slightly lowers the permeability of both gases, while the removal of the dopants causes dramatic increases in the permeability, but a decrease in selectivity. By re-doping the polyaniine membrane the selectivity of $H_2/N_2$ is enhanced by preferentially blocking larger pores. (Reprinted from Ref. 28 with permission from AAAS.)

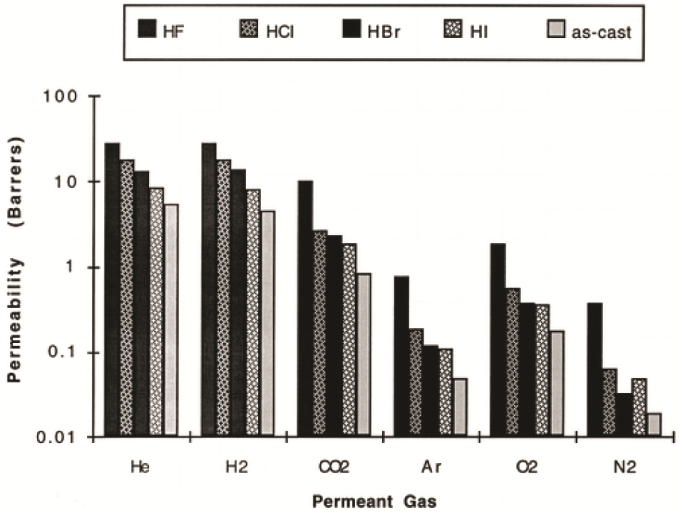


**FIGURE 2-10** Permeability of gases through polyaniline membranes doped with aqueous halogen acids. Note that smaller gases such as He and $H_2$ have the highest permeabilities with larger gases such as $N_2$ have the lowest permeability. Doping and de-doping the membranes with aqueous halogen acids leads to the highest permeability for HF, followed by HCl, HBr and HI which is consistent with the relative sizes of the hydrated ions. (Adapted with permission from Ref. 48. Copyright (1996) American Chemical Society)

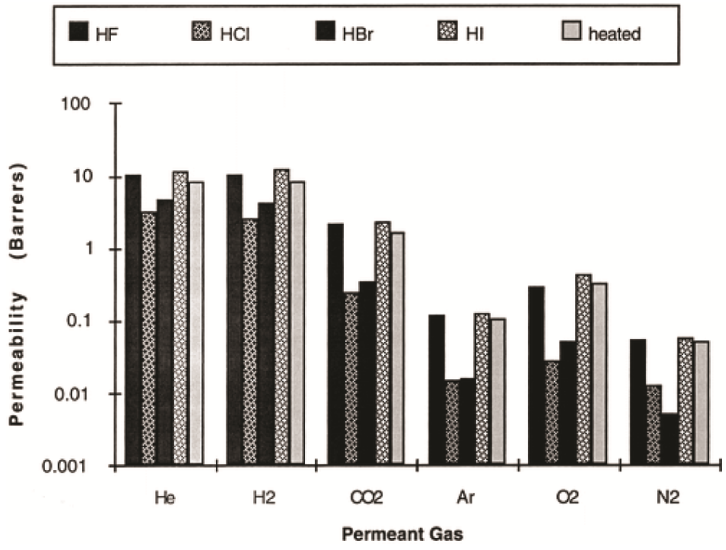


**FIGURE 2-11** The permeability of gases through polyaniline membranes doped with anhydrous halogen acid gases and de-doped with anhydrous ammonia followed by removal of the salt through sublimation. Note that the trend in permeabilities is generally reversed from that observed with the aqueous acids as HBr and HI doped/de-doped membranes are now more permeable than HCl doped/de-doped membranes. (Adapted with permission from Ref. 48. Copyright (1996) American Chemical Society)

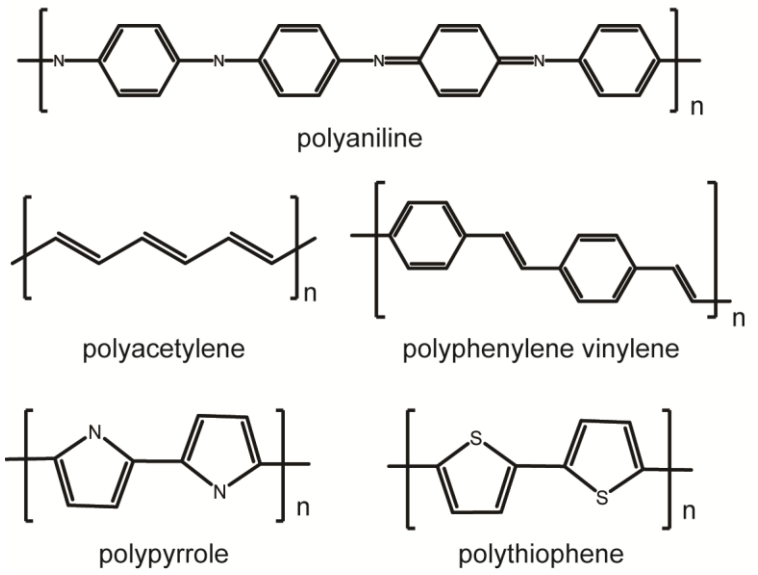


**FIGURE 2-12**Chemical structures of common conducting polymers.

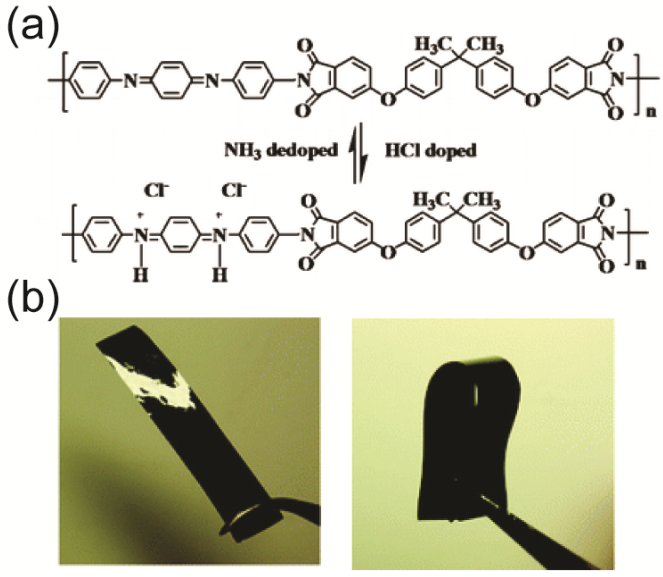


**FIGURE 2-13**(a) An amino-capped trimer and polyimide co-polymer that can be doped and de-doped reversibly. (b) Photos of the co-polymer membrane showing a similar appearance as polyaniline films and also possesses flexibility. (Reprinted with permission from Ref. 64. Copyright (2011) American Chemical Society)

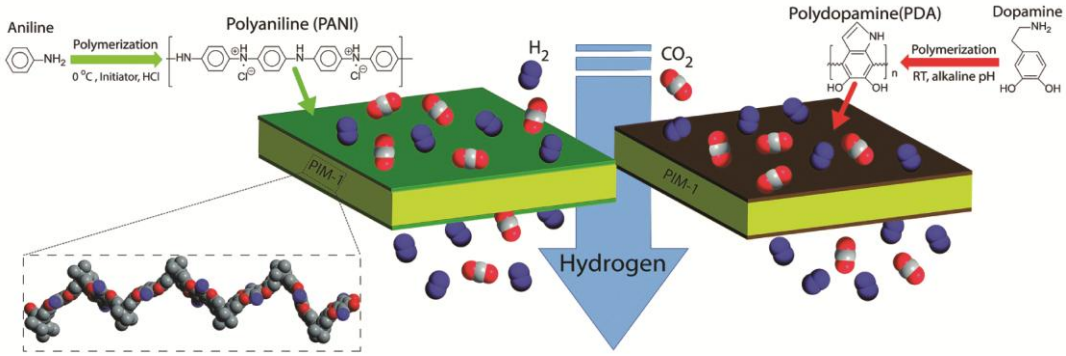


**FIGURE 2-14** A schematic illustration showing the *in situ* polymerization of polyaniline (left) and polydopamine (right) on top of a PIM-1 substrate under different polymerization conditions. The membranes exhibited excellent $H_2/O_2$ selectivities. (Adapted from Ref. 65 with permission of The Royal Society of Chemistry.)

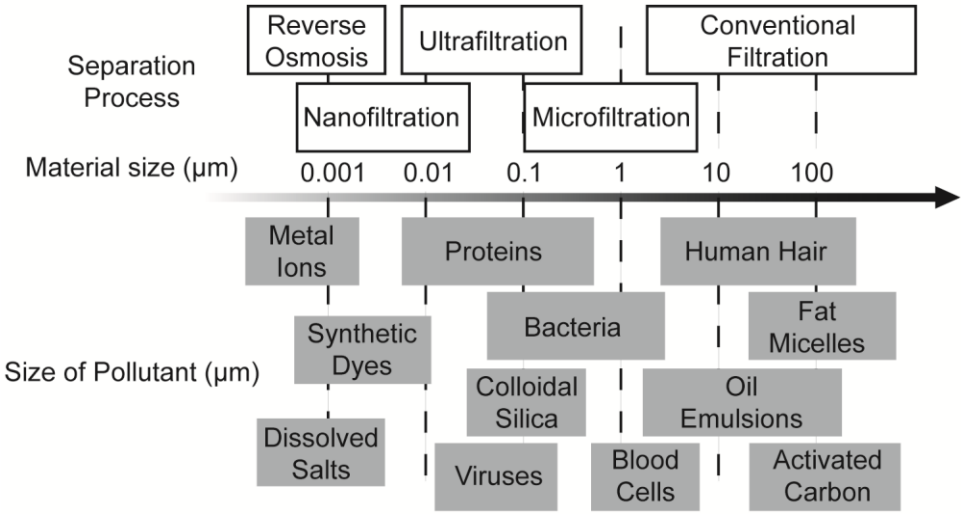


**FIGURE 2-15** Polymer membranes can be designed to reject different size pollutants.

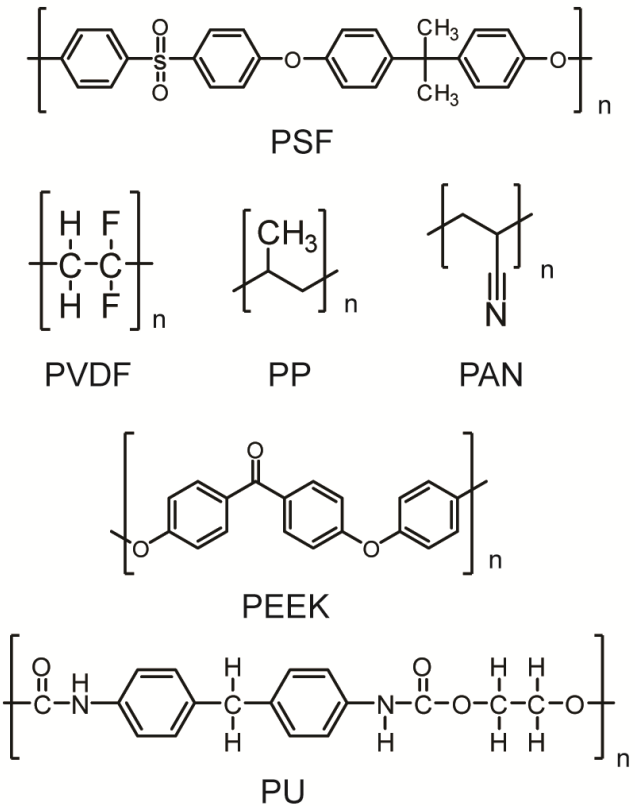


**FIGURE 2-16** Chemical structures of polymers for commercial UF membranes including polysulfone (PSF), polyvinylidene fluoride (PVDF), polypropylene (PP), polyacrylonitrile (PAN), polyether ether ketone (PEEK), and polyurethane (PU).


**FIGURE 2-17** Photographs of fouled filtration modules. Adapted from Ref. 95 with permission from The Royal Society of Chemistry.

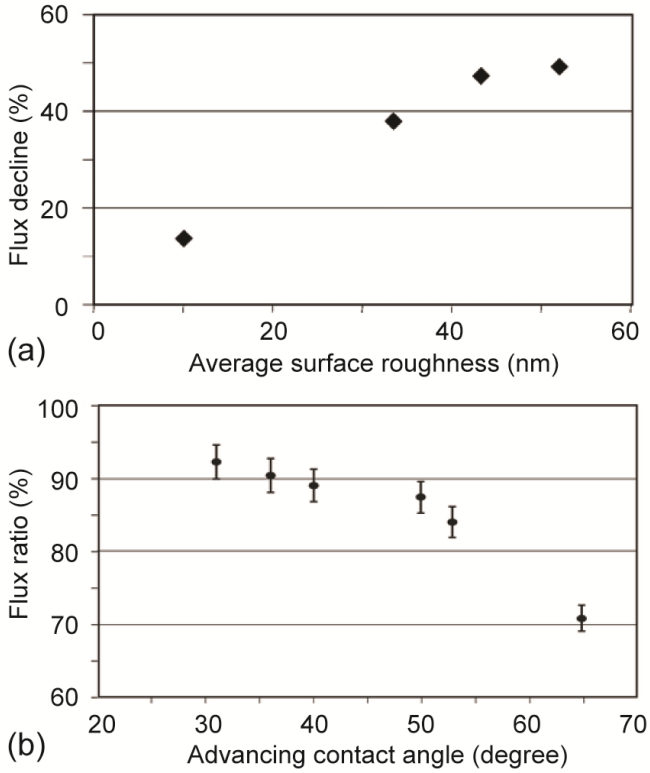


**FIGURE 2-18** Plots showing that (a) the roughness of a RO membrane is proportional to the flux decline; and (b) the flux recovery is higher when the contact angle is below 50 degrees. Adapted from Ref. 96 and 102 with permission from The Royal Society of Chemistry.

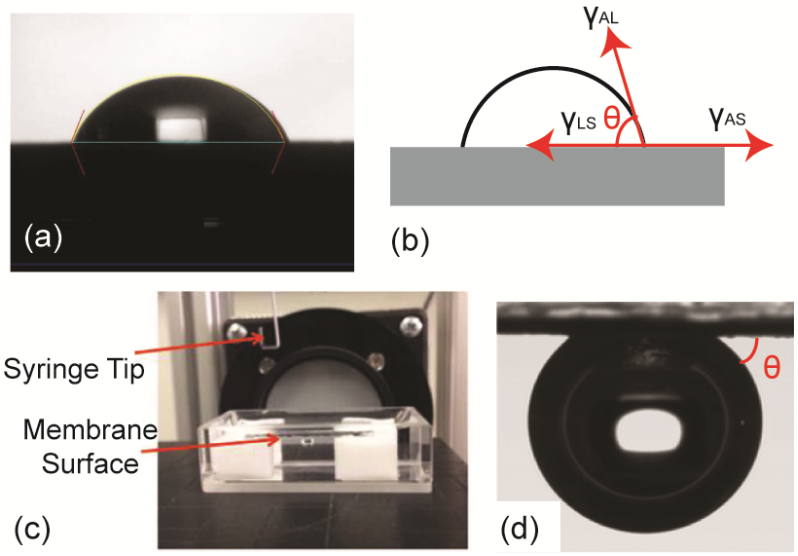


**FIGURE 2-19** Images showing (a) the traditional way of measuring contact angles by placing a water droplet on the membrane surface. (b) The contact angle can be calculated via Young's equation (Equation 5-4). (c) The captive bubble setup for measuring contact angle for (d) air bubbles. (Reprinted with permission from Ref.151. Copyright (2013) American Chemical Society)

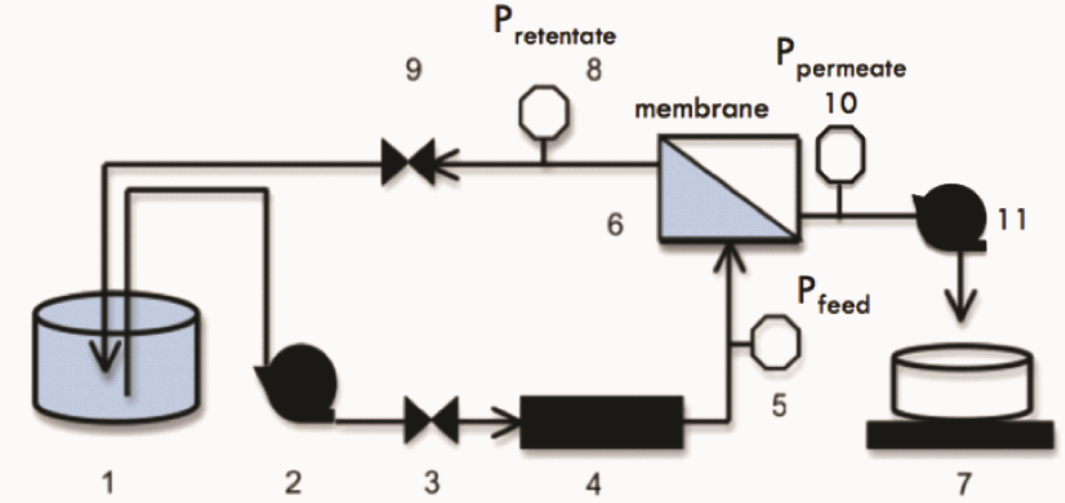


**FIGURE 2-20** A schematic illustration showing a homemade cross-flow system. (1: feed tank; 2, 11: pump; 3,9: valve; 4: flow meter; 5,8,10: pressure gauge; 6: cross-flow cell; 7: electronic balance) (Reprinted with permission from Ref.151. Copyright (2013) American Chemical Society)

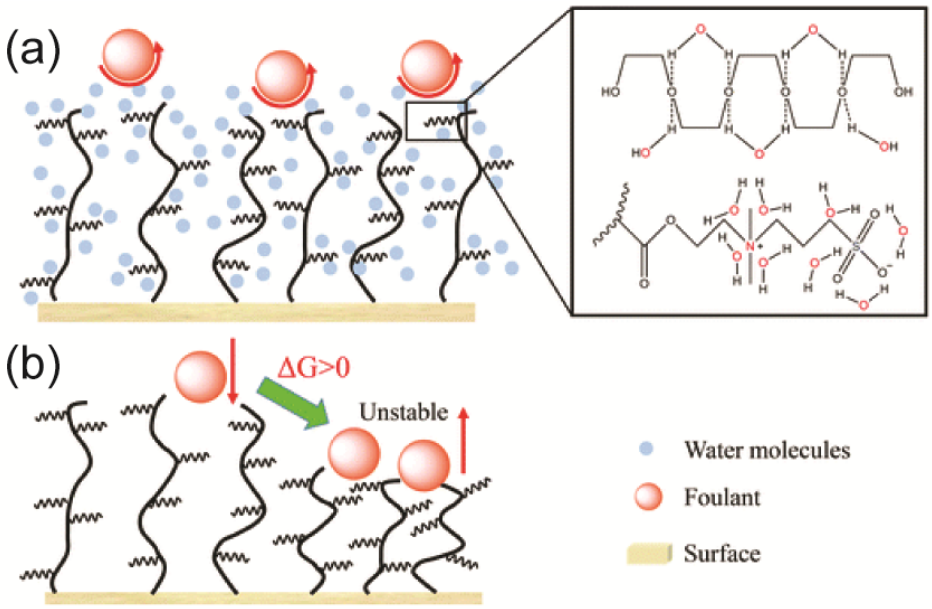


**FIGURE 2-21** Schematic illustrations showing a) grafted hydrophilic polymers forming a hydration layer so that foulants do not adhere to the membrane surface; and (b) polymer chains compressed by foulants that are entropy unfavorable. (Adapted from Ref. 85 with permission of The Royal Society of Chemistry.)

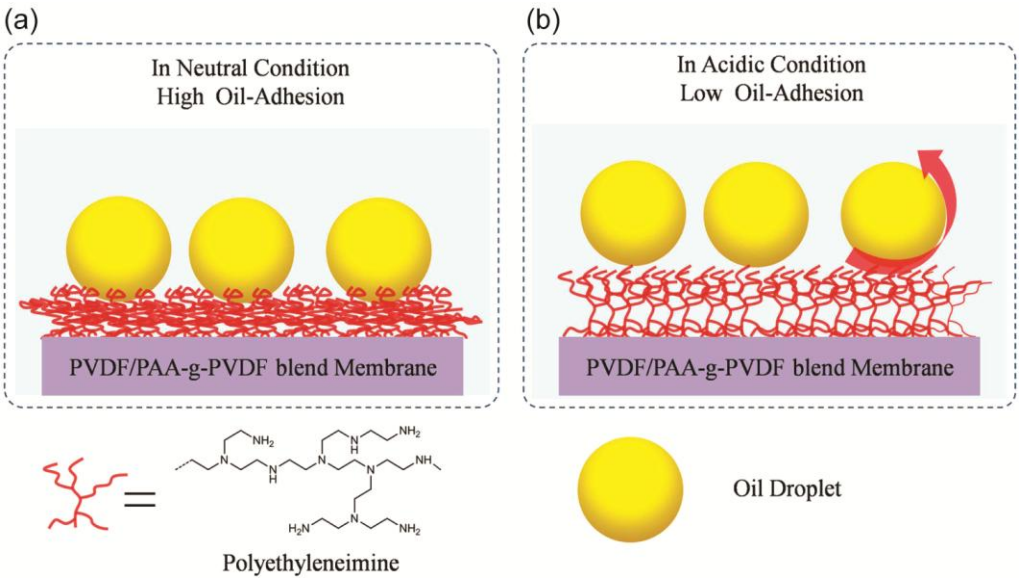


**FIGURE 2-22** Schematic showing that (a) foulants can compress a polymer membrane as they attach onto the surface; and (b) the polymer chains can swell when exposed to an acidic environment, repelling the foulants. (Reprinted from Ref. 140, Copyright (2015), with permission from Elsevier.)

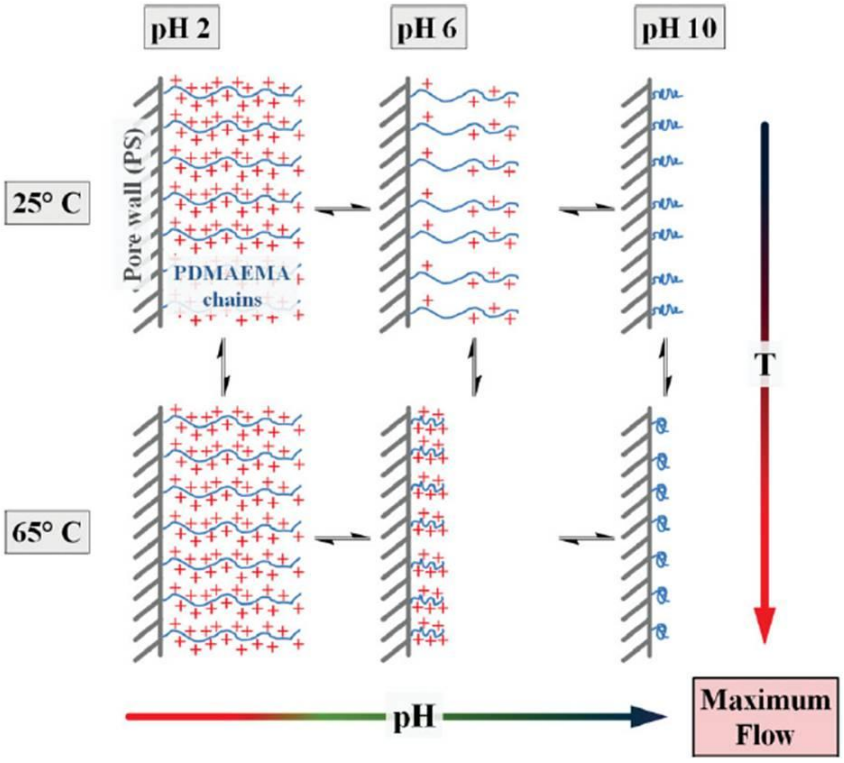


**FIGURE 2-23** Polymers that are responsive to both temperature and pH can transit between a globule state and a coiled state. (Reprinted from Ref. 141, Copyright (2016), with permission from Elsevier.)

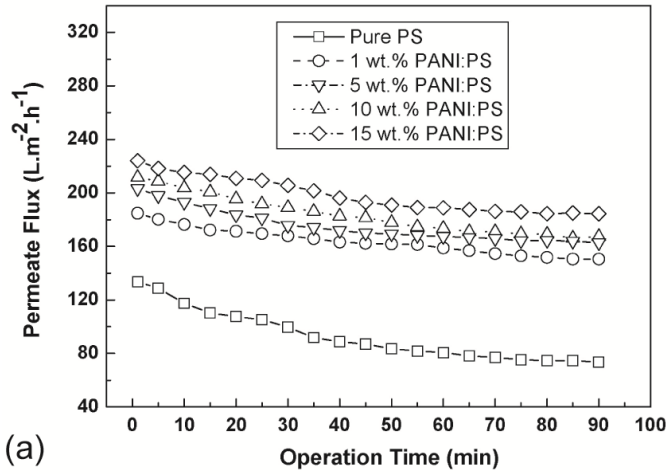


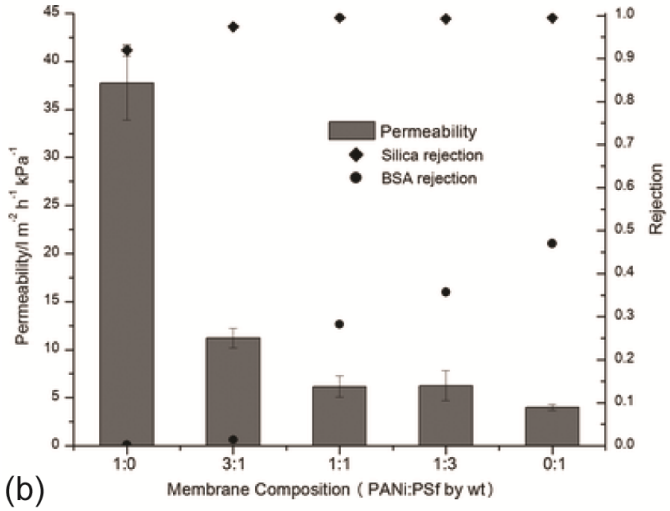


**FIGURE 2-24** (a) Polysulfone membranes when blended with polyaniline exhibit higher permeation fluxes. (Reprinted from Ref. 142, Copyright (2008), with permission from Elsevier.) (b) Polyaniline/polysulfone composite membranes show a drastic decrease in the permeation flux and increase for the BSA rejection as the ratio of polyaniline decreases. (Adapted from Ref. 143 with permission of The Royal Society of Chemistry.)

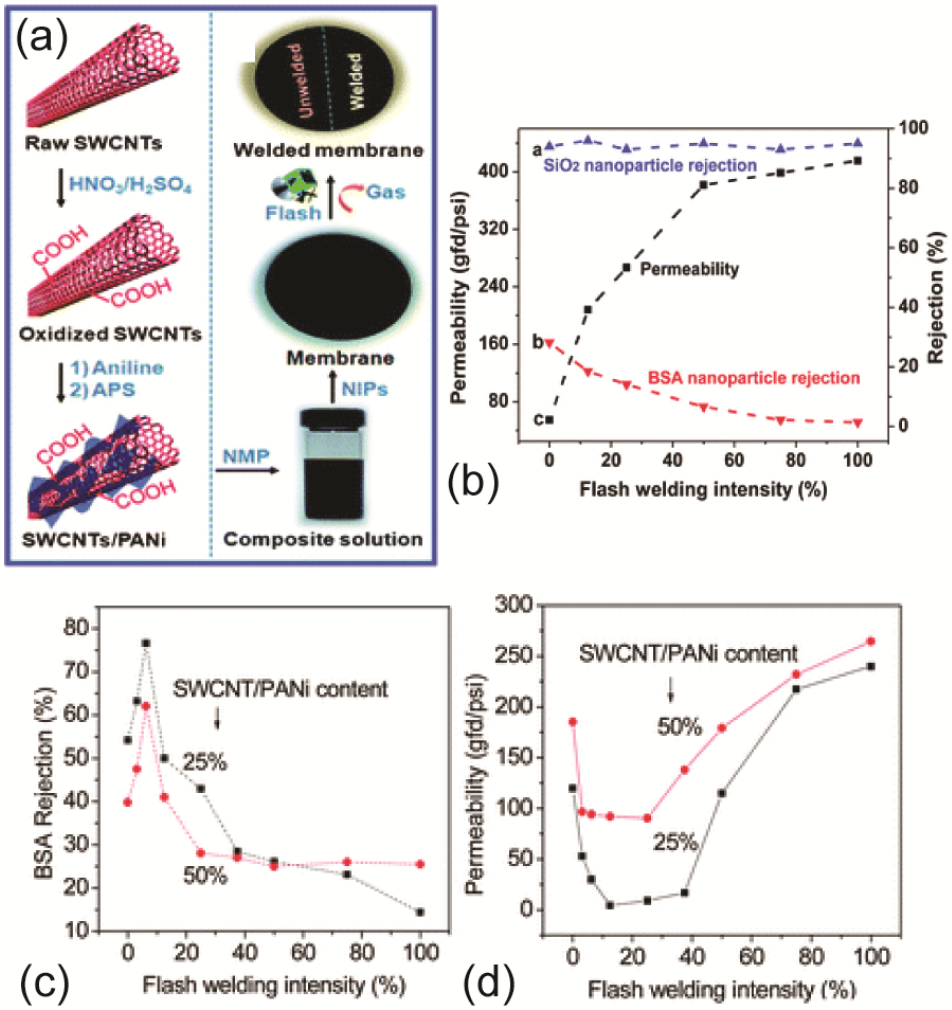


**FIGURE 2-25** (a) An illustration of the procedure for fabricating a polyaniline/SWCNT membrane, followed by flash welding. (b) A pristine polyaniline/SWCNT membrane exhibits an increase in permeability, a decrease in BSA rejection, while keeping its silica nanoparticle rejections essentially unchanged even as the welding intensity increases. (Reproduced Ref. 147 with permission of The Royal Society of Chemistry.) Polyaniline and SWCNT blended with a base polymer show (c) better BSA rejection rates, and (d) lower percentages of polyaniline result in higher permeation flux. (Reproduced from Ref. 149 with permission of The Royal Society of Chemistry.)

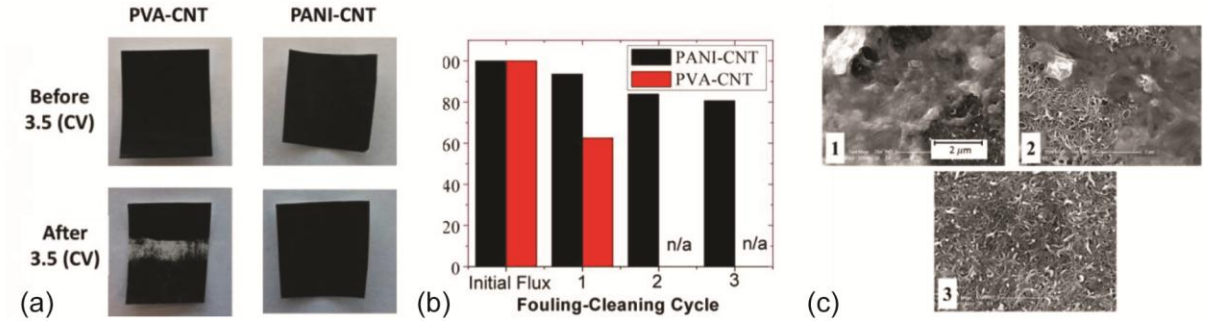


**FIGURE 2-26** (a) Images of PVA/CNT and polyaniline/CNT membranes before and after applying a voltage. (b) The polyaniline/CNT membrane showed a very high flux recovery, while the PVA/CNT membrane had a 60% decline after its first fouling cycle. (c) SEM images show the membrane surfaces after (1) BSA fouling; (2) washing with water; and (3) applying a voltage. (Reprinted with permission from Ref. 150. Copyright (2016) American Chemical Society)

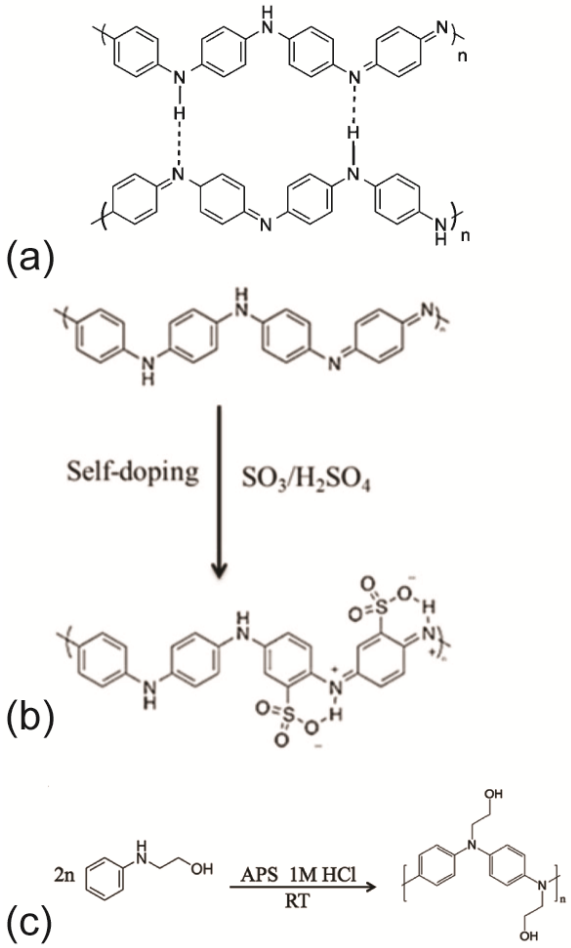


**FIGURE 2-27** Chemical structures showing (a) hydrogen bonding formation between polyaniline chains that result in gelation; (Reprinted with permission from Ref. 151, Copyright (2013) American Chemical Society.) (b) the procedure for synthesizing sulfonated polyaniline and (c) the synthesis of nPANI. (Adapted from Ref. 152 and 153 with permission of The Royal Society of Chemistry)

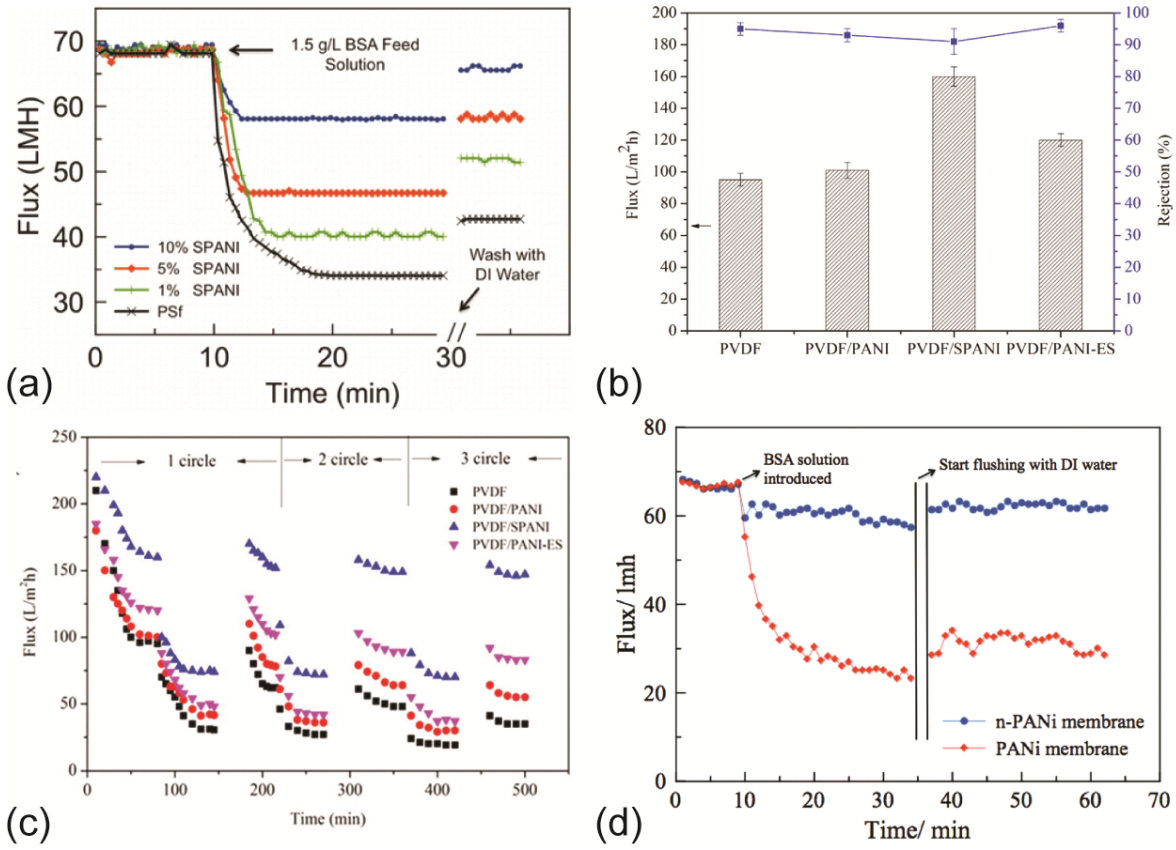


**FIGURE 2-28** Plots showing (a) much lower flux declines in polysulfone membranes incorporating SPANI; (Reprinted with permission from Ref. 151, Copyright (2013) American Chemical Society.) (b) a SPANI composite exhibiting the highest flux permeation; (c) a SPANI composite exhibiting the highest flux recovery; (d) an nPANI membrane exhibits an 11% flux decline after BSA fouling, which is much lower than that of a PANI membrane. (Adapted from Ref. 152 and 153 with permission of The Royal Society of Chemistry)

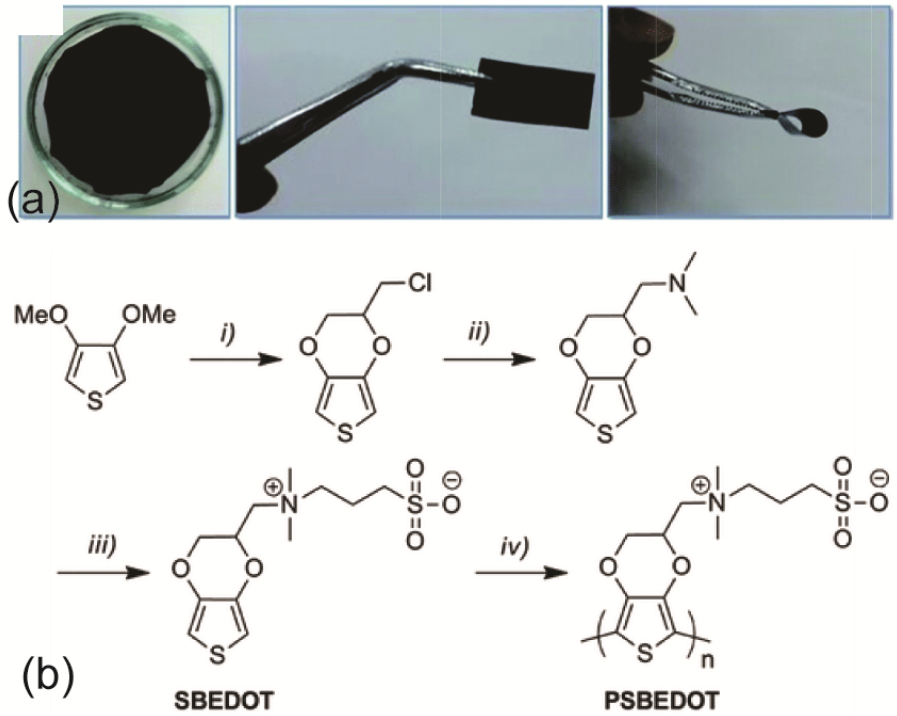


**FIGURE 2-29** (a) Photos showing a flexible ultrafiltration membrane comprised of rGO and polythiophene; (Reproduced from Ref. 167 with permission of The Royal Society of Chemistry) (b) the synthesis route for an electroactive polythiophene block co-polymer. (Adapted from Ref 168 published by The Royal Society of Chemistry)

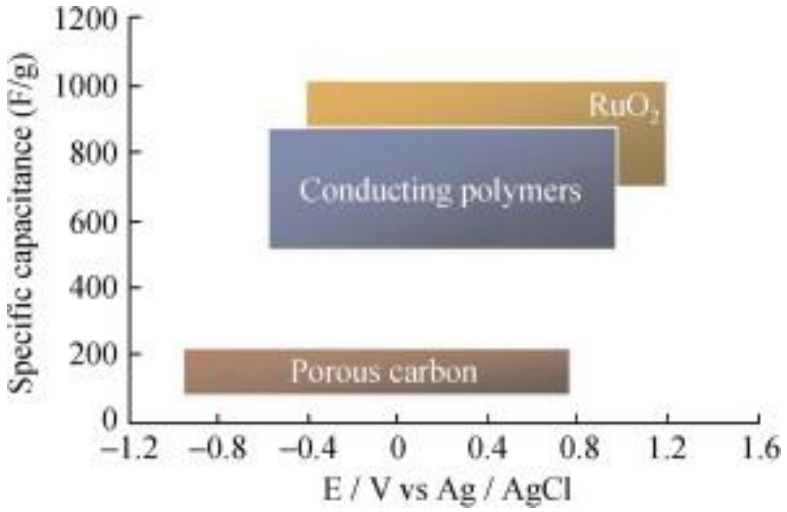


**FIGURE 2-30** Plot of specific capacitance vs. potential comparing the capacitance ranges for porous carbon, conducting polymers and $RuO_2$ (Reprinted from Ref. 183. Copyright 2008, with permission from Elsevier.)

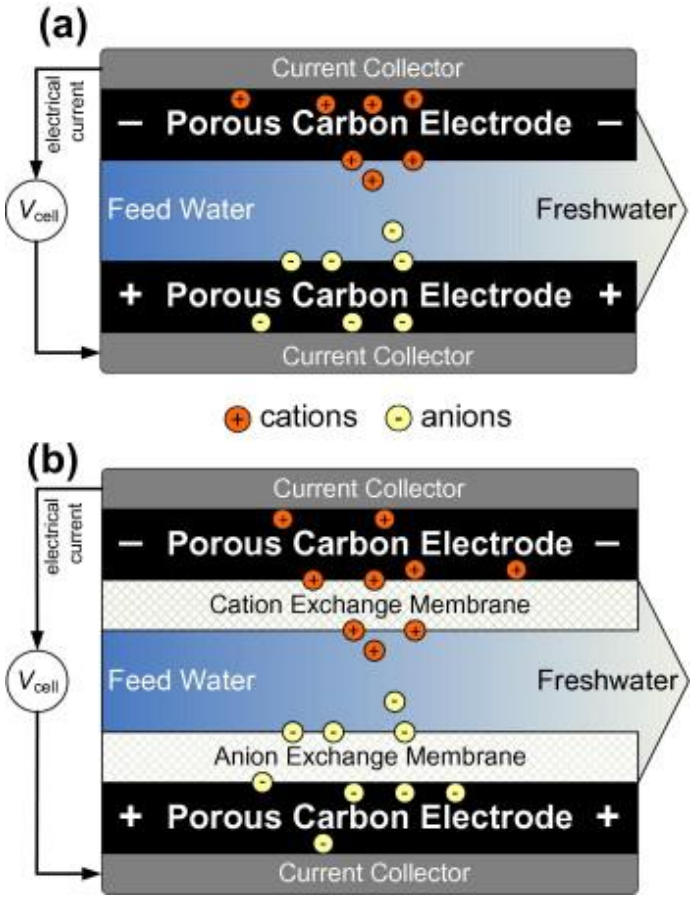


**FIGURE 2-31** Schematic diagrams showing a flow-by configuration for (a) capacitive deionization (CDI) and (b) modified MCDI under an applied potential. Ions are adsorbed onto the corresponding electrode of opposite charge. (Reprinted with permission from Ref. 190. Copyright 2013, with permission from Elsevier.)

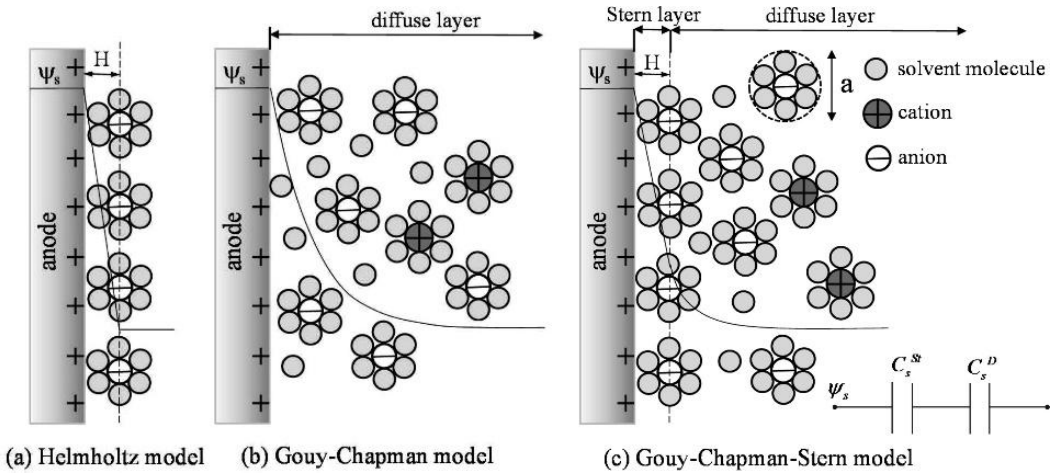


**FIGURE 2-32** Illustrations of ion adsorption: (a) the Helmholtz model, (b) the Gouy-Chapman model, and (c) the Gouy-Chapman-Stern model. (Reprinted with permission from Ref. 194. Copyright 2011, American Chemical Society.)

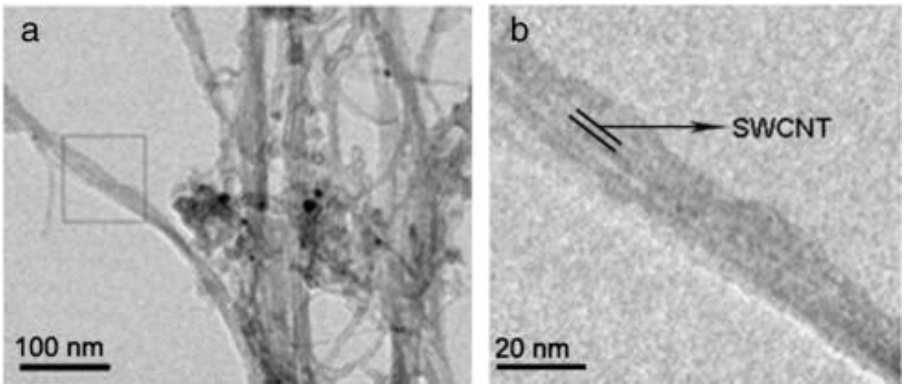


**FIGURE 2-33** TEM images of (a) a single walled carbon nanotube/PANI composite and (b) a magnified view of the composite showing PANI coated along the walls of the carbon nanotubes. (Reprinted from Ref. 203. Copyright 2012, with permission from Elsevier.)

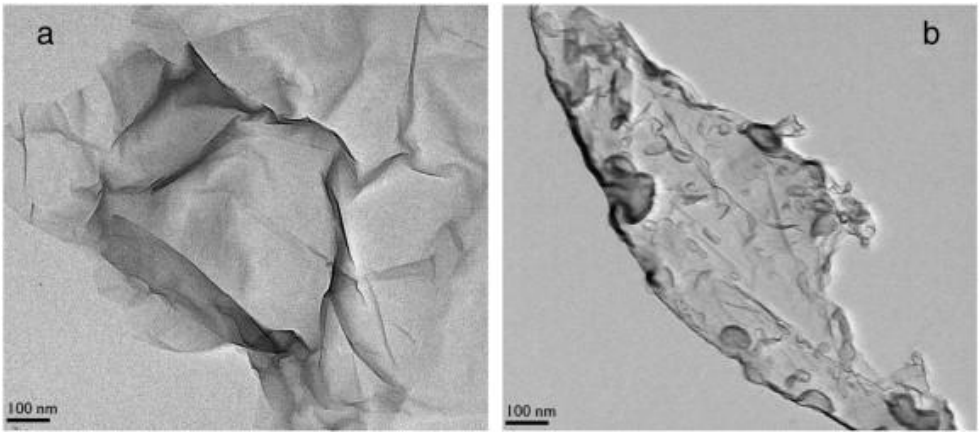


**FIGURE 2-34** TEM images of (a) graphene oxide and (b) graphene oxide/PANI nanocomposite with PANI located at the edges of the graphene oxide sheets. (Reprinted from Ref. 211. Copyright 2014, with permission from Elsevier.)

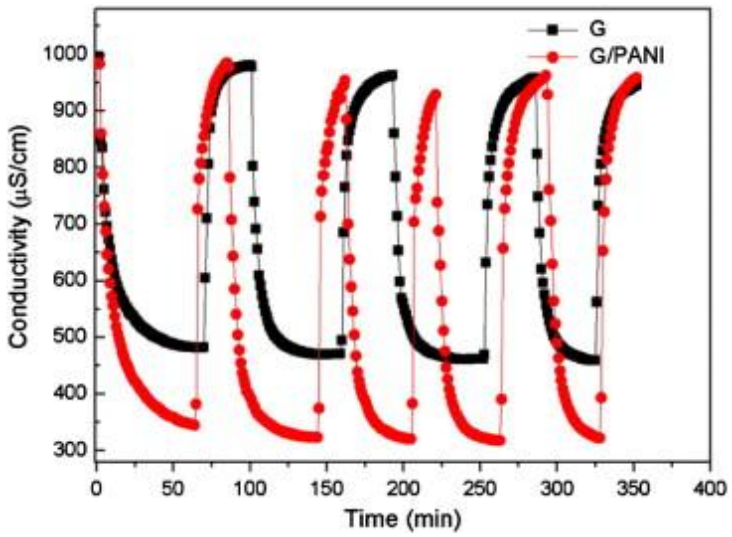


**FIGURE 2-35** Regeneration performance of a graphene electrode (black squares) compared with a graphene/polyaniline composite electrode (red circles). (Reprinted from Ref. 183. Copyright 2008, with permission from Elsevier.)

## REFERENCES


1 Koros, W. J. & Fleming, G. K. Membrane-based gas separation. *Journal of Membrane Science* **83**, 1-80 (1993).

2 Tsutomo Nakagawa, Y. O. *Membrane science and technology*. (Marcel Dekker, Inc., 1992).

3 Mulder, M. *Basic principles of membrane technology*. (Springer Science+Business Media Dordrecht, 1991).

4 Alexander Stern, S. Polymers for gas separations: The next decade. *Journal of Membrane Science* **94**, 1-65 (1994).

5 Haggin, J. Membrane technology has achieved success, yet lags potential. *Chemical & Engineering News Archive* **68**, 22-26 (1990).

6 Kerry, F. *Industrial gas handbook: Gas separation and purification*. 1st edn, 275-280 (CRC Press, 2007).

7 Bernardo, P. & Clarizia, G. *30 years of membrane technology for gas separation*. Vol. 32 (2013).

8 Jiang, D.-e., Cooper, V. R. & Dai, S. Porous graphene as the ultimate membrane for gas separation. *Nano Letters* **9**, 4019-4024 (2009).

9 Kim, H. W. *et al.* Selective gas transport through few-layered graphene and graphene oxide membranes. *Science* **342**, 91-95 (2013).

10 Li, H. *et al.* Ultrathin, molecular-sieving graphene oxide membranes for selective hydrogen separation. *Science* **342**, 95-98 (2013).

11 Yoo, B. M., Shin, J. E., Lee, H. D. & Park, H. B. Graphene and graphene oxide membranes for gas separation applications. *Current Opinion in Chemical Engineering* **16**, 39-47 (2017).

12 Rodenas, T. *et al.* Metal–organic framework nanosheets in polymer composite materials for gas separation. *Nature materials* **14**, 48 (2015).

13 Bae, T. H. *et al.* A high-performance gas-separation membrane containing submicrometer-sized metal–organic framework crystals. *Angewandte Chemie International Edition* **49**, 9863-9866 (2010).

14 Fu, J. *et al.* Fabrication of cof-mof composite membranes and their highly selective separation of h2/co2. *Journal of the American Chemical Society* **138**, 7673-7680 (2016).

15 Powell, C. E. & Qiao, G. G. Polymeric co2/n2 gas separation membranes for the capture of carbon dioxide from power plant flue gases. *Journal of Membrane Science* **279**, 1-49 (2006).

16 Du, N., Park, H. B., Dal-Cin, M. M. & Guiver, M. D. Advances in high permeability polymeric membrane materials for co2 separations. *Energy & Environmental Science* **5**, 7306-7322 (2012).

17 D.R. Paul, P. Y. s. *Polymeric gas separation membranes*. (CRC Press, 1994).

18 Spillman, R. W. Economics of gas separation membranes. *Chemical engineering progress* **85**, 41-62 (1989).

19 Sanders, D. F. *et al.* Energy-efficient polymeric gas separation membranes for a sustainable future: A review. *Polymer* **54**, 4729-4761 (2013).

20 R.E. Kesting, A. K. F. *Polymeric gas separation membranes*. (Wiley, 1993).

21 Henis, J. M. & Tripodi, M. K. The developing technology of gas separating membranes. *Science* **220**, 11-17 (1983).

22 Pandey, P. & Chauhan, R. S. Membranes for gas separation. *Progress in Polymer Science* **26**, 853-893 (2001).

23 Robeson, L. M. Correlation of separation factor versus permeability for polymeric membranes. *Journal of membrane science* **62**, 165-185 (1991).

24 Robeson, L. M. The upper bound revisited. *Journal of Membrane Science* **320**, 390-400 (2008).

25 Freeman, B. D. Basis of permeability/selectivity tradeoff relations in polymeric gas separation membranes. *Macromolecules* **32**, 375-380 (1999).

26 Tourillon, G. & Garnier, F. Morphology of conducting organic polymers: Polythiophene and poly(3-methyl thiophene). *Journal of Polymer Science: Polymer Physics Edition* **22**, 33-39 (1984).

27 Karasz, F. E. *et al.* Nascent morphology of polyacetylene. *Nature* **282**, 286 (1979).

28 Anderson, M. R., Mattes, B. R., Reiss, H. & Kaner, R. B. Conjugated polymer films for gas separations. *Science* **252**, 1412-1415 (1991).

29 Tiitu, M., Hiekkataipale, P., Hartikainen, J., Mäkelä, T. & Ikkala, O. Viscoelastic and electrical transitions in gelation of electrically conducting polyaniline. *Macromolecules* **35**, 5212-5217 (2002).

30 Macdiarmid, A. G. *et al.* "Polyaniline": Interconversion of metallic and insulating forms. *Molecular Crystals and Liquid Crystals* **121**, 173-180 (1985).

31 Huang, J., Virji, S., Weiller, B. H. & Kaner, R. B. Polyaniline nanofibers: Facile synthesis and chemical sensors. *Journal of the American Chemical Society* **125**, 314-315 (2003).

32 Huang, J. & Kaner, R. B. A general chemical route to polyaniline nanofibers. *Journal of the American Chemical Society* **126**, 851-855 (2004).

33 Yue, J., Epstein, A. J., Zhong, Z., Gallagher, P. K. & Macdiarmid, A. G. Thermal stabilities of polyanilines. *Synthetic Metals* **41**, 765-768 (1991).

34 Trchová, M., Šeděnková, I., Tobolková, E. & Stejskal, J. Ftir spectroscopic and conductivity study of the thermal degradation of polyaniline films. *Polymer Degradation and Stability* **86**, 179-185 (2004).

35 Virji, S., Huang, J., Kaner, R. B. & Weiller, B. H. Polyaniline nanofiber gas sensors: Examination of response mechanisms. *Nano letters* **4**, 491-496 (2004).

36 Novák, P., Müller, K., Santhanam, K. & Haas, O. Electrochemically active polymers for rechargeable batteries. *Chemical Reviews* **97**, 207-282 (1997).

37 Snook, G. A., Kao, P. & Best, A. S. Conducting-polymer-based supercapacitor devices and electrodes. *Journal of Power Sources* **196**, 1-12 (2011).

38 Wu, Q., Xu, Y., Yao, Z., Liu, A. & Shi, G. Supercapacitors based on flexible graphene/polyaniline nanofiber composite films. *ACS nano* **4**, 1963-1970 (2010).

39 Wessling, B. Passivation of metals by coating with polyaniline: Corrosion potential shift and morphological changes. *Advanced Materials* **6**, 226-228 (1994).

40 Lu, W. *et al.* Use of ionic liquids for π-conjugated polymer electrochemical devices. *Science* **297**, 983-987 (2002).

41 Baker, C. O. *et al.* Monolithic actuators from flash-welded polyaniline nanofibers. *Advanced Materials* **20**, 155-158 (2008).

42 Jager, E. W., Smela, E. & Inganäs, O. Microfabricating conjugated polymer actuators. *Science* **290**, 1540-1545 (2000).

43 Baker, C. O., Huang, X., Nelson, W. & Kaner, R. B. Polyaniline nanofibers: Broadening applications for conducting polymers. *Chemical Society Reviews* **46**, 1510-1525 (2017).

44 Li, D., Huang, J. & Kaner, R. B. Polyaniline nanofibers: A unique polymer nanostructure for versatile applications. *Accounts of Chemical Research* **42**, 135-145 (2009).

45 Kang, E., Neoh, K. & Tan, K. Polyaniline: A polymer with many interesting intrinsic redox states. *Progress in Polymer Science* **23**, 277-324 (1998).

46 Focke, W. W., Wnek, G. E. & Wei, Y. Influence of oxidation state, ph, and counterion on the conductivity of polyaniline. *Journal of Physical Chemistry* **91**, 5813-5818 (1987).

47 Wu, H. *et al.* Stable li-ion battery anodes by in-situ polymerization of conducting hydrogel to conformally coat silicon nanoparticles. *Nature communications* **4**, 1943 (2013).

48 Conklin, J. A., Anderson, M. R., Reiss, H. & Kaner, R. B. Anhydrous halogen acid interaction with polyaniline membranes: A gas permeability study. *The Journal of Physical Chemistry* **100**, 8425-8429 (1996).

49 Nightingale, E. R. Phenomenological theory of ion solvation. Effective radii of hydrated ions. *The Journal of Physical Chemistry* **63**, 1381-1387 (1959).

50 Masuda, T., Tang, B. Z., Higashimura, T. & Yamaoka, H. Thermal degradation of polyacetylenes carrying substituents. *Macromolecules* **18**, 2369-2373 (1985).

51 Shirakawa, H. The discovery of polyacetylene film: The dawning of an era of conducting polymers (nobel lecture). *Angewandte Chemie International Edition* **40**, 2574-2580 (2001).

52 Pellegrino, J. The use of conducting polymers in membrane-based separations. *Annals of the New York Academy of Sciences* **984**, 289-305 (2003).

53 Illing, G., Hellgardt, K., Wakeman, R. & Jungbauer, A. Preparation and characterisation of polyaniline based membranes for gas separation. *Journal of Membrane Science* **184**, 69-78 (2001).

54 Illing, G., Hellgardt, K., Schonert, M., Wakeman, R. J. & Jungbauer, A. Towards ultrathin polyaniline films for gas separation. *Journal of Membrane Science* **253**, 199-208 (2005).

55 Ding, L., Wang, X. & Gregory, R. Thermal properties of chemically synthesized polyaniline (eb) powder. *Synthetic Metals* **104**, 73-78 (1999).

56 Mathew, R., Mattes, B. R. & Espe, M. P. A solid state nmr characterization of cross-linked polyaniline powder. *Synthetic Metals* **131**, 141-147 (2002).

57 Gupta, Y., Hellgardt, K. & Wakeman, R. J. Enhanced permeability of polyaniline based nano-membranes for gas separation. *Journal of Membrane Science* **282**, 60-70 (2006).

58 Kuwabata, S. & Martin, C. R. Investigation of the gas-transport properties of polyaniline. *Journal of Membrane Science* **91**, 1-12 (1994).

59 Giel, V. *et al.* Polyaniline/polybenzimidazole blends: Characterisation of its physico-chemical properties and gas separation behaviour. *European Polymer Journal* **77**, 98-113 (2016).

60 Su, T. M. *et al.* Polyaniline/polyimide blends for pervaporation and gas separation studies. *Synthetic Metals* **84**, 801-802 (1997).

61 Orlov, A. V. *et al.* Structure and gas separation properties of composite films based on polyaniline. *Journal of Applied Polymer Science* **89**, 1379-1384 (2003).

62 Zhao, J., Wang, Z., Wang, J. & Wang, S. High-performance membranes comprising polyaniline nanoparticles incorporated into polyvinylamine matrix for co2/n2 separation. *Journal of Membrane Science* **403-404**, 203-215 (2012).

63 Giel, V., Morávková, Z., Peter, J. & Trchová, M. Thermally treated polyaniline/polybenzimidazole blend membranes: Structural changes and gas transport properties. *Journal of Membrane Science* **537**, 315-322 (2017).

64 Weng, C.-J. *et al.* Mechanically and thermally enhanced intrinsically dopable polyimide membrane with advanced gas separation capabilities. *Macromolecules* **44**, 6067-6076 (2011).

65 Ghalei, B. *et al.* Surface functionalization of high free-volume polymers as a route to efficient hydrogen separation membranes. *Journal of Materials Chemistry A* **5**, 4686-4694 (2017).

66 Liang, W. & Martin, C. R. Gas transport in electronically conductive polymers. *Chemistry of Materials* **3**, 390-391 (1991).

67 Kamada, K., Kamo, J., Motonaga, A., Iwasaki, T. & Hosokawa, H. Gas permeation properties of conducting polymer/porous media composite membranes i. *Polymer journal* **26**, 141 (1994).

68 Parthasarathy, R. V., Menon, V. P. & Martin, C. R. Unusual gas-transport selectivity in a partially oxidized form of the conductive polymer polypyrrole. *Chemistry of Materials* **9**, 560-566 (1997).

69 Gulsen, D., Hacarloglu, P., Toppare, L. & Yilmaz, L. Effect of preparation parameters on the performance of conductive composite gas separation membranes. *Journal of Membrane Science* **182**, 29-39 (2001).

70 Hacarlioglu, P., Toppare, L. & Yilmaz, L. Polycarbonate–polypyrrole mixed matrix gas separation membranes. *Journal of Membrane Science* **225**, 51-62 (2003).

71 Musselman, I. H. *et al.* Poly(3-dodecylthiophene) membranes for gas separations. *Journal of Membrane Science* **152**, 1-18 (1999).

72 Elimelech, M. The global challenge for adequate and safe water. *Journal of Water Supply: Research and Technology - Aqua* **55**, 3-10 (2006).

73 Shannon, M. A. *et al.* Science and technology for water purification in the coming decades. *Nature* **452**, 301 (2008).

74 Huang, Y., Li, J., Chen, X. & Wang, X. Applications of conjugated polymer based composites in wastewater purification. *RSC Advances* **4**, 62160-62178 (2014).

75 Zhang, R. *et al.* Antifouling membranes for sustainable water purification: Strategies and mechanisms. *Chemical Society Reviews* **45**, 5888-5924 (2016).

76 Rana, D. & Matsuura, T. Surface modifications for antifouling membranes. *Chemical Reviews* **110**, 2448-2471 (2010).

77 Yan, J. *et al.* Preparation of a graphene nanosheet/polyaniline composite with high specific capacitance. *Carbon* **48**, 487-493 (2010).

78 Bajpai, M., Rai, N. & Bajpai, S. K. Equilibrium adsorption studies on removal of diclofenac sodium from aqueous solution using sawdust–polyaniline (sd–pan) composites. *Journal of Applied Polymer Science* **125**, 1382-1390 (2012).

79 Mansour, M. S., Ossman, M. E. & Farag, H. A. Removal of cd (ii) ion from waste water by adsorption onto polyaniline coated on sawdust. *Desalination* **272**, 301-305 (2011).

80 Ansari, R. & Dezhampanah, H. Application of polyaniline/sawdust composite for removal of acid green 25 from aqueous solutions: Kinetics and thermodynamic studies. *European Chemical Bulletin* **2**, 220-225 (2013).

81 Mi, B. & Elimelech, M. Organic fouling of forward osmosis membranes: Fouling reversibility and cleaning without chemical reagents. *Journal of Membrane Science* **348**, 337-345 (2010).

82 Kim, Y., Elimelech, M., Shon, H. K. & Hong, S. Combined organic and colloidal fouling in forward osmosis: Fouling reversibility and the role of applied pressure. *Journal of Membrane Science* **460**, 206-212 (2014).

83 Magin, C. M., Cooper, S. P. & Brennan, A. B. Non-toxic antifouling strategies. *Materials Today* **13**, 36-44 (2010).

84 Lejars, M., Margaillan, A. & Bressy, C. Fouling release coatings: A nontoxic alternative to biocidal antifouling coatings. *Chemical Reviews* **112**, 4347-4390 (2012).

85 Lade, H. *et al.* Exploring the potential of curcumin for control of n-acyl homoserine lactone-mediated biofouling in membrane bioreactors for wastewater treatment. *RSC Advances* **7**, 16392-16400 (2017).

86 Nabe, A., Staude, E. & Belfort, G. Surface modification of polysulfone ultrafiltration membranes and fouling by bsa solutions. *Journal of Membrane Science* **133**, 57-72 (1997).

87 Susanto, H. & Ulbricht, M. Photografted thin polymer hydrogel layers on pes ultrafiltration membranes: Characterization, stability, and influence on separation performance. *Langmuir* **23**, 7818-7830 (2007).

88 Sun, Q., Su, Y., Ma, X., Wang, Y. & Jiang, Z. Improved antifouling property of zwitterionic ultrafiltration membrane composed of acrylonitrile and sulfobetaine copolymer. *Journal of membrane science* **285**, 299-305 (2006).

89 Ricq, L., Narçon, S., Reggiani, J.-C. & Pagetti, J. Streaming potential and protein transmission ultrafiltration of single proteins and proteins in mixture: B-lactoglobulin and lysozyme. *Journal of Membrane Science* **156**, 81-96 (1999).

90 Fane, A. G., Fell, C. J. D. & Suki, A. The effect of ph and ionic environment on the ultrafiltration of protein solutions with retentive membranes. *Journal of Membrane Science* **16**, 195-210 (1983).

91 McDonogh, R. M., Bauser, H., Stroh, N. & Chmiel, H. Concentration polarisation and adsorption effects in cross-flow ultrafiltration of proteins. *Desalination* **79**, 217-231 (1990).

92 Vrijenhoek, E. M., Hong, S. & Elimelech, M. Influence of membrane surface properties on initial rate of colloidal fouling of reverse osmosis and nanofiltration membranes. *Journal of Membrane Science* **188**, 115-128 (2001).

93 Li, H., Fane, A. G., Coster, H. G. L. & Vigneswaran, S. Observation of deposition and removal behaviour of submicron bacteria on the membrane surface during crossflow microfiltration. *Journal of Membrane Science* **217**, 29-41 (2003).

94 Pang, C. M., Hong, P., Guo, H. & Liu, W.-T. Biofilm formation characteristics of bacterial isolates retrieved from a reverse osmosis membrane. *Environmental Science & Technology* **39**, 7541-7550 (2005).

95 Werber, J. R., Osuji, C. O. & Elimelech, M. Materials for next-generation desalination and water purification membranes. *Nature Reviews Materials* **1**, 16018 (2016).

96 Tadmor, R. Line energy and the relation between advancing, receding, and young contact angles. *Langmuir* **20**, 7659-7664 (2004).

97 de Gennes, P. G. Wetting: Statics and dynamics. *Reviews of Modern Physics* **57**, 827-863 (1985).

98 Mittal, K. L. *Contact angle, wettability and adhesion*. Vol. 4 (CRC Press, 2006).

99 Xinwei, H. *High-performance water filtration membranes using surface modification and new materials* PhD thesis, University of California, Los Angeles, (2016).

100 Kim, K. J., Fane, A. G. & Fell, C. J. D. The performance of ultrafiltration membranes pretreated by polymers. *Desalination* **70**, 229-249 (1988).

101 Brink, L. E. S. & Romijn, D. J. Reducing the protein fouling of polysulfone surfaces and polysulfone ultrafiltration membranes: Optimization of the type of presorbed layer. *Desalination* **78**, 209-233 (1990).

102 Grebenyuk, V. D., Chebotareva, R. D., Peters, S. & Linkov, V. Surface modification of anion-exchange electrodialysis membranes to enhance anti-fouling characteristics. *Desalination* **115**, 313-329 (1998).

103 Reddy, A. V. R., Mohan, D. J., Bhattacharya, A., Shah, V. J. & Ghosh, P. K. Surface modification of ultrafiltration membranes by preadsorption of a negatively charged polymer: I. Permeation of water soluble polymers and inorganic salt solutions and fouling resistance properties. *Journal of Membrane Science* **214**, 211-221 (2003).

104 Akhtar, S., Hawes, C., Dudley, L., Reed, I. & Stratford, P. Coatings reduce the fouling of microfiltration membranes. *Journal of Membrane Science* **107**, 209-218 (1995).

105 Galjaard, G., Buijs, P., Beerendonk, E., Schoonenberg, F. & Schippers, J. C. Pre-coating (epce® ) uf membranes for direct treatment of surface water. *Desalination* **139**, 305-316 (2001).

106 Poźniak, G., Gancarz, I., Bryjak, M. & Tylus, W. N-butylamine plasma modifying ultrafiltration polysulfone membranes. *Desalination* **146**, 293-299 (2002).

107 Kumar, R., Isloor, A. M., Ismail, A. F. & Matsuura, T. Synthesis and characterization of novel water soluble derivative of chitosan as an additive for polysulfone ultrafiltration membrane. *Journal of Membrane Science* **440**, 140-147 (2013).

108 Shi, Q. *et al.* Grafting short-chain amino acids onto membrane surfaces to resist protein fouling. *Journal of Membrane Science* **366**, 398-404 (2011).

109 Ostuni, E., Chapman, R. G., Holmlin, R. E., Takayama, S. & Whitesides, G. M. A survey of structure−property relationships of surfaces that resist the adsorption of protein. *Langmuir* **17**, 5605-5620 (2001).

110 Statz, A. R., Meagher, R. J., Barron, A. E. & Messersmith, P. B. New peptidomimetic polymers for antifouling surfaces. *Journal of the American Chemical Society* **127**, 7972-7973 (2005).

111 Huang, J. *et al.* Fabrication of polyethersulfone-mesoporous silica nanocomposite ultrafiltration membranes with antifouling properties. *Journal of Membrane Science* **423-424**, 362-370 (2012).

112 Vatanpour, V., Madaeni, S. S., Moradian, R., Zinadini, S. & Astinchap, B. Fabrication and characterization of novel antifouling nanofiltration membrane prepared from oxidized multiwalled carbon nanotube/polyethersulfone nanocomposite. *Journal of Membrane Science* **375**, 284-294 (2011).

113 Liu, S. *et al.* Antibacterial activity of graphite, graphite oxide, graphene oxide, and reduced graphene oxide: Membrane and oxidative stress. *ACS nano* **5**, 6971-6980 (2011).

114 Gao, W. in *Graphene oxide: Reduction recipes, spectroscopy, and applications* 61-95 (Springer, 2015).

115 Xu, Z. *et al.* Photocatalytic antifouling pvdf ultrafiltration membranes based on synergy of graphene oxide and tio2 for water treatment. *Journal of Membrane Science* **520**, 281-293 (2016).

116 Choi, W., Choi, J., Bang, J. & Lee, J.-H. Layer-by-layer assembly of graphene oxide nanosheets on polyamide membranes for durable reverse-osmosis applications. *ACS Applied Materials & Interfaces* **5**, 12510-12519 (2013).

117 Huang, X., Marsh, K. L., McVerry, B. T., Hoek, E. M. V. & Kaner, R. B. Low-fouling antibacterial reverse osmosis membranes via surface grafting of graphene oxide. *ACS Applied Materials & Interfaces* **8**, 14334-14338 (2016).

118 McVerry, B. T. *et al.* Scalable antifouling reverse osmosis membranes utilizing perfluorophenyl azide photochemistry. *Macromolecular Rapid Communications* **35**, 1528-1533 (2014).

119 Zheng, J., Li, L., Chen, S. & Jiang, S. Molecular simulation study of water interactions with oligo (ethylene glycol)-terminated alkanethiol self-assembled monolayers. *Langmuir* **20**, 8931-8938 (2004).

120 Shao, Q., He, Y. & Jiang, S. Molecular dynamics simulation study of ion interactions with zwitterions. *The Journal of Physical Chemistry B* **115**, 8358-8363 (2011).

121 Wu, C. & Wang, X. Globule-to-coil transition of a single homopolymer chain in solution. *Physical review letters* **80**, 4092 (1998).

122 Sherman, E. & Haran, G. Coil–globule transition in the denatured state of a small protein. *Proceedings of the National Academy of Sciences* **103**, 11539-11543 (2006).

123 Dutta, K. & De, S. Smart responsive materials for water purification: An overview. *Journal of Materials Chemistry A* **5**, 22095-22112 (2017).

124 Shevate, R., Karunakaran, M., Kumar, M. & Peinemann, K.-V. Polyanionic ph-responsive polystyrene-b-poly(4-vinyl pyridine-n-oxide) isoporous membranes. *Journal of Membrane Science* **501**, 161-168 (2016).

125 Nunes, S. P. *et al.* Switchable ph-responsive polymeric membranes prepared via block copolymer micelle assembly. *ACS Nano* **5**, 3516-3522 (2011).

126 Li, Y. *et al.* Thermoresponsive gating characteristics of poly(n-isopropylacrylamide)-grafted porous poly(vinylidene fluoride) membranes. *Industrial & Engineering Chemistry Research* **43**, 2643-2649 (2004).

127 Li, S. & D'Emanuele, A. On–off transport through a thermoresponsive hydrogel composite membrane. *Journal of Controlled Release* **75**, 55-67 (2001).

128 Lin, X., Huang, R. & Ulbricht, M. Novel magneto-responsive membrane for remote control switchable molecular sieving. *Journal of Materials Chemistry B* **4**, 867-879 (2016).

129 Li, J.-J., Zhu, L.-T. & Luo, Z.-H. Electrospun fibrous membrane with enhanced swithchable oil/water wettability for oily water separation. *Chemical Engineering Journal* **287**, 474-481 (2016).

130 Zhu, Y., Xie, W., Li, J., Xing, T. & Jin, J. Ph-induced non-fouling membrane for effective separation of oil-in-water emulsion. *Journal of Membrane Science* **477**, 131-138 (2015).

131 Gajda, M. & Ulbricht, M. Capillary pore membranes with grafted diblock copolymers showing reversibly changing ultrafiltration properties with independent response to ions and temperature. *Journal of Membrane Science* **514**, 510-517 (2016).

132 Fan, Z., Wang, Z., Sun, N., Wang, J. & Wang, S. Performance improvement of polysulfone ultrafiltration membrane by blending with polyaniline nanofibers. *Journal of Membrane Science* **320**, 363-371 (2008).

133 Guillen, G. R., Farrell, T. P., Kaner, R. B. & Hoek, E. M. V. Pore-structure, hydrophilicity, and particle filtration characteristics of polyaniline-polysulfone ultrafiltration membranes. *Journal of Materials Chemistry* **20**, 4621-4628 (2010).

134 Zhao, S. *et al.* Antifouling and antibacterial behavior of polyethersulfone membrane incorporating polyaniline@silver nanocomposites. *Environmental Science: Water Research & Technology* **3**, 710-719 (2017).

135 Teli, S. B., Molina, S., Sotto, A., Calvo, E. G. & Abajob, J. d. Fouling resistant polysulfone–pani/tio2 ultrafiltration nanocomposite membranes. *Industrial & Engineering Chemistry Research* **52**, 9470-9479 (2013).

136 Pereira, V. R., Isloor, A. M., Ahmed, A. A. & Ismail, A. F. Preparation, characterization and the effect of pani coated tio2 nanocomposites on the performance of polysulfone ultrafiltration membranes. *New Journal of Chemistry* **39**, 703-712 (2015).

137 Liao, Y. *et al.* Carbon nanotube-templated polyaniline nanofibers: Synthesis, flash welding and ultrafiltration membranes. *Nanoscale* **5**, 3856-3862 (2013).

138 Huang, J. & Kaner, R. B. Flash welding of conducting polymer nanofibres. *Nature Materials* **3**, 783 (2004).

139 Liao, Y., Li, X.-G., Hoek, E. M. V. & Kaner, R. B. Carbon nanotube/polyaniline nanofiber ultrafiltration membranes. *Journal of Materials Chemistry A* **1**, 15390-15396 (2013).

140 Duan, W., Ronen, A., Walker, S. & Jassby, D. Polyaniline-coated carbon nanotube ultrafiltration membranes: Enhanced anodic stability for in situ cleaning and electro-oxidation processes. *ACS applied materials & interfaces* **8**, 22574-22584 (2016).

141 McVerry, B. T. *et al.* Fabrication of low-fouling ultrafiltration membranes using a hydrophilic, self-doping polyaniline additive. *Chemistry of Materials* **25**, 3597-3602 (2013).

142 Zhao, X. & He, C. Efficient preparation of super antifouling pvdf ultrafiltration membrane with one step fabricated zwitterionic surface. *ACS Applied Materials & Interfaces* **7**, 17947-17953 (2015).

143 Huang, X. *et al.* Novel chlorine resistant low-fouling ultrafiltration membrane based on a hydrophilic polyaniline derivative. *Journal of Materials Chemistry A* **3**, 8725-8733 (2015).

144 Liao, Y. *et al.* Bulk synthesis, optimization, and characterization of highly dispersible polypyrrole nanoparticles toward protein separation using nanocomposite membranes. *Journal of Colloid and Interface Science* **386**, 148-157 (2012).

145 Liu, J., Tian, C., Xiong, J. & Wang, L. Polypyrrole blending modification for pvdf conductive membrane preparing and fouling mitigation. *Journal of Colloid and Interface Science* **494**, 124-129 (2017).

146 Formoso, P., Pantuso, E., De Filpo, G. & Nicoletta, F. P. Electro-conductive membranes for permeation enhancement and fouling mitigation: A short review. *Membranes* **7**, 39 (2017).

147 Liu, L. *et al.* Conductive and hydrophilic polypyrrole modified membrane cathodes and fouling reduction in mbr. *Journal of Membrane Science* **429**, 252-258 (2013).

148 Liao, Y. *et al.* Highly dispersible polypyrrole nanospheres for advanced nanocomposite ultrafiltration membranes. *Materials Horizons* **1**, 58-64 (2014).

149 Saf, A. O., Akin, I., Zor, E. & Bingol, H. Preparation of a novel psf membrane containing rgo/pth and its physical properties and membrane performance. *RSC Advances* **5**, 42422-42429 (2015).

150 Cao, B. *et al.* Electroactive poly(sulfobetaine-3,4-ethylenedioxythiophene) (psbedot) with controllable antifouling and antimicrobial properties. *Chemical Science* **7**, 1976-1981 (2016).

151 Zhao, R., Porada, S., Biesheuvel, P. M. & van der Wal, A. Energy consumption in membrane capacitive deionization for different water recoveries and flow rates, and comparison with reverse osmosis. *Desalination* **330**, 35-41 (2013).

152 Brogioli, D. Extracting renewable energy from a salinity difference using a capacitor. *Physical Review Letters* **103**, 058501 (2009).

153 Jia, B. & Zhang, W. Preparation and application of electrodes in capacitive deionization (cdi): A state-of-art review. *Nanoscale research letters* **11**, 64 (2016).

154 Oren, Y. Capacitive deionization (cdi) for desalination and water treatment—past, present and future (a review). *Desalination* **228**, 10-29 (2008).

155 Gryglewicz, G., Machnikowski, J., Lorenc-Grabowska, E., Lota, G. & Frackowiak, E. Effect of pore size distribution of coal-based activated carbons on double layer capacitance. *Electrochimica Acta* **50**, 1197-1206 (2005).

156 Porada, S. *et al.* Direct prediction of the desalination performance of porous carbon electrodes for capacitive deionization. *Energy & Environmental Science* **6**, 3700-3712 (2013).

157 Zou, L., Morris, G. & Qi, D. Using activated carbon electrode in electrosorptive deionisation of brackish water. *Desalination* **225**, 329-340 (2008).

158 Wang, G. *et al.* Activated carbon nanofiber webs made by electrospinning for capacitive deionization. *Electrochimica Acta* **69**, 65-70 (2012).

159 Farmer, J. C., Fix, D. V., Mack, G. V., Pekala, R. W. & Poco, J. F. Capacitive deionization of nacl and nano3 solutions with carbon aerogel electrodes. *Journal of the Electrochemical Society* **143**, 159-169 (1996).

160 Gabelich, C. J., Tran, T. D. & Suffet, I. H. M. Electrosorption of inorganic salts from aqueous solution using carbon aerogels. *Environmental Science & Technology* **36**, 3010-3019 (2002).

161 Porada, S. *et al.* Water desalination using capacitive deionization with microporous carbon electrodes. *ACS Applied Materials & Interfaces* **4**, 1194-1199 (2012).

162 Li, H., Zou, L., Pan, L. & Sun, Z. Novel graphene-like electrodes for capacitive deionization. *Environmental Science & Technology* **44**, 8692-8697 (2010).

163 Liu, Y. *et al.* Review on carbon-based composite materials for capacitive deionization. *RSC Advances* **5**, 15205-15225 (2015).

164 Sheng, L. *et al.* Ultra-high toughness all graphene fibers derived from synergetic effect of interconnected graphene ribbons and graphene sheets. *Carbon* **120**, 17-22 (2017).

165 Peng, C., Zhang, S., Jewell, D. & Chen, G. Z. Carbon nanotube and conducting polymer composites for supercapacitors. *Progress in Natural Science* **18**, 777-788 (2008).

166 Murphy, G. W. & Caudle, D. D. Mathematical theory of electrochemical demineralization in flowing systems. *Electrochimica Acta* **12**, 1655-1664 (1967).

167 Johnson, A. & Newman, J. Desalting by means of porous carbon electrodes. *Journal of the Electrochemical Society* **118**, 510-517 (1971).

168 Dai, K., Shi, L., Fang, J., Zhang, D. & Yu, B. Nacl adsorption in multi-walled carbon nanotubes. *Materials Letters* **59**, 1989-1992 (2005).

169 Li, L., Zou, L., Song, H. & Morris, G. Ordered mesoporous carbons synthesized by a modified sol–gel process for electrosorptive removal of sodium chloride. *Carbon* **47**, 775-781 (2009).

170 Li, H., Lu, T., Pan, L., Zhang, Y. & Sun, Z. Electrosorption behavior of graphene in nacl solutions. *Journal of Materials Chemistry* **19**, 6773-6779 (2009).

171 Lee, J.-B., Park, K.-K., Eum, H.-M. & Lee, C.-W. Desalination of a thermal power plant wastewater by membrane capacitive deionization. *Desalination* **196**, 125-134 (2006).

172 Porada, S., Zhao, R., van der Wal, A., Presser, V. & Biesheuvel, P. M. Review on the science and technology of water desalination by capacitive deionization. *Progress in Materials Science* **58**, 1388-1442 (2013).

173 Delahay. *Double layer and electrode kinetics*. (John Wiley & Sons, 1965).

174 Yates, D. E., Levine, S. & Healy, T. W. Site-binding model of the electrical double layer at the oxide/water interface. *Journal of the Chemical Society, Faraday Transactions 1: Physical Chemistry in Condensed Phases* **70**, 1807-1818 (1974).

175 Helmholtz, H. Ueber einige gesetze der vertheilung elektrischer ströme in körperlichen leitern mit anwendung auf die thierisch-elektrischen versuche. *Annalen der Physik* **165**, 211-233 (1853).

176 Wang, H. & Pilon, L. Accurate simulations of electric double layer capacitance of ultramicroelectrodes. *The Journal of Physical Chemistry C* **115**, 16711-16719 (2011).

177 Pandolfo, T., Ruiz, V., Sivakkumar, S. & Nerkar, J. in *Supercapacitors: Materials, systems, and applications* 69-109 (Wiley-VCH Verlag GmbH & Co. KGaA, 2013).

178 Simon, P., Taberna, P.-L. & Béguin, F. in *Supercapacitors* 131-165 (Wiley-VCH Verlag GmbH & Co. KGaA, 2013).

179 Rouquerol, J. *et al.* Recommendations for the characterization of porous solids (technical report). *Pure and Applied Chemistry* **66**, 1739-1758 (1994).

180 Fan, J. *et al.* Synthesis and properties of carbon nanotube-polypyrrole composites. *Synthetic Metals* **102**, 1266-1267 (1999).

181 Zengin, H. *et al.* Carbon nanotube doped polyaniline. *Advanced Materials* **14**, 1480-1483 (2002).

182 Chen, G. Z. *et al.* Carbon nanotube and polypyrrole composites: Coating and doping. *Advanced Materials* **12**, 522-526 (2000).

183 He, B. *et al.* Rapid charge-transfer in polypyrrole–single wall carbon nanotube complex counter electrodes: Improved photovoltaic performances of dye-sensitized solar cells. *Journal of Power Sources* **256**, 170-177 (2014).

184 Benson, J. *et al.* Multifunctional cnt-polymer composites for ultra-tough structural supercapacitors and desalination devices. *Advanced Materials* **25**, 6625-6632 (2013).

185 Yan, C., Zou, L. & Short, R. Single-walled carbon nanotubes and polyaniline composites for capacitive deionization. *Desalination* **290**, 125-129 (2012).

186 Wang, Y., Zhang, L., Wu, Y., Xu, S. & Wang, J. Polypyrrole/carbon nanotube composites as cathode material for performance enhancing of capacitive deionization technology. *Desalination* **354**, 62-67 (2014).

187 Wang, Z., Wang, Y., Ma, D., Xu, S. & Wang, J. Investigations on the fouling characteristics of ion-doped polypyrrole/carbon nanotube composite electrodes in capacitive deionization by using half cycle running mode. *Separation and Purification Technology* **192**, 15-20 (2018).

188 Cai, Y. *et al.* Optimization on electrode assemblies based on ion-doped polypyrrole/carbon nanotube composite in capacitive deionization process. *Journal of Electroanalytical Chemistry* **768**, 72-80 (2016).

189 Geim, A. K. Random walk to graphene (nobel lecture). *Angewandte Chemie International Edition* **50**, 6966-6985 (2011).

190 Zhang, Y. *et al.* Polypyrrole nanowire modified graphite (ppy/g) electrode used in capacitive deionization. *Synthetic Metals* **160**, 1392-1396 (2010).

191 Stoller, M. D., Park, S., Zhu, Y., An, J. & Ruoff, R. S. Graphene-based ultracapacitors. *Nano Letters* **8**, 3498-3502 (2008).

192 El-Kady, M. F., Strong, V., Dubin, S. & Kaner, R. B. Laser scribing of high-performance and flexible graphene-based electrochemical capacitors. *Science* **335**, 1326-1330 (2012).

193 Yan, C., Kanaththage, Y. W., Short, R., Gibson, C. T. & Zou, L. Graphene/polyaniline nanocomposite as electrode material for membrane capacitive deionization. *Desalination* **344**, 274-279 (2014).

194 Jianhua, L. *et al.* Preparation of an amide group-connected graphene–polyaniline nanofiber hybrid and its application in supercapacitors. *ACS Applied Materials & Interfaces* **4**, 2870-2876 (2012).

195 Qin, T. *et al.* Freestanding flexible graphene foams@ polypyrrole@ mno 2 electrodes for high-performance supercapacitors. *Journal of Materials Chemistry A* **4**, 9196-9203 (2016).

196 Gu, X. *et al.* Facile fabrication of graphene-polypyrrole-mn composites as high-performance electrodes for capacitive deionization. *Journal of Materials Chemistry A* **3**, 5866-5874 (2015).

197 Wang, Y., Wang, R., Xu, S., Liu, Q. & Wang, J. Polypyrrole/polyaniline composites with enhanced performance for capacitive deionization. *Desalination and Water Treatment* **54**, 3248-3256 (2015).

198 Aldalbahi, A. *et al.* Construction of a novel three-dimensional pedot/rvc electrode structure for capacitive deionization: Testing and performance. *Materials* **10**, 847 (2017).

199 Rebattet, L., Escoubes, M., Pinéri, M. & Geniès, E. M. Gas sorption in polyaniline powders and gas permeation in polyaniline films. *Synthetic Metals* **71**, 2133-2137 (1995).

200 Chang, M.-J., Myerson, A. S. & Kwei, T. K. Gas transport in ring substituted polyanilines. *Polymer Engineering & Science* **37**, 868-875 (1997).

201 Lee, Y. M., Ha, S. Y., Lee, Y. K., Suh, D. H. & Hong, S. Y. Gas separation through conductive polymer membranes. 2. Polyaniline membranes with high oxygen selectivity. *Industrial & Engineering Chemistry Research* **38**, 1917-1924 (1999).

202 Stolarczyk, A., Łapkowski, M. & Nowicka, M. Gas separation investigations on polyaniline composite membranes. *Polimery* **45** (2000).

203 Chatzidaki, E. K., Favvas, E. P., Papageorgiou, S. K., Kanellopoulos, N. K. & Theophilou, N. V. New polyimide–polyaniline hollow fibers: Synthesis, characterization and behavior in gas separation. *European Polymer Journal* **43**, 5010-5016 (2007).

204 Stolarczyk, A., Turczyn, R., Januszkiewicz-Kaleniak, A., Domagała, W. & Imach, S. Determination and comparison of ideal and practical selectivity coefficients of membranes containing different conductive polymers. *Acta Phys. Pol. A* **124**, 563-566 (2013).

205 Chang, K. *et al.* Preparation and comparative properties of membranes based on pani and three inorganic fillers. *Express Polymer Letters* **8** (2014).

206 Andreeva, D. V. *et al.* Effect of polymerization conditions of pyrrole on formation, structure and properties of high gas separation thin polypyrrole films. *Thin Solid Films* **406**, 54-63 (2002).

207 Chen, X., Hong, L., Chen, X., Yeong, W. H. A. & Chan, W. K. I. Aliphatic chain grafted polypyrrole as a precursor of carbon membrane. *Journal of Membrane Science* **379**, 353-360 (2011).

208 Reid, B. D., Ebron, V. H. M., Musselman, I. H., Ferraris, J. P. & Balkus, K. J. Enhanced gas selectivity in thin film composite membranes of poly(3-(2-acetoxyethyl)thiophene). *Journal of Membrane Science* **195**, 181-192 (2002).

209 Fan, Z., Wang, Z., Duan, M., Wang, J. & Wang, S. Preparation and characterization of polyaniline/polysulfone nanocomposite ultrafiltration membrane. *Journal of Membrane Science* **310**, 402-408 (2008).

210 Zhao, S. *et al.* Performance improvement of polysulfone ultrafiltration membrane using panieb as both pore forming agent and hydrophilic modifier. *Journal of Membrane Science* **385-386**, 251-262 (2011).

211 Zhao, S. *et al.* Performance improvement of polysulfone ultrafiltration membrane using well-dispersed polyaniline–poly(vinylpyrrolidone) nanocomposite as the additive. *Industrial & Engineering Chemistry Research* **51**, 4661-4672 (2012).

212 Teli, S. B., Molina, S., Calvo, E. G., Lozano, A. E. & de Abajo, J. Preparation, characterization and antifouling property of polyethersulfone–pani/pma ultrafiltration membranes. *Desalination* **299**, 113-122 (2012).

213 Zhao, S., Wang, Z., Wang, J. & Wang, S. Poly(ether sulfone)/polyaniline nanocomposite membranes: Effect of nanofiber size on membrane morphology and properties. *Industrial & Engineering Chemistry Research* **53**, 11468-11477 (2014).

214 Zhu, S. *et al.* Improved performance of polyamide thin-film composite nanofiltration membrane by using polyetersulfone/polyaniline membrane as the substrate. *Journal of Membrane Science* **493**, 263-274 (2015).

215 Jiang, B. *et al.* Improvement of antifouling performance of poly(l-lactic acid) membranes through incorporating polyaniline nanoparticles. *Journal of Applied Polymer Science* **134**, n/a-n/a (2017).

216 Hudaib, B., Gomes, V., Shi, J., Zhou, C. & Liu, Z. Poly (vinylidene fluoride)/polyaniline/mwcnt nanocomposite ultrafiltration membrane for natural organic matter removal. *Separation and Purification Technology* **190**, 143-155 (2018).

217 Yan, C., Zou, L. & Short, R. Polyaniline-modified activated carbon electrodes for capacitive deionisation. *Desalination* **333**, 101-106 (2014).

218 Zornitta, R. L. *et al.* High-performance activated carbon from polyaniline for capacitive deionization. *Carbon* **123**, 318-333 (2017).

219 Liu, Q., Wang, Y., Zhang, Y., Xu, S. & Wang, J. Effect of dopants on the adsorbing performance of polypyrrole/graphite electrodes for capacitive deionization process. *Synthetic Metals* **162**, 655-661 (2012).

## CHAPTER 3. GREEN $CO_2$NCRETE™ FOR SUSTAINABLE CONSTRUCTION

"Reprinted from Lin, C.-W.; Wang, B.; Kaner, R.B.; Sant G.N. "Green $CO_2$ncrete™ for Sustainable Construction" *Green Chemistry: The Nexus Blog*, 2017."

Scientists and engineers at the University of California, Los Angeles (UCLA) are developing an innovative way of embedding carbon dioxide ($CO_2$) into concrete. Specifically, the process secures $CO_2$ produced by power plants, cement plants, and other point-source emitters, and embeds it into 3D-printed building materials and components. The work seeks to mitigate the $CO_2$ impact of cement production [N.B.: upon mixing with sand, stone and water, cement forms a "composite" referred to as 'concrete'], which currently accounts for nearly 9 percent of anthropogenic $CO_2$ emissions. In light of the ever-increasing demand for concrete worldwide (e.g., in China and India), it is crucial, now more than ever, to address the environmental impact of this ubiquitous building material.

To alleviate the $CO_2$ emissions associated with cement production – the most $CO_2$-intensive component in concrete – we designed a closed-loop process for manufacturing building materials as shown in **Figure34-1** [1]. First, quarried limestone ($CaCO_3$) is calcined to produce lime (CaO) – a process that releases (mineralized) $CO_2$ embedded within it. Second, lime is reacted with water to form portlandite ($Ca(OH)_2$), which is mixed into slurry with sand, mineral aggregates, water and performance modifying agents. The slurry can be formed into modular structural elements such as beams and columns, using advanced shape stabilization method like 3D printing. Finally, the shaped-stabilized structural elements are reacted with $CO_2$ released during calcination, or from other point-source emitters (e.g., coal and natural gas power plants) to produce the building components from $CO_2$NCRETE™. This process of re-embedding mineralized $CO_2$ within building materials not only reduces the effective $CO_2$ emissions creating

a cementing agent with greatly reduced $CO_2$ impact, but also acts to reduce the impacts of electricity generation using fossil-fuels.

Though a related year-long approach has been attempted recently in Iceland, our team at UCLA was able to accelerate the carbonation process at near-ambient conditions in terms of temperature and pressure, thereby offering new, beneficial routes for the practical and economical use of $CO_2$. In addition, by sourcing lime from industrial alkaline waste streams, a negative life-cycle carbon footprint can be achieved. This technology seeks to re-imagine how we perceive and address the emissions of greenhouse gases (GHGs) associated with process intensive industries today.

Beyond the realization of a new building material, the broader "Carbon Upcycling" effort emphasizes a vital need for technology integration and value creation. While membrane technologies are used for the capture and enrichment of $CO_2$, 3D printing has proven an efficient method to fabricate building components like beams, columns and slabs. But 3D printing has not yet impacted the construction industry despite its aggressive adoption by various industries and even for personal use. Therefore, as a lab scale proof-of-concept, our team at UCLA has 3D-printed a beam several centimeters in length, composed of our new construction material. The Lego-like 3D-printed building blocks offer greater design flexibility and ease in on-site assembly, offering newfound efficiency for construction operations. The present challenge lies in scaling 3D printing building blocks up from centimeters to meters in size, and then to tens of meters as required for practical buildings, roads and bridges.

Our "Carbon Upcycling" team – comprised of an interdisciplinary group of UCLA researchers led by Gaurav Sant, Associate Professor; Henry Samueli, Fellow in Civil and Environmental Engineering; Richard Kaner, Distinguished Professor in Chemistry &

Biochemistry and Materials Science & Engineering; Laurent Pilon, Professor in Mechanical & Aerospace Engineering and Bioengineering; J. R. DeShazo, Professor of Public Policy at the Luskin School of Public Affairs; and Mathieu Bauchy, Assistant Professor of Civil & Environmental Engineering – has recently advanced to the semi-finals of the NRG COSIA Carbon XPRIZE competition. This competition challenges and stimulates people to respond to the global issue of $CO_2$ emission. As such, our team is in the midst of transitioning its technology from the laboratory-scale to the pilot-scale by demonstrating the ability to scale up: (1) $CO_2$ separation and enrichment, (2) the carbonation of large volumes of portlandite, and (3) the size of the 3D printed $CO_2$NCRETE$^{TM}$ building blocks – all while minimizing the overall consumption of water and electricity.

Our team has made substantial progress so far, and seeks to make transformative contributions to how *$CO_2$ management* is approached by the construction sector. Indeed, this style of breakthrough advancement can only be realized when a highly motivated team from different disciplines comes together to solve important problems of global and societal relevance. We look forward to bringing sustainable building materials like $CO_2$NCRETE$^{TM}$ to fruition, an outcome enabled and promoted by green chemistry at large.

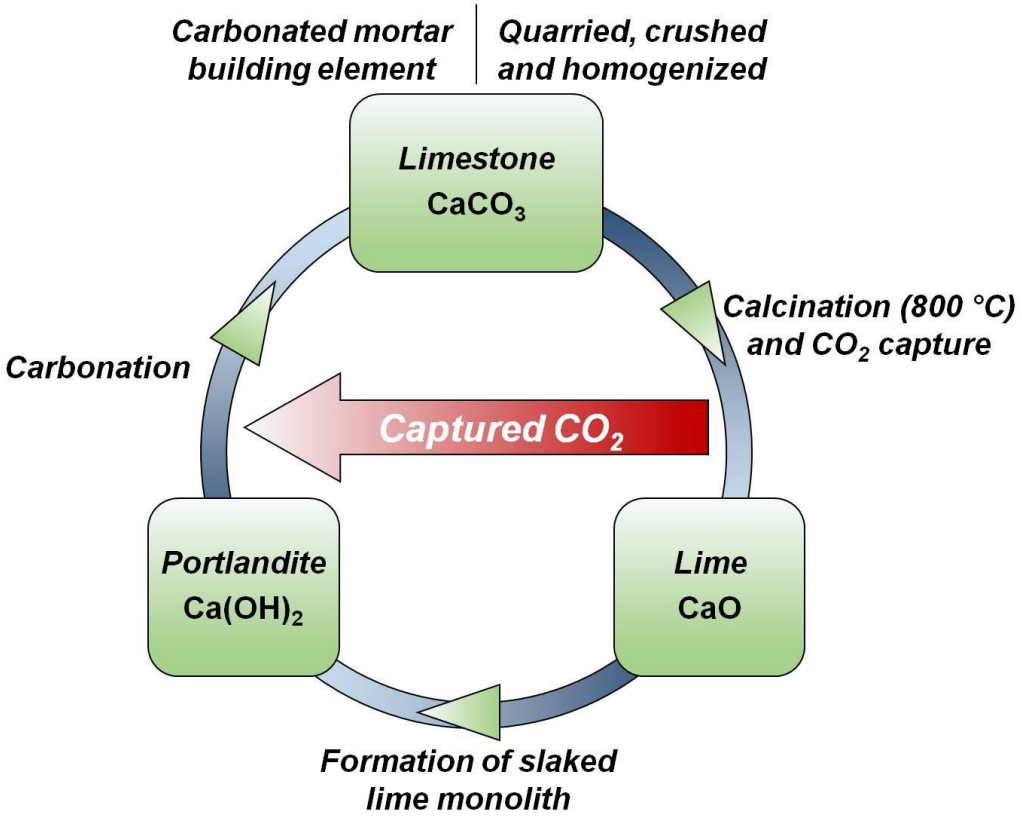


**Figure 3-1.** An illustration of the cementation process that ensures "closed-loop" reuse of mineralized $CO_2$ within the process cycle. [1]

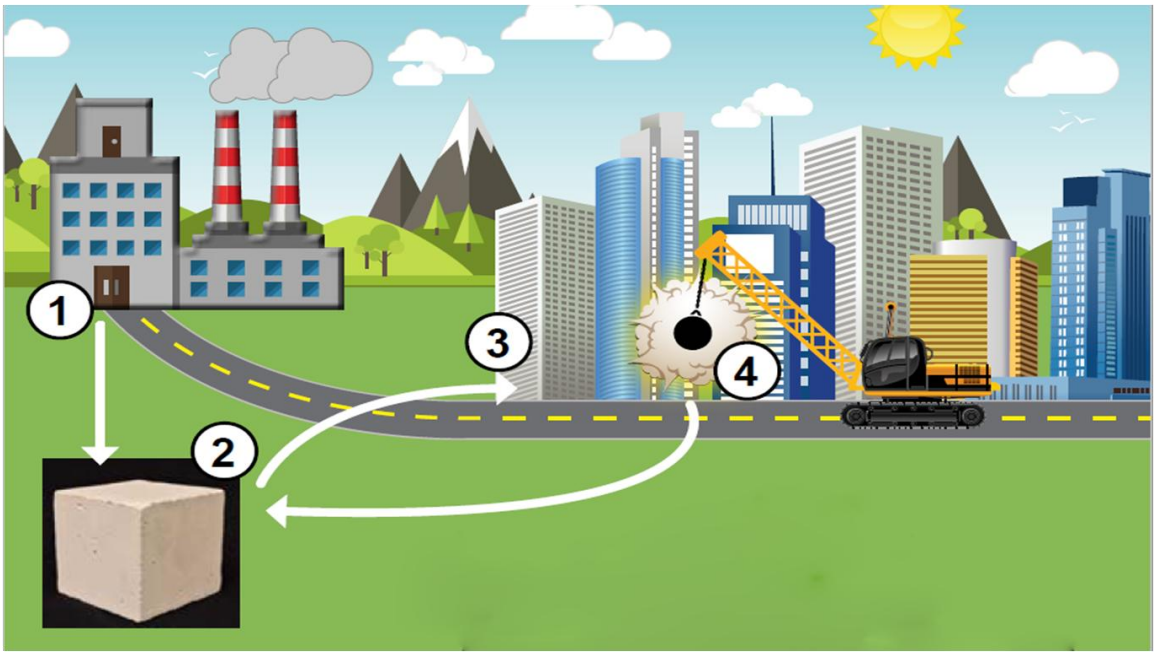


**Figure 3-2.** The cycle of $CO_2$ uptake: 1. $CO_2$ is separated and captured from power plants. 2. $CO_2$ is embedded in $CO_2$NCRETE™ building blocks. 3. $CO_2$NCRETE™ building blocks are assembled in to building structures. 4. $CO_2$NCRETE™ building blocks are recycled into new structures.

## References

[1] K. Vance, G. Falzone, I. Pignatelli, M. Bauchy, M. Balonis, G.Sant, “Direct Carbonation of Ca(OH)2 Using Liquid and Supercritical CO2: Implications for Carbon-Neutral Cementation”, *Industrial & Engineering Chemistry Research*, **2015**, 54(36), 8908-8918

# CHAPTER 4. 3D FREEZE-CASTING OF CELLULAR GRAPHENE FILMS FOR ULTRAHIGH-POWER-DENSITY SUPERCAPACITORS



Due to the large fluctuations in electricity generation from renewable sources, energy-storage devices with high power density are urgently needed for storing energy and supplying electricity on demand. Electrochemical capacitors, known as supercapacitors, have attracted a great deal of attention because of their high power densities, long life spans, and fast charging capabilities.[1–3] Supercapacitors can provide power density in excess of 10 kW $kg^{-1}$, which is 10 times larger than currently possible with lithium-ion batteries. They are ideal energy storage candidates in applications where high power densities are needed such as for energy recapture and delivery in hybrid vehicles, electric vehicles, smart grids, and backup power for electric utilities and factories.[4] Unlike batteries that are limited by slow chemical reactions, supercapacitors store charge through highly reversible ion adsorption or fast redox reactions, which enables fast energy capture and delivery.[5–7]

Recently, significant research efforts have focused on increasing energy densities of supercapacitors.[8–10] Unfortunately, these energy density enhancements usually come at the cost of losses in power or cycling capability, which are the most important characteristics of supercapacitors. Without high power density and long cycling capability, supercapacitors are reduced to mediocre battery-like energy-storage devices.[11] In practice, high-power supercapacitors are desirable for numerous applications, including heavy-duty loading applications, harvesting regenerative braking energy, and load leveling in a smart electric grid.[12]

In these situations, a large amount of energy needs to be either stored or delivered in high-power-density energy-storage devices. Therefore, high power density is still an essential property for the practical applications of supercapacitors.

The electrode material is the central component of supercapacitors and largely dictates their ultimate energy-storage performances. Owing to its extraordinary properties, such as high electrical conductivity as well as high specific surface area, and a wide stable potential window, graphene, a one atom-thin 2D flake of carbon, holds great promise as a high-performance electrode material for supercapacitors.[13–16] Graphene film, often called graphene paper, is an important macroscopic structure of graphene. A number of methods, such as blade-coating,[17] spray-coating,[18] layer-by-layer assembly,[19] interfacial self assembly,[20] and filtration assembly[21,22] have been developed to fabricate graphene films. However, due to the shear stress, interfacial tension or vacuum compression during the fabrication process, the 2D layered graphene sheets can easily restack to form dense lamellar microstructures, which lose most of the surface area of the original graphene sheets. Recently, Li and coworkers demonstrated that the presence of a nonvolatile liquid electrolyte that can serve as an effective "spacer" to prevent the irreversible π–π stacking between graphene sheets.[23] However, these fabricated dense layered graphene films lack sufficient open hierarchical pores, which serve as ion-buffering reservoirs and high-speed ion transport channels for effective electrochemical kinetic processes. The presence of these hierarchical pores is a critical factor for obtaining high power densities and short charging times.[24] Therefore, it is important to fabricate graphene film electrodes with continuous hierarchical pores, especially to achieve high-power-density supercapacitors.

Here we demonstrate that 3D hierarchical porous graphene films can be readily fabricated by filtration assembly of partially reduced graphene oxide (GO) and a subsequent freeze-casting

process. The resulting porous graphene films exhibit a combination of useful properties including: good electrical conductivity, high mechanical strength, and extreme high performance in supercapacitors. Furthermore, this new 3D porous graphene film is not only useful in supercapacitors, but also has promising potential in broad applications, such as sensors, catalysis, batteries, gas absorption, hydrogen storage, and scaffolds for electronic and medical applications.

Among various methods developed for the fabrication of porous materials, freeze-casting has attracted considerable attention recently, as it is a versatile, readily accessible and inexpensive solution-phase technique that can employ the controlled crystallization of a suspension to induce ordered hierarchical porous architectures.[25] Generally, the freeze-casting technique is a phase segregation process. As a liquid suspension freezes, spontaneous phase segregation gathers the dispersed particles to the space between the solvent crystals, followed by sublimation of the solidified frozen solvent template from the solid to the gas phase under reduced pressure. This creates a 3D network, where the pores become a replica of the solvent crystals.

To date, freeze-casting has been adopted to introduce high porosity into a variety of compact materials, endowing them with several novel properties and opening up the possibility for new applications. For example, cellular ceramics have been formed that are useful as light-weight insulators or filters,[26–28] which can withstand high temperatures and exhibit high compressive strength. Additionally, polymers with or without inorganic nanofillers (e.g., carbon nanotubes or clay) have been created as tissue engineering substrates or scaffolds for energy storage electrodes. Due to these previous results, the variety of materials successfully processed by this technique suggests that the underlying principles dictating the porous structure formation

mechanisms rely on physical parameters, morphology of the "particles" and the interactions with solutions rather than the chemical properties.

**Figure 4-1** a–e schematically illustrates the fabrication procedures for the porous graphene film. In this work, we chose GO, which can be produced in bulk from graphite at low cost, as a precursor to fabricate porous graphene films. The diameters of the GO sheets are in the range of several micrometers, with a typical thickness of approximately 1.2 nm (Figure S4-1, Supporting Information). According to a literature report,[29] the thickness of a GO monolayer is approximately 1–1.4 nm, which is thicker than an ideal monolayer of graphene (thickness ≈0.34 nm), due to the presence of functional groups and adsorbed molecules. Since the functional groups make GO strongly hydrophilic and negatively charged, the single layer GO sheet can be homogeneously dispersed in an aqueous solution. However, if one directly freeze-casts a GO dispersion, it will only result in a randomly oriented porous brittle monolith. A number of parameters, including the size and density of the "particles", their size distribution, and their shape, will affect the interactions between the "particles" and solution, which results in modifying the solidification kinetics of the freezing procedure and the resulting pore structure. Only the fraction of "particles" in suspension achieved up to a specific percolation threshold, known as the entrapped "particles" during the freezing process, can form a continuous 3D porous network. Therefore, we introduce pre-reduction and control the reduction time to adjust the size, shape, and size distribution and carry out filtration assembly to increase the density of the dispersion to achieve the percolation threshold.

As shown in a photo (Figure S4-2, Supporting Information) and scanning electron microscopic (SEM) images (Figure S4-3, Supporting Information), the lamellar GO sheets gradually grow up to partially reduced GO micro-gels when pre-reduction time increases from 5

up to 30 min. Then we process all these pre-reduced GO samples with the same procedures shown in Figure 4-1 until we get graphene films. After filtering this pre-reduced GO dispersion, we drop the film into liquid nitrogen to solidify the water molecule inside and between the microgels. Under ideal conditions, continuous ice crystals are formed and grow into the pre-reduced GO networks. The pre-reduced GO sheets are rejected from the advancing solidification front and are collected between the gaps of growing ice crystals. The framework should also accommodate the 9% positive solidification volume expansion for liquid water changed to solidified ice crystals. The morphology of the solidified ice crystals will largely dictate the porous characteristics of the final graphene films. Once complete solidification of hydro-film is achieved, the porosity is created where the ice crystals were. Then, the subsequent higher temperature long-term reduction strengthens the connection between pre-reduced GO gels and further increase the degree of reduction.

After a series of comparable experiments, we found that only the 30 min pre-reduced sample can be assembled into the ideal 3D porous graphene film (Figure S4-4, Supporting Information). According to the mechanism of forming porosity by freeze-casting, we conclude two main reasons for the necessity of the pre-reduction to form the porosity of the graphene films. First, the 3D micro-gel structures effectively resist the aggregation of the GO sheets during the filtration assembly and leave sufficient space for the solidification of water. In contrast, the compact configuration of filtered 2D GO sheets jams the redistribution during freezing procedure. Second, during the growth of GO sheets to micro-gels, the particle size was increasing and the 2D lamellar sheets were changing to 3D micro networks. In order to assemble the integral porous graphene film, the “particles” in suspension must be rejected from the advancing solidification front in freezing procedure. The thermodynamic condition for

a “particle” to be rejected by the solidification front is that the interfacial free energies satisfy this following criterion:

$$\Delta\sigma = \sigma_{sp} - (\sigma_{lp} + \sigma_{sl}) > 0 \qquad (4\text{-}1)$$

where $\sigma_{sp}$, $\sigma_{lp}$, and $\sigma_{sl}$ are the interfacial free energies associated with the solid (ice)-particle (pre-reduced GO micro-gel or GO sheets), liquid (water)-particle and solid–liquid interface, respectively. As illustrated in **Figure 4-2**, the size increase and morphology change decrease the contact interface area between the “particles” and solid phase and provide more contact interface area between liquid and solid phases, which results in the augmentation of $\sigma_{sp}$ and drop in $\sigma_{sl}$. This makes the pre-reduced GO micro-gel system more likely to satisfy the pre-mentioned criterion (Equation (4-1)). In addition, the filtration assembly process is a useful way to increase the density of the particles in the suspension to approach the percolation threshold, which is another critical condition for forming a continuous 3D porous network during the freeze-casting process.

The X-ray diffraction (XRD) pattern (Figure S4-6, Supporting Information) of GO is characterized by a strong peak at $2\theta = 11.7°$. Pre-reduced GO exhibits a significant decline in the intensity of the “GO” peak at 10.8° while a broad peak develops at 24°, which indicates the partial reduction of GO, and the creation of extended graphene sheets. After completion of the process, the XRD pattern only shows a broad “graphene” peak, which suggests that reduction of the 3D porous reduced graphene oxide (RGO) films has occurred. These results are also supported by 1. The X-ray photoelectron spectra (XPS) C1s spectrum where changes are observed in the peaks corresponding to oxygen containing groups (Figure S4-7, Supporting Information) and 4-2. The intensity ratio of the D and G peaks in Raman spectroscopy (Figure S4-8, Supporting Information).

**Figure 4-3** a presents a typical cross-section SEM image of a 3D porous RGO fi lm under low magnifi cation, which exhibits a continuous open network with a uniform thickness of 12.6 μm. The honeycomb-like structures indicate that the pores are a replica of the ice crystals. As shown in the high-magnification SEM images, Figure 4-3c,d, the pore sizes are in the range of hundreds of nanometers to several micrometers and the pore walls consist

of thin layers of graphene sheets, which is consistent with transmission electron microscopy (TEM) results (Figure 4-3e). The TEM (Figure 4-3e,f) and high-resolution TEM images also reveal that there are many crumpled 5–10 nm graphene sheets stacked on the surface of the graphene walls that are several tens of nanometers thick. This is likely due to rejection from the solidification front that pushes the dispersed pre-reduced GO sheets into the gaps between the ice crystals formed during the freezing process. The clear lattice fringes (Figure 4-3g,h) and typical sixfold symmetry diffraction pattern provide further evidence for the nearly complete reduction of the 3D porous RGO films. The reduction process is associated with significant changes in the electrical properties of the film. For comparison, two electrode $I - V$ conductivity tests were carried out for GO, pre-reduced GO and 3D porous RGO films, as presented in Figure S4-9 in the Supporting Information. The GO film exhibits nonlinear and asymmetric behavior, with a differential conductivity value ranging from $1.3 \times 10^{-3}$ S m$^{-1}$ to $4.5 \times 10^{-3}$ S m$^{-1}$ depending on the gate voltage. The pre-reduced GO films show a more linear and symmetric curve, with a stable conductivity of 10.3 S m$^{-1}$. The 3D porous RGO films give a completely linear $I - V$ curve associated with a high conductivity of 1905 S m$^{-1}$. Because of its high electrical conductivity and continuous open porous structure, the fabricated graphene films hold promise as high-performance supercapacitor electrodes. Furthermore, in spite of their highly porous microstructure, the as-prepared 3D porous RGO films exhibited good tensile strength of 18.7

MPa (Figure S4-10, Supporting Information), which is higher than previous reports for porous graphene films (0.92–3.2 MPa, Table S4-3, Supporting Information).[30–32]

The unique properties of 3D porous RGO films enable their excellent performance as supercapacitor electrodes. A symmetric two-electrode supercapacitor was fabricated by using 3D porous RGO films as the active materials and 1.0 M $H_2SO_4$ as the electrolyte as shown schematically in Figure S4-11 in the Supporting Information. Cyclic voltammetry (CV) curves taken at scan rates from 0.2 to 20 V $s^{-1}$ are shown in **Figure 4-4**a and Figure S4-12 in the Supporting Information. They demonstrate that the 3D porous RGO electrodes retain their rectangular shape and high current densities, even at an extremely high scan rate of 20 V $s^{-1}$. The rectangular nature of the CV curves indicates ideal electrical double-layer capacitor (EDLC) behavior for the 3D porous RGO films. In a control experiment, a stacked RGO film was fabricated via a previous reported method using vacuum filtering of chemically reduced GO sheets.[33] As shown in the cross-section SEM images (Figure S4-5, Supporting Information), the RGO consists of stacked lamellar graphene sheets, which is different from the 3D porous RGO films in this work. The schematic illustrations presented in Figure 4-4e,f show the easier ion diffusion and minimized electron transport resistance for a 3D porous RGO film compared with an RGO film. The CV (Figure 4-4b and Figure S4-12 and S4-13, Supporting Information) and galvanostatic charge/discharge (Figure S4-14, Supporting Information) curves show a significant electrochemical performance enhancement for the 3D porous RGO films when compared with the RGO film electrodes. The more rectangular shape of the CV curves at a high scan rate of 1000 mV $s^{-1}$ and more triangular shape of the galvanostatic charge/discharge curves at a high current density of 100 A $g^{-1}$ indicate a better capacitive performance and electrolyte ion transport of the 3D porous RGO electrode. The larger area of the CV curve and longer discharge time also

predict a higher capacitance. The high linear dependence ($R^2$ = 0.9986) of the discharge current on the scan rate up to high scan rates indicates an ultrahigh power capability for the 3D porous RGO electrode. The specific capacitance based on the active materials of these two supercapacitor electrodes was derived from the galvanostatic charge/discharge data and is summarized in Figure 4-4 c. The 3D porous RGO film exhibited an ultrahigh gravimetric capacitance of 284.2 F $g^{-1}$ at a current density of 1 A $g^{-1}$, and retained ~61.2% (173.8 F $g^{-1}$) of its initial capacitance when the current density was increased up to 500 A $g^{-1}$. In contrast, the RGO only had a gravimetric capacitance of 181.3 F $g^{-1}$ at 1 A $g^{-1}$ and a capacitance retention of only 27.8% (50.4 F $g^{-1}$) at 500 A $g^{-1}$. The cycling stability of the electrodes was examined by performing 10 000 charge/discharge cycles at a current of 25 A $g^{-1}$ (Figure 4-4d). The 3D porous RGO films exhibited a capacitive retention of 97.6%, which compares favorably to the 86.2% shown by the RGO films. There are two reasons for the higher improved cycling performance of the 3D porous RGO films compared with the RGO films. First, as shown in the XPS results (Figure S4-7, Supporting Information) the oxygen content of the 3D porous RGO films (15.6%) is lower than that of the RGO films (21.3%). These additional oxygen-containing functional groups, especially carboxyl, epoxy, and alkoxy, at the surface of the carbon likely introduce pseudo-capacitance, due to some Faradaic reactions. These functional groups and their related pseudo-capacitance are not as stable as pure carbon based double layer capacitance. Thus, during long-term cycling a decrease in capacitance will occur, just like that observed with other common pseudo-capacitive materials. Furthermore, the Faradaic reactions may also damage the stability of the aqueous electrolyte to a certain extent. Second, the 3D porous RGO films exhibit lower internal resistance and charge transport resistance, which will be discussed in detail in the following electrochemical impedance spectroscopy (EIS) discussion part. This means that the 3D

porous RGO films will suffer lower charge losses during long-term cycling, which further increases the cycling stability of the 3D porous RGO electrodes.

EIS is a very useful method to analyze electrolyte ion transport and other electrochemical behavior. Figure 4-4g shows the comparison of the Nyquist plots of the 3D porous RGO film and the RGO film electrodes. The Nyquist plot of the 3D porous RGO film features a nearly vertical curve, indicating an ideal capacitive performance. A close-up observation of the high frequency regime reveals a semicircle with a ~45° Warburg region. The Nyquist plot of the 3D porous RGO electrode shows a shorter Warburg region and a smaller semicircle, indicating a lower charge transfer resistance and more efficient electrolyte ion diffusion when compared to the RGO electrode. In order to better understand the interfacial electrochemical behavior of the supercapacitors, we fit the Nyquist plots to an equivalent circuit (Figure 4-4h) and summarize the specific values for the different circuit elements in Table S4-2 in the Supporting Information. The details of the relationship between the Nyquist plot and the equivalent circuit are illustrated in the EIS Analysis section in the Supporting Information. The internal resistances ($R_s$) are 0.202 and 0.244 Ω; with charge transport resistances ($R_{ct}$) of 0.181 and 1.04 Ω obtained by fitting the 3D porous RGO film and RGO film supercapacitors, respectively. These low resistance values indicate the high electron conductivity along the graphene walls and high-speed ion migration through the 3D open pores. The open surfaces of the 3D porous RGO films can be easily accessed by electrolyte ions without a diffusion limit, which guarantees a large capacitance at high current density/scan rate. In contrast, the condensed layer structure of RGO films only provides a narrow neck-like channel and confined pores for electrolyte ion transport, which results in increased resistance and suppressed capacitances. This was further confirmed by Bode plots (Figure 4-4i). The characteristic frequency $f_0$ at the phase angle of −45° marks the transition

point from resistive behavior to capacitive behavior. The 3D porous RGO supercapacitor exhibits an $f_0$ of 55.7 Hz, which corresponds to a time constant ($\tau_0 = 1/ f_0$) of 17.8 ms, which is significantly lower than 91.7 ms exhibited by the RGO supercapacitor. This time constant for the 3D porous RGO supercapacitor is even lower than some pure-carbon-based micro-supercapacitors, e.g., 26 ms for onion-like carbon,[34] and 700 ms for activated carbon.[34] This extremely low time constant provides further evidence for the high-speed ion diffusion and transport inside the 3D porous RGO electrodes.

The sum of $R_s$ and $R_{ct}$ are the chief contributors to the equivalent series resistance (ESR), which mainly limits the specific power density of a supercapacitor. Thus, the low ESR, high capacitance, and nearly ideal electrolyte ion transport of the 3D porous RGO electrodes provide the extremely high power density of 282 kW $kg^{-1}$ and high energy density of 9.9 W h $kg^{-1}$, even with only a 1.0 V potential window using an aqueous electrolyte. This high power density from the 3D porous RGO supercapacitor is close to that of an aluminum electrolytic capacitor and much higher than most previously reported EDLCs, pseudo-capacitors, and even asymmetric supercapacitors (Table S4-4, Supporting Information). It is worth noting that our calculations are based on the power density obtained by dividing the energy density by the discharging time (see Supporting Information, Calculations). This means the value of the power density of the device has actually been achieved. Some of the extremely high power densities reported previously are calculated from the square of the potential window divided by four times the ESR, which is the theoretical ideal maximum power density of a supercapacitor. The actual highest power density achieved by a supercapacitor is generally much lower than this ideal maximum value.[35]

In order to demonstrate the performance of the 3D porous RGO films for use in flexible energy-storage devices, we assembled all-solid-state flexible supercapacitors by using $H_3PO_4$

/poly(vinyl alcohol) (PVA) gel as the electrolyte (Figure S4-16a,b, Supporting Information). These flexible all-solid-state supercapacitors exhibited excellent electrochemical performance under the bending test conditions. The CV curves obtained at different bending angles (Figure S4-16c, Supporting Information) show nearly the same capacitive behavior and the overall capacitance decrease is less than 1%, demonstrating that the change of electrochemical properties under different bending angles is negligible. The 3D porous RGO-based all-solid-state supercapacitor exhibited an areal capacitance of 34 mF $cm^{-2}$ estimated from the CV curve at a scan rate of 50 mV $s^{-1}$. To further characterize the cycling stability, CV cycling tests were carried out for 500 bending cycles at a scan rate of 50 mV $s^{-1}$ by repeated bending from 0° to 135°. As shown in Figure S4-16d in the Supporting Information, a decay of only 9% of the discharge capacitance was observed, indicating very good mechanical stability of the all-solid-state capacitor based on 3D porous RGO. The great flexibility and capacitive performance of these all-solid state supercapacitors can be attributed to the previously mentioned high mechanical robustness and electrical conductivity of the 3D porous RGO films and the favorable accessibility of the gel electrolyte in the highly interconnected 3D porous network structure.

The high loading mass of active materials is a critical factor in the total performance of a supercapacitor, as discussed in an earlier paper.[11] Vacuum filtration, the method used in this research to fabricate electrodes, is a common method for preparing graphene or graphene-based films due to its easy manipulation. One of the advantages of the filtration method is the convenience in controlling the thickness and mass loading of an as-filtered film simply by adjusting the volume of the dispersion used. Thus, in order to increase the electrochemical performance of the total device, we increased the loading mass of the active electrode material by simply increasing the dispersion volume. As can be seen in cross-sectional SEM images

(**Figure 4-5a,b**) the as-prepared films maintain their highly porous microstructure when the thickness is increased to 20.4 μm, i.e., twice the loading (3D porous RGO-2), and to 44.7 μm, a fivefold increase in the loading (3D porous RGO-5). Because of the high electrical conductivity and excellent ion transport inside the porous electrodes, the CV curves (Figure 4-5c) maintain their rectangular shapes even when the scan rate is increased up to 1.0 V $s^{-1}$. The current density increases significantly as the loading mass of the 3D porous RGO film is increased. As a result, the gravimetric capacitance only decreased by 6.6% (to 265.5 F $g^{-1}$) and 15% (to 241.5 F $g^{-1}$) at the mass loadings of twice and fivefold, respectively (Figure 4-5d). Meanwhile, the areal capacitance increases from 56.8 to 109 and 246 mF $cm^{-2}$ (Figure 4-5e), respectively.

In order to further evaluate the practical potential of the 3D porous RGO supercapacitors, we calculated the energy density and power density based on the total device, which means the values were normalized by the total volume including the two electrodes, current collectors, electrolyte and separator. As summarized in a Ragone plot (Figure 4-5f) and in comparison with Table S4-4 in the Supporting Information, our devices exhibit high power densities (7.8–14.3 kW $kg^{-1}$). Furthermore, by increasing the mass loading of the active materials, the 3D porous RGO supercapacitor can store a high energy density up to 1.11 W h $L^{-1}$, which is even comparable to supercapacitors based on organic electrolytes or ionic liquids.[13]

The freeze-casting and filtration techniques used in producing 3D porous graphene films are mainly related to some basic parameters, such as the shape and size of the original materials, and their surface tension and dispersibility. Thus, this method could provide a universal pathway to assemble 2D materials into 3D porous macrostructures. The current method appears more adaptable than previous routes to fabricate 3D graphene films, such as a hydrothermal method,[36] CVD,[32] interfacial gelation,[30] and template-directed ordered assembly.[37] The

highly porous microstructure, high conductivity, and strong mechanical properties endow the 3D porous RGO film with a potential for many applications.

High-power-density supercapacitors are an ideal application that makes use of all of the above-mentioned advantages. High power density will continue to attract increasing attention, especially for conditions in which huge amounts of energy need to be input or output in a limited time, such as load-leveling the emerging smart electrical grid, flash charging electronics, and quick acceleration for electric vehicles. However, the power densities of most previously reported supercapacitors are generally limited by the narrow or confined electrolyte ion transport channels. Our 3D porous RGO films can satisfy the main requirements for high-power-density supercapacitor electrodes. The open and connected pores provide high-speed electrolyte ion transport and freely accessible graphene surfaces for forming electrical double layers. The high electrical conductivity and robust mechanical strength ensure high efficiency in exporting electrons to an outside load. Furthermore, these 3D porous RGO networks can be further scaled-up in their loading mass and/or thickness due to the controllable filtration process.

In summary, we have developed a method combining freezecasting and filtration to effectively synthesize 3D porous graphene films. This facile and scalable fabrication approach could become a general pathway for the synthesis of 3D porous films by assembling 2D materials. A high-performance supercapacitor has been fabricated by using these 3D porous graphene films as the active material. With their highly porous microstructure, superior electrical conductivity and exceptional mechanical strength, the supercapacitor exhibited both very high power densities and energy densities. This research could open up exciting opportunities for 3D porous film fabrication and a wide range of high-power-density applications.

**Acknowledgements**

This work was supported by Nanotech Energy, Inc (RBK). Y.S. would like to thank the China Scholarship Council for financial support for studying abroad at UCLA. H.W. would like to thank the Programs of Shanghai Academic Research Leader (16XD1400100) and Eastern Scholar.

**Supplementary Information**

**Materials and Methods**

**Preparation of 3D porous reduced graphene oxide (RGO) film.** GO was prepared from natural graphite flakes by a modified Hummers' method, as previously described.[38] In a typical procedure, as-synthesized GO was suspended in water to give a homogeneous aqueous dispersion with a concentration of 3 mg $ml^{-1}$. Then 1 ml of GO dispersion was mixed with 7 mg ascorbic acid in a 20 ml cylindrical glass vial. After being vigorously shaken for a few minutes, the mixture was then placed in a 50 ℃ oven for 5 to 50 minutes to obtain different degrees of reduction, i.e. partially reduced GO. The partially reduced GO dispersion was next vacuum filtrated through a cellulose membrane (0.22 μm pore size). The vacuum was disconnected immediately once no free dispersion was left on the filter paper. Both the filter membrane and partially reduced GO film were vertically immersed into a liquid nitrogen bath to freeze them for 30 minutes. After being thawed at room temperature, the film was transferred into a cylindrical glass vial and placed in a 100 ℃ oven overnight to obtain further reduction. The 3D porous RGO films were then transferred to a Petri dish and immersed in deionized water for one day to remove any remaining ascorbic acid. Thicker 3D porous RGO films were prepared by simply increasing the amount of GO to 2 or 5 ml and ascorbic acid to 14 or 35 mg. The thickness of the

3D porous RGO films, as measured from cross-sectional SEM images, were found to be ~12.6, 20.4 and 44.7 μm, respectively. The areal loading mass of the 3D porous RGO films are ~0.2, 0.41 and 1.02 mg $cm^{-2}$, respectively. As a control, chemically reduced graphene film was fabricated by vacuum filtering chemically reduced GO sheets, as previously reported.[39] The loading mass and the thickness of this RGO is ~0.2 mg cm-2 and ~2.1 μm, respectively.

**Fabrication of 3D porous RGO- and RGO- supercapacitors.** 3D porous RGO and RGO films were cut into 1 cm × 1 cm square pieces and then carefully peeled off from the filter membrane. Next, the freestanding electrode films were immersed into 1.0 M $H_2SO$= aqueous electrolyte overnight to exchange their interior water with electrolyte. Subsequently, the 3D porous RGO film slices were placed onto platinum foils. Two similar 3D porous RGO films on separate metal foils were directly used as electrodes without adding any other additives or further treatments. These two electrodes were separated by an ion-porous separator (polypropylene membrane, NKK MPF30AC100) and assembled into a sandwich architecture supercapacitor and tightly sealed with Kapton tape.

All-solid-state supercapacitors were fabricated by simply replacing the aqueous electrolyte and separator with a PVA/$H_3PO_4$ gel electrolyte. In a typical procedure, 1.0 g of polyvinyl alcohol (PVA, molecular weight 89,000-98,000, Sigma-Aldrich) powder was mixed with 10 ml of DI water. The mixture was heated to 90℃ under constant stirring until the solution turned clear. After cooling, 1.0 g of concentrated phosphoric acid was added and the viscous solution was stirred for 6 h. Finally, the clear solution was cast onto the surface of the electrode films and assembled into supercapacitors with the same procedure as used for the aqueous electrolyte supercapacitors.

**Physicochemical characterization** The morphology and microstructure of the prepared films were investigated by means of field emission scanning electron microscopy (FE-SEM, JEOL 6701F) and transmission electron microscopy (TEM, FEI TF20). X-ray diffraction patterns were collected on a Panalytical X'Pert Pro X-ray Powder Diffractometer with Cu-Kα radiation (λ = 1.54184 Å). Raman spectroscopy measurements were performed using a Renishaw Via laser micro-Raman system (Renishaw) at an excitation wavelength of 633 nm. Atomic force microscopy images were recorded using a Bruker Dimension 5000 Scanning Probe Microscope in tapping mode (Bruker Dimension 5000). Tensile strength of the each film was tested on a tensile testing machine (Q800 DMA (Dynamic Mechanical Analyzer)). X-ray photoelectron spectroscopy data were collected with a Kratos AXIS Ultra DLD spectrometer using a monochromatic AlKα X-ray source ($h\nu$ = 1486.6 eV).

**Electrochemical characterization** All the electrochemical experiments were carried out using a two-electrode system with a Bio-Logic VMP3 potentiostat. The EIS measurements were performed at open circuit potential with a sinusoidal signal over a frequency range from 1 MHz to 10 mHz at an amplitude of 10 mV. The cycle life tests were conducted by galvanostatic charge/discharge measurements. Calculations of the specific capacitance and the energy and power densities are discussed in detail in the following sections.

**Calculations** Despite the impressive developments achieved during the last decade in the field of supercapacitor research, inconsistent calculations have led to misunderstandings and make comparing results from different research groups difficult. Thus, here we carefully illustrate in detail our calculation methods for determining the different parameters needed for evaluating the performance of the supercapacitors. The capacitance of a supercapacitor (Ccell) in a two-

electrode system was calculated from its galvanostatic charge/discharge curves at different current densities using:

$$C_{cell} = i_{discharge}/(dV/dt) \quad \text{(S4-1)}$$

where $i_{discharge}$ is the discharge current, t is the discharge time, the potential range of $V$ is the voltage drop upon discharge excluding the *IR* drop, and dV/dt is the slope of the discharge curve (in volts per second, V/s). Alternatively, $C_{cell}$ can be calculated from CV curves by integrating the discharge current ($i$) vs. potential (V) plots using the following equation:

$$C_{cell} = \frac{\int_{V_{min}}^{V_{max}} i dV}{Vv} \quad \text{(S4-2)}$$

where $i$ is the current in the negative CV curve, $v$ is the scan rate, and $V$ ($V = V_{max} - V_{min}$) represents the potential window.

Specific capacitances of single electrode active material were calculated based on the mass and area or volume of the single electrode. Since a symmetric two-electrode supercapacitor actually consists of two equivalent single-electrode capacitors in series, the total capacitance of the two electrodes and the capacitances of the positive and negative electrodes follow Equation (S4-3):

$$C_{positive} = C_{negative} \quad \text{(S4-3)}$$

$$\frac{1}{C_{cell}} = \frac{1}{C_{positive}} + \frac{1}{C_{negative}} \quad \text{(S4-4)}$$

Thus $C_{positive} = C_{negative} = 2C_{cell}$.

In addition, the mass and volume of a single electrode accounts for half of the total mass and volume of the two-electrode system ($M_{single\text{-}electrode} = 1/2\ M_{two\text{-}electrode}$, $V_{single\text{-}electrode} = 1/2\ V_{two\text{-}electrode}$). The area of a single electrode is equivalent to the area of the two-electrode system ($S_{single\text{-}electrode} = S_{two\text{-}electrode}$) with Specific capacitances of the active material calculated according to the following equations:

$$C_{Specific\ capacitance,M} = \frac{C_{single-electrode}}{M_{single-electrode}} = 4\frac{C_{cell}}{M_{two-electrode}} \quad \text{(S4-5)}$$

$$C_{Specific\ capacitance,S} = \frac{C_{single-electrode}}{S_{single-electrode}} = 2\frac{C_{cell}}{S_{two-electrode}} \quad \text{(S4-6)}$$

$$C_{Specific\ capacitance,V} = \frac{C_{single-electrode}}{V_{single-electrode}} = 4\frac{C_{cell}}{V_{two-electrode}} \quad \text{(S4-7)}$$

Analogously, specific capacitances of the two-electrode system were calculated based on the mass and area or volume of the two electrodes according to the following formulae:

$$C_{two-electrode,M} = C_{cell}/M_{two-electrode} \quad \text{(S4-8)}$$

$$C_{two-electrode,S} = C_{cell}/S_{two-electrode} \quad \text{(S4-9)}$$

$$C_{two-electrode,V} = C_{cell}/V_{two-electrode} \quad \text{(S4-10)}$$

Thus, $C_{specific\ capacitance,\ M} = 4\ C_{two\text{-}electrode,\ M}$, $C_{specific\ capacitance,\ S} = 2\ C_{two\text{-}electrode,\ M}$, and $C_{specific\ capacitance,\ V} = 4\ C_{two\text{-}electrode,\ V}$. Then, the specific energy densities of the electrode materials based on the mass and area or volume of the active materials were obtained from the equations:

$$E_{electrode,x} = \frac{1}{2} C_{two-electrode,x} \times (V - V_{IRdrop})^2 \quad \text{(S4-11)}$$

where $E_{electrode,\ x}$ and $C_{two\text{-}electrode,\ x}$ represent the energy densities and specific capacitance of the two electrodes based on different evaluating units (mass, area or volume), the $V$ is the potential window in volts, and $V_{IRdrop}$ is the voltage IR drop at the beginning of the discharge part of the galvanostatic charge/discharge curves. The power densities of the electrode material based on different units were calculated using the following equations:

$$P_{electrode,x} = \frac{E_{electrode,x}}{t_{discharge}} \quad \text{(S4-12)}$$

where $t_{discharge}$ is the discharge time from the galvanostatic curves at different charge/discharge current densities.

It is worth highlighting that the specific capacitance of each device was calculated taking into account the entire (mass, area or volume) of the stacked device. This includes the active materials, current collector, separator, and electrolyte. Thus, the specific capacitances of the device were calculated from the equations:

$$C_{device,M} = C_{cell}/M_{device} \quad \text{(S4-13)}$$

$$C_{device,S} = C_{cell}/S_{device} \quad \text{(S4-14)}$$

$$C_{device,V} = C_{cell}/V_{device} \quad \text{(S4-15)}$$

Therefore, the energy densities and power densities of the total device were calculated by the following equations:

$$E_{device,x} = \frac{1}{2} C_{device,x} \times \left(V - V_{IRdrop}\right)^2 \quad \text{(S4-16)}$$

$$P_{device,x} = \frac{E_{device,x}}{t_{discharge}} \quad \text{(S4-17)}$$

**Electrochemical impedance spectroscopy (EIS) analysis** The measured Nyquist plots was well fitted on the basis of an equivalent Randles circuit in Figure 4h by using the following equation:

$$\mathrm{Z} = R_s + \frac{1}{j\omega C_{dl} + \frac{1}{R_{ct} + W_o}} + \frac{1}{j\omega C_l + \frac{1}{R_{leak}}} \quad \text{(S4-18)}$$

where $R_s$ is the cell internal resistance, $C_{dl}$ is the double layer capacitance, $R_{ct}$ is the charge transfer resistance, $W_o$ is the Warburg element, $C_l$ is the low frequency mass capacitance, and $R_{leak}$ is the low frequency leakage resistance. As illustrated in Supplementary Figure S4-15, these resistor and capacitor elements in the equivalent circuit are related to specific parts in the

Nyquist plot. At high frequency, the point of intersection on the real axis represents the internal resistance $R_s$, which includes the intrinsic electronic resistance of the electrode material, the ohmic resistance of the electrolyte, and the interfacial resistance between the electrode and the current collector. The semicircular in the high frequency region provides the behavior of the interfacial charge transfer resistance $R_{ct}$ and the double layer capacitance $C_{dl}$. After the semicircle, the Nyquist plot exhibits a straight long tail almost perpendicular to the x-axis and stretching to the low frequency region. This almost ideal vertical line represents the mass capacitance $C_l$, and the inclined angle suggests a resistive element, which is the leakage resistance $R_{leak}$. The transmission line with an angle of nearly 45 degrees to the x-axis from high frequency to the midfrequency represents the Warburg element $W_o$, which is expressed as:

$$W_o = \frac{A}{(j\omega)^n} \tag{S4-19}$$

Where A is the Warburg coefficient, ω is the angular frequency, and n is an exponent. All the values fit using these elements are summarized in Supplementary Table S4-3.

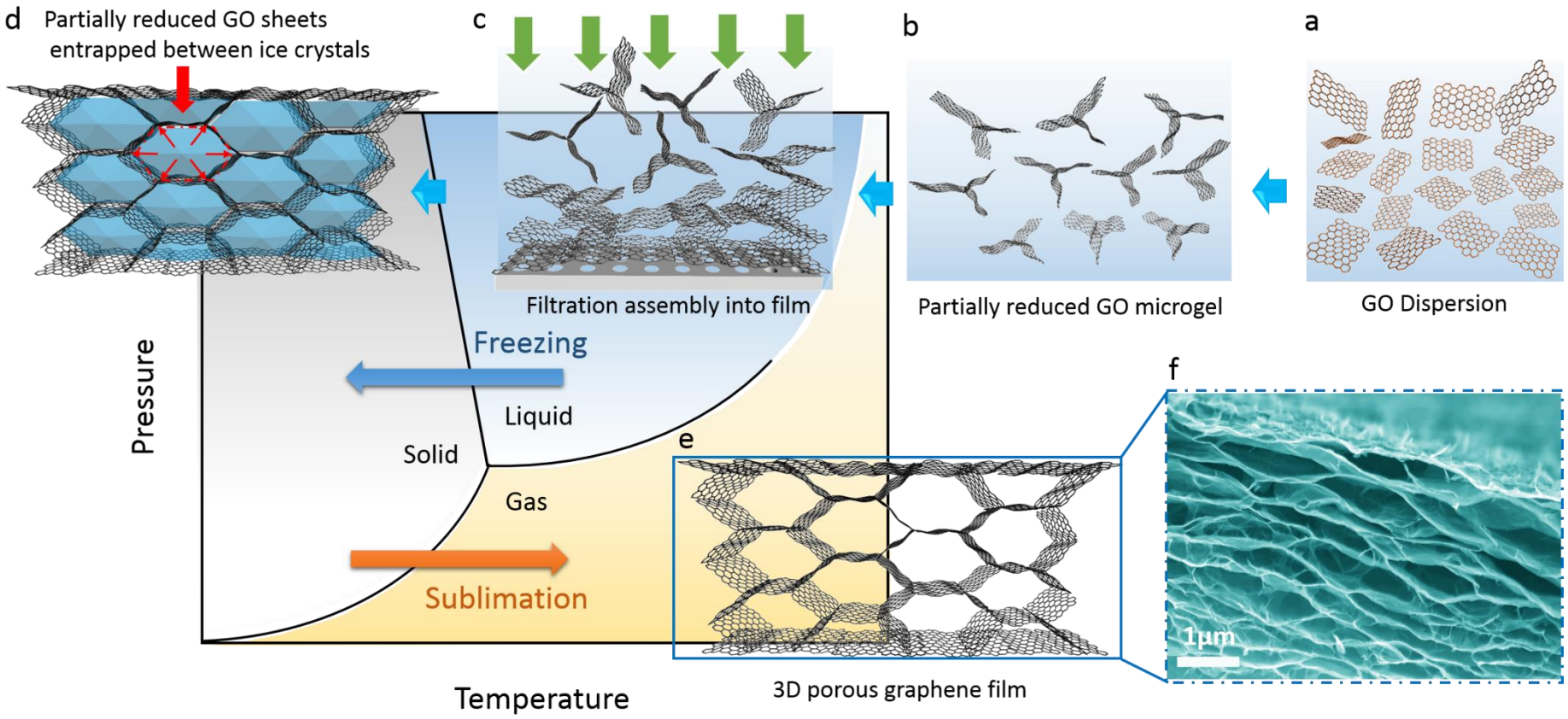


**Figure 4-1.** Mechanism of forming a 3D porous microstructure. a–e) Schematic illustration of the formation of a porous graphene film through prereduction, filtration assembly and freeze-casting. The water phase diagram shows the status of the aqueous solution during the different procedures. f) A typical cross-section SEM image of a porous graphene film.

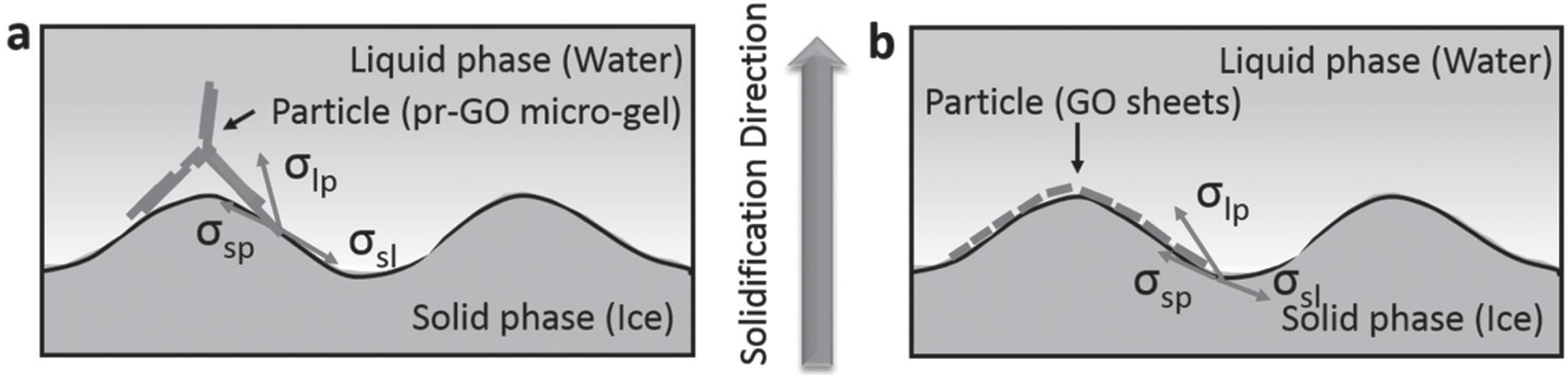


**Figure 4-2.** Schematic illustration of the interfacial free energies between the solvent solidification front and the "particles" in suspension. a) The prereduced GO micro-gel system and b) the GO sheets system.

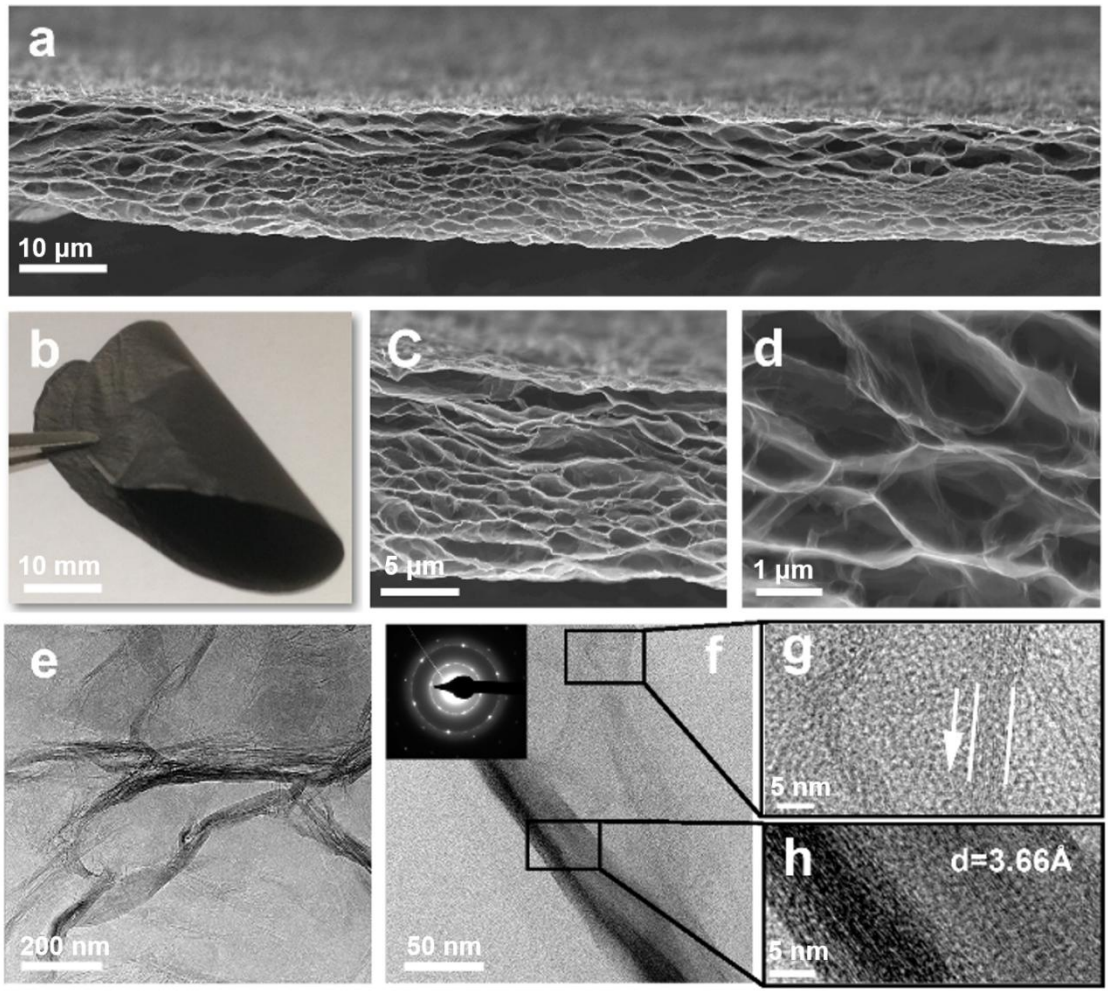


**Figure 4-3.** Morphology of 3D porous RGO films. a) Cross-section SEM image of a 3D porous RGO fi lm after long-term reduction. b) Photograph of a bent 3D porous RGO film. c,d) Partially enlarged views of (a) under higher magnification. e) TEM image of a graphene film wrapped pore inside a 3D porous RGO film. f–h) Low-magnification (f) and high-magnification (g,h) TEM images of the graphene pore walls. The inset image of (f) is the diffraction pattern of the graphene walls.

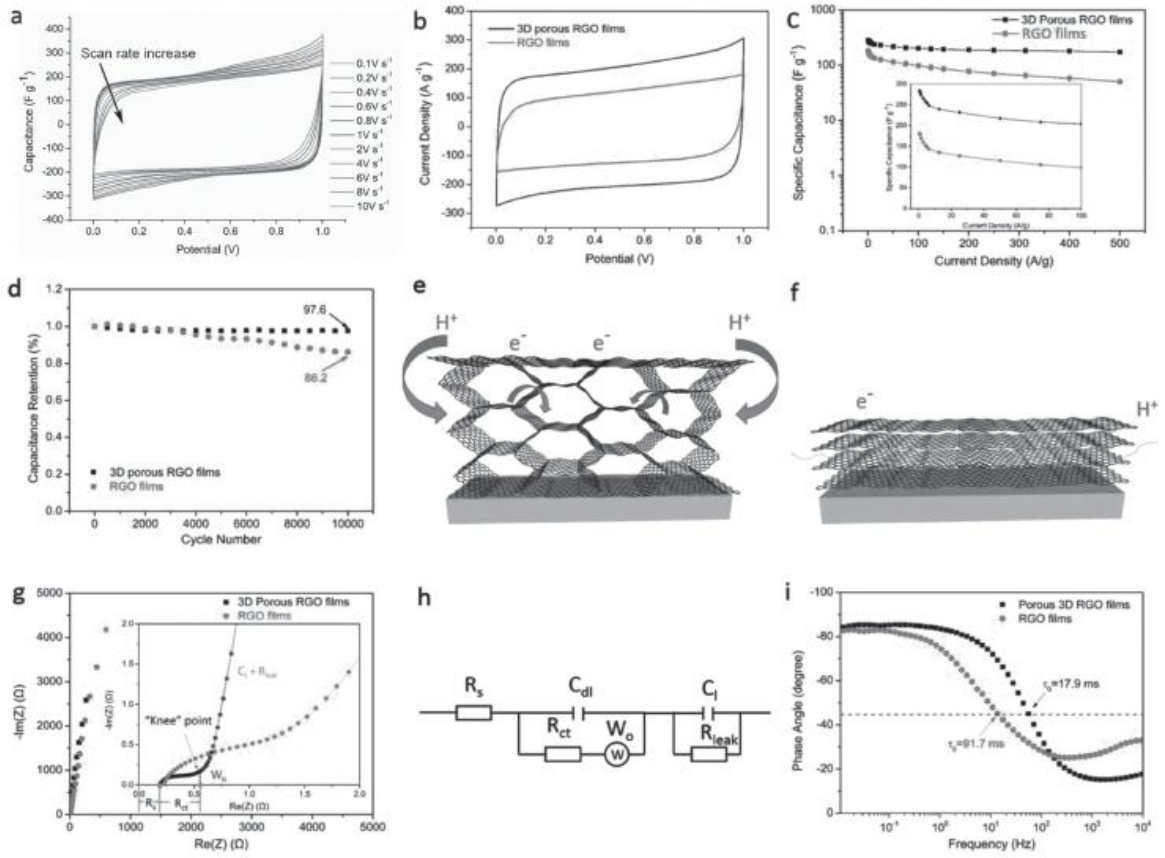


**Figure 4-4.** Electrochemical performance. a) Cyclic voltammetry profiles at different scan rates for a 3D porous RGO fi lm in 1.0 M $H_2SO_4$ electrolyte. b–i) Comparison of supercapacitors based on a 3D porous RGO film and an RGO film. b) Comparison of cyclic voltammetry profiles for a 3D porous RGO film and RGO films under the same scan rate of 1 V $s^{-1}$. c) Comparison of the specific capacitances under different current densities. d) Comparison of cycling stability after 10,000 cycles. e, f) Schematic illustration of ion and electron transport in a 3D porous RGO film and an RGO film. g) Electrochemical impedance spectroscopy data. The inset in (e) shows the magnified high-frequency region and the resistor and capacitor elements in an equivalent circuit related to the specific parts in the Nyquist plot. h) A Randles equivalent circuit. The equivalent circuit is used to fit the Nyquist spectra. i) Bode plots of phase angle versus frequency.

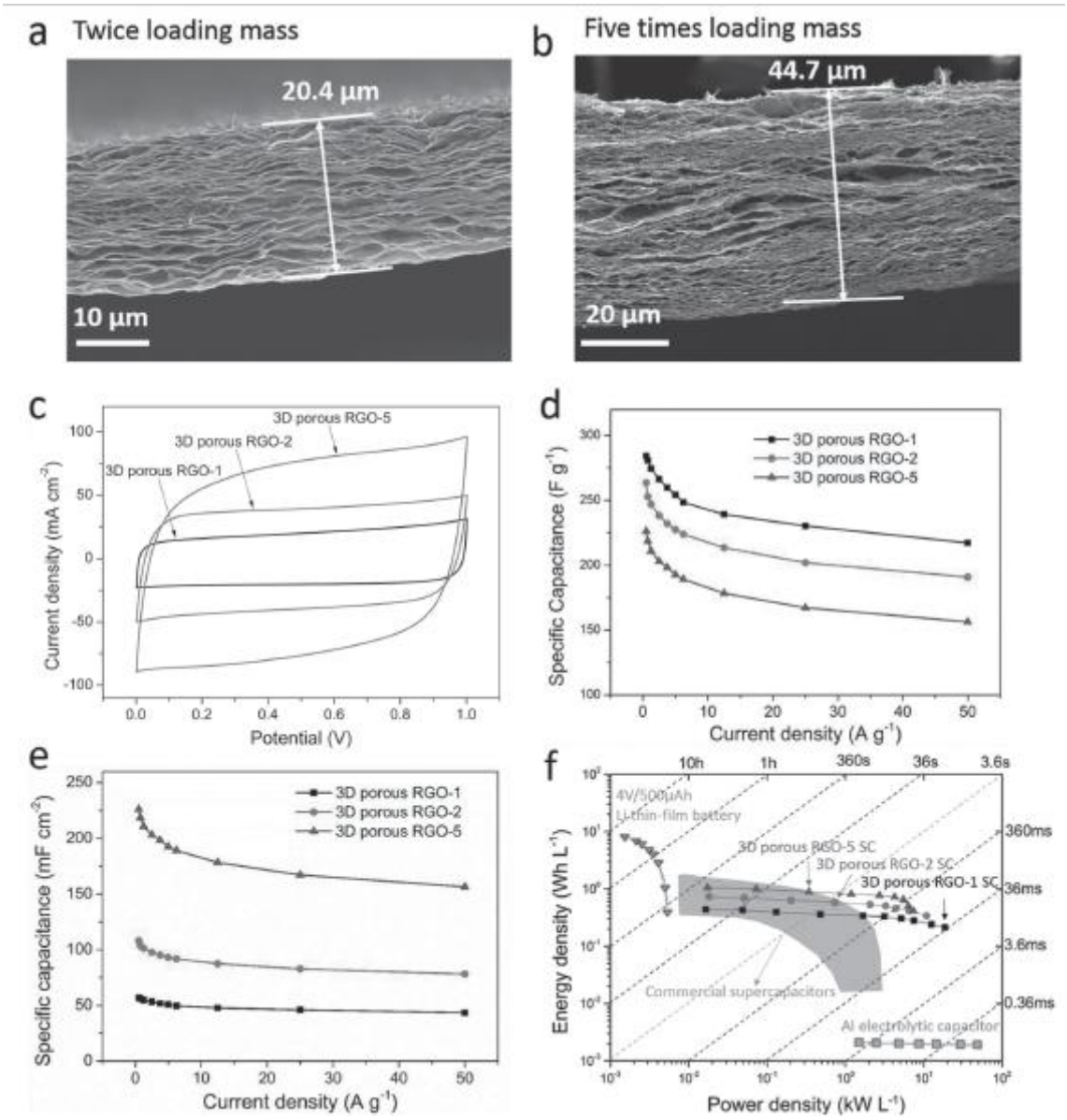


**Figure 4-5.** Supercapacitor performance of 3D porous RGO films with increased loading mass. Cross-section SEM images of 3D porous RGO films with different increased loading mass: a) Two times the loading mass, b) five times the loading mass. c) Comparative cyclic voltammetry curves of 3D porous RGO films with different loading masses at a scan rate of 1 V $s^{-1}$. d) Gravimetric capacitance of 3D porous RGO electrodes with different mass loadings versus different current densities. e) Areal capacitances of 3D porous RGO electrodes versus different current densities (with different active materials loading mass) f) Ragone plot of the volumetric power density versus energy density for 3D porous RGO supercapacitors compared to lithium thin-film batteries,[34] commercial supercapacitors with organic electrolytes,[7,35] and an aluminum electrolytic capacitor.[13]

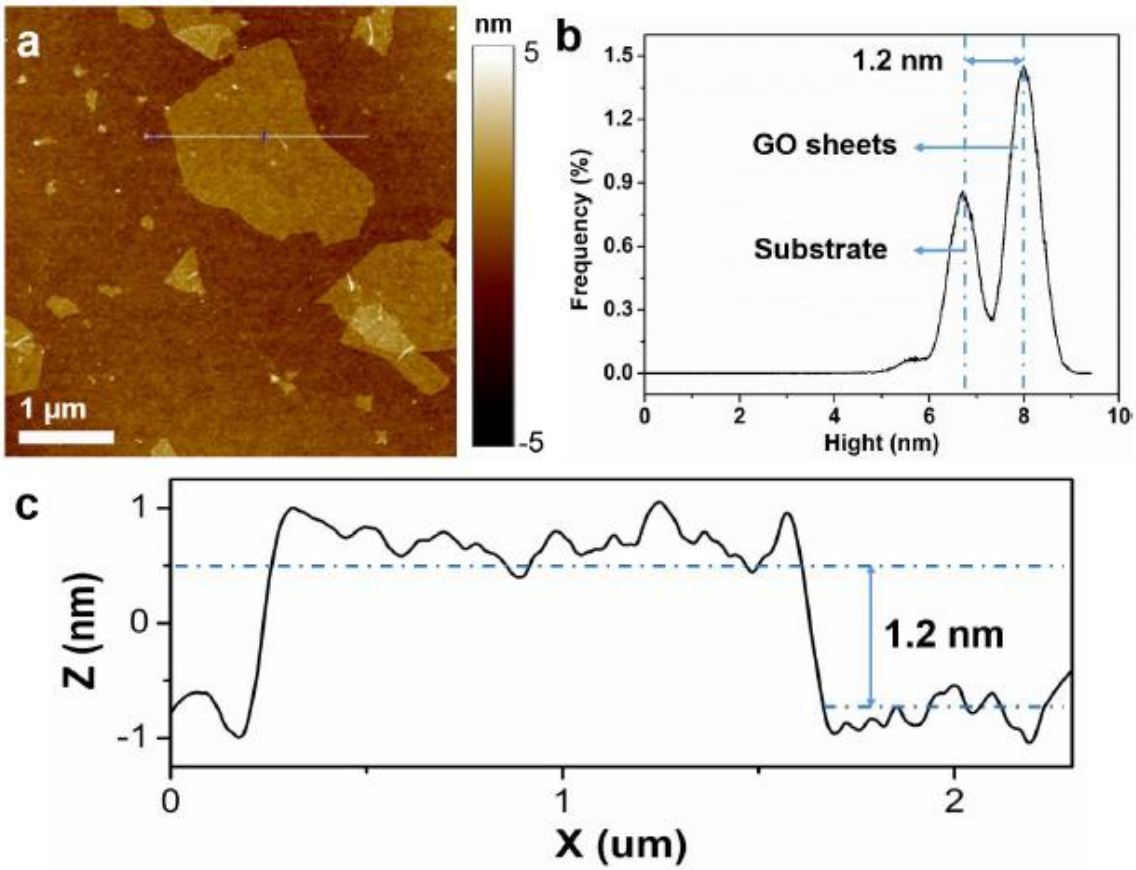


**Figure S4-1**. (a) An AFM image of GO sheets; (b) The height distribution diagram from the AFM image; (c) The height profile of the line scan shown in the AFM image.

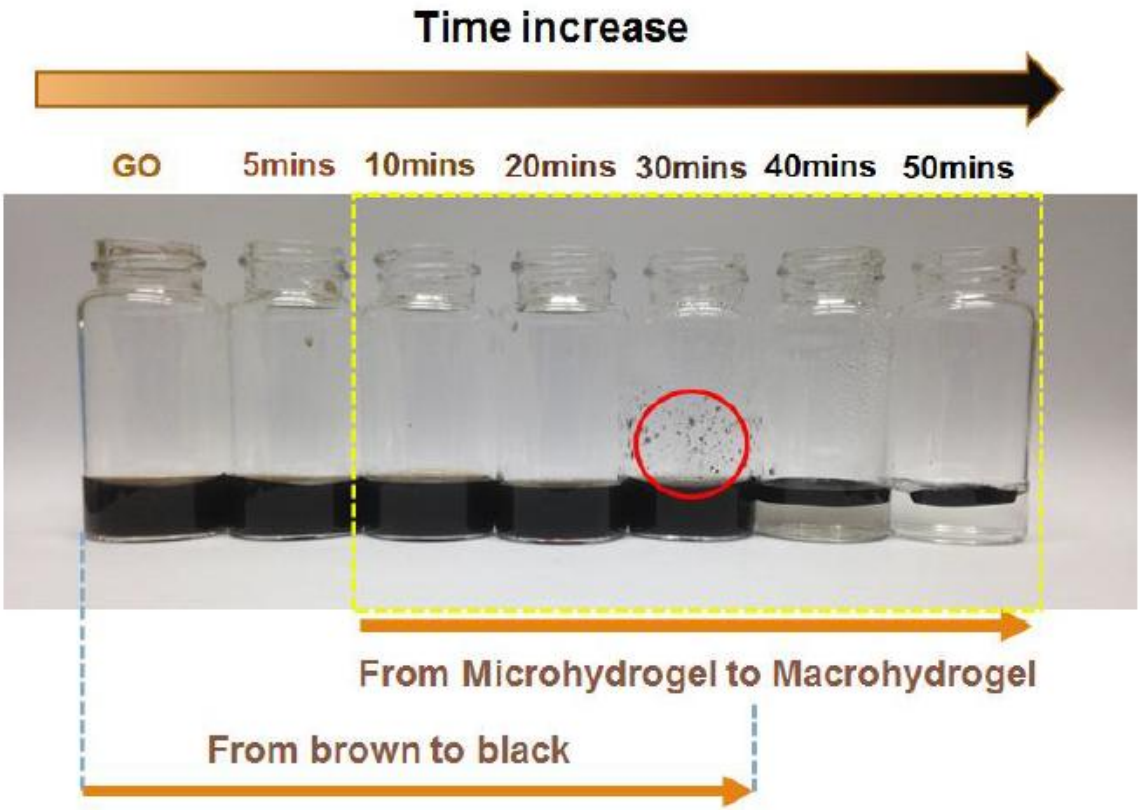


**Figure S4-2**. Optical images of GO dispersions after being subjected to pre-reduction by ascorbic acid for different times.

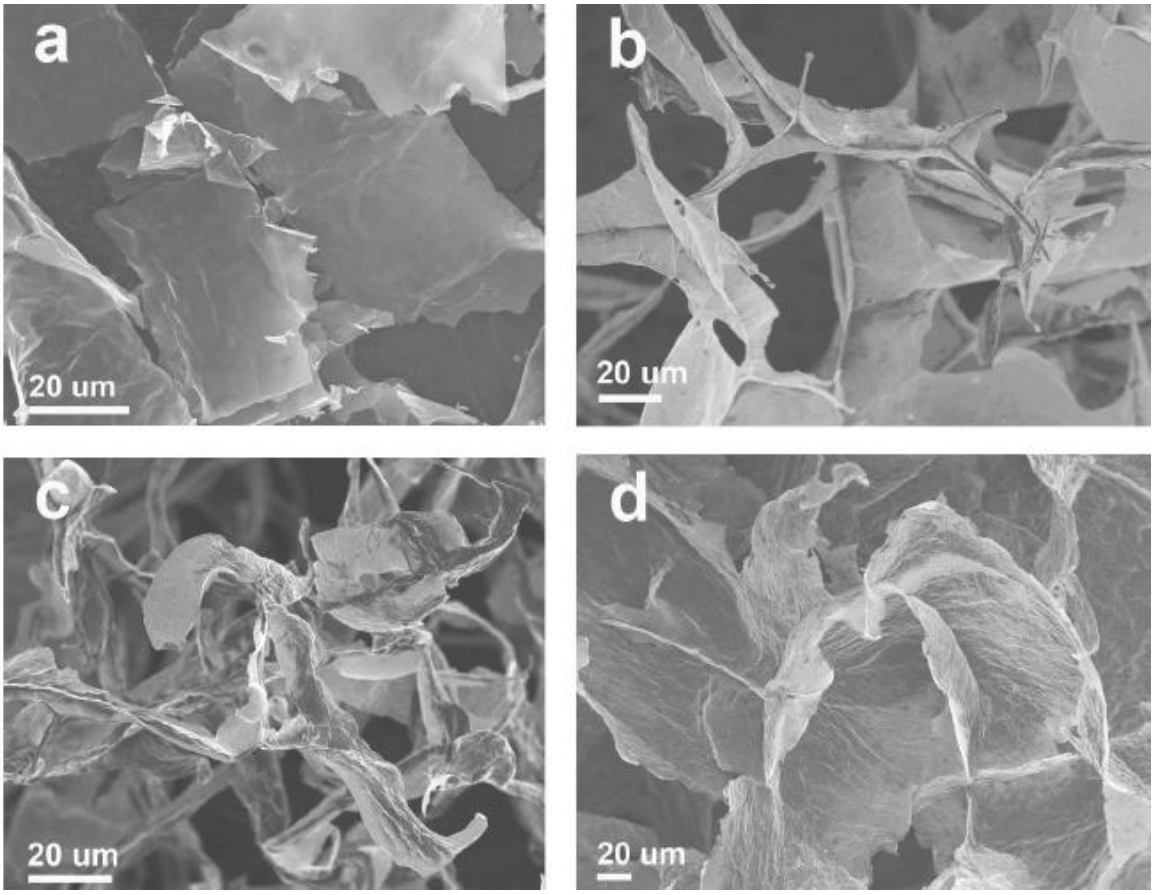


**Figure S4-3**. SEM images of partially reduced GO samples underdifferent reduction times: (a) 5 min, (b) 10 min, (c) 20 min, and (d) 30 min.

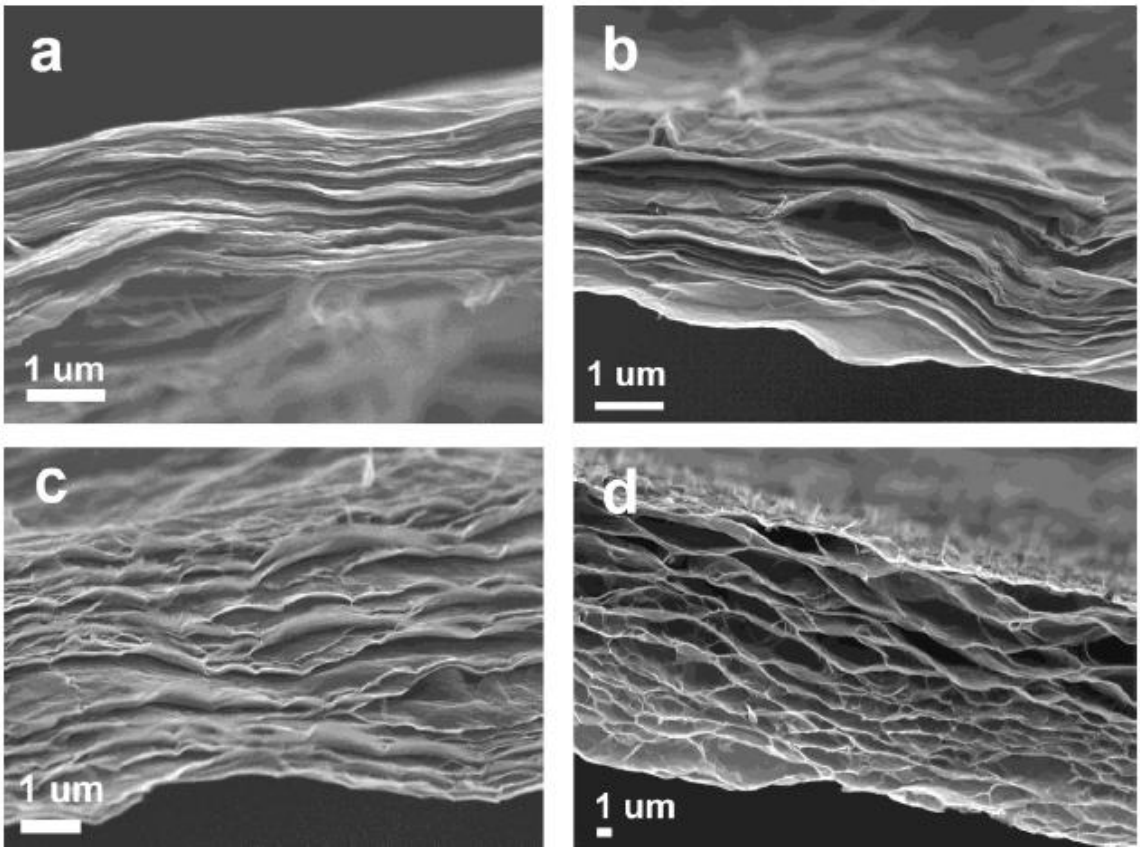


**Figure S4-4.** Cross-section SEM images of the 3D porous RGO films with different pre-reduced times: (a) 5 min, (b) 10 min, (c) 20 min, and (d) 30 min.

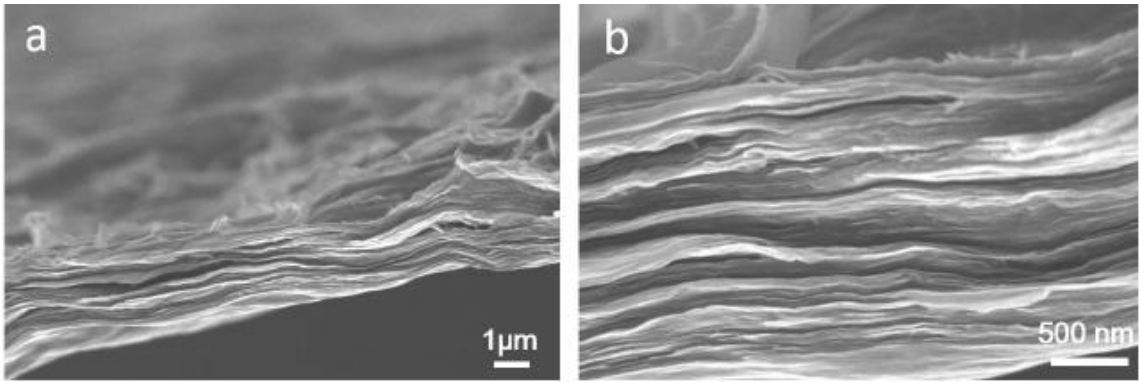


**Figure S4-5.** Cross-section SEM images of the RGO films under (a) low and high magnification.

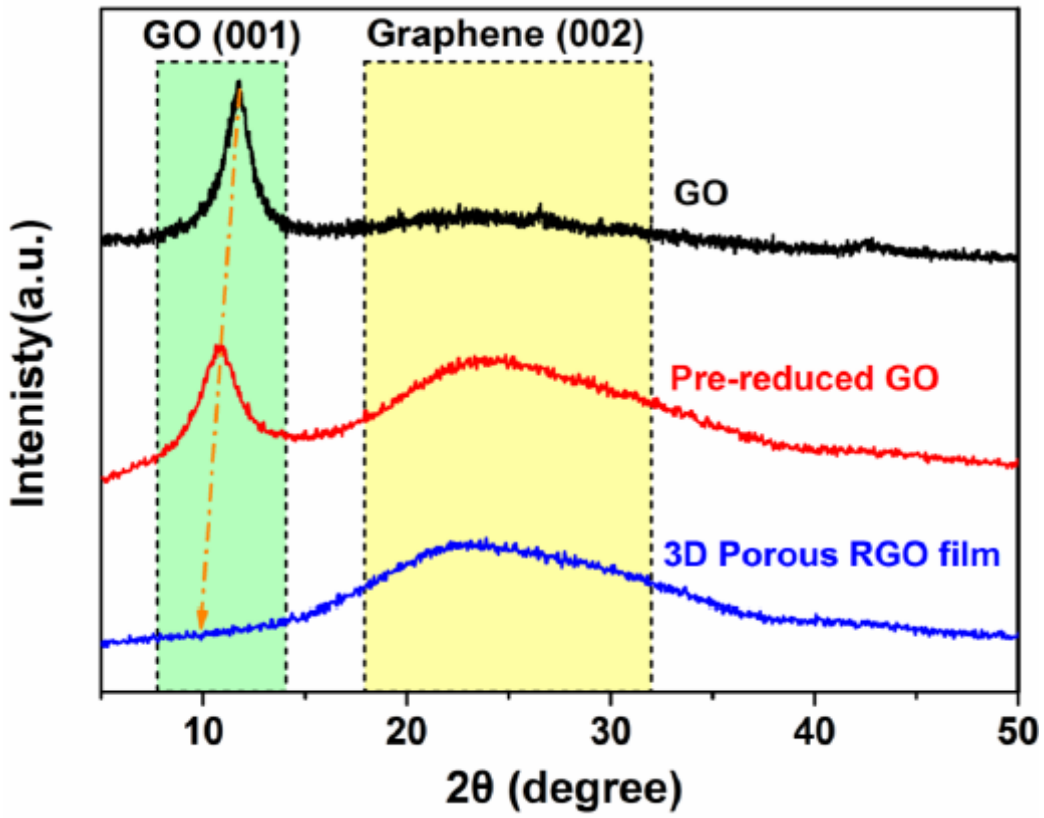


**Figure S4-6.** XRD patterns for the samples under different reduction procedures.

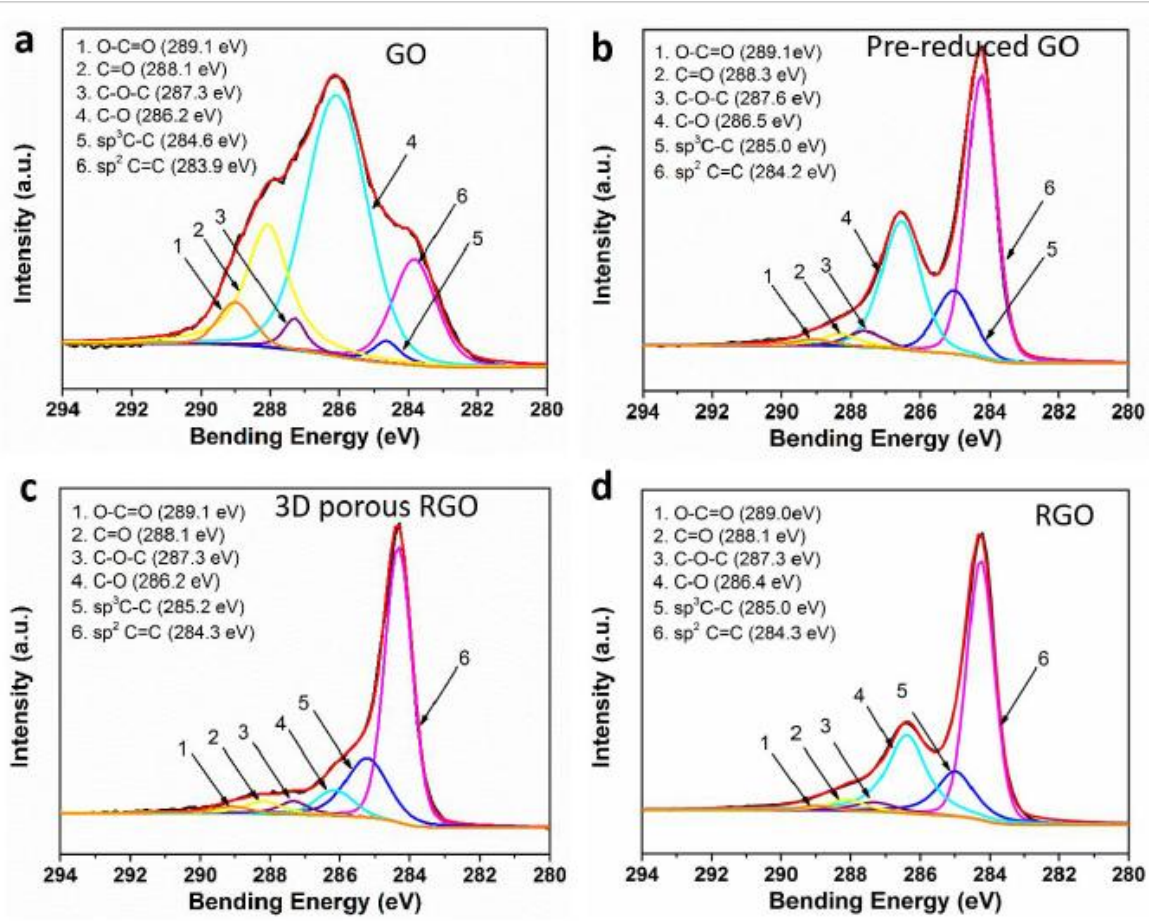


**Figure S4-7.** X-ray photoelectron spectra $C_{1s}$ profiles for (a) GO, (b) pre-reduced GO, (c) 3D porous RGO and (d) RGO.

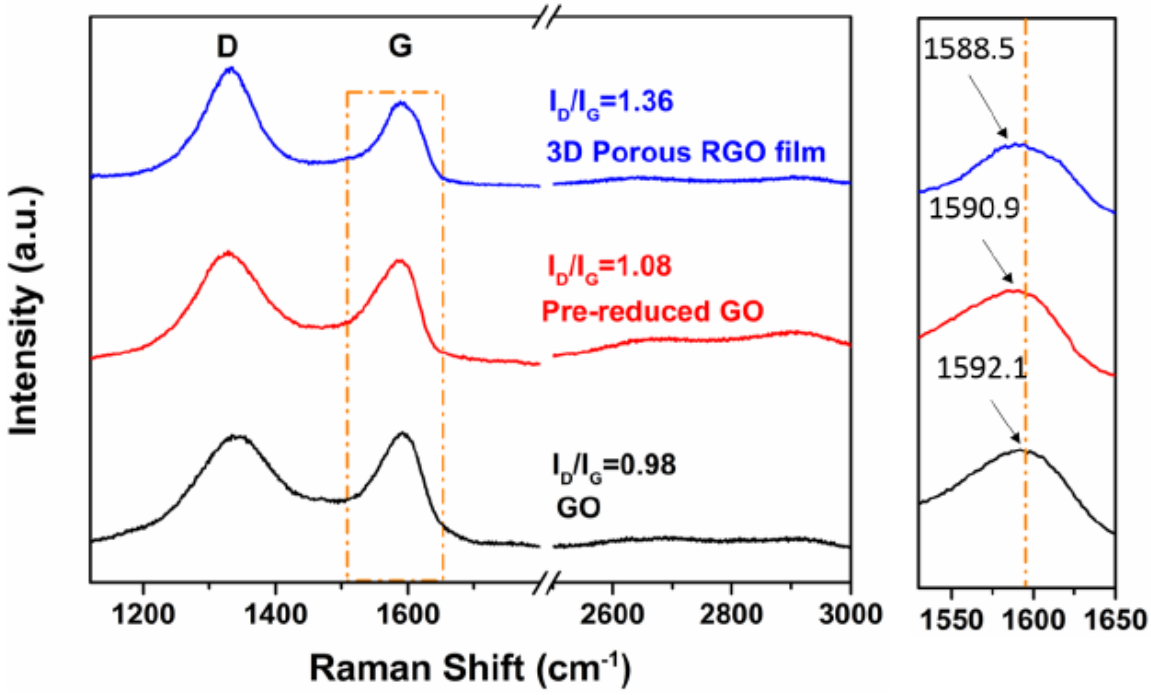


**Figure S4-8.** Raman spectra for GO, pre-reduced GO and 3D porous RGO films. The figure on the left highlights the G peaks and their position for these samples.

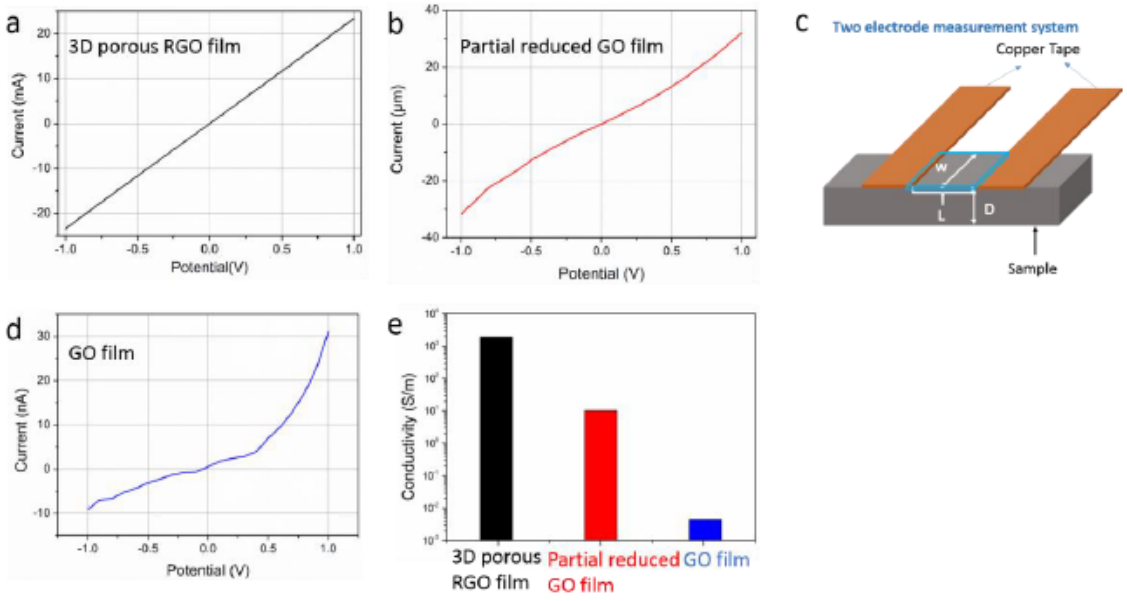


**Figure S4-9.** (a), (b) and (d) show the I-V curves of 3D porous RGO film, partial reduced GO film, and GO film, respectively. 3D porous RGO film exhibits a current that is several orders of magnitude higher, confirming a significant increase in conductivity. (c) Schematical illustration of a two-electrode measurement system. (e) Comparison of electrical conductivity values for a 3D porous RGO film, a partially reduced GO film, and a GO film.

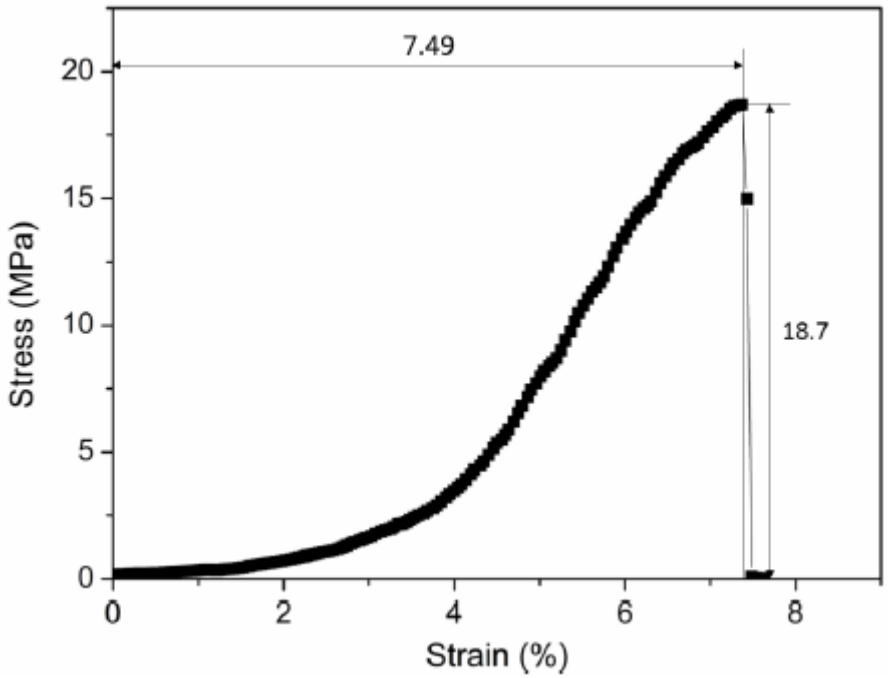


**Figure S4-10.** A strain-stress curve for the 3D porous RGO film. To evaluate mechanical properties, strain-stress curves of the 3D porous RGO film were tested on a tensile testing machine. The tensile strength approaches 18.7 MPa. Due to the porous microstructure, its strain can be up to 7.5%.

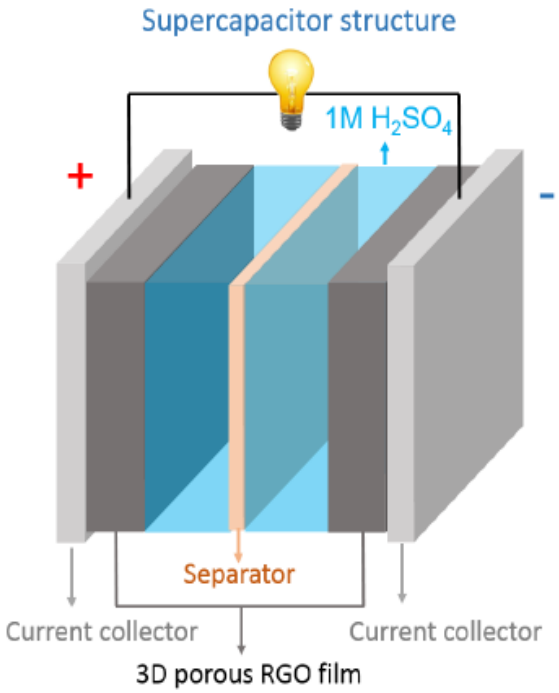


**Figure S4-11.** Schematic illustration of the structure of the fabricated symmetric two-electrode supercapacitor.

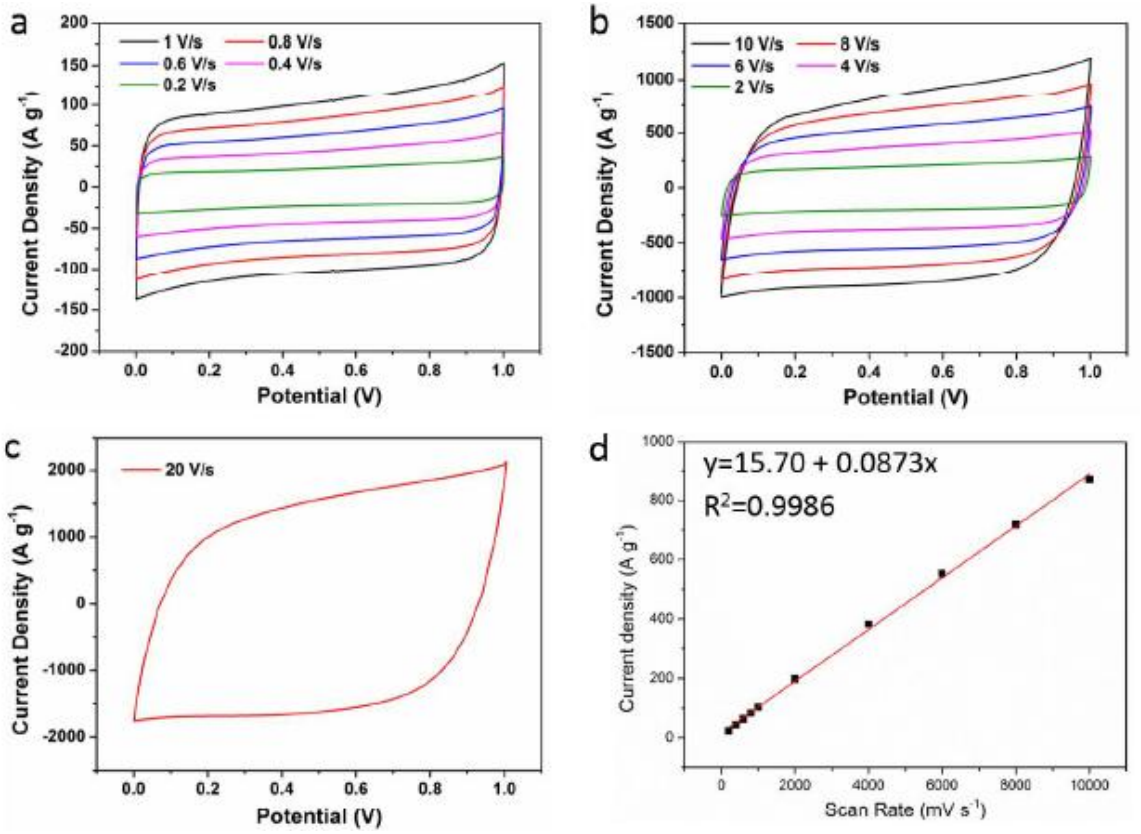


**Figure S4-12.** Cyclic voltammetry profiles of a 3D porous RGO film supercapacitor in 1.0 M $H_2SO_4$ aqueous electrolyte at different scan rates: (a) 0.2 mV/s to 1 V/s, (b) 2 V/s to 10 V/s, and (c) 20 V/s. (d) The dependence of the discharge current (extracted from the CV profiles at 0.5 V for the discharge curves) versus voltage scan rates. The highly linear dependent relationship ($R^2$ = 0.9986) of the discharge current on the scan rate up to high scan rates indicates ultra-high power capability.

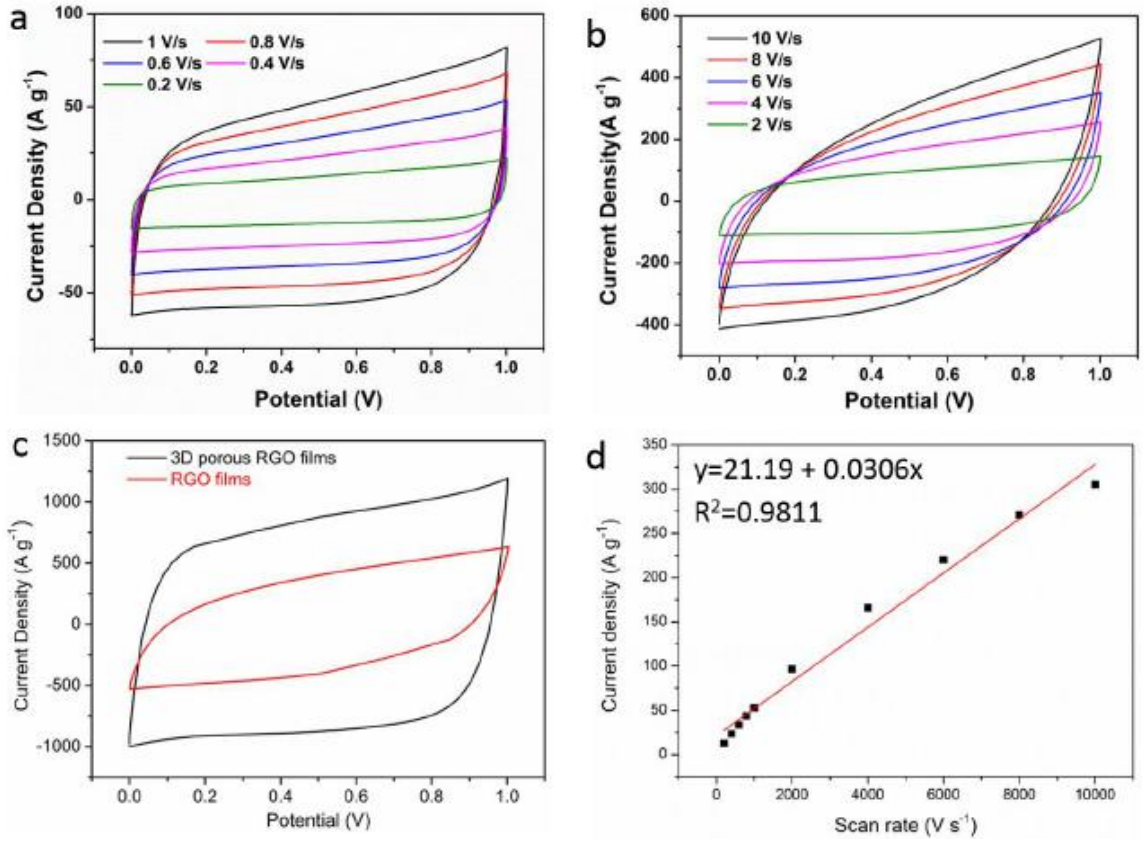


**Figure S4-13.** Cyclic voltammetry profiles of a RGO film supercapacitor at different scan rates: (a) 0.2 mV/s to 1 V/s; (b) 2 V/s to 10 V/s; and (c) 20 V/s. Comparison of cyclic voltammetry profiles for 3D porous RGO films and RGO films at the same scan rate of 10 V/s. (d) The dependence of the discharge current versus voltage scan rates. The relatively lower linear dependence ($R^2$ = 0.9811) of discharge current indicates the lower power capability of RGO films.

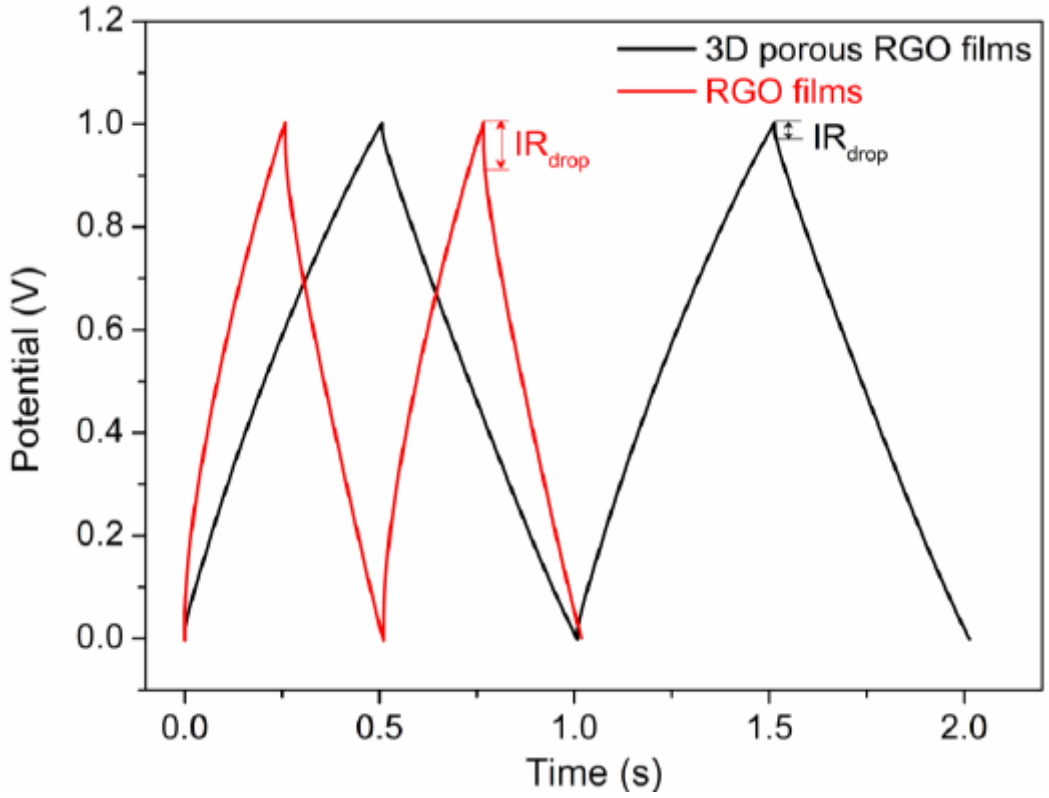


**Figure S4-14.** Comparison of galvanostatic charge/discharge profiles for RGO and 3D porous RGO films at the same current density of 100 A $g^{-1}$. Note that the current density is the applied current divided by the total mass of the two-electrode active materials. It is evident that 3D porous RGO electrode exhibits a smaller voltage drop (IR drop) at the starting point of the discharge curve, which indicates a lower equivalent series resistance (ESR).

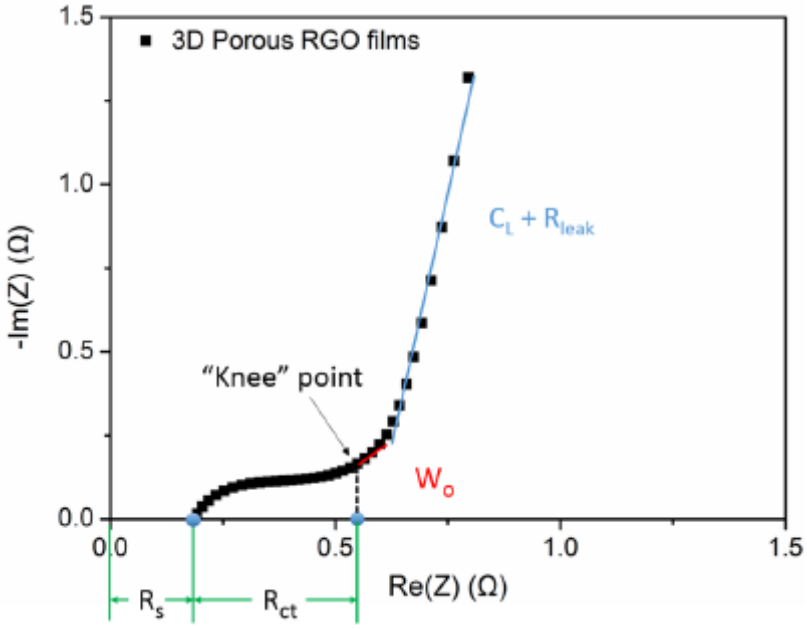


**Figure S4-15.** Illustration of specific elements in the Nyquist spectra.

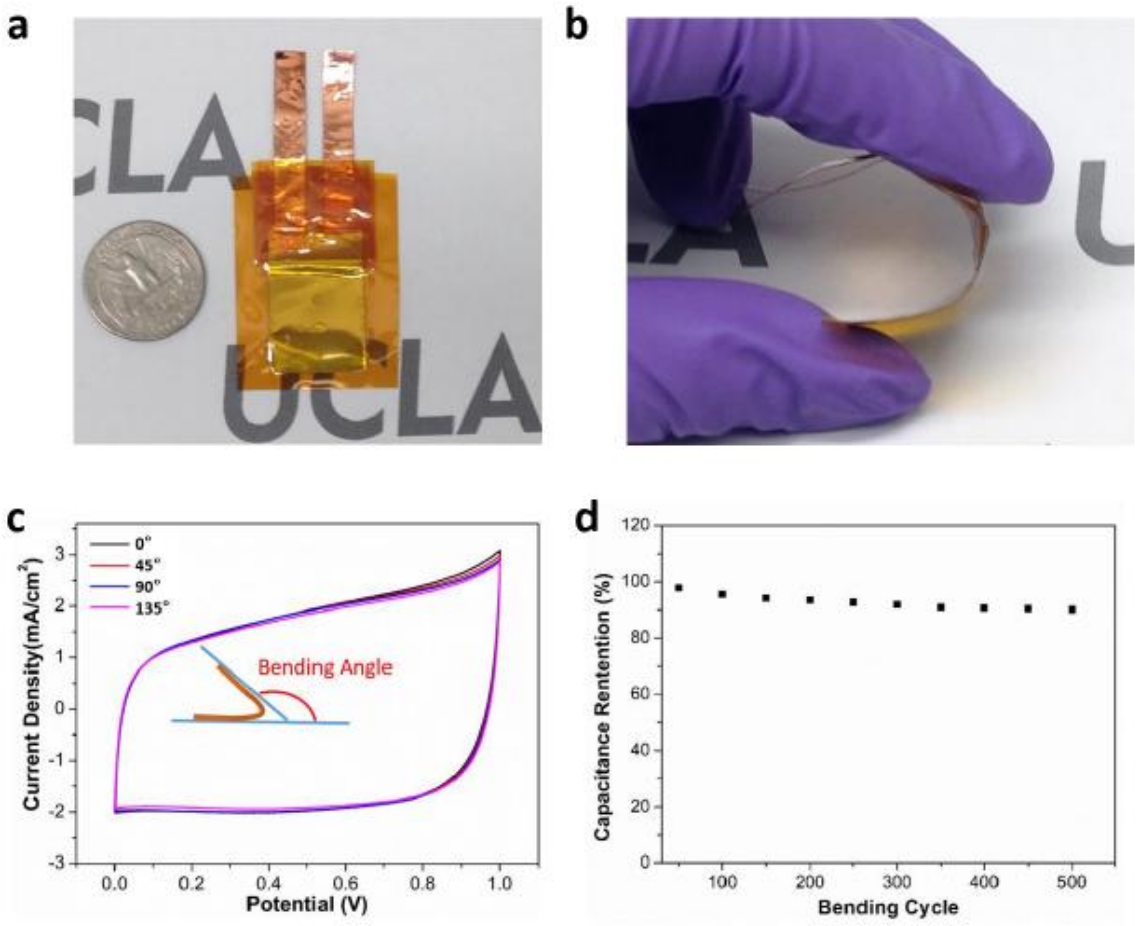


**Figure S4-16.** Capability of an all solid-state 3D porous RGO supercapacitor under bending conditions. (a, b) optical images of all solid-state 3D porous RGO supercapacitors under straight and bent conditions, respectively. (c) Cyclic voltammogram (CV) curves of an all solid-state supercapacitor tested at a scan rate of 50 mV $s^{-1}$ under different bending angles. (d) Cycling stability of an all solid-state supercapacitor under bending tests repeated for 500 cycles. The device can be bent arbitrarily without any obvious decrease in the performance compared to its planar state. The device retains about 91% of the initial capacitance after 500 cycles when tested under the bent state (applying a bending angle of 135°).

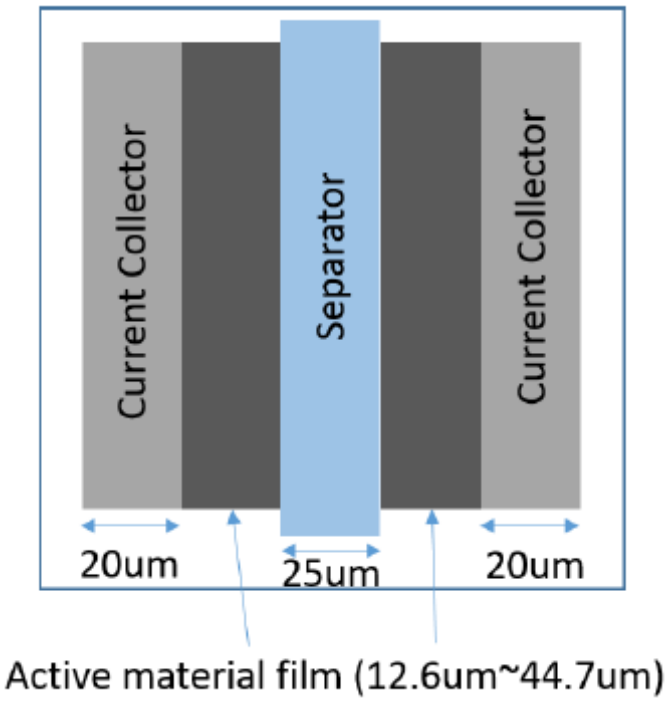


**Figure S4-17.** Schematic diagrams showing cross-section structure of different elements of a supercapacitor with their thicknesses. According to the different thicknesses of the active material films, the effective volume of RGO, 3D porous RGO-1, 3D porous RGO-2 and 3D porous RGO-5 supercapacitors are $6.9\times10^{-3}$ $cm^{-3}$, $9.0\times10^{-3}$ $cm^{-3}$, $10.5\times10^{-3}$ $cm^{-3}$, and $15.4\times10^{-3}$ $cm^{-3}$, respectively.

**Table S4-1.** Results of XPS Analyses

| Samples | O-C=O | C=O | C-O-C | C-O | $sp^3$ C-C | $sp^2$ C=C | $C_{1s}$ | $O_{1s}$ |
|---|---|---|---|---|---|---|---|---|
| GO | 4.93% | 21.5% | 2.94% | 51.9% | 2.5% | 16.3% | 53.2% | 46.8% |
| Pre-reduced GO | 1.90% | 3.51% | 3.65% | 30.1% | 14.2% | 46.7% | 77.4% | 22.6% |
| 3D porous RGO films | 2.17% | 4.82% | 4.09% | 7.5% | 22.3% | 59.1% | 84.4% | 15.6% |
| RGO | 1.4% | 3.73% | 3.65% | 28.7% | 14.8% | 47.6% | 78.7% | 21.3% |

**Table S4-2.** Equivalent circuit parameters[a]

| Fitting Parameters | Rs(Ω) | Rct(Ω) | Cdl ($\mu F/cm^2$) | A($\Omega . S^{-n}$) | n | $C_F$ (F/g) | $R_{leak}$ (kΩ) |
|---|---|---|---|---|---|---|---|
| Porous 3D RGO | 0.202 | 0.181 | 51.2 | 95.3 | 0.413 | 195.2 | 26.8 |
| RGO | 0.244 | 1.04 | 27.6 | 78.7 | 0.264 | 109.4 | 21.8 |

[a]Obtained from the fitting results for components of the equivalent circuit fitted with the impedance spectra.

**Table S4-3.** Comparison of Electrical Conductivity, Failure Strain and Tensile Strength of Our Work with Other Porous Graphene Films

| Sample | | Conductivity (S/m) | Strain (%) | Tensile strength (MPa) | Young's modulus (GPa) | Ref. |
|---|---|---|---|---|---|---|
| Porous graphene films | 3D porous RGO films | 1,905 | 7.5 | 18.7 | 0.56 | Our work |
| | RGO foam | NA | 10 | 3.2 | 0.04 | 40 |
| | Graphene gel film | 103.3 | 3.3 | 0.92 | NA | 41 |
| | 3D graphene foam/PDMS | 1,000 | 94 | 1.7 | NA | 42 |
| Compact graphene paper | Graphene oxide paper | NA | 0.1 | 28.9 | 32 | 43 |
| | PVA/RGO paper | 5265 | 2.67 | 189 | 10.4 | 44 |
| | rGO-PCDO | 23230 | 6.9 | 129.6 | NA | 45 |
| | Graphene paper | 11800 | 0.83 | 293.3 | 41.8 | 46 |
| | PVA/Graphene | NA | 1.8 | 42 | 1.04 | 47 |

**Table S4-4.** Comparison of Performances of Carbon-based Aqueous Supercapacitors

| Sample | Mass loading (mg $cm^{-2}$) | Active materials density (g $cm^{-3}$) | $C_{specific\ capacitance}$ | | $E_{electrode}$ | | $P_{electrode}$ | | $E_{device}$ | $P_{device}$ | Ref. |
|---|---|---|---|---|---|---|---|---|---|---|---|
| | | | F $g^{-1}$ | F $cm^{-3}$ | Wh $kg^{-1}$ | Wh $L^{-1}$ | kW $kg^{-1}$ | kW $L^{-1}$ | Wh $L^{-1}$ | kW $L^{-1}$ | |
| RGO | 0.2 | 0.95 | 181.3 | 172.2 | 6.3 | 6.0 | 70.8 | 67.3 | 0.188 | 2.11 | This work |
| 3D porous RGO-1 | 0.2 | 0.16 | 284.2 | 45.5 | 9.9 | 1.58 | 282 | 51.1 | 0.260 | 14.3 | |
| 3D porous RGO-2 | 0.41 | 0.20 | 265.5 | 53.0 | 9.2 | 1.84 | 135 | 28 | 0.710 | 10.8 | |
| 3D porous RGO-5 | 1.02 | 0.23 | 241.5 | 55.2 | 8.3 | 1.92 | 58.3 | 13.5 | 1.11 | 7.8 | |
| Pillared Graphene paper | 0.41 | NA | 138 | NA | 4.8 | NA | 5.1 | NA | NA | NA | 48 |
| CNT/graphene sponge | 1.7 | NA | NA | NA | 7.1 | NA | 48 | NA | NA | NA | 49 |
| Graphene-Cellulose paper | 0.675 | NA | 120 | NA | ~8.3 | NA | ~23.7 | NA | NA | NA | 50 |
| Filtered graphene paper | 0.45 | NA | 215 | NA | 7.47 | NA | NA | NA | NA | NA | 51 |
| Liquid mediated graphene | ~1.0 | 0.13~1.33 | 203~192 | 26.4~255 | 7.05~6.67 | 0.91~8.87 | NA | NA | NA | NA | 52 |
| Chemically reduced graphene | 4.55 | 0.38 | 135 | 51.3 | 4.69 | 1.78 | NA | NA | NA | NA | 53 |
| Laser scribed graphene | 0.036 | 0.048 | 222 | 10.7 | 7.7 | 0.37 | NA | NA | NA | NA | 54 |
| Commercial activated carbon | NA | 0.5~0.7 | 160~200 | 80~120 | 5.56~6.94 | NA | NA | NA | 1.1 | 0.156 | 52. 55 |
| Asymmetric supercapacitor | NA | NA | NA | NA | 23.2 | NA | 10 | NA | NA | NA | 56 |
| NPG/$MnO_2$ | NA | NA | 1145 | 1160 | 57 | NA | 16 | NA | NA | NA | 57 |

**REFERENCES**


[1] P. Simon, Y. Gogotsi, *Nat. Mater.* **2008**, *7*, 845.

[2] B. Conway, *Electrochemical Supercapacitors: Scientific Fundamentals and Technological Applications* , Kluwer Academic/Plenum Publishers, New York **1999**.

[3] M. Ghidiu, M. R. Lukatskaya, M.-Q. Zhao, Y. Gogotsi, M. W. Barsoum, *Nature* **2014**, *516*, 78.

[4] B. Dunn, H. Kamath, J.-M. Tarascon, *Science* **2011**, *334*, 928.

[5] P. Simon, Y. Gogotsi, B. Dunn, *Science* **2014**, *343*, 1210.

[6] M. Acerce, D. Voiry, M. Chhowalla, *Nat. Nanotechnol.* **2015**, *10*, 313.

[7] P. Simon, Y. Gogotsi, *Acc. Chem. Res.* **2012**, *46*, 1094.

[8] J. Yan, Q. Wang, T. Wei, Z. Fan, *Adv. Energy Mater.* **2014**, *4*, 1300816.

[9] D. Yu, K. Goh, H. Wang, L. Wei, W. Jiang, Q. Zhang, L. Dai, Y. Chen, *Nat. Nanotechnol.* **2014**, *9*, 555.

[10] M. R. Lukatskaya, O. Mashtalir, C. E. Ren, Y. Dall'Agnese, P. Rozier, P. L. Taberna, M. Naguib, P. Simon, M. W. Barsoum, Y. Gogotsi, *Science* **2013**, *341*, 1502.

[11] Y. Gogotsi, P. Simon, *Science* **2011**, *334*, 917.

[12] J. R. Miller, P. Simon, *Science* **2008**, *321*, 651.

[13] M. F. El-Kady, V. Strong, S. Dubin, R. B. Kaner, *Science* **2012**, *335*, 1326.

[14] M. D. Stoller, S. Park, Y. Zhu, J. An, R. S. Ruoff, *Nano Lett.* **2008**, *8*, 3498.

[15] Y. Shao, M. F. El-Kady, L. J. Wang, Q. Zhang, Y. Li, H. Wang, M. F. Mousavi, R. B. Kaner, *Chem. Soc. Rev.* **2015**, *44*, 3639.

[16] R. Raccichini, A. Varzi, S. Passerini, B. Scrosati, *Nat. Mater.* **2015**, *14*, 271.

[17] Y. Shao, H. Wang, Q. Zhang, Y. Li, *NPG Asia Mater.* **2014**, *6*, e119.

[18] S. Gilje, S. Han, M. Wang, K. L. Wang, R. B. Kaner, *Nano Lett.* **2007**, *7*, 3394.

[19] F. Günes, H.-J. Shin, C. Biswas, G. H. Han, E. S. Kim, S. J. Chae, J.-Y. Choi, Y. H. Lee, *ACS Nano* **2010**, *4*, 4595.

[20] S. Gan, L. Zhong, T. Wu, D. Han, J. Zhang, J. Ulstrup, Q. Chi, L. Niu, *Adv. Mater.* **2012**, *24*, 3958.

[21] X. Yang, J. Zhu, L. Qiu, D. Li, *Adv. Mater.* **2011**, *23*, 2833.

[22] Y. Shao, H. Wang, Q. Zhang, Y. Li, *J. Mater. Chem. C* **2013**, *1*, 1245.

[23] X. Yang, C. Cheng, Y. Wang, L. Qiu, D. Li, *Science* **2013**, *341*, 534.

[24] X. Wang, Y. Zhang, C. Zhi, X. Wang, D. Tang, Y. Xu, Q. Weng, X. Jiang, M. Mitome, D. Golberg, Y. Bando, *Nat. Commun.* **2013**, 4.

[25] S. Deville, *Adv. Eng. Mater.* **2008**, *10*, 155.

[26] S. Samitsu, R. Zhang, X. Peng, M. R. Krishnan, Y. Fujii, I. Ichinose, *Nat. Commun.* **2013**, *4*, 2653.

[27] F. Bouville, E. Maire, S. Meille, B. Van de Moortèle, A. J. Stevenson, S. Deville, *Nat. Mater.* **2014**, *13*, 508.

[28] S. Deville, E. Maire, G. Bernard-Granger, A. Lasalle, A. Bogner, C. Gauthier, J. Leloup, C. Guizard, *Nat. Mater.* **2009**, *8*, 966.

[29] G. Eda, M. Chhowalla, *Adv. Mater.* **2010**, *22*, 2392.

[30] U. N. Maiti, J. Lim, K. E. Lee, W. J. Lee, S. O. Kim, *Adv. Mater.* **2014**, *26*, 615.

[31] Z. Niu, J. Chen, H. H. Hng, J. Ma, X. Chen, *Adv. Mater.* **2012**, *24*, 4144.

[32] Z. Chen, W. Ren, L. Gao, B. Liu, S. Pei, H.-M. Cheng, *Nat. Mater.* **2011**, *10*, 424.

[33] D. Li, M. B. Muller, S. Gilje, R. B. Kaner, G. G. Wallace, *Nat. Nanotechnol.* **2008**, *3*, 101.

[34] D. Pech, M. Brunet, H. Durou, P. Huang, V. Mochalin, Y. Gogotsi, P.-L. Taberna, P. Simon, *Nat. Nanotechnol.* **2010**, *5*, 651.

[35] A. Burke, *Electrochim. Acta* **2007**, *53*, 1083.

[36] Y. Xu, Z. Lin, X. Huang, Y. Liu, Y. Huang, X. Duan, *ACS Nano* **2013**, *7*, 4042.

[37] C.-M. Chen, Q. Zhang, C.-H. Huang, X.-C. Zhao, B.-S. Zhang, Q.-Q. Kong, M.-Z. Wang, Y.-G. Yang, R. Cai, D. Sheng Su, *Chem. Commun.* **2012**, *48*, 7149.

[38] N. I. Kovtyukhova, P. J. Ollivier, B. R. Martin, T. E. Mallouk, S. A. Chizhik, E. V. Buzaneva and A. D. Gorchinskiy, *Chem. Mater.*, 1999, **11**, 771-778.

[39] D. Li, M. B. Muller, S. Gilje, R. B. Kaner and G. G. Wallace, *Nat. Nanotechnol.*, 2008, **3**, 101-105.

[40] Z. Niu, J. Chen, H. H. Hng, J. Ma and X. Chen, *Adv. Mater.*, 2012, **24**, 4144-4150.

[41] U. N. Maiti, J. Lim, K. E. Lee, W. J. Lee and S. O. Kim, *Adv. Mater.*, 2014, **26**, 615-619.

[42] Z. Chen, W. Ren, L. Gao, B. Liu, S. Pei and H.-M. Cheng, *Nat. Mater.*, 2011, **10**, 424-428.

[43] D. A. Dikin, S. Stankovich, E. J. Zimney, R. D. Piner, G. H. B. Dommett, G. Evmenenko, S. T. Nguyen and R. S. Ruoff, *Nature*, 2007, **448**, 457-460.

[44] Y.-Q. Li, T. Yu, T.-Y. Yang, L.-X. Zheng and K. Liao, *Adv. Mater.*, 2012, **24**, 3426-3431.

[45] Q. Cheng, M. Wu, M. Li, L. Jiang and Z. Tang, *Angew. Chem. Int. Edit.*, 2013, **52**, 3750-3755.

[46] H. Chen, M. B. Müller, K. J. Gilmore, G. G. Wallace and D. Li, *Adv. Mater.*, 2008, **20**, 3557-3561.

[47] X. Zhao, Q. Zhang, D. Chen and P. Lu, *Macromolecules*, 2010, **43**, 2357-2363.

[48] G. K. Wang, X. Sun, F. Y. Lu, H. T. Sun, M. P. Yu, W. L. Jiang, C. S. Liu and J. Lian, *Small*, 2012, **8**, 452-459.

[49] Z. Xu, Z. Li, C. M. B. Holt, X. Tan, H. Wang, B. S. Amirkhiz, T. Stephenson and D. Mitlin, *J. Phys. Chem. Lett.*, 2012, **3**, 2928-2933.

[50] Z. Weng, Y. Su, D.-W. Wang, F. Li, J. Du and H.-M. Cheng, *Adv. Energy Mater.*, 2011, **1**, 917-922.

[51] X. Yang, J. Zhu, L. Qiu and D. Li, *Adv. Mater.*, 2011, **23**, 2833-2838.

[52] X. Yang, C. Cheng, Y. Wang, L. Qiu and D. Li, *Science*, 2013, **341**, 534-537.

[53] M. D. Stoller, S. Park, Y. Zhu, J. An and R. S. Ruoff, *Nano Lett.*, 2008, **8**, 3498-3502.

[54] M. F. El-Kady, V. Strong, S. Dubin and R. B. Kaner, *Science*, 2012, **335**, 1326-1330.

[55] A. Burke, *Electrochim. Acta*, 2007, **53**, 1083-1091.

[56] H. Gao, F. Xiao, C. B. Ching and H. Duan, *ACS Appl. Mater. Inter.*, 2012, **4**, 2801-2810.

[57] X. Lang, A. Hirata, T. Fujita and M. Chen, *Nat. Nanotechnol.*, 2011, **6**, 232-236.

# CHAPTER 5. CHARACTERIZATION OF ANILINE TETRAMER BY MALDI TOF MASS SPECTROMETRY UPON OXIDATIVE AND REDUCTIVE CYCLING

"Reprinted from (Li, R.; Lin, C.-W.; Shao, Y.; Chang C.W.; Yao, F.-K.; Kowal, M.D.; Wang, H.; Yeung, M.T.; Huang S.-C.; Kaner, R.B. "Characterization of Aniline Tetramer by MALDI TOF Mass Spectrometry upon Oxidative and Reductive Cycling" *Polymers*, 2016, 8, 401. DOI: 10.3390/polym8110401)."

## ABSTRACT

By combining electrochemical experiments with mass spectrometric analysis, it is found that using short chain oligomers to improve the cycling stability of conducting polymers in supercapacitors is still problematic. Cycling tests via cyclic voltammetry over a potential window of 0 to 1.0 V or 0 to 1.2 V in a two-electrode device configuration resulted in solid-state electropolymerization and chain scission. Electropolymerization of the aniline tetramer to generate long chain oligomers is shown to be possible despite the suggested decrease in reactivity and increase in intermediate stability with longer oligomers. Because aniline oligomers are more stable towards reductive cycling when compared to oxidative cycling, future conducting polymer/oligomer-based pseudocapacitors should consider using an asymmetric electrode configuration.

## INTRODUCTION

In the search for materials for high-energy-density supercapacitors, much research has been carried out on conducting polymers, including polyaniline, polypyrrole and polythiophene [1–5]. When these materials are applied in pseudocapacitors, the bulk of the charge storage is derived from redox reactions and results in their high capacitance, energy density, and low cost.

However, conducting polymers suffer from poor cycling stability. The generally acknowledged explanation is the degradation that results from the stretching and swelling of polymer chains [6,7]. To limit swelling and improve cycling life, composites of conducting polymers with carbonaceous material such as graphene, monolithic carbon, carbon nanotubes, and carbonaceous shells have been made [8–11]; this not only reinforces the mechanical stability, but also provides greater conductivity, surface area, and enhanced charge transport. Besides choosing materials to provide a good physical support for conducting polymers, the selection of a suitable operating potential window is arguably more crucial. A small potential window limits the charge storage ability, whereas a large potential window can cause over-oxidation and/or over-reduction of the conducting polymers, leading to device degradation.

Polyaniline stands out among conducting polymers for its ease of doping/dedoping and tunable conductivity. Upon partial oxidation from its leucoemeraldine base (LEB) form or partial reduction from the pernigraniline base (PNG) to the emeraldine base (EB) and doping with strong acids, conducting polyaniline salts are formed. The general rule of thumb when applying polyaniline to supercapacitors and improving cycling stability is to limit applied potentials below 0.6 V versus Ag/AgCl to avoid over-oxidation [12,13]. Studies carried out on the effect of potential on polyaniline have shown that over-oxidation occurs with the generation of degradation products such as quinoneimine species which accompany a great decrease in charge retention [12,14,15].

On the other hand, aniline tetramer is an appealing candidate with great potential for supercapacitors. With its shorter chain length, it is less susceptible to volumetric degradation that results from long chain swelling during the charging and discharging processes. As Yan *et al.* [13] have demonstrated, the aniline tetramer/graphene oxide composite exhibits good cycling

stability after 2000 cycles using a potential window of −0.05 to 0.7 V versus Ag/AgCl. However, further reduction in the fluctuation of capacitance retention is only achieved with the narrowed potential window of 0 to 0.55 V versus Ag/AgCl [13]. The goal of this study is to use Matrix-Assisted Laser Desorption Ionization Time-of-Flight Mass Spectroscopy (MALDI TOF MS) to investigate any side products produced during cycling stability tests of aniline tetramer under different potential windows. Insights into the degradation mechanism of aniline tetramer can be gained and correlated with device operation which can greatly help in the design of future devices. In addition, a fundamental understanding of the response of aniline tetramer during oxidative or reductive cycling with varying potential can be achieved.

## MATERIALS AND METHODS

### *Synthesis of Graphene Oxide*

In an ice bath, 20 g of graphite (ASBURY 3775, Warren, NJ, USA) was stirred for 20 min in pre-chilled concentrated sulfuric acid (Fisher, Waltham, MA, USA). $KMnO_4$ (Fisher, Waltham, MA, USA) (120 g) was added over the course of 30 min to maintain the reaction temperature below 15 ℃. After an additional 30 min of stirring the reaction mixture, ice was removed from the ice bath. The reaction was stirred for another 3 h in a water bath and quenched with 6 kg of crushed ice and 120 mL of 30% $H_2O_2$ (Fisher, Waltham, MA, USA). Synthesized graphene oxide crashed out after 24 h. Three washes with 10% HCl (Fisher, Waltham, MA, USA) and five washes with distilled water were carried out for initial purification. The graphene oxide was then further purified using dialysis for two weeks.

*Synthesis of Aniline Tetramer [16]*

First 0.8 g of *N*-phenyl-1,4-phenylenediamine (Sigma Aldrich, St. Louis, MO, USA) was dispersed in chilled 1.0 M HCl solution for 30 min. Then 1.4 g of ferric chloride (Merck, Elkton, VA, USA) was added in one addition and the solution was continuously stirred for an additional 2 h while ice was added to the ice bath to maintain the temperature at approximately 0 ℃. The product was collected via centrifugation, de-doped with ammonium hydroxide, and continuously washed with a water and ethanol solution (1:3) for a minimum of 10 times. The purity of the product was confirmed via MALDI TOF MS.

*Construction of Symmetric Devices*

A solution of aniline tetramer was dispersed in ethanol and mixed with a solution of graphene oxide and carboxymethylcellulose/styrene-butadiene binder (MTI Corp., Richmond, CA, USA) through multiple sonication steps. The ratio of aniline tetramer to graphene oxide is maintained at a 5:1 ratio by weight. The ratio of total active material, aniline tetramer and graphene oxide to polymer binder is maintained at a 9:1 ratio by weight. The prepared solution was drop-cast onto 1.5 cm by 2 cm graphite foils with a controlled loading of 0.9 mg/cm$^2$ and air dried. Copper tape served as the electrical connector and isolated from the electrolyte with Kapton tape. Supercapacitor devices were assembled with prepared slides, separator, 1.0 M $H_2SO_4$ electrolyte and secured with Kapton tape. All the cyclic voltammetry measurements were carried out using a Bio-Logic VMP3 potentiostat. Three-electrode measurements were carried out using platinum mesh as the counter electrode and a Ag/AgCl reference electrode.

*Measurements*

For zeta-potential measurements, the pH of the polyaniline or aniline tetramer solution was tuned by adding NaOH. Values of pH were determined using a pH meter (HANNA, HI9318, Woonsocket, RI, US). The DTS cell was placed in a Malvern Zetasizer (Nano ZS 3600, Worcestershire, UK) for measuring the zeta potential.

Mass spectra for devices were collected by carefully scraping materials off current collectors. The analyte was dissolved in a mixture of ethanol and dimethyl sulfoxide (1:1) solution. A matrix solution was prepared which contained 10 mg of 2,5-dihydroxybenzoic acid (DHB) dissolved in 50 μL of acetonitrile and 50 μL of 10% trifluoroacetic acid (TFA) in water. Equal volumes of each solution were pipetted, mixed and dried on the MALDI TOF plate. Spectra shown in Figure 5-3 were acquired with an Applied Biosystems Voyager-De-STR MALDI TOF. Subsequent spectra were acquired with a Bruker UltraFlex MALDI TOF (Bruker Daltonics Inc., Billerica, MA, US). The UV–vis spectra were taken on a Shimadzu UV-3101 PC UV–vis-NIR Scanning Spectrophotometer with quartz cuvettes. The Scanning electron microscope (SEM) images were taken on an FEI Nova 230 (FEI, Hillsboro, OR, USA).

## RESULTS AND DISCUSSION

*Polyaniline and Aniline Tetramer*

Aniline tetramer, the smallest representative unit of polyaniline [17], exhibits very similar redox and doping chemistry to polyaniline. Figure 5-1a illustrates the structures of the different oxidation states of aniline tetramer and the corresponding redox transitions. This is also illustrated through the electrochemical characterization of aniline tetramer in the solid state. Figure 5-1b shows the cyclic voltammetry (CV) plots obtained with varying scan rates in a

three-electrode configuration using a potential window of −0.05 to 0.9 V vs. Ag/AgCl. In each of the CV curves, two redox peaks are observed during scans which correspond to the transitions between the three possible oxidation states; thus it is comparable to polyaniline [18]. The insulating emeraldine base (EB) state of aniline tetramer can be doped with acids to achieve the electrically conductive state known as emeraldine salt (ES). UV–vis spectra show the same doping chemistry for both polyaniline (solid lines) and aniline tetramer (dotted lines) in *N*-methyl-2-pyrrolidone (Figure 5-2a). The absorption peaks at around 600 nm for undoped polyaniline and aniline tetramer are attributed to the benzenoid-to-quinoid transition [19–21]. The emerging peaks at around 400 nm after acid doping are the characteristic peaks for bipolarons [22,23]. In solution, both aniline tetramer and polyaniline exhibit high zeta potential, conferring stable charged species at low and high pH values, as shown in Figure 5-2b. With almost identical doping chemistry and properties as polyaniline, aniline tetramer could be simply considered as polyaniline without its polymer nature.

*Cycled Redox of Aniline Tetramer in Solution*

In the experiments described above, aniline tetramer and polyaniline were shown to exhibit similar properties and chemistries. While polymerization from aniline monomer is commonly used to synthesize polyaniline, to the best of our knowledge, mass spectrum analysis on aniline tetramer electropolymerization under different potentials has not yet been reported. To understand the dependence of electropolymerization on the applied potential, repeated CV cycling tests were carried out on aniline tetramer dissolved in solution. This set-up allows the free movement of molecules and an increase in collision frequency. Experiments were carried out with 10 mM aniline tetramer with 1.0 M tetrabutylammonium perchlorate as the conducting electrolyte and 1.0 mM perchloric acid in acetonitrile. The addition of perchloric acid serves as a

proton source so the deprotonation of aniline tetramer during oxidation can become reversible. A potentiodynamic technique was used where the applied potential is continuously varied in a cyclic manner within a potential window of 0 to 0.8 V, 0 to 1.0 V, and 0 to 1.2 V versus Ag/AgCl. These potentials were chosen so that aniline tetramer was charged with increasing levels beyond its different redox peaks in each experiment. Figure 5-3 shows the CV plots at cycles of 10, 50, and 100 to display the general trend during the course of electropolymerization. Note that the redox peaks observed in the spectra are less pronounced as aniline tetramer must diffuse to the working electrode for redox reactions to take place. In addition, studies done by Shacklette et al. have shown that through the use of crystalline active materials, sharper redox peaks were observed [24].

MALDI TOF data collected after 100 CV scans at scan rates of 5 mV/s with varying potential windows are also shown in Figure 5-3. MALDI TOF is an attractive technique due to the ease of spectral interpretation and peak assignments permitted by the soft ionization method which greatly reduces the fragmentation of the molecules [25]. Peaks corresponding to aniline oligomers are labeled as different n-mers in parenthesis along with the detected $m/z$ values. It can be seen that the distribution of intermediate oligomer peaks shifts towards higher n-mers with increasing potential windows. In the potential window of 0 to 0.8 V, the aniline octamer ($m/z$ = 727) has the highest percent intensity, whereas aniline 10-mer ($m/z$ = 909) is the most dominant peak observed for the window from 0 to 1.2 V. With a potential window of 1.0 V, higher-order n-mers such as 14-mer and 16-mer were produced with low-percent intensity and lower-order n-mers were observed as the predominant species. For the distribution of peaks to shift to predominantly 10-mers, an even larger potential window of 1.2 V was required.

The trend in mass spectrum peaks supports the established notion that continuous polymerization of conjugated intermediates occurs only through increasing the reactivity of the system by applying a higher potential window. This is necessitated by the decrease in reactivity of longer-chain-length monomers. In addition, with increasing chain lengths, the acidity of the protons in charged and resonance-stabilized intermediates decreases, which hinders deprotonation and re-aromatization without sufficient energy in the system [26]. Closer examination of mass spectrum peaks shows the formation of oligomers with predominantly even numbers of aniline units. These data suggest that the chain breakage of oligomers must have occurred during the process of repeated CV cycling tests. If only the direct coupling of molecules had occurred, higher-order aniline oligomer peaks should only consists of aniline octamer, 12-mer and 16-mer. Instead, the oligomer peaks consistently differ by two aniline units. Note that chain breakage must also have occurred down to one aniline unit during polymerization to explain the appearance of the 5-mer in the 0 to 1.0 V potential window mass spectrum.

As shown above, the aniline tetramer polymerizes to a distribution of higher-order oligomer species when a potential is applied in a cyclic manner between 0 and the end-switching potentials specified above (0.8, 1.0 and 1.2 V). In each CV scan, the species in solution were oxidized and reduced through all three of the redox states. In order for aniline tetramer to be used in a supercapacitor application, the stability of the material as a function of the potential must be optimized. Therefore, symmetric supercapacitor devices were fabricated with aniline tetramer, predominantly in the EB state, and a graphene oxide composite to understand the experimental parameters of the potential and solid-state setup on aniline tetramer electropolymerization.

*Aniline Tetramer as the Active Material in Supercapacitors*

The active material containing aniline tetramer, graphene oxide flakes and polymer binders was deposited on graphite foil. Graphene oxide was added to provide aniline tetramer with a scaffold during repeated redox cycles, while the polymer binder was used to prevent the dissolution of the material. Graphene oxide was used instead of graphene in the fabrication of the electrodes because the relative hydrophilicity of graphene oxide allows for a more straightforward solution processing procedure and creates a more homogeneous solution of active material for drop-casting. The smooth and conductive film created can be seen in Figure 5-4a. A cross-sectional view of the electrode clearly shows the active material deposited on a graphite foil (Figure 5-4b). However, the expanded image does not show a typical layered graphene/graphene oxide structure [27] due to the relatively small amounts of graphene oxide added into the fabrication of the active material (Figure 5-4c).

In a symmetric two-electrode setup, an electrodynamic equilibrium exists between the two identical electrodes, the applied potential should therefore be theoretically equally distributed over both electrodes. In a typical pseudocapacitor device setup, the material on the positive electrode is oxidized, while the negative electrode material is reduced during charging until the potential difference established between the two electrodes is equal to the set potential. Specifically in the fabricated devices of this study, transitions from the EB to the PNG (pernigraniline) state occur for one electrode during device charging, while the EB state is reduced to the LEB (leucoemeraldine) state for the other electrode. During device discharging, the PNG and LEB states are converted back to the EB state on the respective electrodes (Figure 5-5).

The potential windows used for the devices were chosen to investigate the stability of the aniline tetramer with increasing levels of charging past the respective redox peaks. Figure 5-6 shows the CV graphs and MALDI TOF spectra for both sides of the electrode of three different devices with potential windows of 0 to 0.8 V, 0 to 1.0 V, and 0 to 1.2 V. The mass spectra peak with an *m*/*z* value of 366 corresponds to the EB state of the protonated aniline tetramer. For ease of spectra interpretation, only the CV spectra collected at 500, 1000, and 1500 cycles for each device with different potential windows are shown. In each set of CV curves, the redox peak observed demonstrates the Faradaic processes occurring in the system. The observed current plateau past the redox peak signifies a double-layer charge storage mechanism and is found in each device. There is a gradual shift in the anodic redox peak towards less positive potentials accompanying a decrease in the current intensity with the increasing cycle number. This suggests diminishing Faradaic charge/discharge properties with the degradation of some redox-active aniline tetrameric material. After 1500 cycles, the device with a potential window of 0.8 V retains 75.2% of its initial capacitance, the 1.0 V device maintains 62.9%, while only 58.6% remains for the 1.2 V device. In all the mass spectra (Figure 5-6), the aniline tetramer mass peak is still observed with a high percent intensity. This can be attributed to the dissolution of the electrode material during the course of electrochemical studies which is observed directly after disassembling the supercapacitor device for MALDI TOF testing. With the loss of charge and diffusion-controlled charge transport upon material dissolution, much of the aniline tetramer may have been prevented from undergoing redox reactions. The relatively rapid deterioration of the device performance can also be attributed to the dissolution of the active material.

The middle and right columns of Figure 5-6 show the MALDI TOF spectra of electrode side A and B upon 10,000 repeated CV cycles. A quick comparison between the mass spectra from

both electrodes for the three devices shows an exceedingly different trend in the *m*/*z* values detected. Peaks with an *m*/*z* value as high as 1260 and 1259 are shown for electrode A of the devices with 1.0 V and 1.2 V potential windows, respectively. This peak can be assigned to the 14-mer aniline oligomer. In contrast, peaks signifying breakage of the aniline tetramer chains are observed for electrode side B. A 72.1% intensity peak with an *m*/*z* value of 219 is observed for the device with a 0.8 V potential window. A peak at *m*/*z* of 219 is observed in all spectra collected for electrode side B with varying intensities. Mass spectra corresponding to the electrodes for devices with potential windows of 1.0 and 1.2 V, respectively, demonstrate the effects of over-oxidation and over-reduction for aniline tetramer material. With repeated CV tests, the aniline tetramer undergoes degradation and solid-state polymerization on the different electrodes. In addition, the observance of higher-order aniline oligomer peaks for electrode A of 1.0 and 1.2 V as opposed to the 0.8 V device implies that similar to electropolymerization in solution, solid-state electropolymerization can only occur when sufficient energy is provided in the form of an increasing potential window. Likewise, shorter distances between chains could facilitate cross-linking or branching of aniline tetramer chains [28].

As demonstrated by mass spectrometry analysis, a major contributor to the poor cycling stability of the devices with large potential windows is the electropolymerization and degradation of the aniline tetramer material. However, the lack of polymerization for electrode side A and the significant degradation of material observed for electrode side B of the device with the potential window 0 to 0.8 V suggest an even more important general property for members belonging to the conducting polymer family. Specifically, the asymmetry in the capabilities of the aniline tetramer to undergo oxidative cycling and reductive cycling compromises the overall device cycling stability in a symmetric configuration. The relative instability of conducting polymers in

the reduced state compared to their oxidized state has also been observed in studies carried out on other types of conducting polymers [29,30]. In the case of polythiophene, very negative potentials are required for reversible n-doping [2]. This potential is generally beyond the potential window range chosen for supercapacitor applications due to the limitation imposed by the stability of commonly used electrolytes [31]. Therefore, in symmetric devices, only reversible oxidative redox processes can take place. Furthermore, Borjas and Buttry have investigated the inconsistencies in the rigidity of polythiophene film during film growth under the application of negative potentials compared to positive potentials, which suggests instability of the film in a reduced state, and they propose the cause to be chain breakage [32]. In the case of the aniline tetramer, as Figure 5-6 demonstrates, there is a relative symmetry between the oxidation and reduction potentials which are both within the limits of commonly used electrolytes in the system. The mechanism by which aniline tetramer-based devices degrade is the generation of non-conducting species as shown by the MALDI TOF spectra. An additional factor compromising the overall device cycling is the lower stability of the negative electrode when undergoing Faradaic processes compared to the positive electrode, which causes both electrodes to be somewhat p-doped after being fully discharged [33]. Future pseudocapacitor device design using aniline tetramers should therefore choose a different electrode material with a stable negative potential window range and a n-doped cycling stability comparable to the p-doped cycling stability of the aniline tetramer.

## CONCLUSIONS

In this study, the limitations of aniline tetramer in the field of supercapacitors are revealed which helps in deriving guidelines for future pseudocapacitor designs. Although it may appear that the mechanical instability of polyaniline can be ameliorated through using

shorter-chain-length aniline tetramer, here, it is observed that aniline tetramer is susceptible to polymerization when a large potential window is applied. Electropolymerization of aniline tetramer dissolved in acetonitrile was also shown to be a viable method to form long chain aniline oligomers, generating large amounts of aniline 10-mer using a potential window of 0 to 1.2 V. The advantage of charging supercapacitor devices with higher potential windows is greater energy density. However, the caveat is the instability of materials past certain potential ranges which works against a long cycle life. MALDI TOF was used to monitor the change in the aniline tetramer after cycling under different potential windows. An asymmetry was observed in the stability between n-doping and p-doping cycling processes of aniline tetramer in a real-world two-electrode device configuration, which potentially contributes to the degradation of the overall device performance, even when using a narrow potential window of 0 to 0.8 V. Therefore, future pseudocapacitor construction designs with aniline tetramer should explore using asymmetric configurations where a different material that is not only stable in the potential range of the device, but also possesses n-doping cycling stability comparable to the p-doping process of aniline tetramer, is used.

## ACKNOWLEDGMENTS

The authors thank Xin Cong for help with MALDI TOF and the NSF-CBET 1337065 grant for financial support.

## AUTHOR CONTRIBUTIONS

Rebecca L. Li synthesized aniline tetramers, fabricated aniline tetramer-based supercapacitors, and performed the experiment of electropolymerization of aniline tetramer in solutions. Cheng-Wei Lin conceived the idea, measured MALDI TOF, and UV–vis spectra. Yuanlong

Shao helped assemble devices and guided data analysis related to electrochemistry. Che Wei Chang and Fu-Kai Yao performed zeta potential testing. Matthew D. Kowal synthesized graphene oxide. Haosen Wang performed the CV testing with various scan rates. Michael T. Yeung acquired SEM images. Shu-Chuan Haung and Richard B. Kaner supervised the experiments and data analysis. All authors contributed to the paper.

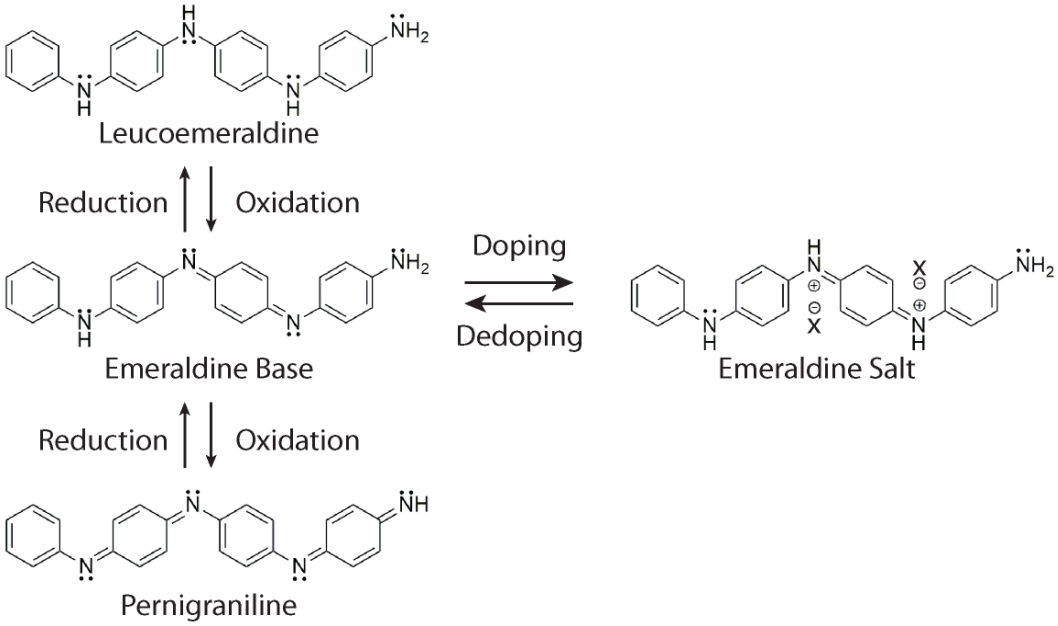


(**a**)

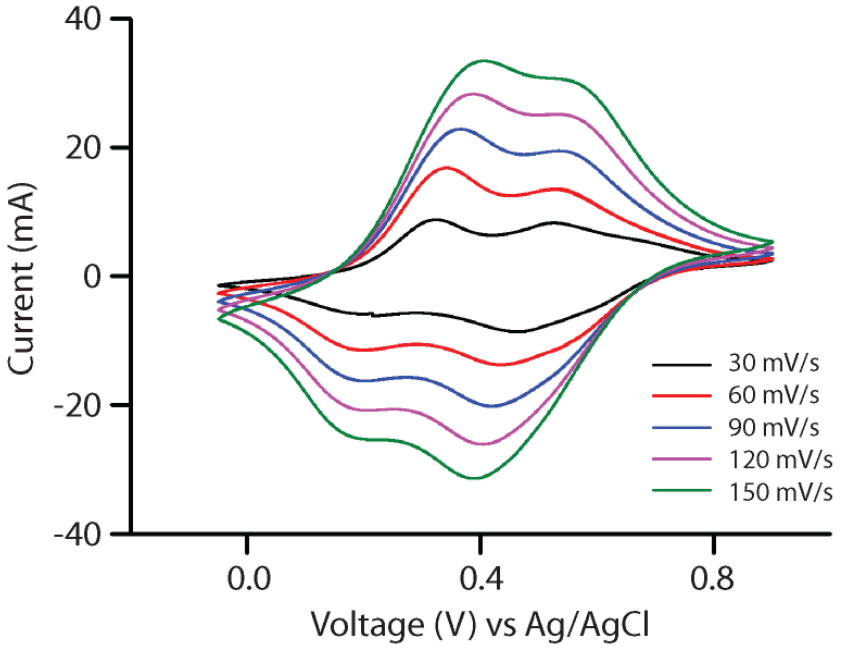


(**b**)

**Figure 5-1.** (**a**) Structures exhibiting the redox chemistry and doping properties of aniline tetramer; (**b**) cyclic voltammetry (CV) measurements on aniline tetramer film in a three-electrode configuration as a function of scan rate.

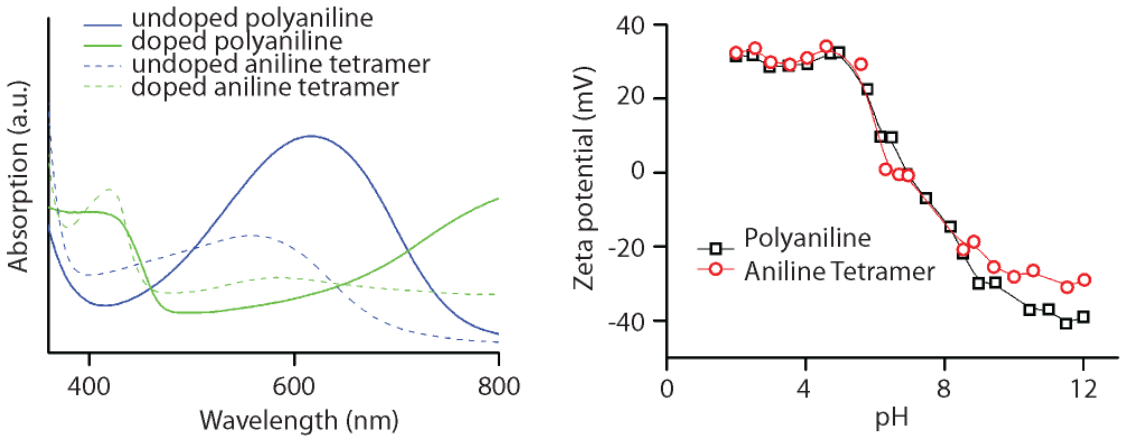


**(a)** **(b)**

**Figure 5-2.** (**a**) UV–visible spectra of polyaniline and aniline tetramer demonstrating a color change from blue to green upon doping each in its emeraldine base state; (**b**) Zeta potential spectra of polyaniline and aniline tetramer exhibiting similar characteristics as a function of pH.

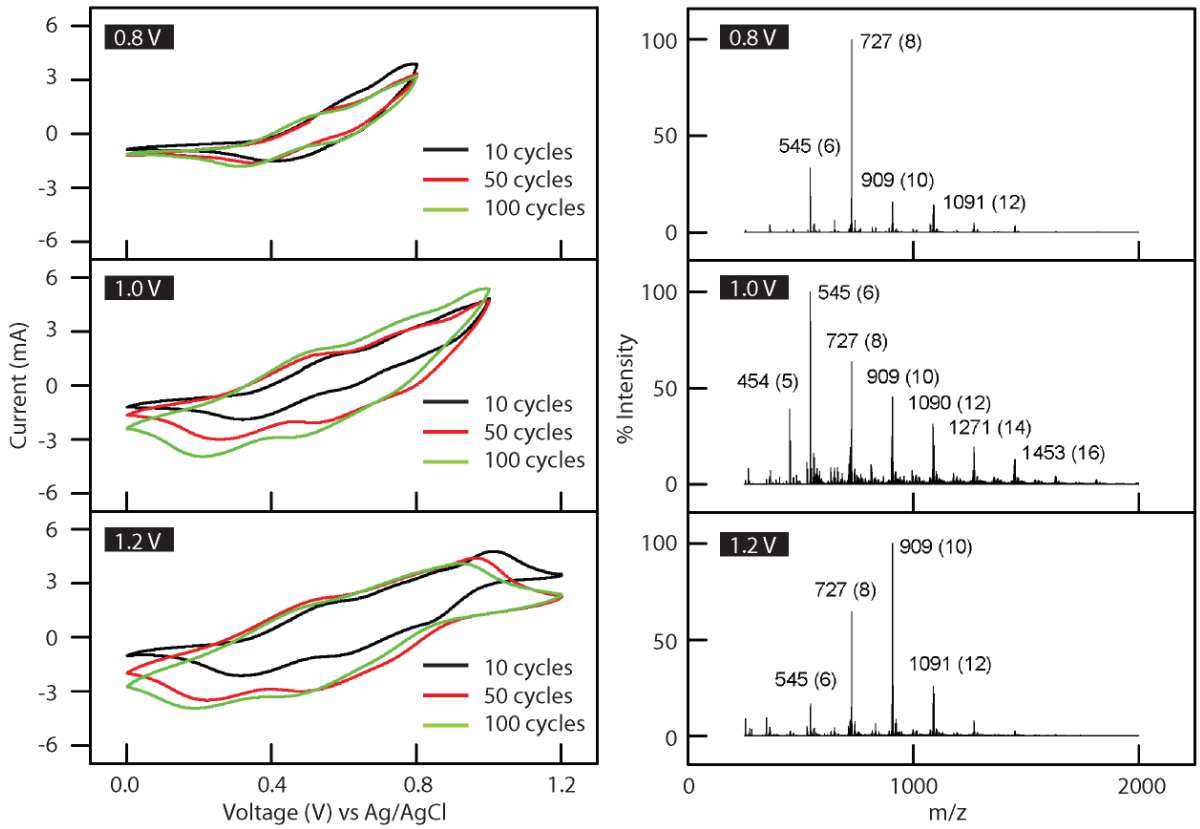


**Figure 5-3.** Electropolymerization of aniline tetramer in solution through repeated CV cycling with varying potential windows and the change in aniline oligomer distribution shown by Matrix-Assisted Laser Desorption Ionization Time-of-Flight (MALDI TOF) spectrometry.

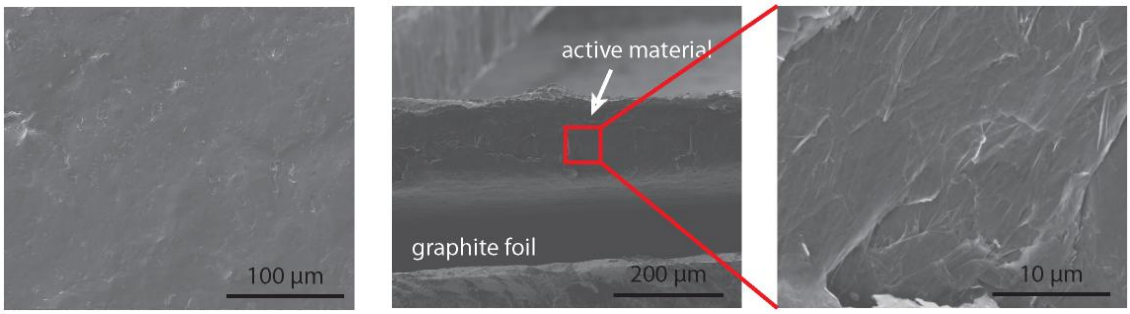


(**a**) (**b**) (**c**)

**Figure 5-4.** Scanning electron microscope (SEM) image of fabricated aniline tetramer and graphene oxide composite electrode: (**a**) top view; (**b**) cross-section of composite on current collector graphite foil; (**c**) expanded view of cross-section.

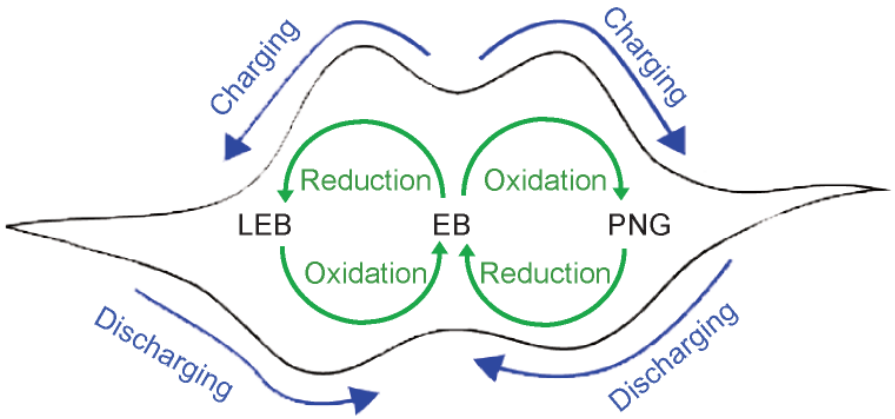


**Figure 5-5.** Schematic of the different redox transitions of aniline tetramer that occur on each electrode during device charging and discharging.

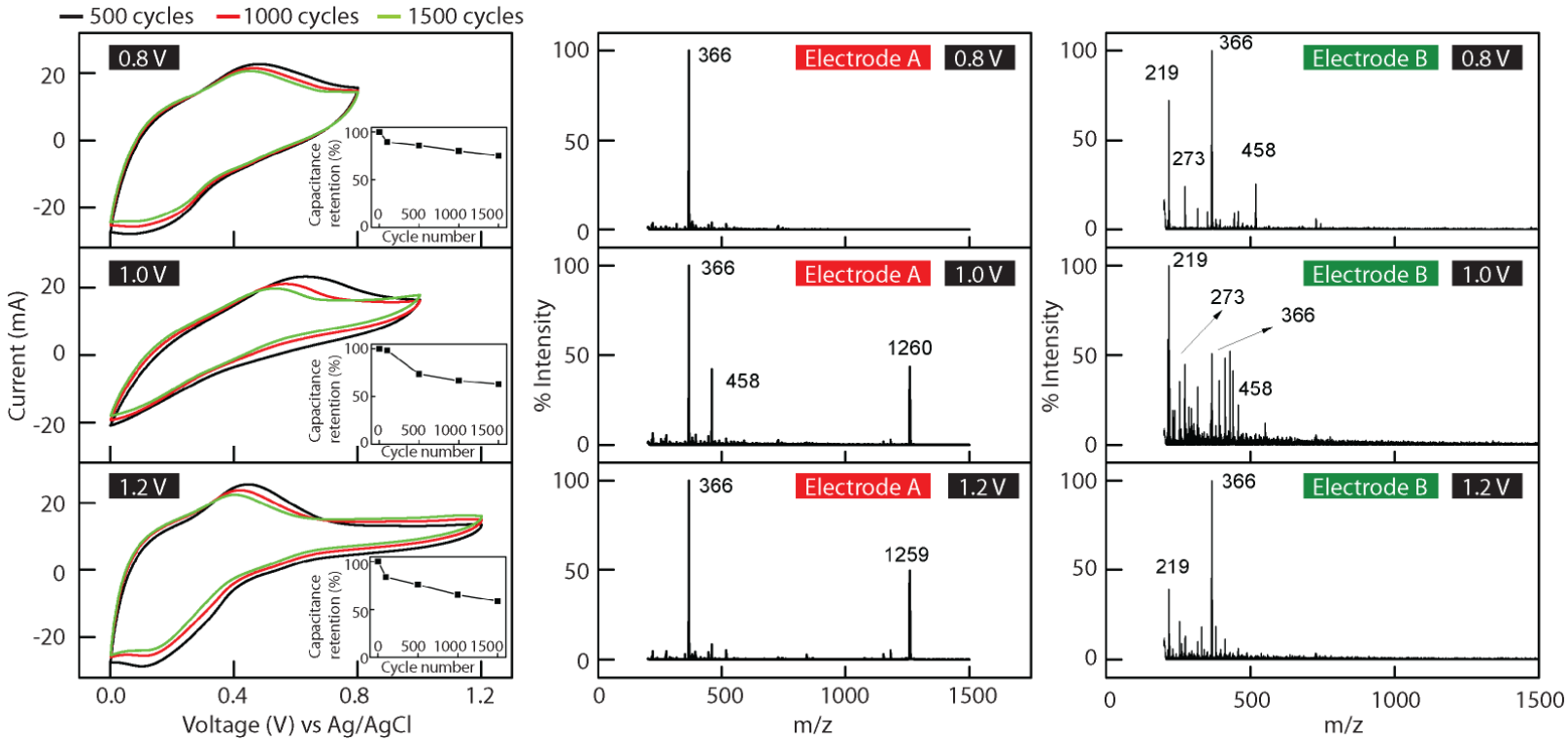


**Figure 5-6.** Select cyclic voltammetry spectra, taken throughout device cycling tests under different potential windows with their corresponding MALDI TOF spectra from electrodes A and B, showing peak polymerization and degradation after cycling. Inserts in the CV diagram plots show the percent capacitance retention as a function of cycle number.

## REFERNCES


1. Biswas, S.; Drzal, L.T. Multi layered nanoarchitecture of graphene nanosheets and polypyrrole nanowires for high performance supercapacitor electrodes. *Chem. Mater.* **2010**, *22*, 5667–5671.
2. Laforgue, A.; Simon, P.; Sarrazin, C.; Fauvarque, J.F. Polythiophene-based supercapacitors. *J. Power Sources* **1999**, *80*, 142–148.
3. Zhang, K.; Zhang, L.L.; Zhao, X.S.; Wu, J.S. Graphene/polyaniline nanofiber composites as supercapacitor electrodes. *Chem. Mater.* **2010**, *22*, 1392–1401.
4. Shi, Y.; Peng, L.L.; Ding, Y.; Zhao, Y.; Yu, G.H. Nanostructured conductive polymers for advanced energy storage. *Chem. Soc. Rev.* **2015**, *44*, 6684–6696.
5. Yu, Z.N.; Tetard, L.; Zhai, L.; Thomas, J. Supercapacitor electrode materials: Nanostructures from 0 to 3 dimensions. *Energy Environ. Sci.* **2015**, *8*, 702–730.
6. Herod, T.E.; Schlenoff, J.B. Doping-induced strain in polyaniline—Stretch electrochemistry. *Chem. Mater.* **1993**, *5*, 951–955.
7. Zhao, Y.; Liu, B.R.; Pan, L.J.; Yu, G.H. 3D nanostructured conductive polymer hydrogels for high-performance electrochemical devices. *Energy Environ. Sci.* **2013**, *6*, 2856–2870.
8. Fu, H.; Du, Z.J.; Zou, W.; Li, H.Q.; Zhang, C. Carbon nanotube reinforced polypyrrole nanowire network as a high-performance supercapacitor electrode. *J. Mater. Chem. A* **2013**, *1*, 14943–14950.
9. Liu, T.Y.; Finn, L.; Yu, M.H.; Wang, H.Y.; Zhai, T.; Lu, X.H.; Tong, Y.X.; Li, Y. Polyaniline and polypyrrole pseudocapacitor electrodes with excellent cycling stability. *Nano Lett.* **2014**, *14*, 2522–2527.
10. Shen, J.L.; Yang, C.Y.; Li, X.W.; Wang, G.C. High-performance asymmetric supercapacitor based on nanoarchitectured polyaniline/graphene/carbon nanotube and activated graphene electrodes. *ACS Appl. Mater. Interfaces* **2013**, *5*, 8467–8476.

11. Wu, Q.; Xu, Y.X.; Yao, Z.Y.; Liu, A.R.; Shi, G.Q. Supercapacitors based on flexible graphene/polyaniline nanofiber composite films. *ACS Nano* **2010**, *4*, 1963–1970.
12. Kabumoto, A.; Shinozaki, K.; Watanabe, K.; Nishikawa, N. Electrochemical degradation of polyaniline. *Synth. Met.* **1988**, *26*, 349–355.
13. Yan, J.; Yang, L.P.; Cui, M.Q.; Wang, X.; Chee, K.; Nguyen, V.C.; Kumar, V.; Sumboja, A.; Wang, M.; Lee, P.S. Aniline tetramer-graphene oxide composites for high performance supercapacitors. *Adv. Energy Mater.* **2014**, *4*, 7.
14. Fusalba, F.; Gouerec, P.; Villers, D.; Belanger, D. Electrochemical characterization of polyaniline in nonaqueous electrolyte and its evaluation as electrode material for electrochemical supercapacitors. *J. Electrochem. Soc.* **2001**, *148*, A1–A6.
15. Santino, L.M.; Lu, Y.; Acharya, S.; Bloom, L.; Cotton, D.; Wayne, A.; D'Arcy, J.M. Enhancing cycling stability of aqueous polyaniline electrochemical capacitors. *ACS Appl. Mater. Interfaces* **2016**, *8*, 29452–29460.
16. Wang, Y.; Tran, H.D.; Liao, L.; Duan, X.F.; Kaner, R.B. Nanoscale morphology, dimensional control, and electrical properties of oligoanilines. *J. Am. Chem. Soc.* **2010**, *132*, 10365–10373.
17. Wang, Y.; Tran, H.D.; Kaner, R.B. Applications of oligomers for nanostructured conducting polymers. *Macromol. Rapid Commun.* **2011**, *32*, 35–49.
18. D'Arcy, J.M.; Tran, H.D.; Tung, V.C.; Tucker-Schwartz, A.K.; Wong, R.P.; Yang, Y.; Kaner, R.B. Versatile solution for growing thin films of conducting polymers. *Proc. Natl. Acad. Sci. USA* **2010**, *107*, 19673–19678.
19. Cao, Y.; Li, S.Z.; Xue, Z.J.; Guo, D. Spectroscopic and electrical characterization of some aniline oligomers and polyaniline. *Synth. Met.* **1986**, *16*, 305–315.

20. Epstein, A.J.; Ginder, J.M.; Zuo, F.; Bigelow, R.W.; Woo, H.S.; Tanner, D.B.; Richter, A.F.; Huang, W.S.; Macdiarmid, A.G. Insulator-to-metal transition in polyaniline. *Synth. Met.* **1987**, *18*, 303–309.
21. Stafstrom, S.; Bredas, J.L.; Epstein, A.J.; Woo, H.S.; Tanner, D.B.; Huang, W.S.; Macdiarmid, A.G. Polaron lattice in highly conducting polyaniline—Theoretical and optical studies. *Phys. Rev. Lett.* **1987**, *59*, 1464–1467.
22. Bredas, J.L.; Street, G.B. Polarons, bipolarons, and solitons in conducting polymers. *Accounts Chem. Res.* **1985**, *18*, 309–315.
23. Wang, C.L.; Su, Z.B.; Martino, F. Bipolaron dynamics in nearly degenerate quasi-one-dimensional polymers. *Phys. Rev. B* **1986**, *33*, 1512–1515.
24. Shacklette, L.W.; Wolf, J.F.; Gould, S.; Baughman, R.H. Structure and properties of polyaniline as modeled by single-crystal oligomers. *J. Chem. Phys.* **1988**, *88*, 3955–3961.
25. Dolan, A.R.; Wood, T.D. Analysis of polyaniline oligomers by laser desorption ionization and solventless maldi. *J. Am. Soc. Mass Spectrom.* **2004**, *15*, 893–899.
26. Heinze, J.; Frontana-Uribe, B.A.; Ludwigs, S. Electrochemistry of conducting polymers-persistent models and new concepts. *Chem. Rev.* **2010**, *110*, 4724–4771.
27. Yang, C.Y.; Shen, J.L.; Wang, C.Y.; Fei, H.J.; Bao, H.; Wang, G.C. All-solid-state asymmetric supercapacitor based on reduced graphene oxide/carbon nanotube and carbon fiber paper/polypyrrole electrodes. *J. Mater. Chem. A* **2014**, *2*, 1458–1464.
28. Wei, Y.; Hsueh, K.F.; Jang, G.W. A study of leucoemeraldine and the effect of redox reactions on the molecular-weight of chemically prepared polyaniline. *Macromolecules* **1994**, *27*, 518–525.
29. Arbizzani, C.; Mastragostino, M.; Meneghello, L. Polymer-based redox supercapacitors: A comparative study. *Electrochim. Acta* **1996**, *41*, 21–26.

30. Snook, G.A.; Kao, P.; Best, A.S. Conducting-polymer-based supercapacitor devices and electrodes. *J. Power Sources* **2011**, *196*, 1–12.
31. Rudge, A.; Davey, J.; Raistrick, I.; Gottesfeld, S.; Ferraris, J.P. Conducting polymers as active materials in electrochemical capacitors. *J. Power Sources* **1994**, *47*, 89–107.
32. Borjas, R.; Buttry, D.A. Eqcm studies of film growth, redox cycling, and charge trapping of normal-doped and para-doped poly(thiophene). *Chem. Mater.* **1991**, *3*, 872–878.
33. Bryan, A.M.; Santino, L.M.; Lu, Y.; Acharya, S.; D'Arcy, J.M. Conducting polymers for pseudocapacitive energy storage. *Chem. Mater.* **2016**, *28*, 5989–5998.

# CHAPTER 6. DIRECT GRAFTING OF TETRAANILINE VIA PERFLUOROPHENYLAZIDE PHOTOCHEMISTRY TO CREATE ANTIFOULING, LOW BIO-ADHESION SURFACES

"Reprinted from Lin, C.-W.; Aguilar, S.; Rao, E.; Mak, W.H.; Huang, X.; Jun, D.; He, N.; Chen, D.; Curson, P.; McVerry, B.T.; Hoek, E.M.V.; Huang, S.-C.; Kaner, R.B. "Direct Grafting of Tetraaniline via Perfluorophenylazide Photochemistry to Create Antifouling, Low Bio-Adhesion Surfaces" *Chemical Science*, 2019, 10, 4445-4457. DOI: 10.1039/C8SC04832K"

## ABSTRACT

Conjugated polyaniline has shown anticorrosive, hydrophilic, antibacterial, pH-responsive, and pseudocapacitive properties making it of interest in many fields. However, *in situ* grafting of polyaniline without harsh chemical treatments is challenging. In this study, we report a simple, fast, and non-destructive surface modification method for grafting tetraaniline (TANI), the smallest conjugated repeat unit of polyaniline, onto several materials via perfluorophenylazide photochemistry. The new materials are characterized by nuclear magnetic resonance (NMR) and electrospray ionization (ESI) mass spectroscopy. TANI is shown to be covalently bonded to important carbon materials including graphite, carbon nanotubes (CNTs), and reduced graphene oxide (rGO), as confirmed by transmission electron microscopy (TEM). Furthermore, large area modifications on polyethylene terephthalate (PET) films through dip-coating or spray-coating demonstrate the potential applicability in biomedical applications where high transparency, patternability, and low bio-adhesion are needed. Another important application is preventing biofouling in membranes for water purification. Here we report the first oligoaniline grafted water filtration membranes by modifying commercially available polyethersulfone (PES) ultrafiltration (UF) membranes. The modified membranes are hydrophilic as demonstrated by

captive bubble experiments and exhibit extraordinarily low bovine serum albumin (BSA) and *Escherichia coli* adhesions. Superior membrane performance in terms of flux, BSA rejection and flux recovery after biofouling are demonstrated using a cross-flow system and dead-end cells, showing excellent fouling resistance produced by the *in situ* modification.

## INTRODUCTION

Polyaniline, a well-studied conjugated polymer known for its simple acid/base doping/de-doping chemistry and facile synthesis,[1–5] has been widely applied to chemical gas sensors for ammonia detection,[4,6] chemical and electrochemical actuators,[7,8] non-volatile memory devices,[9] supercapacitors,[10] water filtration membranes,[11] anticorrosive coatings,[12] tissue engineering,[13] among other uses.[14,15] In the realm of coatings,[16,17] and membranes,[11,18–21] researchers often blend polyaniline with other matrix materials in order to obtain the hydrophilic and antibacterial characteristics of polyaniline at the surface.[22–26] However, low solubility and gelation of polyaniline during processing, have hindered the development of improved materials.[27,28] Therefore, grafting polyaniline onto other materials is crucial in order to achieve more robust coatings and functionalize surfaces for enhanced performance.[29,30] Due to difficulties in processing polyaniline, chemically grafting polyaniline is often performed by functionalizing end groups with amines,[31–33] amidation reactions with carboxylic groups,[34–37] diazotization reactions with diazonium salts,[38–40] and nitrogen doping[41] followed by oxidative polymerization. However, such modification processes require chemically inert and mechanically strong materials in order to sustain the harsh pretreatments. In addition, the abovementioned methods are only suitable for materials within the micro- and nanoscale regime, which limit the feasibility of modifying large surfaces with such hydrophilic, pH-responsive, and antibacterial polyaniline.

Herein, we report a newly synthesized molecule, 4-azidotetrafluorobenzoyl tetraaniline (ATFB-TANI), which can be used to couple tetraaniline (TANI) to other materials. TANI, the smallest representative repeat unit of polyaniline, is known to have similar properties to polyaniline, but can be readily dissolved in common organic solvents for facile processing.[42–44] This bridging group is based on the solid foundation of perfluorophenylazide photochemistry,[30] which can undergo addition and insertion reactions when exposed to UV light.[45–49] Thus, with the assistance of perfluorophenylazide, TANI can now be covalently photografted onto carbon nanotubes (CNTs) and reduced graphene oxide (rGO) without pretreatments. Furthermore, large area modifications through dip-coating and spray-coating on polyethylene terephthalate (PET) films with high transparencies and low bio-adhesions show great potential to apply this material for biomedical uses.

Another application that could greatly benefit from a coating that prevents bio-fouling is ultrafiltration (UF) membranes. Typical commercial UF membranes are made of polyethersulfone (PES), polyvinylidene fluoride (PVDF), polysulfone (PSF), polypropylene (PP), or polyurethane (PU).[50,51] The hydrophobic nature of these matrix polymers leads to protein adherence to their surfaces and the proliferation of bacteria.[52,53] Additionally, the accumulation of both organic and inorganic foulants on membrane surfaces over time, *i.e.* fouling, can severely lower the permeation flux and the filtration efficiency, often damaging the membranes.[54–58] In order to surmount these problems, scientists and engineers have already developed a couple rule-of-thumbs for designing antifouling membranes. First, hydrophilic membrane surfaces have been suggested as a method to form a few-molecule-thick hydration nanolayer, which may prevent foulant adhesions and cake formation. Second, stimuli-responsive polymers grafted onto

membrane surfaces can undergo a coil-to-globule transition to "release" the accumulated foulants when exposed to a stimulus during washing cycles.[50,51,59,60]

To date, all the reported polyaniline-based filtration membranes are formed by blending polyaniline with base polymers. For instance, in 2008, Fan *et al.* reported a UF membrane made by blending polyaniline with PSF, doubling the pure water flux compared to a pristine PSF membrane and lessening the flux decline.[11,18] Since then, other researchers have reported UF membranes composed of polyaniline blended with base polymer, including PES, PSF, PVDF, *etc*.[21,61–65] Blending-in polyaniline enhances the membrane's hydrophilicity, thereby decreasing the flux decline and improving the flux recovery. Even more hydrophilic membranes were reported by further mixing CNTs into polyaniline-blended UF membranes; however, bovine serum albumin (BSA) rejection decreased due to the formation of larger porosity in these membranes.[66–68] McVerry *et al.* and Zhao *et al.* incorporated self-doped sulfonated polyaniline (SPANI) into PSF and PVDF UF membranes, respectively, with superior hydrophilicity. The zwitterionic nature of SPANI resulted in a high flux recovery and high BSA rejection rate.[20,69]

The blending strategy mentioned above is straightforward but has several limitations: 1) The processability of polyaniline during membrane casting needs to be improved as polyaniline only appears dispersible in dimethyl sulfoxide (DMSO) and *N*-methyl-2-pyrrolidone (NMP). 2) The crucial pore size of the composite membranes that directly affects the water flux and rejection rate has to be tuned experimentally by trial and error. 3) The mechanical properties of the resultant composite membranes are strongly dependent on the intrinsic properties of polyaniline and the percentage blended in. As polyaniline possesses a more rigid backbone,[70,71] the flexibility of its membranes are limited. 4) The confined polyaniline chains embedded in composite membranes cannot undergo a coil-to-globule transition when treated with acids in

order to actively repel foulants. In order to graft polyaniline onto membranes or attach bridging groups to polyaniline through chemical reactions, dissolving polyaniline in DMSO or NMP is inevitable. However, DMSO and NMP are strong organic solvents that can readily dissolve and destroy the base UF membranes during the modification process. Hence, grafting polyaniline onto membrane surfaces without damaging the base UF membranes has so far been unsuccessful.

Here we report the first oligoaniline modified filtration membranes via photografting ATFB-TANI onto commercially available PES UF membranes. The modified membrane surfaces show enhanced hydrophilicity and improved performance in terms of antifouling ability, BSA rejection, and preventing bio-adhesions. This fast, facile, and non-destructive modification process offers a new route to graft conducting oligoanilines and can serve as the initiator for further polymerization as well.

## RESULTS AND DISCUSSION

In order to graft TANI onto large scale membrane surfaces without ruining the base polymer membranes, perfluorophenylazide was applied due to its fast and non-destructive photochemistry. As shown in **Figure 6-1a**, TANI and 4-azidotetrafluorobenzoic acid (ATFB) were stirred under basic conditions for 48 hours in order to complete the coupling reaction. Upon light activation, the phenylazides on ATFB-TANI undergo decomposition of nitrogen ($N_2$) to form singlet phenylnitrenes, and the highly reactive phenylnitrene radicals can undergo C=C addition and C-H and N-H insertion reactions.[72] The synthesized ATFB-TANI complex was confirmed by the peak shifts observed in $^{19}$F-NMR (**Figure 6-1c**) when compared to the ATFB starting molecule (**Figure 6-1b**), along with the electrospray ionization (ESI) spectrum with a mass observed within 0.7 ppm of the expected mass (**Figure 6-1d**). As a small molecule, ATFB-TANI can be

dissolved in a wide range of organic solvents, including toluene, tetrahydrofuran, chloroform, acetone, ethanol, acetonitrile, methanol, and NMP, as shown in **Figure 6-1e** with the color differences being attributed to solvatochromism.[42,73] The relatively high solubility of ATFB-TANI in common organic solvents compared to polyaniline indicates its advantageous processability. In this report, we chose ethanol as the solvent to carry out modifications, mainly due to its low toxicity, high solubility toward ATFB-TANI, low solubility toward polyethersulfone membranes, and high miscibility with water.

Here we demonstrate that facile surface modification using ATFB-TANI can be applied to several important materials, which specifically undergo C=C addition reactions, creating covalent bonds with phenylnitrenes after UV light exposure. In **Figure 6-2a,b**, a lab grade Petri dish made of polystyrene becomes more hydrophilic after modification as indicated by water droplets spreading out and a very faint blue color. The water droplet contact angle as measured by a goniometer decreased from 63° to 42° (**Figure 6-2c,d**). Analogously, a modified compressed graphite pellet also exhibits a decreased contact angle (**Figure 6-2f,g**) indicating increased hydrophilicity (**Figure 6-2e**). Furthermore, the ATFB-TANI molecule provides a simple way to graft TANI onto carbon nanotubes (CNTs) (**Figure 6-2h)** and reduced graphene oxide (rGO) (**Figure 6-2k)**. Conventionally, grafting polyaniline onto CNTs or GO/rGO requires surface functional groups via harsh chemical pre-treatments in order to obtain active sites for chemical grafting or polymerization.[35,41,74] Here, conducting TANI is successfully chemically grafted onto these materials via a non-destructive photochemical method (**Figure 6-2i,j,l**).

Since ATFB-TANI can dissolve in common organic solvents, large-scale modifications are possible. **Figure 6-3a** shows polyethylene terephthalate (PET) films subjected to an increasing number of dip-coatings. The coating process was performed by repeated dip-coating,

UV light exposure, and ethanol washing. Both undoped (EB) and doped (ES) PET films show a gradual decrease in the transparency as the number of coating layers is increased. The percent transmittance of both EB and ES PET films is around 95% for a monolayer, and about 80% after 15 layers of modification (**Figure 6-3b,c**). The sheet resistances of the doped conducting PET films decrease from around $10^{11}$ Ω/sq (**Figure S6-1**) to $10^{9}$ Ω/sq. (**Figure 6-3d**). The high sheet resistances may be explained by the rather sparse grafting density, and short chains of TANI that do not greatly enhance carrier hopping.[75] The modified films show similar sheet resistances, implying that the ATFB-TANI molecules grafted onto previous layers may react with those on pre-modified molecules, resulting in the loss of some conjugation for the pre-existing layers.

Spray-coating combined with stencil masks is a method often used for large scale patterning. The schematic in **Figure 6-3e** demonstrates how ATFB-TANI molecules dissolved in an ethanol solution can be airbrushed onto PET films using stencil masks to form a "UCLA" pattern. This achieves a highly transparent UCLA patterned coating after exposure to UV light and an ethanol rinse, as shown in **Figure 6-3f**. Such a facile, fast, and non-destructive modification wtih ATFB-TANI to make highly transparent coatings could prove useful for biomedical applications such as artificial skin. The idea is to prevent common infections such as those caused by *Staphylococcus epidermidis* (*S. epidermidis*).[76–78] Adhesion tests on both modified and unmodified PET films were carried out by exposure to *S. epidermidis*. The observed images with stained cells on unmodified (**Figure 6-3g**), and one, five, and ten-fold modified (**Figure 6-3h,i,j**) PET films show a readily noticeable drop in the number of cells adhered (**Figure S6-2**). A statistical bar graph reveals that the surface coverage percentage of *S. epidermidis* drops more than 50% from the unmodified to the more modified films (**Figure 6-3k**). Note that the surface coverage of *S. epidermidis* for five-fold modified PET films is significantly

lower than the one-fold ones, but similar with the ten-fold ones, indicating that the surface modification can be effective with no more than five times of treatment.

Next, we grafted TANI onto polyethersulfone (PES) UF membranes. The unmodified UF PES membranes appear white, while the modified membranes exhibit a lightblue color even after rinsing with DI water and ethanol (**Figure 6-4a**). Unlike the modification of colored materials, one can directly observe the modification of these initially transparent membranes as they develop a blue hue. The colored modification also makes any surface imperfections on the membrane readily visible (**Figure 6-4b)**. Similar to aniline oligomers and polyaniline, ATFB-TANI can undergo a doping/de-doping process by treating with acids/bases. During the doping process, the imine nitrogens in the blue emeraldine base form become protonated, forming the green emeraldine salt form with the positively charged backbone surrounded by counter-anions to balance the charge (**Figure 6-4c**).[79] The modified membrane can be reversibly protonated with acid and deprotonated with base, switching from the blue emeraldine base form to the green emeraldine salt form (**Figure 6-4d**). Note that the color change of the modified membranes takes a slightly longer time, about 3 to 5 seconds more, than protonating/deprotonating in solution. The reason is simply due to the slower diffusion rate of the dopants in solids when compared to liquids. **Figure 6-4e** shows the UV-vis spectra of both the blue emeraldine base (EB) and the green emeraldine salt (ES) forms of ATFB-TANI dissolved in DMSO. Similar to TANI, the broad peak at ~600 nm, *i.e.* the blue color, can be attributed to the benzenoid to quinoid excitation transition, while the sharper peak for emeraldine salt at ~440 nm can be attributed to the allowed optical transition from the highest occupied molecular orbital (HOMO) to the higher bipolaron state.[42,80–82]

To confirm the chemical grafting of ATFB-TANI onto the PES membrane surfaces, we performed the same modification procedure with TANI instead of ATFB-TANI in an ethanol solution. Without the assistance of azides, the TANI modified membrane after the treatment of UV light maintained its unaltered white color after rinsing with ethanol (**Figure 6-4f**). In contrast, the ATFB-TANI modified PES membrane remained blue after rinsing with ethanol, indicating that the blue color of ATFB-TANI modified membranes is not stained, and the ATFB-TANI is successfully grafted on by photochemistry. The degree of grafting (DG) of ATFB-TANI onto a membrane is 9.74±1.30 $\mu g/cm^2$, which is comparable to previous reports for the degree of grafting for other polymers ($200 < DG < 1000\ \mu g/cm^2$), in terms of the number of moles per surface area.[83,84,85] **Figure S6-3** shows a modified membrane soaked in water for nearly one year, the blue color indicates the excellent stability of the grafting. Attempting a more careful examination using attenuated total reflectance infrared (ATR-IR) spectroscopy did not show the difference between the unmodified and modified membranes (**Figure 6-5a**), likely due to the small amount of ATFB-TANI attached. Hence, a more sensitive and precise surface technique, such as X-ray photoelectron spectroscopy (XPS), was needed. The XPS spectra, as shown in **Figure 6-5b**, cannot clearly differentiate the azide signal at 406.5 eV due to the existence of a high nitrogen signal from the commercially available unmodified membranes. However, the fluorine peak at 687.6 eV is evident, revealing that a small amount of ATFB-TANI has indeed been grafted onto the membrane.[86–88]

Due to the high-water permeability of these PES membranes, their hydrophilicity was examined using a captive bubble contact angle goniometer. A previous study showed that TANI decorated polymeric films possess lower contact angles.[89] The interfacial energy of TANI/water is comparatively smaller than PES/water, resulting in more rounded air bubbles, *i.e.* lower

contact angles, for modified membranes (**Figure 6-5c**). Although the interfacial energy of modified membranes is expected to change when exposed to acids because of the protonation of the imine nitrogens, the contact angles observed were consistently around 30 degrees different between unmodified and modified membranes at various pH values, as can be seen in **Figure 6-5d**. This phenomenon can be explained by the insignificant differences in interfacial energy due to the very small amount of surface modification. The relatively more hydrophilic nature of the modified surfaces at different pH values indicates that these membranes are capable of being operated under harsh conditions. Polyaniline films may also possess increased roughness which can affect the contact angle measurement;[90] TANI, as a small molecule, slightly increases the surface roughness, from 2.72 nm to 3.49 nm for the unmodified and modified membranes, respectively (**Figure S6-4**).

To evaluate their antifouling properties, the PES membranes were subjected to a 1.0 g/L of bovine serum albumin (BSA) solution with a pressure of 50 psi. The membranes were first compacted with deionized (DI) water until the permeation flux reached equilibrium. After exposure to the 1.0 g/L BSA feed solution, the permeation flux decreased dramatically due to the formation of a cake layer during the fouling process.[51] As shown in **Figure 6-6a**, the modified membrane exhibited a smaller flux decline after 45 minutes of BSA fouling compared to the unmodified one. The reason may be the more hydrophilic surfaces created after modification; however, the improvement is not significant likely due to the high pressure (50 psi) applied. As mentioned above, the hydrophilic surfaces of the modified membranes form a few-nanometer-thick hydration layer that prevents the adhesion of foulants directly onto the membrane surfaces. Thus, the foulant BSA will experience much lower adhesion forces from the modified membranes. Hence, the modified membranes were tested with cycles of fouling and water

washes. The water wash should remove much of the accumulated BSA from the more hydrophilic membrane surfaces due to lower interaction forces and thus give a higher recovery rate. In **Figure 6-6b**, the modified membranes were repeatedly water washed for 5 minutes after 45 minutes of BSA fouling. Note that the water wash duration on the graph shows about 10 minutes because of the extra time spent on cleaning and filling the water tank. The flux recovery percentages were found to be 73.30±2.41%, 60.77±2.41%, and 56.59±0.15% for the first, second, and third fouling experiments, respectively, carried out on the modified membranes. Note that the average flux recovery of the modified membranes after three times fouling (56.59±0.15%), is still comparable to the first flux recovery of the unmodified membranes (56.35±6.45%) and other polyaniline blended membranes.[91–94] The flux recovery percentages decrease with each cycle due to the irreversible fouling that occurrs from the BSA, preventing a full recovery on both the modified and unmodified membranes.

In addition, the modified membranes possess a better BSA rejection rate of 97.53±1.12%, comparable to polyaniline composite UF membranes,[11,18,21,95,94] while the unmodified membranes possess a rejection rate of only 91.66±0.85%. Furthermore, the modified membranes have slightly higher water permeation flux compared to the unmodified membranes.[91] This counter-intuitive increase in the permeation flux is likely due to slight swelling of the PES membranes induced by their immersion in ethanol during the modification process.[96] The performances of both unmodified and modified membranes are summarized in **Table 6-1**.

Conjugated aniline oligomers can be easily protonated and deprotonated under different pH conditions. We performed fouling on modified membranes, followed by washing with water at different pH values. However, washing at different pHs did not give superior results to washing at neutral pH, indicating that the doping/de-doping of TANI did not effectively expel

BSA during the wash cycle.[97] Based on the Derjaguin-Landau-Verwey-Overbeek (DLVO) theory,[98] polyaniline nanofibers are able to form stable colloids within a pH range from 2.2 to 3.5, while forming precipitates at pH values less than 1.5 and greater than ~5.[99] The pH responsive polyaniline nanofibers swell from a coiled state to a globule state when exposed to an appropriate pH environment. However, TANI only forms a stable dispersion in a solution of pH = 1 (zeta potential equals to 14.83 mV), as shownin **Figure 6-7a** (15 hours standing)**,** and it has been observed to last for at least 6 months. The moderately destabilized TANI under pH = 0.5 and more stabilized dispersion under pH = 2 after adding 0.1 M NaCl indicate that the TANI has a very narrow pH range for being stabilized in suspension (**Figure 6-7b**). Therefore, for future research, in order for the grafted TANI molecules to be able to repel foulants merely via changes of solution pH, knowing the precise pH of the solution and the isoelectric point for the chosen foulants will be crucial.

Another key indicator for evaluating membranes is the adhesion of microorganisms and the proliferation of bacteria on the membrane surfaces. As such, we performed experiments in which both unmodified and modified PES membranes were soaked in BSA solutions, and *E. coli* cultured in Luria-Bertani broth, followed by observing the surface coverage of BSA and *E. coli* adherence under a fluorescent microscope. Intermediately modified membranes (designated 1.0 mM modified) were also used in these tests in order to examine the effects of the ATFB-TANI attachment on the UF membranes. In **Figure 6-8a** it can be seen that the modified membranes show significantly lower BSA adhesion compared to the unmodified membranes. The quantified BSA surface coverage is 4.10±0.47%, 0.148±0.077% and 0.033±0.025% for the unmodified, 1.0 mM and 2.0 mM modified membranes, respectively (**Figure 6-8b**). The extremely low adhesions are believed to be due to the hydration layer created at the surface of the hydrophilic ATFB-

TANI modified membranes. The low BSA adhesion also provides an explanation for the higher flux recovery and BSA rejection observed with the modified membranes. Note that we used pH neutral water for both membrane fouling tests and BSA adhesion testing, so the TANI is not positively charged enough to have a strong interaction with negatively charged BSA. Severe flux decline and very low flux recovery were observed when using hydrochloric acid (pH=1, 2) for membrane fouling testings.[97] On the other hand, although polyaniline has been reported as an antibacterial material,[22,65] we could not find any membrane filtration related studies with *E. coli*. As *E. coli* is known to have stronger interactions with hydrophobic materials,[100] we expected that the hydrophilic modification would prevent *E. coli* adhesion. As can be seen in **Figure 6-8d**, the live *E. coli* surface coverage for unmodified membranes is 7.66±2.12%, which drops dramatically for the 1.0 mM and 2.0 mM modified membranes to 0.242±0.216% and 0.057±0.058%, respectively. The dead *E. coli* surface coverage was found to be 5.44±2.04%, 0.396±0.275%, and 0.187±0.053%, respectively. While these results do not suggest that TANI possesses antibacterial properties, they do indicate that only a small amount of modification is needed to dramatically lessen the adherence of *E. coli* by up to two orders of magnitude.

## CONCLUSIONS

By synthesizing a novel ATFB-TANI molecule with a UV reactive azide group, a facile method for chemically grafting conjugated TANI onto important materials including graphite, carbon nanotubes, reduced graphite oxide and polymers is now available. Dip-coating or spray-coating with stencil masks leads to highly transparent, patterned, and low *S. epidermidis* adhesive PET films that show potential for low bio-adhesion coatings. Unlike conventional composite membranes, ATFB-TANI molecules can be grafted onto commercial polysulfone ultrafiltration membranes without complex pre-treatments. The TANI modified membranes exhibit increased

hydrophilic surfaces, leading to low flux decline, high flux recovery, a high rate of BSA rejection, and low BSA and *E. coli* adhesions. The design concept of the ATFB-TANI molecule may inspire other modifications for grafting a variety of conjugated oligo/polymers to create hydrophilic and low bio-adhesion surfaces or to help with other materials suffering from processability issues.

## EXPERIMENTAL SECTION

**Materials.** Polyether sulfone **(**PES) UF membranes were purchased from Synder Filtration (LX, 300 kDa). Aniline dimer, ferric chloride hexahydrate, bovine serum albumin (BSA) (heat shock fraction, pH = 7, ≥98%), sodium azide ($NaN_3$), acetone, sodium hydroxide (NaOH), methanol, triethylamine ($NEt_3$), 4-dimethylaminopyridine (DMAP), dichloromethane (DCM), ammonium hydroxide, and deuterated dimethyl sulfoxide ($d_6$-DMSO) were purchased from Sigma Aldrich. *Escherichia coli (E. coli)*, Luria-Bertani (LB) broth, and *S. Epidermidis* were purchased from ATCC. Graphite powder (SP-1 325) for making graphite pellets was purchased from Bay Carbon Inc. The multi-walled carbon nanotubes (MWCNTs) (outer diameter >50 nm; length = 10-20 μm; purity >95 wt%) were purchased from Cheap Tubes. Polystyrene Petri dishes were purchased from Fisher Scientific. Polyethylene terephthalate (PET) films (PP2950) were purchased from 3M. All chemicals were used as received.

### ATFB-TANI Synthesis.

Tetraaniline. Tetraaniline (TANI) was synthesized through a modified method.[101,102] Aniline dimer, *N*-phenyl-1,4-phenylenediamine powders (1.89 g, 7 mmol, 1 equiv.) were rapidly stirred with hydrochloric acid (50 mL, 0.1 M) for 30 min in a 250 mL round bottom flask. Ferric chloride hexahydrate (2.76 g, 15 mmol, 2.1 equiv.) was dissolved in hydrochloric acid (50 mL,

0.1 M) and quickly poured into the round bottom flask followed by an additional 50 mL of 0.1 M hydrochloric acid. The reaction was stirred at room temperature for about two hours. The precipitate was centrifuged and washed with 0.1 M hydrochloric acid multiple times (at least 3 times with 50 mL per wash) in order to fully remove iron ions. The precipitate was then mixed with ammonium hydroxide (50 mL, 2.0 M) and acetone (300 mL) for 30 min resulting in a bright blue solution. The solution turns gray if the iron ions are not completely removed during the hydrochloric acid wash. The acetone was removed using a rotory evaporator. The dispersion was then centrifuged and washed with DI water several times until the supernatant became pH neutral. The powder was collected after the precipitate was rinsed out with ethanol and air dried overnight, producing a blue solid with a 65% yield. The Matrix Assisted Laser Desorption/Ionization (MALDI) spectrum of TANI is presented in **Figure S6-5**.

4-Azidotetrafluorobenzoate. $NaN_3$ (0.154 g, 2.38 mmol, 1.07 equiv.) and pentafluorobenzoate (0.499 g, 2.21 mmol, 1 equiv.) were mixed together in a solution of acetone (20 mL) and water (7 mL) and refluxed for 10 hours. The mixture was cooled and water (20 mL) was added to form a white precipitate. The precipitate was then filtered and washed with $CHCl_3$ (3 times) and left to dry to produce a white solid (82% yield). $^{19}F$ NMR (400 MHz; $CDCl_3$): δ 138.858 (m, 2F), 151.113 (m, 2F).

4-Azidotetrafluorobenzoic acid. 4-Azidotetrafluorobenzoate (0.473 g, 2.12 mmol, 1 equiv.) was dissolved in methanol (10 mL). A 20% NaOH solution (0.8 mL) was added slowly to a stirring solution of 4-azidotetrafluorobenzoate and then stirred overnight. The reaction was next cooled to 0 ℃ in an ice bath and slowly acidified with 2 N HCl to reach a pH < 1, then extracted with $CHCl_3$ (3 times) and dried to produce a white solid (yield = 89%). $^{19}F$ NMR (400 MHz; $D_6$-acetone): δ 141.323 (m, 2F), 151.660 (m, 2F).

ATFB-TANI. 4-Azidotetrafluorobenzoic acid (0.552 g, 2.35 mmol, 1 equiv.), trimethylamine (0.260 g, 2.58 mmol, 1.1 equiv.) and 4-dimethylaminopyridine (0.287 g, 2.35 mmol, 1 equiv.) were dissolved in 10 mL of DCM. TANI (1.11 g, 3.05 mmol, 1.3 equiv.) was then added and stirred for 48 hours at room temperature. The reaction mixture was then washed with DI water (3 times). After evaporation under reduced pressure, a violet solid product (yield = 84%) was collected and used without further purification. The product was stored in the dark before use. $^{19}$F NMR (400 MHz; $D_6$-acetone): δ 137.357 (m, 2F), 150.801 (m, 2F).

**Modification.** The commercial PES membranes were soaked in DI water, renewed every few hours, for at least two days in order to remove the chemicals added for transportation and storage. First, solutions of 1.0 mM and 2.0 mM ATFB-TANI in ethanol were prepared. The unmodified membranes were quickly rinsed with ethanol in order to remove any residual water that may lead to uneven modifications. The membranes were then dipped into the ATFB-TANI ethanol solution for one minute before irradiation with a handheld UV light (254 nm) for one minute. The UV-treated membranes were rinsed with ethanol and DI water, respectively. The grafted membranes were soaked in DI water for another 24 hours before use. In order to modify the Petri dishes, 0.5 mL of 2.0 mM ATFB-TANI solution was pipetted onto a Petri dish and gently swirled. The Petri dish was exposed to UV light for 90 seconds before rinsing with ethanol several times. The graphite pellets were made by compressing graphite powders with a hydraulic press at 10,000 lb.; ~0.2 mL of 2.0 mM ATFB-TANI solution was then drop-cast on top of the pellets followed by UV treatment for one minute, rinsing with ethanol and then DI water. The multi-walled carbon nanotubes (MWCNTs) were dispersed in a 2.0 mM ATFB-TANI ethanol solution (300 μg $mL^{-1}$). The dispersion was ultrasonicated with a tip-ultrasonication processor (Ultrasonics FS-300N, 20% power) in an ice bath for 10 min. The well-dispersed

solution (2.5 mL) was exposed to UV light for 3 minutes, followed by drop-casting onto a glass slide and gentle rinsing with ethanol in order to remove the unreacted ATFB-TANIs. The TEM samples were prepared by tapping TEM grids on the glass slide. The graphene oxide (GO) was synthesized through a modified Hummer's method, as reported elsewhere.[102] As described previously,[103] a GO aqueous solution was mixed with ascorbic acid and after vacuum filtration, the ascorbic acid was rinsed out and dried in a 100 ℃ oven overnight. The reduced GO (rGO) film was ultrasonicated with 2.0 mM ATFB-TANI ethanol solution for 1 minute, followed by UV treatment for 3 minutes. The PET films were dipped into ATFB-TANI solutions for 10 seconds and exposed to UV light for another minute, rinsed with ethanol and air dried. The spray-coatings on SWCNT films and the UCLA pattern on the PET film with stencil masks were carried out by spraying 2.0 mM solution with an Image® Dual Action airbrush. The airflow rate was 5 standard cubic feet per minute (SCFH) with approximately 1 mL of solution sprayed out per minute.

**Membrane Performance Testing.** To measure fouling, membranes were placed in a stainless holder. A feed tank was connected to a mechanical pump, which flowed feed solutions across the membrane with an effective area of 17 $cm^2$. A pressure gauge was placed between the pump and the membrane holder to monitor the input pressure. The output after membrane filtration was monitored with a flow meter, and its readings were recorded by a connected computer. The membranes were first compacted with DI water at 50 psi until the flow reached a steady value. The fouling test began by introducing 1.0 g/L of BSA solution for 45 minutes. The flow decline percentage was calculated based on the equation:

$$\text{Flow Decline (\%)} = (1 - J_f / J_i) \times 100\% \qquad (6\text{-}1)$$

where $J_f$ is the flux after 45 min of fouling, and $J_i$ is the equilibrated flux after compaction. After fouling, the feed tank was refilled with DI water which was flowed across the membrane for 5 minutes in a washing procedure, before carrying out the next fouling cycle. The flow recovery percentage is defined as:

$$\text{Flow Recovery (\%)} = J_R / J_i \times 100\% \quad (6\text{-}2)$$

where $J_R$ is the flux reading after 5 min of DI water washing. It should be noted that the inlet pressure was not tuned after its original setting to 50 psi during membrane compaction; therefore, the flux fluctuations may be attributed to both the accumulation of foulants and the change in transmembrane pressures (TMP).

The BSA rejection performance testing on the PES UF membranes was conducted in a stainless-steel dead-end stirred filtration cell (Sterlitech Corp., Kent, WA) with an active membrane area of approximately 110 $cm^2$. The stirred cell was filled with DI water and pressurized. The water flow rate was recorded using a digital flow meter (FlowCal 5000, Tovatech LLC, South Orange, NJ). The membrane was then compacted at 50 psi until the flow rate was stable, approximately 1 hour for each membrane. BSA rejection of each membrane was characterized by filling the stirred cell with 1.0 g/L of BSA solution and pressurized it at 50 psi. The BSA rejection rate was calculated through the equation:

$$R = 1 - A_p / A_f \quad (6\text{-}3)$$

where $A_p$ and $A_f$ are the absorbance values of the permeate solution and the feed solution at a wavelength of 279 nm, respectively.

**Bacterial and BSA Adhesion Testing.** The antifouling properties of the ATFB-TANI modified PES membranes were investigated by a bacterial adhesion experiment using *E. coli* as a

model organism. *E. coli* cell cultures were suspended in Luria-Bertani broth for 24 hours at 35 $^{o}$C. 1 cm$^{2}$ samples of modified and unmodified membranes were then soaked in the *E. coli* suspension (~1 x10$^{7}$ CFU/ mL) (CFU = colony forming unit) at 37 $^{o}$C while shaken at 35 rpm for 24 hrs. The samples were then removed from the suspension and rinsed with a 1 M PBS buffer solution to remove any unbound cells. Membrane samples were then immersed and stained in a SYTO 9 dye solution (live/dead Baclight Bacterial Viability Kit) for 20 minutes. The samples were again rinsed with the 1 M PBS buffer solution. The samples were then immersed in a propidium iodide solution (PI) for 20 minutes and again rinsed with the 1 M PBS solution. SYTO 9 labels nucleic acids of both live and dead cells, whereas PI only labels nucleic acids of dead cells. When both dyes are present, PI exhibits a stronger affinity for nucleic acids than SYTO 9 and therefore SYTO 9 is displaced on the nucleic acids of dead cells. Images were then taken using a fluorescence microscope using different filters to view the SYTO9 and PI dyes. For BSA adhesion test, the green fluorescence protein (GFP) BSA was dissolved in DI water (concentration equals to 50 µg/mL), and samples of the membranes were immersed in that solution and placed in an incubator at 37 $^{o}$C and 50 rpm. After 24 hours, the samples were removed, rinsed with DI water and imaged using a fluorescent microscope. Image analysis was performed using ImageJ. The surface coverage values were quantified by dividing the number of colored pixels by the total number of pixels.

**Characterization.** The synthesized TANI was characterized by a Bruker UltraFlex Matrix Assisted Laser Desorption/Ionization (MALDI-TOF) spectrometer with 2,5-dihydroxybenzoic acid (DHB) as the matrix. NMR spectra were carried out on a Bruker AV300. Electrospray ionization mass spectrometry (ESI-MS) in methanol solvent was utilized to determine the composition of ATFB-TANI by comparison to Leucine Enkephalin. During ESI-

MS characterization, a signal for ATFB-TANI $(C_{31}H_{19}N_7F_4O)^+$ was observed at 583.1748 m/z and had an isotope pattern consistent with C, H, N, and O incorporation. The observed high-resolution ESI-MS for ATFB-TANI differed from the calculated masses by 0.7 ppm. UV-vis spectra were taken on a Shimadzu UV-3101 PC UV-vis-NIR scanning spectrometer with quartz cuvettes. The membrane topographies were investigated using a Bruker Dimension FastScan Probe Microscope (SPM) with silicon tips on nitride levers (Bruker Scanasyst-air) under the Tapping mode. The root-mean-square roughness and the image process were carried out by the software NanoScope Analysis. The conventional contact angles were measured through a First 10 Å ngstroms Contact Angle Goniometer. The captive bubble contact angles were measured through a homemade setup where the membranes were clamped on glass substrates. The membrane was then faced down and immersed into a transparent acrylic box. Air bubbles were placed through a U-shape needle connected to a syringe. The transmission electron microscopy (TEM) images were collected on a Tecnai TF20 TEM (FEI Inc.) operated under low dose mode. The electrical performances of PET films were measured via a probe station HP 4155B using toothless alligator clips as the metal contacts. The measured Amperes were corrected to zero at zero voltage. The attenuated total reflectance infrared (ATR-IR) spectra were acquired on a PerkinElmer Spectrum One spectrometer equipped with a universal ATR sampling accessory. The XPS data were acquired using a Kratos Axis Ultra DLD spectrometer equipped with a monochromatic Al Kα X-ray source. The pH values of TANI dispersions (optical images) were calibrated by a pH meter (Mettler Toledo). For measuring the zeta potentials, around 4 mg of aniline tetramer and polyaniline nanofibers, synthesized by interfacial polymerization, were sonicated and vortexed until the powders were well-dispersed. 1.0 M $HCl_{(aq)}$ and 1.0 M $NaOH_{(aq)}$ (PanReact AppliChem) were used to adjust each solution to a total volume of about 15 mL with

the desired pH value. The zeta potential values were measured via a Malvern Zetasizer Nano-ZS. For measuring the degree of grafting (DG), membranes were punched into circles with the diameter equal to 0.7 cm, and the weight ($W_i$) of the dried unmodified membrane measured using a microbalance (Mettler Toledo) recorded. The weights of dried modified membrane were then recorded as $W_f$. The degree of grafting is defined as:

$$DG = \frac{Wf - Wi}{A} \tag{6-4}$$

where A stands for the surface area of the membranes tested.

## AUTHOR CONTRIBUTIONS

C.-W.L. and S.A. synthesized TANI, ATFB-TANI and measured the cross-flow membrane performances, BSA rejection, contact angles, transmittances, electrical performance and performed modifications. E.R. tested BSA, *E. coli* and *S. epidermidis* adhesions and analyzed them with ImageJ. W.H.M. made the AFM and XPS measurements. X.H. conceived the idea and obtained preliminary antifouling experiments and *E. coli* adhesion tests. N.H. helped measure the membrane fouling before and after modification. D.C. helped design the ATFB-TANI molecule. D.J. built the cross-flow system and the BSA rejection setup. P.C. helped make and modify the membranes. B.T.M. helped modify membranes and guide this work. All authors helped in writing the manuscript.

## ACKNOWLEDGMENTS

The authors thank Dr. Martin Ignacio for help with UV-vis, contact angle, and XPS measurements, Dr. Chris Turner for help making the acrylic box for captive bubble measurements, Jacqueline Yang for preliminary *E. coli* tests, Shuangmei Xue and Chen-Hao Ji

for help with BSA rejection measurements, Matthew D. Kowal for making the graphite pellets and synthesizing the graphene oxide, Jakhangirkhodja Tulyagankhodjaev for preliminary contact angle measurements, Georgiy Akopov for acquiring SEM images, and Mackenzie Anderson for help with XPS measurements. The ESI instrumentation is maintained and made available through the support of Dr. Gregory Khitrov (University of California, Los Angeles Molecular Instrumentation Center – Mass Spectrometry Facility in the Department of Chemistry). The authors thank Dr. Robert S. Jordan for helpful discussions on designing the ATFB-TANI molecule. The authors also thank Prof. Jason Woo and Peng Lu for assistance measuring I-V electrical characteristics of PET films, Jeong Hoon Ko and Prof. Heather D. Maynard for help acquiring infrared spectra, and Alexandra Polasko and Prof. Shaily Mahendra for the bacterial tests. The authors would like to thank Chia-Liang Cheng's lab (Physics, NDHU), Yen-Peng Ho's lab (Chemistry, NDHU), Wenjea T. Tseng's lab (Materials Science and Engineering, NCHU) and Jacky Lin (Malvern in Taipei) for their help in the zeta potential measurements.

The authors thank the National Science Foundation CBET Grant 1337065, the USA/China Clean Energy Research Center for Water-Energy Technologies (CERC-WET), and the UC Grand Challenge Program for financial support. C.-W. L. thanks the support from the UCLA Dissertation Year Fellowship. In addition, W.H.M. and S.A. would like to each acknowledge their UCLA Eugene V. Cota-Robles Fellowship and P.C. a Clare Booth Luce Fellowship. This project was additionally supported by the National Center for Research Resources Grant Number S10RR025631. The content is solely the responsibility of the authors and does not necessarily represent the official views of the National Center for Research Resources or the National Institutes of Health.

## SUPPORTING INFORMATION

The measured I-V curve of pristine PET film, the MALDI-TOF spectrum of synthesized tetraaniline, the microscope images of surface coverage of *Staphylococcus epidermidis* on unmodified and modified PET films, stability of the modified PES membrane, and the atomic force microscope images showing topologies of unmodified and modified PES membranes are provided in the Supporting Information.

**Table 6-1.** Summary of Membrane Performance

| Membrane | Pure water permeability at 50 psi (LMH) | BSA rejection (%) | Flux decline (%) | Flux recovery (%) | Contact angle at pH 7 (degree) | Root-mean-square roughness (nm) |
|---|---|---|---|---|---|---|
| Unmodified | 181±21.0 | 91.06±0.85 | 46.85±5.22 | 56.35±6.45 | 76.3±1.6 | 2.72±0.30 |
| Modified | 227±4.9 | 97.53±1.12 | 40.70±8.95 | 73.30±2.41 | 49.8±0.4 | 3.49±0.47 |

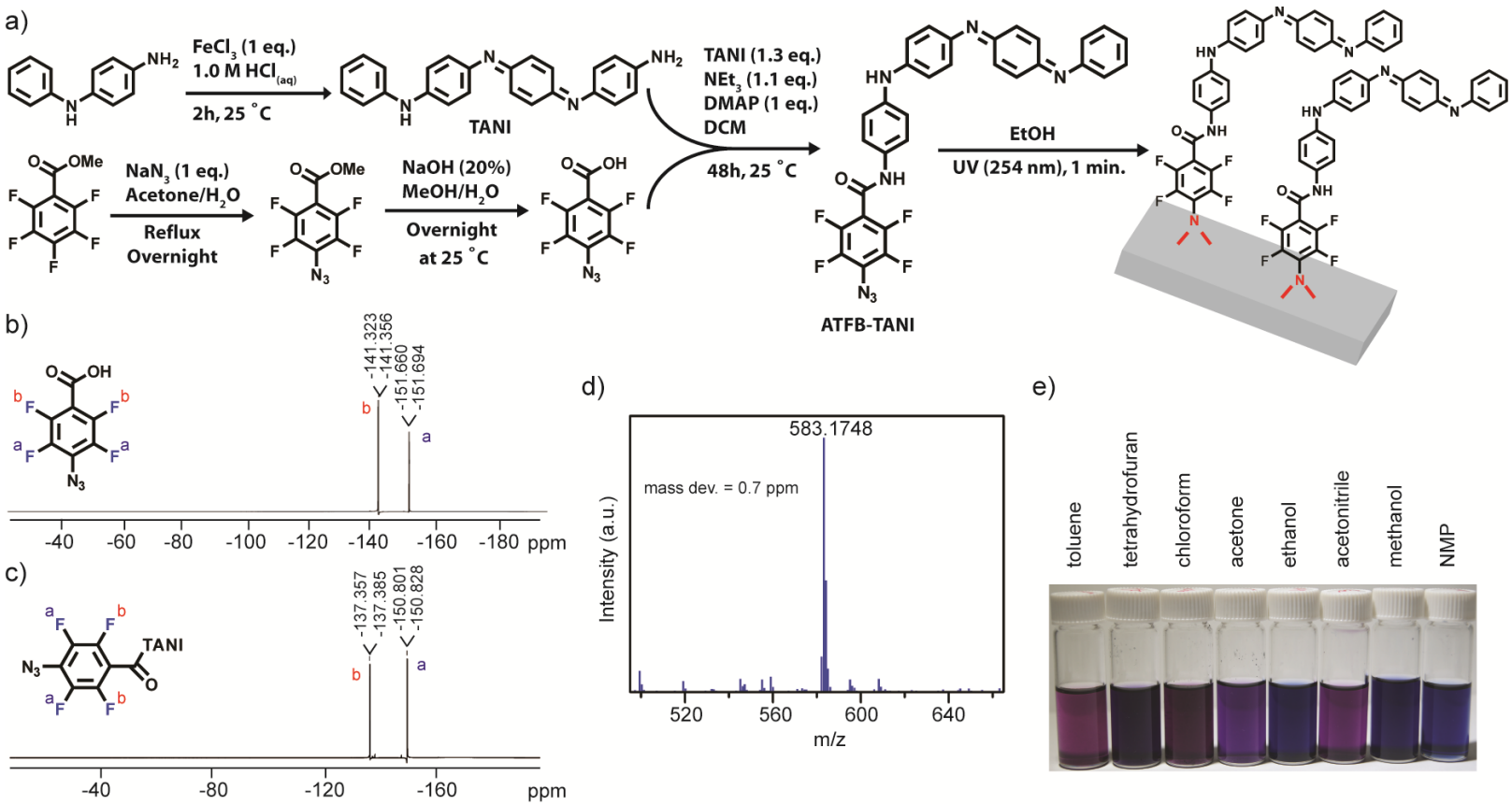


**Figure 6-1.** The synthesis procedure and characterizations of 4-azidotetrafluorobenzoyl-tetraaniline (ATFB-TANI). (a) ATFB-TANI was synthesized by coupling tetraaniline (TANI) with 4-azidotetrafluorobenzoic acid (ATFB). The ATFB-TANI can be covalently grafted onto the substrates by utilizing azide photochemistry. The $^{19}$F-NMR spectra of (b) ATFB and (c) ATFB-TANI. (d) Electrospray ionization (ESI) spectrum showing the molar mass of ATFB-TANI is 0.7 ppm away from the calculated value. (e) Photo showing ATFB-TANI can be dissolved in common organic solvents.

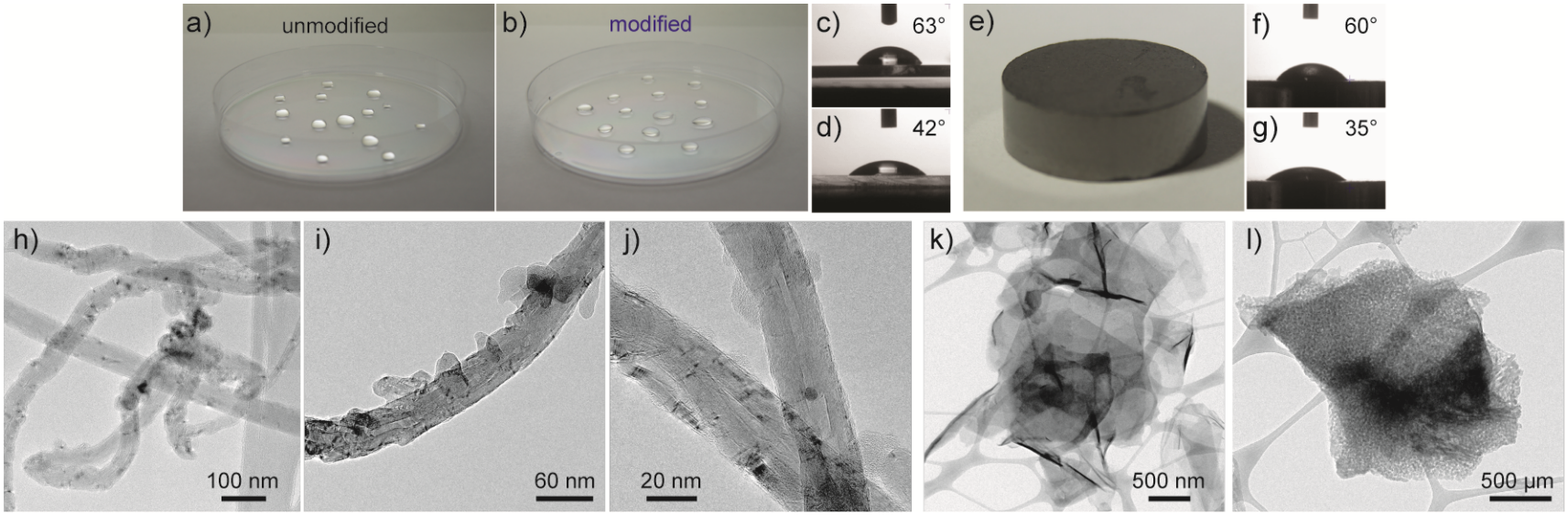


**Figure 6-2.** Images of water droplets on (a) an unmodified and (b) a modified polystyrene-based petri dish. The contact angles of (c) unmodified and (d) modified petri dish are 63° and 42°, respectively. The contact angle of (e) a compressed graphite pellet decreases from (f) 60 ° to (g) 35 ° after modification. The transmission electron microscopy (TEM) bright field images of (h) unmodified, (i, j) modified multi-walled carbon nanotubes (MWCNTs) and (k) unmodified and (l) modified reduced graphene oxide (rGO).

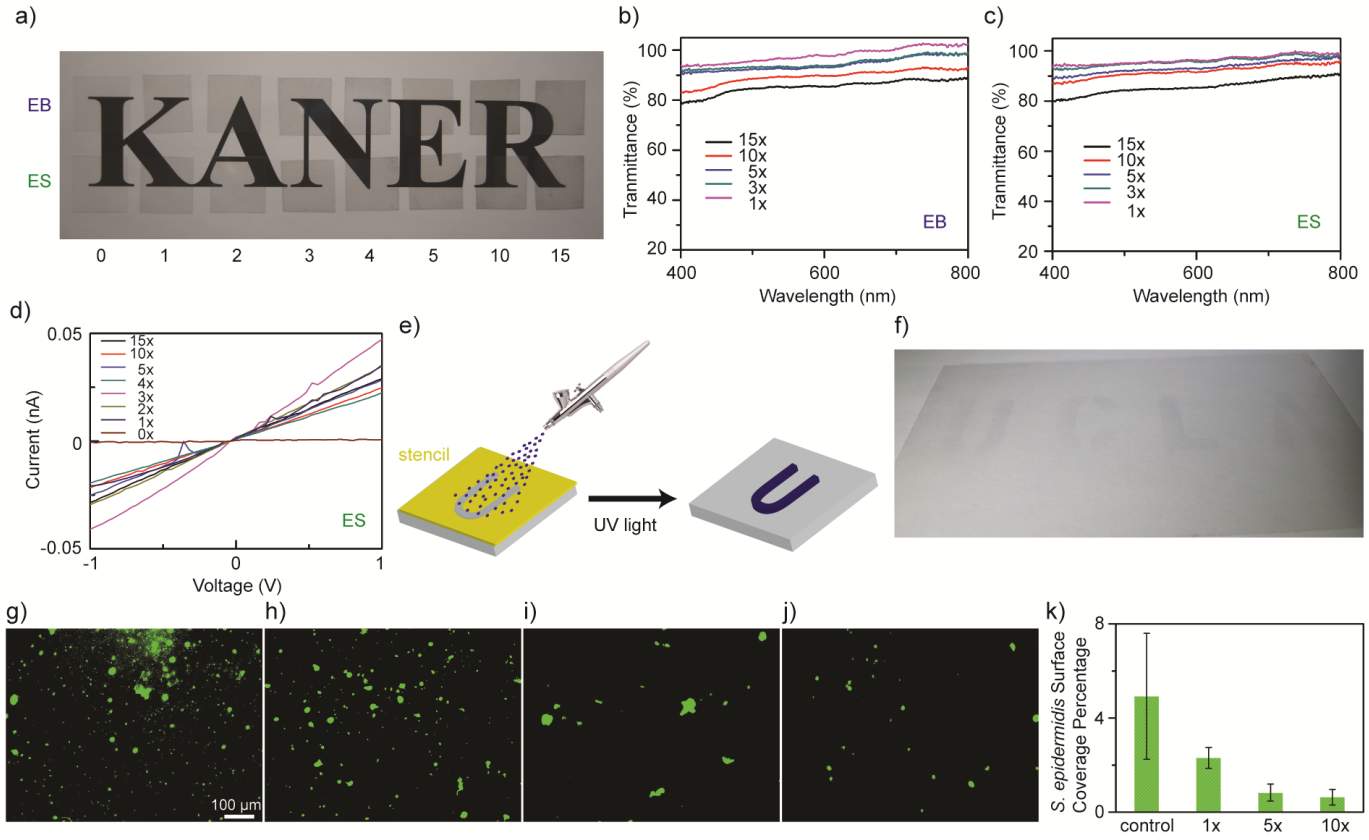


**Figure 6-3.** (a) Undoped (EB) and HCl doped (ES) polyethylene terephthalate (PET) films with different numbers of modifications showing their transparencies. UV-vis spectra show the transmittances of (b) undoped and (c) doped PET films with a pristine PET film as the reference. (d) The measured I-V curves of a pristine PET film and modified PET films after doping. (e) A schematic showing (f) a UCLA pattern by spray-coating ATFB-TANI solutions on top of a 13.5 cm x 8.0 cm PET film through stencil masks, followed by UV light exposure. Microscopic images showing the surface coverage of *Staphylococcus epidermidis* on the (g) unmodified, (h) 1, (i) 5, and (j) 10 times modified PET films, along with (k) a statistics bar graph. ((g-j) are under the same magnification.)

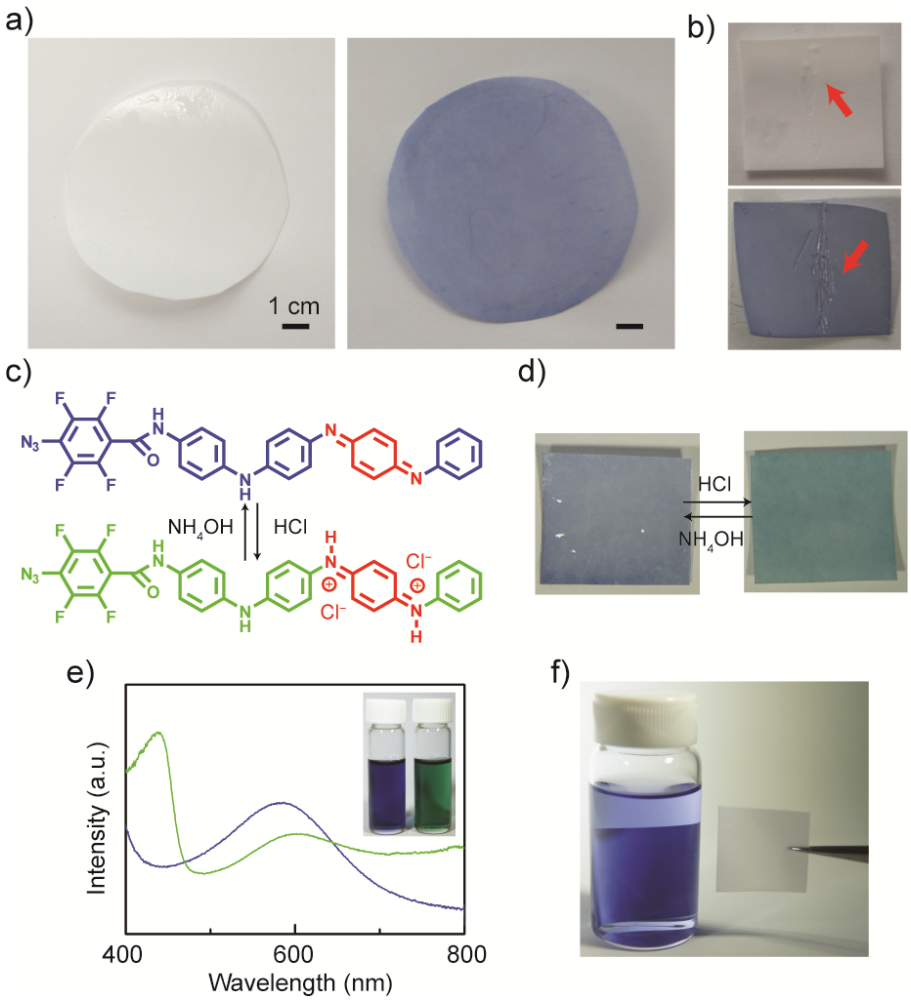


**Figure 6-4.** (a) Photographs of unmodified (left) and modified (right) polyethersulfone (PES) membranes. (b) Scratches are easily seen on the modified membrane (bottom) compared to the unmodified one (top). The (c) ATFB-TANI molecule and (d) the modified membrane can be protonated and deprotonated when treated with acids and bases. (e) The UV-vis spectra and photo (inset) of undoped (blue) and doped (green) ATFB-TANI dissolved in dimethyl sulfoxide (DMSO). (f) UV light treated TANI stained membranes showed colorless after rinsing in a vial of ethanol.

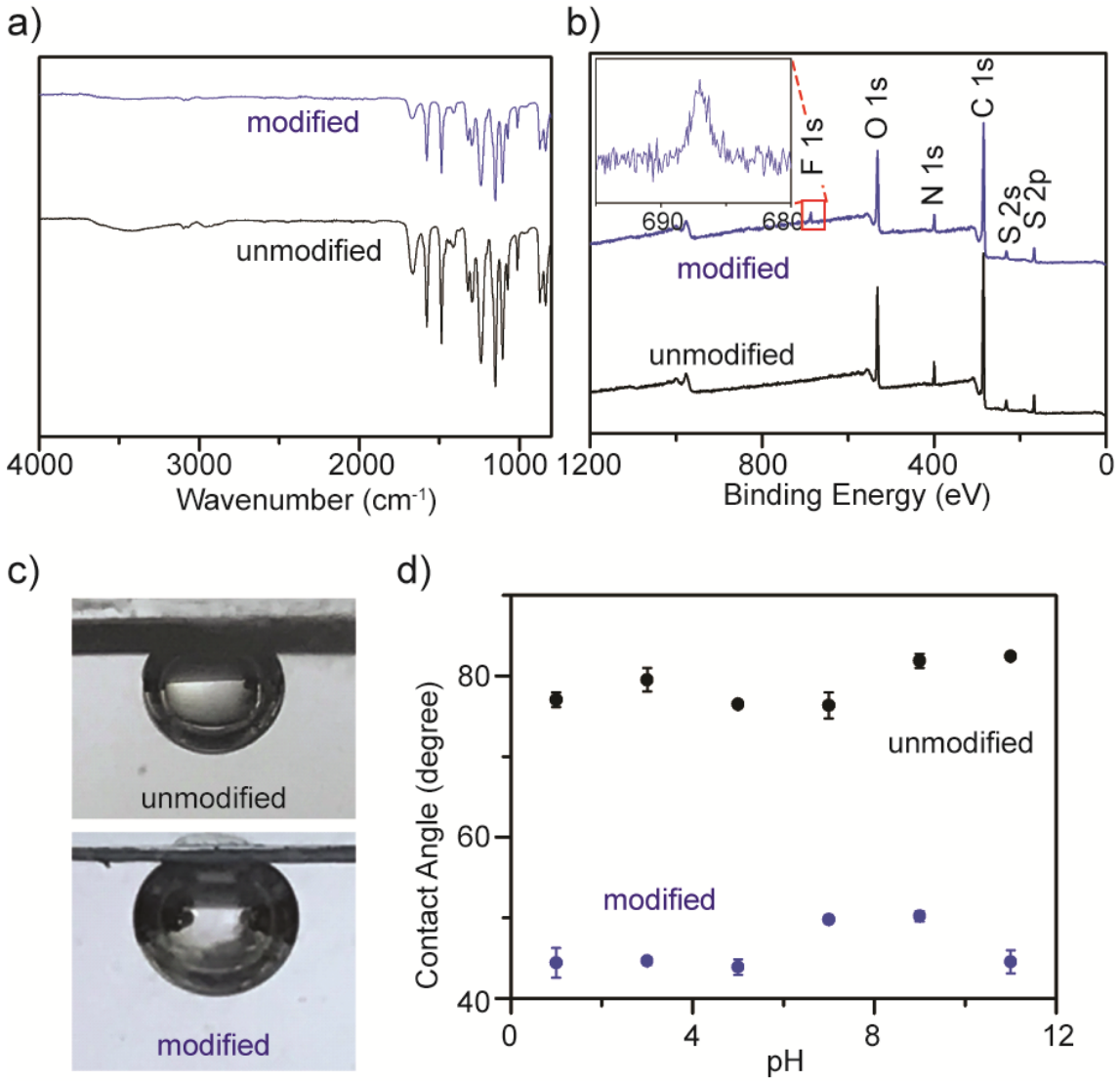


**Figure 6-5.** (a) ATR-IR spectra of both modified and unmodified PES membranes. (b) X-ray spectroscopy (XPS) spectra and F 1s spectra (inset) of the modified and unmodified membrane surfaces. (c) Captive bubble images under deionized water, and (d) contact angles under different pH aqueous solutions of modified and unmodified membranes.

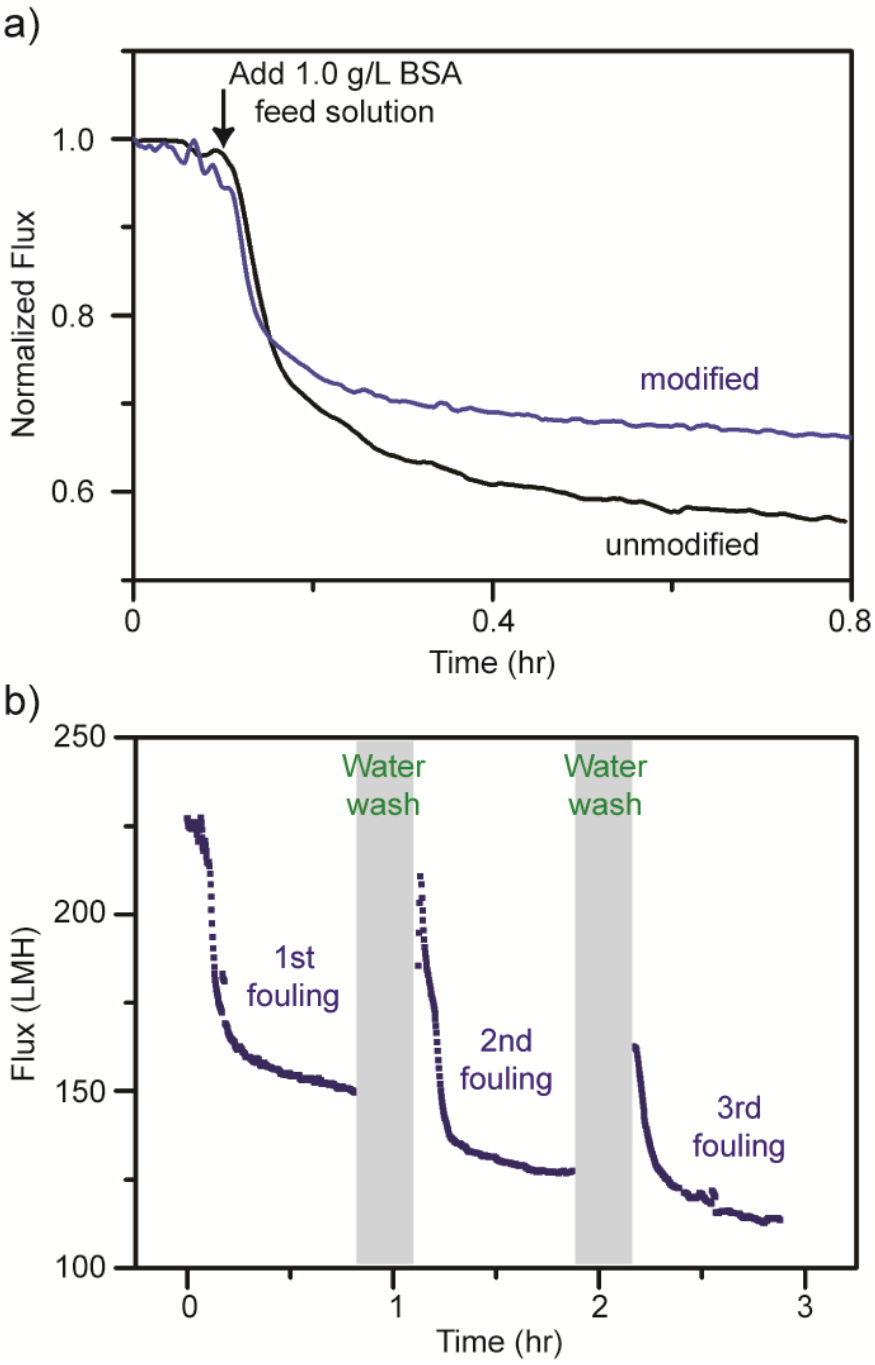


**Figure 6-6.** (a) Flux decline for unmodified and modified PES membranes after adding bovine serum albumin (BSA). (b) Flux declines and recoveries of a modified membrane after three cycles of fouling and water washing.

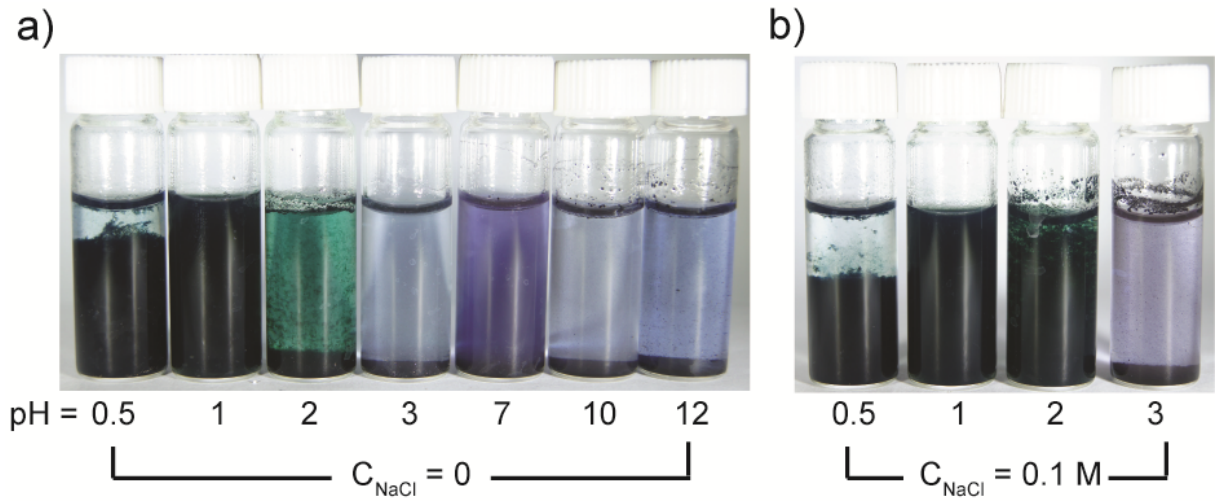


**Figure 6-7.** Optical images of TANI dispersed in aqueous solutions (2 mg/ml) at different pH and (b) with 0.1 M NaCl added after standing for 15 hours.

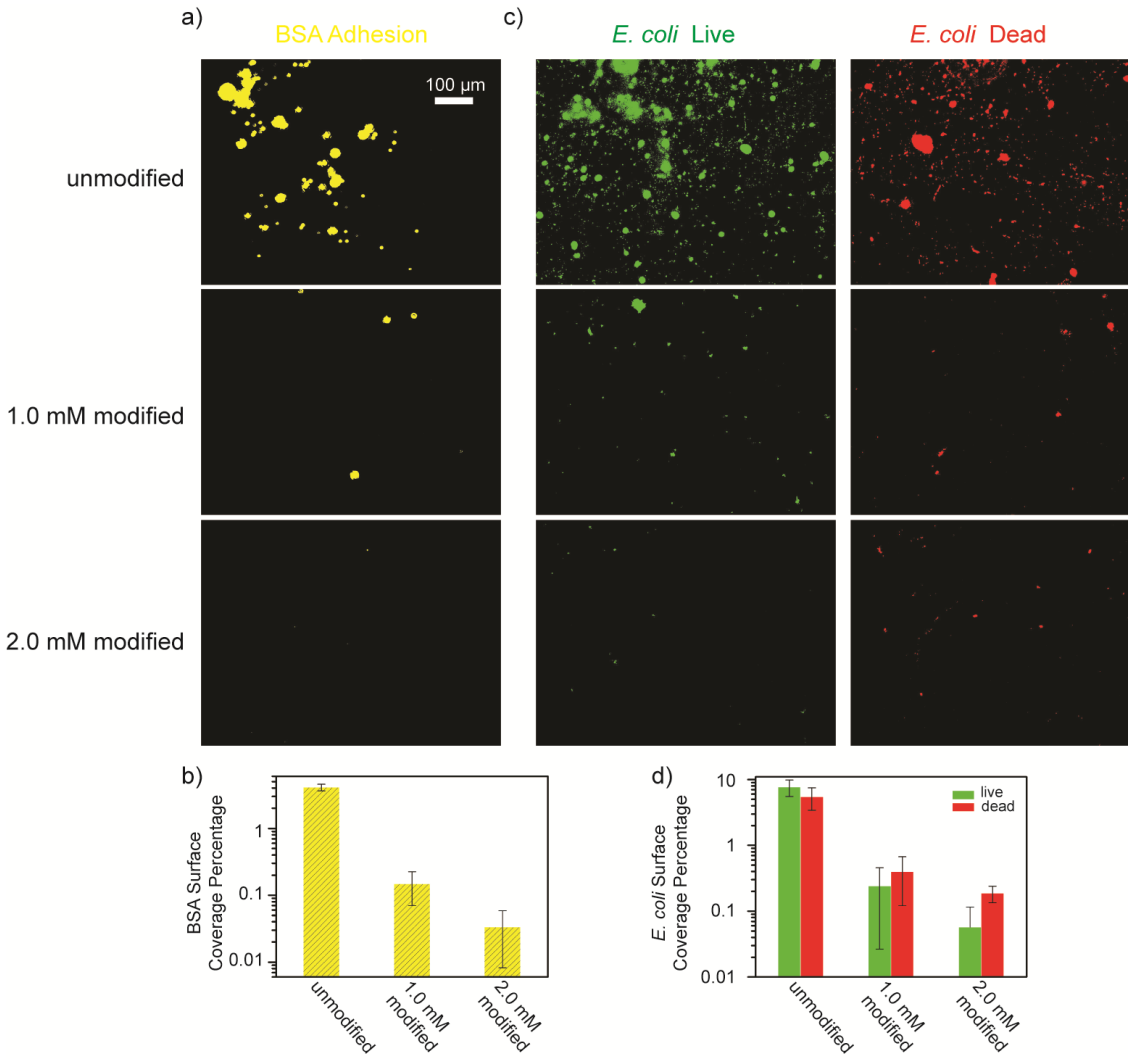


**Figure 6-8.** (a) BSA and (c) *E. coli* adhesion test microscopic images and (b, d) their surface coverage percentages of unmodified, 1.0 mM and 2.0 mM modified PES membranes. (All images share the same scale bar.)

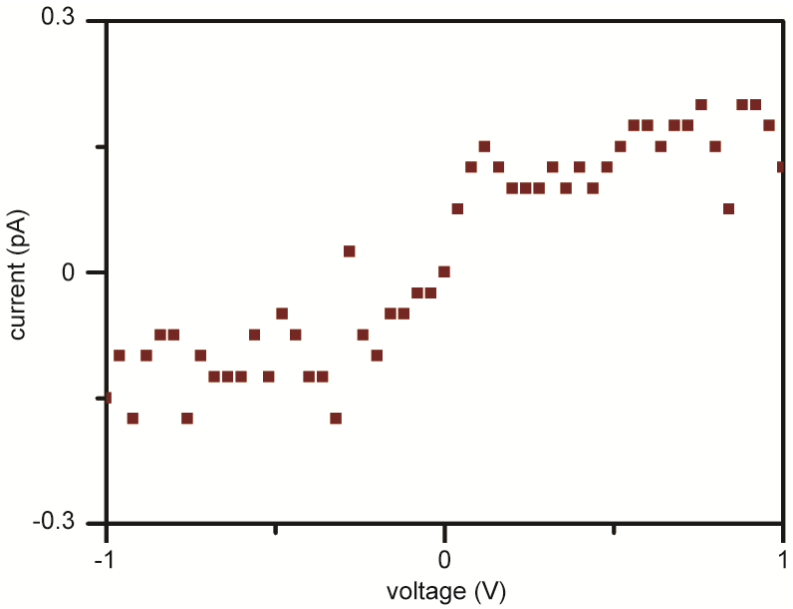


**Figure S6-1.** The I-V characteristic of the unmodified PET film.

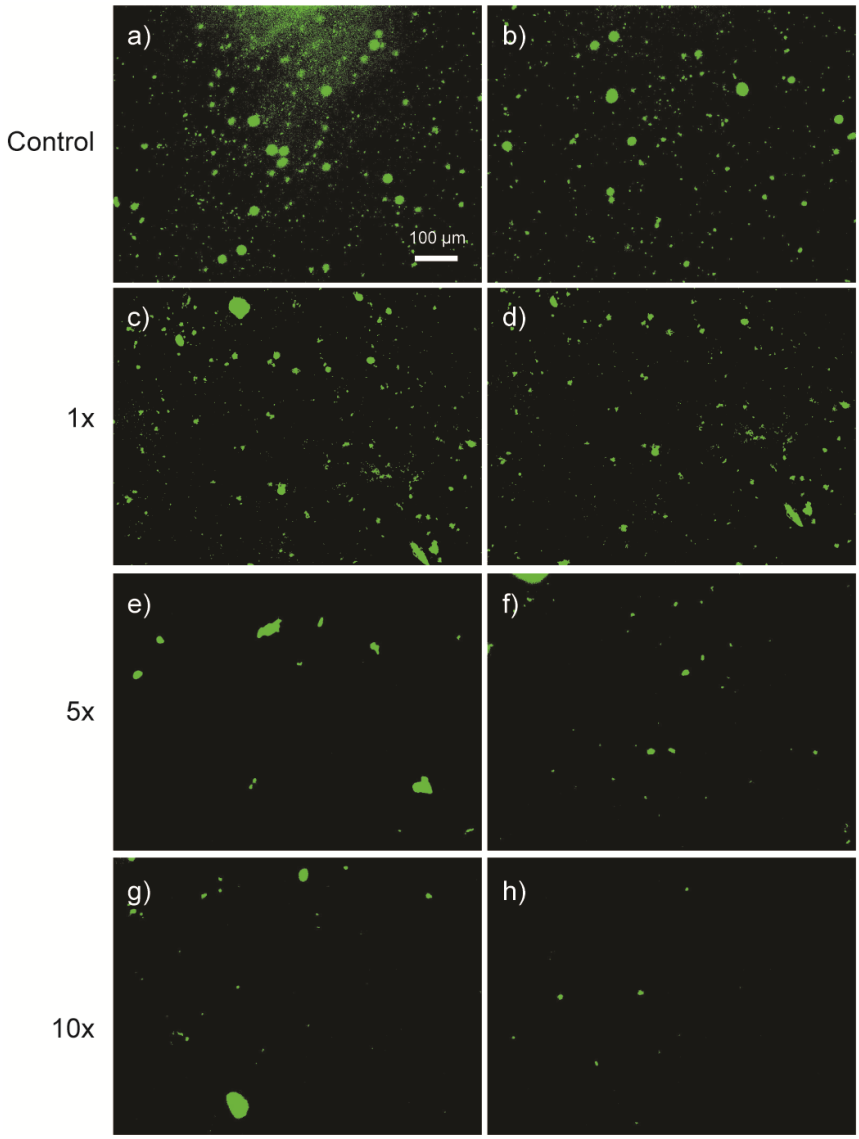


**Figure S6-2.** Microscopic images showing the surface coverage of *Staphylococcus epidermidis* on the (a, b) unmodified, (c, d) 1, (e, f) 5, and (g, h) 10 times modified PET films.

**Figure S6-3.** Photo showing a modified PES membrane which has been kept in water for almost one year.

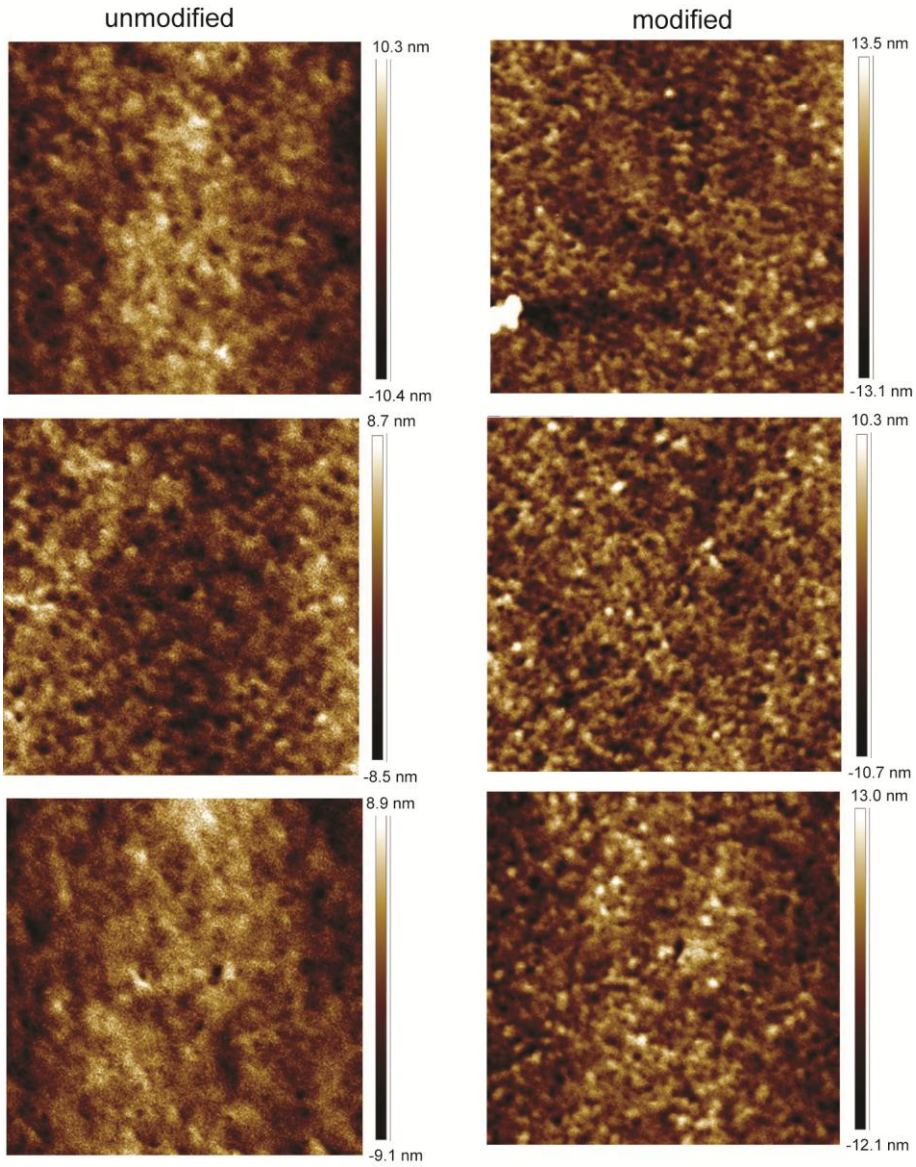


**Figure S6-4.** Atomic force microscope images showing topologies of (left column) unmodified, and (right column) modified PES membranes.

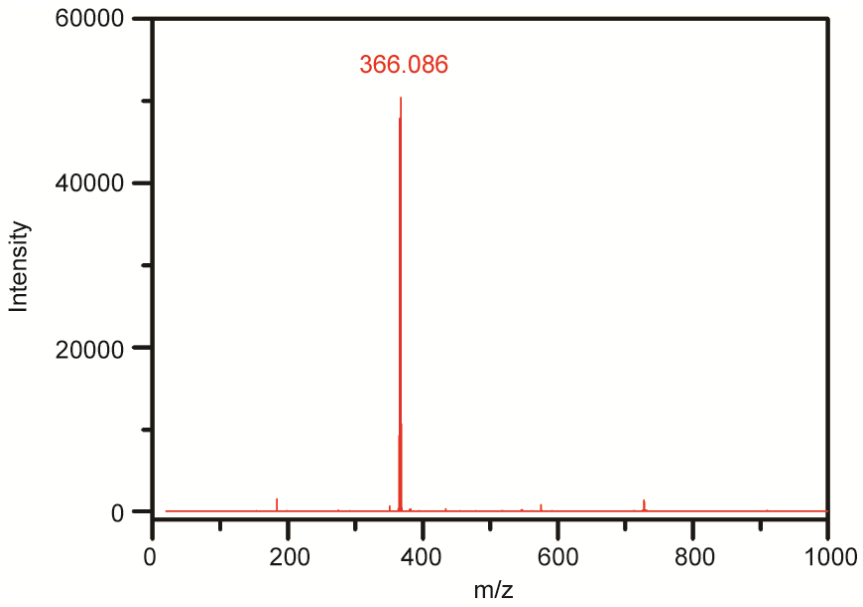


**Figure S6-5.** MALDI-TOF spectrum showing the molar mass of synthesized TANI.

## REFERENCES


1 A. J. Heeger, *Angew. Chemie Int. Ed.*, 2001, **40**, 2591–2611.

2 A. G. Macdiarmid, *Angew. Chemie Int. Ed.*, 2001, **40**, 2581–2590.

3 H. Shirakawa, *Angew. Chemie Int. Ed.*, 2000, **40**, 2574–2580.

4 J. Huang, S. Virji, B. H. Weiller and R. B. Kaner, *J. Am. Chem. Soc.*, 2003, **125**, 314–315.

5 J. Huang and R. B. Kaner, *J. Am. Chem. Soc.*, 2004, **126**, 851–855.

6 S. Virji, J. Huang, R. B. Kaner and B. H. Weiller, *Nano Lett.*, 2004, **4**, 491–496.

7 C. O. Baker, B. Shedd, P. C. Innis, P. G. Whitten, G. M. Spinks, G. G. Wallace and R. B. Kaner, *Adv. Mater.*, 2008, **20**, 155–158.

8 J. Gao, J.-M. Sansinena and H.-L. Wang, *Mater. Res. Soc. Symp. Proc.*, 2002, **698**, 17–22.

9 R. J. Tseng, J. Huang, J. Ouyang and R. B. Kaner, *Nano Lett.*, 2005, **5**, 1–4.

10 G. A. Snook, P. Kao and A. S. Best, *J. Power Sources*, 2011, **196**, 1–12.

11 Z. Fan, Z. Wang, M. Duan, J. Wang and S. Wang, *J. Memb. Sci.*, 2008, **310**, 402–408.

12 Z. Tian, H. Yu, L. Wang, M. Saleem, F. Ren, P. Ren, Y. Chen, R. Sun, Y. Sun and L. Huang, *RSC Adv.*, 2014, **4**, 28195–28208.

13 N. K. Guimard, N. Gomez and C. E. Schmidt, *Prog. Polym. Sci.*, 2007, **32**, 876–921.

14 S. Bhadra, D. Khastgir, N. K. Singha and J. H. Lee, *Prog. Polym. Sci.*, 2009, **34**, 783–810.

15 D. Li, J. Huang and R. B. Kaner, *Acc. Chem. Res.*, 2009, **42**, 135–145.

16 A. Pud, N. Ogurtsov, A. Korzhenko and G. Shapoval, *Prog. Polym. Sci.*, 2003, **28**, 1701–1753.

17 P. K. Prabhakar, S. Raj, P. R. Anuradha, S. N. Sawant and M. Doble, *Colloids Surfaces B Biointerfaces*, 2011, **86**, 146–153.

18 Z. Fan, Z. Wang, N. Sun, J. Wang and S. Wang, *J. Memb. Sci.*, 2008, **320**, 363–371.

19 X. Huang, B. T. McVerry, C. Marambio-Jones, M. C. Y. Wong, E. M. V. Hoek and R. B. Kaner, *J. Mater. Chem. A*, 2015, **3**, 8725–8733.

20 X. Zhao and C. He, *ACS Appl. Mater. Interfaces*, 2015, **7**, 17947–17953.

21 S. Zhao, Z. Wang, J. Wang and S. Wang, *Ind. Eng. Chem. Res.*, 2014, **53**, 11468–11477.

22 M. R. Gizdavic-Nikolaidis, J. R. Bennett, S. Swift, A. J. Easteal and M. Ambrose, *Acta Biomater.*, 2011, **7**, 4204–4209.

23 M. S. Tamboli, M. V Kulkarni, R. H. Patil, W. N. Gade, S. C. Navale and B. B. Kale, *Colloids Surfaces B Biointerfaces*, 2012, **92**, 35–41.

24 X. Liang, M. Sun, L. Li, R. Qiao, K. Chen, Q. Xiao and F. Xu, *Dalt. Trans.*, 2012, **41**, 2804–2811.

25 Z. Zhang, Z. Wei and M. Wan, *Macromolecules*, 2002, **35**, 5937–5942.

26 D. S. Dhawale, R. R. Salunkhe, V. S. Jamadade, D. P. Dubal, S. M. Pawar and C. D. Lokhande, *Curr. Appl. Phys.*, 2010, **10**, 904–909.

27 D. Yang and B. R. Mattes, *J. Polym. Sci. Part B Polym. Phys.*, 2002, **40**, 2702–2713.

28 D. Yang and B. R. Mattes, *Synth. Met.*, 1999, **101**, 746–749.

29 J. J. Orlando, J. B. Burkholder, S. A. McKeen and A. R. Ravishankara, *J. Geophys. Res.*, 1991, **96**, 5013–5023.

30 P. Roger, L. Renaudie, C. Le Narvor, B. Lepoittevin, L. Bech and M. Brogly, *Eur. Polym. J.*, 2010, **46**, 1594–1603.

31 J. Liu, J. An, Y. Zhou, Y. Ma, M. Li, M. Yu and S. Li, *ACS Appl. Mater. Interfaces*, 2012, **4**, 2870–2876.

32 L. Lai, H. Yang, L. Wang, B. Teh, J. Zhong, H. Chou, L. Chen, W. Chen, Z. Shen and R. Ruoff, *ACS Nano*, 2012, **6**, 5941–5951.

33 J. An, J. Liu, Y. Zhou, H. Zhao, Y. Ma, M. Li, M. Yu and S. Li, *J. Phys. Chem. C*, 2012, **116**, 19699–19708.

34 M. Kotal, A. K. Thakur and A. K. Bhowmick, *ACS Appl. Mater. Interfaces*, 2013, **5**, 8374–8386.

35 N. A. Kumar, H. Choi, Y. R. Shin, D. W. Chang and L. Dai, *ACS Nano*, 2012, 1715–1723.

36 J. An, J. Liu, Y. Zhou, H. Zhao, Y. Ma, M. Li, M. Yu and S. Li, *J. Phys. Chem. C*, 2012, **116**, 19699–19708.

37 Z. F. Li, H. Zhang, Q. Liu, Y. Liu, L. Stanciu and J. Xie, *Carbon N. Y.*, 2014, **71**, 257–267.

38 X. Liu, P. Shang, Y. Zhang, X. Wang, Z. Fan, B. Wang and Y. Zheng, *J. Mater. Chem. A*, 2014, **2**, 15273–15278.

39 V. D. Filimonov, M. Trusova, P. Postnikov, E. A. Krasnokutskaya, Y. M. Lee, H. Y. Hwang, H. Kim and K. W. Chi, *Org. Lett.*, 2008, **10**, 3961–3964.

40 H. Ziani-Cherif, K. Imachi and T. Matsuda, *Macromolecules*, 1999, **32**, 3438–3447.

41 A. U. Haq, J. Lim, J. M. Yun, W. J. Lee and T. H. Han, *Small*, 2013, **9**, 3829–3833.

42 C. Lin, R. L. Li, S. Robbennolt, M. T. Yeung, G. Akopov and R. B. Kaner, *Macromolecules*, 2017, **50**, 5892–5897.

43 Y. Wang, H. D. Tran and R. B. Kaner, *Macromol. Rapid Commun.*, 2011, **32**, 35–49.

44 Z. Wei and C. F. J. Faul, *Macromol. Rapid Commmunications*, 2008, **29**, 280–292.

45 J. F. W. Keana and S. X. Cai, *J. Org. Chem.*, 1990, **55**, 3640–3647.

46 S. J. Pastine, D. Okawa, B. Kessler, M. Rolandi, M. Llorente, A. Zettl and J. M. J. Fréchet, *J. Am. Chem. Soc.*, 2008, **130**, 4238–4239.

47 L.-H. Liu and M. Yan, *Acc. Chem. Res.*, 2010, **43**, 1434–1443.

48 S. Brase, C. Gil, K. Knepper and V. Zimmermann, *Angew. Chemie Int. Ed.*, 2005, **44**, 5188–5240.

49 Z. Li, A. Ajami, E. Stankevičius, W. Husinsky, G. Račiukaitis, J. Stampfl, R. Liska and A. Ovsianikov, *Opt. Mater. (Amst).*, 2013, **35**, 1846–1851.

50 D. Rana and T. Matsuura, *Chem. Rev.*, 2010, **110**, 2448–2471.

51 R. Zhang, Y. Liu, M. He, Y. Su, X. Zhao, M. Elimelech and Z. Jiang, *Chem. Soc. Rev.*, 2016, **45**, 5888–5924.

52 J. A. Koehler, M. Ulbricht, G. Belfort and N. York, *Langmuir*, 2000, **16**, 10419–10427.

53 A. Fane, A.G.; Fell, C.J.D.; Suki, *J. Memb. Sci.*, 1983, **16**, 195–210.

54 F. Meng, S. Chae, A. Drews, M. Kraume and H. Shin, *Water Res.*, 2009, **43**, 1489–1512.

55 P. Le-clech, V. Chen and T. A. G. Fane, *J. Memb. Sci.*, 2006, **284**, 17–53.

56 W. Guo, H. Ngo and J. Li, *Bioresour. Technol.*, 2012, **122**, 27–34.

57 A. Drews, *J. Memb. Sci.*, 2010, **363**, 1–28.

58 K. J. Howe and M. M. Clark, *Environ. Sci. Technol.*, 2002, **36**, 3571–3576.

59 S. Dutta, Kingshuk; De, *J. Mater. Chem. A Mater. energy Sustain.*, 2017, **5**, 22095–22112.

60 C. M. Magin, S. P. Cooper and A. B. Brennan, *Mater. Today*, 2010, **13**, 36–44.

61 S. Zhao, Z. Wang, X. Wei, B. Zhao and J. Wang, *J. Memb. Sci.*, 2011, **385**–**386**, 251–262.

62 S. B. Teli, S. Molina, E. G. Calvo, A. E. Lozano and J. de Abajo, *Desalination*, 2012, **299**, 113–122.

63 S. Zhu, S. Zhao, Z. Wang, X. Tian and M. Shi, *J. Memb. Sci.*, 2015, **493**, 263–274.

64 B. Jiang, B. Wang, L. Zhang, Y. Sun, X. Xiao, N. Yang and H. Dou, *J. Appl. Polym. Sci.*, 2017, **44452**, 1–7.

65 S. Zhao, L. Huang, T. Tong, W. Zhang, Z. Wang, J. Wang and S. Wang, *Environ. Sci.*

*Water Res. Technol.*, 2017, **3**, 710–719.

66 Y. Liao, D. Yu, X. Wang, W. Chain and X. Li, *Nanoscale*, 2013, **5**, 3856–3862.

67 W. Duan, A. Ronen, S. Walker and D. Jassby, *ACS Appl. Mater. Interfaces*, 2016, **8**, 22574–22584.

68 B. Hudaib, V. Gomes, C. Zhou and Z. Liu, *Sep. Purif. Technol.*, 2018, **190**, 143–155.

69 B. T. Mcverry, J. A. T. Temple, X. Huang, K. L. Marsh, E. M. V Hoek and R. B. Kaner, *Chem. Mater.*, 2013, **25**, 3597–3602.

70 S. Chen and H. Lee, *Macromolecules*, 1995, **28**, 2858–2866.

71 M. Jaymand, *Prog. Polym. Sci.*, 2013, **38**, 1287–1306.

72 L. H. Liu and M. Yan, *Acc. Chem. Res.*, 2010, **43**, 1434–1443.

73 V. W. Liptay, *Angew. Chemie*, 1969, **81**, 195–206.

74 N. Tsubokawa, *Polym. J.*, 2005, **37**, 637–655.

75 R. H. Baughman and ShackletteL.W., *Phys. Rev. B*, 1989, **39**, 5872–5886.

76 S. Satpathy, S. K. Sen, S. Pattanaik and S. Raut, *Biocatal. Agric. Biotechnol.*, 2016, **7**, 56–66.

77 C. Vuong and M. Otto, *Microbes Infect.*, 2002, **4**, 481–489.

78 M. Otto, *Nat. Rev. Microbiol.*, 2009, **7**, 555–567.

79 J. Jin-Chih and A. G. Macdiarmid, *Synth. Met.*, 1986, **13**, 193–205.

80 B. J.L. and S. G.B., *Acc. Chem. Res.*, 1985, **18**, 309–315.

81 Y. Cao, S. Li, Z. Xue and D. Guo, *Synth. Met.*, 1986, **16**, 305–315.

82 A. Epstein, J. Ginder, F. Zuo, R. Bigelow, H. Woo, D. Tanner, A. Richter, W.-S. Huang and A. MacDiarmid, *Synth. Met.*, 1987, **18**, 303–309.

83 Q. Li, H. H. Lin and X. L. Wang, *Membranes (Basel).*, 2014, **4**, 181–199.

84 T. A. Sergeyeva, H. Matuschewski, S. A. Piletsky, J. Bendig, U. Schedler and M. Ulbricht, *J. Chromatogr. A*, 2001, **907**, 89–99.

85 H. M. Ulbricht and A. Matuschewski, *J. Memb. Sci.*, 1996, **115**, 31–47.

86 B. T. Mcverry, M. C. Y. Wong, K. L. Marsh, J. A. T. Temple, C. Marambio-jones, E. M. V Hoek and R. B. Kaner, *Macromol. Rapid Commun.*, 2014, **35**, 1528–1533.

87 K. Siegmann, J. Inauen, R. Sterchi and M. Winkler, *Surf. Interface Anal.*, 2018, **50**, 205–211.

88 K. Siegmann, J. Inauen, D. Villamaina and M. Winkler, *Appl. Surf. Sci.*, 2017, **396**, 672–680.

89 B. Guo, A. Finne-wistrand and A. Albertsson, *Macromolecules*, 2012, **45**, 352–359.

90 P. Zhou, J. Li, W. Yang, L. Zhu and H. Tang, *Langmuir*, 2018, **34**, 2841–2848.

91 Z. Fan, Z. Wang, N. Sun, J. Wang and S. Wang, *J. Memb. Sci.*, 2008, **320**, 363–371.

92 S. Zhao, Z. Wang, X. Wei, B. Zhao, J. Wang, S. Yang and S. Wang, *J. Memb. Sci.*, 2011, **385**–**386**, 251–262.

93 S. Zhao, Z. Wang, J. Wang and S. Wang, *Ind. Eng. Chem. Res.*, 2014, **53**, 11468–11477.

94 X.-G. Li, D.-G. Yu, W. Chain, E. M. V. Hoek, Y. Liao, X. Wang and R. B. Kaner, *Nanoscale*, 2013, **5**, 3856.

95 Y. Liao, X. G. Li, E. M. V Hoek and R. B. Kaner, *J. Mater. Chem. A*, 2013, **1**, 15390–15396.

96 B. Kaeselev, P. Kingshottb and G. Jonsson, *Desalination*, 2002, **146**, 265–271.

97 L. P. Wang, W. Wang, L. Di, Y. N. Lu and J. Y. Wang, *Colloids Surfaces B Biointerfaces*, 2010, **80**, 72–78.

98 R. J. Hunter, *Foundations of Colloid Science*, Oxford University Press, New York, 1987.

99 D. Li and R. B. Kaner, *Chem. Commun.*, 2005, 3286–3288.

100 L. S. Dorobantu, S. Bhattacharjee, J. M. Foght and M. R. Gray, *Langmuir*, 2009, **25**, 6968–6976.

101 Z. Shao, P. Rannou, S. Sadki, N. Fey, D. M. Lindsay and C. F. J. Faul, *Chem. Eur. J.*, 2011, **17**, 12512–12521.

102 R. L. Li, C. W. Lin, Y. Shao, C. W. Chang, F. K. Yao, M. D. Kowal, H. Wang, M. T. Yeung, S. C. Huang and R. B. Kaner, *Polymers (Basel).*, 2016, **8**, DOI:10.3390/polym8110401.

103 Y. Shao, M. F. El-Kady, C. W. Lin, G. Zhu, K. L. Marsh, J. Y. Hwang, Q. Zhang, Y. Li, H. Wang and R. B. Kaner, *Adv. Mater.*, 2016, 6719–6726.

# CHAPTER 7. FURTHERING OUR UNDERSTANDING OF THE DOPING MECHANISM IN CONJUGATED POLYMERS USING TETRAANILINE

"Reprinted (adapted) with permission from (Lin, C.-W.; Li, R.L.; Robbennolt, S.; Yeung, M.T.; Akopov, G.; Kaner, R.B. "Furthering our Understanding of the Doping Mechanism in Conjugated Polymers Using Tetraaniline" *Macromolecules*, 2017, 50, 15, 5892-5897 DOI: 10.1021/acs.macromol.7b00633).Copyright (2017) American Chemical Society."

## ABSTRACT

Polyaniline is known for reversible acidic doping. However, despite extensive work, little experimental evidence exists for the initial doping mechanism mainly due to the difficulty of synthesizing polyaniline with a uniform chain length. In this study, we partially dope aniline tetramers in order to investigate the initial stage of doping in both solution and the solid state. In solution, we discovered a method for visualizing the doping level due to solvent density differences. The optical results in both the liquid and solid state suggest that the partially doped aniline tetramers are physical mixtures of aniline tetramer in the emeraldine base and emeraldine salt forms. Electron paramagnetic resonance confirms the formation of spinless bipolarons as the major carriers. Therefore, we postulate that the doping mechanism proceeds via a continual increase in the number of doubly doped tetraanilines.

## INTRODUCTION

Polyaniline is one of the most extensively studied conducting polymers,[1-3] with applications as gas sensors,[4, 5] actuators,[6, 7] supercapacitors,[8, 9] and more.[10-15] Many of these applications rely on its innate ability to be chemically modified through p-doping, a process that partially oxidizes the polymer while adding a counter-anion to balance the charge. Polyaniline is readily doped by a

multitude of chemical species which alter its carrier concentration and conductivity.[16, 17] Recent work to improve our understanding of this polymer has moved towards aniline oligomers, which model the conduction of polyaniline with the added advantage of being a small discrete molecule. These oligomers have attracted attention due to their controllable nanoscale morphologies,[18, 19] ionic assemblies,[20, 21] and potential for replacing conjugated polymers in many applications.[22-26] Unlike other organic semiconductors, polyaniline and its oligomers in the emeraldine base (EB) state can be acid doped/protonated to form the conducting emeraldine salt (ES) state. Like other conjugated polymers with a non-degenerate ground state, the doping mechanism of polyaniline and oligoanilines results in polarons that can combine to form lower energy bipolarons as a function of increasing doping level (**Figure 7-1**).[27-33] Here, we consider a simple yet fundamental question: how do the first few dopants order during the initial doping process? This question is very difficult to answer due to the problems of performing such an experiment without a polymer in which all the chains are exactly the same length in order for the dopants to follow the thermodynamically most favorable pathway. Fortunately, an aniline tetramer, which represents the smallest repeat unit of polyaniline, is ideal for carrying out such an experiment since it has precisely two doping sites available (the two imine nitrogens) per molecule and can be made in a uniform length.

Phenyl/phenyl-capped aniline tetramer (TANI) had been examined for its electrochemical properties, suggesting spinless bipolarons as the charge carrying species due to two-electron transfers observed between oxidation states by Shacklette *et al*. in the late 1980's.[34] Javadi,[35] Petrova,[36] and Stafström[37] also mentioned the crossover from the polaron state to the bipolaron state with decreasing chain length. Yet a few years later, Janssen *et al*. claimed that triplet-state di-cation radicals are the stable carriers for TANI.[38] It is certain that TANI forms a bipolaron (a

doubly-charged species)when fully doped, consistent with our Electron Paramagnetic Resonance (EPR) results. What is not certain is the stability of singly-doped TANI as an intermediate. Its stability really determines the initial steps of how conducting polymers are doped. As illustrated in **Figure 7-2**, the existence of singly-doped TANI could lead to all TANI molecules being singly-charged when the doping level reaches 50% (Scheme I). On the other hand, if singly-doped TANI did not exist, half the TANI molecules would be doubly-doped before the next TANI molecule becomes doped (Scheme II). Similar to the partial oxidation of oligothiophenes determining the relationship between the quinoidal stability and the polaron pairs,[39] here we introduce a quantitative, but insufficient, amount of acid dopants to TANI in order to investigate the order and mechanism of doping.

## RESULTS AND DISCUSSION

Unlike polyaniline, TANI can be dissolved in a wide range of solvents as shown in **Figure 7-3a** in order of increasing dielectric constant: toluene, tetrahydrofuran (THF), chloroform, dioxane, acetone, ethanol, acetonitrile (ACN), N-methyl-2-pyrrolidone (NMP), and dimethyl sulfoxide (DMSO). A 1 mg to 40 ml ratio of undoped TANI in its EB state produces a wide variety of blue-violet colors due to solvatochromism.[33, 40] With quantitative calculations, we can dope TANI in ethanol to precise doping levels (the doping level is defined as the ratio between the number of dopants added to the imine nitrogens), resulting in a gradual color change from blue (EB) to green (ES) (**Figure 7-3b**). The UV-vis spectra of the solutions in **Figure 7-3b** were carefully measured, as shown in **Figure 7-3c,d**. The band gap ($\pi$-$\pi^*$ transition) peak is found at ~310 nm (4.01 eV), in agreement with previous studies.[41, 42] The linearly increasing peaks at ~1950 nm correspond to an increasing amount of water of solvation present around the dopants as higher doping levels are achieved. The decreasing peaks at ~600.0 nm (2.07 eV) are believed

to be the excitation transition from benzoid to quinoid, *i.e.* from the EB to the ES state.[28, 41, 43] Therefore, the two characteristic peaks from doping are observed, $\omega_1$ and $\omega_2$, at 1164.0 nm (1.09 eV) and 434.5 nm (2.86 eV), respectively. As no extra peaks are generated upon increasing the doping level, it can be concluded that the major carriers are consistent at all doping levels. More importantly, the absorbance intensities of each spectrum at the two characteristic peaks are linearly proportional to the doping level (**Figure 7-3e**). The good agreement with the Beer-Lambert Law[44] suggests that a given solution at a certain doping level is actually comprised of a proportional mixture of the EB and the ES states in solution, which is consistent with Scheme II, but not Scheme I, in **Figure 7-2**. A comparison of UV-vis spectra between *in situ* doped and a proportional mixture of the EB and ES states in solution are almost identical, as shown in **Figure S7-1**. A schematic energy diagram for TANI is shown in **Figure 7-3f**, where the two allowed optical transitions are the HOMO to the lower bipolaron state ($\omega_1$), and the HOMO to the upper bipolaron state ($\omega_2$). Note the band gap is measured as ~4.01 eV from the UV-vis spectra, hence, the energy differences between the upper bipolaron state to the LUMO, and the HOMO to the lower bipolaron state are 1.09 eV and 1.15 eV, respectively. These two values are expected to be close based on the non-degeneracy of most conducting polymers.[27, 45]

During the doping process, we noticed that a droplet of aqueous acid dopant instantaneously turned green (the ES state) when pipetted into an EB solution in ethanol, resulting in the formation of a green layer at the bottom of the vial within seconds. The layers and color difference are relatively stable and remain stratified for hours to days under static conditions (**Figure 7-4a**). This separation phenomenon, similar to the rainbow observed in a glass density demonstration, might be attributed to: 1. the fast doping reaction and 2. the density difference between the solvents for TANI and dopants (ethanol and water in this case where

$D_{ethanol}$ = 0.79 g/ml and $D_{water}$ = 1.00 g/ml). In **Figure 7-4b**, we demonstrate that the height of the green portion, *i.e.* the doped ES state, over the whole solution quite well reflects the corresponding amount of dopants. The solutions in **Figure 7-4b** share the same UV-vis spectra with those in **Figure 7-3b**. The same phenomena were observed when using different monoprotic acids, including hydrochloric acid (HCl), *para*-toluensulfonic acid (PTSA), nitric acid ($HNO_3$), camphorsulfonic acid (CSA), and perchloric acid ($HClO_4$) as the dopant (**Figure 7-4c**). Various concentrations of dopant solutions and the de-doping process showed identical effect in vials, but the addition of solvents may enhance the Brownian motion.[46] The phenomenon observed in **Figure 7-4** also supports our postulate in Scheme II of **Figure 7-2**, in which the amount of doped TANI molecules is linearly proportional to the amount of dopants. In the case of Scheme I, the green parts would have occupied half the height of the vial at a doping level of 25.0%, and created a uniformly identical color over the whole vial at a doping level of 50.0%. Considering the association, disproportionation, Brownian motion, and other complex issues of solutions, we then carefully investigated the materials in the solid state, which will be addressed in the following paragraphs.

Upon drying, TANI powders in the EB state exhibited a violet color, while the ES state appeared blue. The reflected color shift is attributed to the lower energy absorption of the ES state compared to the EB state. As can be seen in **Figure 7-5**, each sample appears to be a mixture of both blue and violet species, and the percentage of blue particles clearly increases as the doping level increases, indicating that the partially doped powders may be a mixture of both EB and ES powders with certain ratios, *i.e.* Scheme II. We then attempted to further confirm the presence of a mixed phase by controlling the crystallization of both species from the same solution. Although the crystal structure of TANI in the leucoemeraldine base state has been

reported from single crystal X-ray diffraction,[47] it is still difficult to prepare single crystals of both doped and undoped TANI of sufficient quality in the same place to resolve them by transmission electron microscopy or single crystal X-ray diffraction. Hence, powder X-ray diffraction (PXRD) was used to investigate the crystal structures. In order to produce more pronounced PXRD peaks, perchloric acid was used as the dopant.

In **Figure 7-6**, a series of PXRD spectra for TANI powders with different doping levels shows the gradual evolution from one phase to another as the doping level increases. Previous work has shown that diffraction peaks for TANI occur at as around 0.68 nm, 0.78 nm, and 2.40 nm, respectively.[48] The 2.40 nm peak is beyond the range of our measurements. In the case of TANI in the EB state, the d-spacing for the (010) and (100) planes correspond to two minor peaks at 2θ equal to 11.435° and 12.952°, *i.e.* 0.7738 nm and 0.6835 nm, respectively. These two values are in good agreement with the reported values.[48] Another peak at 2θ equal to 23.024° can be attributed to the π- π stacking between TANI molecules, which corresponds with the (020) d-spacing. Note that the relative intensities of the two peaks at 25.081° and 25.948° decrease as the doping level increases (the two dashed lines in the left part of **Figure 7-6**). From the zoom-in area between 16° to 22° (the right part of **Figure 7-6**), it is evident that the two peaks at 17.998° and 20.208° gradually decrease as more $HClO_4$ is introduced. Furthermore, the presence of diffraction peaks that can be indexed to both the EB and ES states suggest that the powder is a physical mixture of doubly-charged and uncharged species. The two peaks at 18.800° and 19.341° in the spectrum of the EB state gradually shift and merge into one dominant peak at 19.021° with a minor shoulder at 19.536° as a function of increasing doping level. If Scheme I applied, the crystal structure of the singly-doped TANI, the one at 50% doping level, should either have different diffraction peaks from EB and ES, or be almost identical to ES. Thus, the

gradual transition of the PXRD spectra from the EB to the fully doped ES state indicates that the partially doped materials are comprised proportionally of both the EB and the ES states of TANI. The evolutions of the PXRD spectra then strongly suggests that the doping mechanism is most closely represented by Scheme II.

Further evidence for Scheme II in the solid state can be seen from the EPRspectra, which detects the number of unpaired electrons. From previous studies, the bipolaron is believed to be the major carrier for a TANI molecule when it is fully protonated,[35] leading to the following assumptions. If Scheme I is applicable, each TANI molecule will be singly-doped at a doping level of 50%, *i.e.* the number of spins per molecule should be equal to 1. The dopants added beyond the 50% doping level will then share a phonon with the first dopant on each TANI molecule, forming spinless bipolarons, thus resulting in a decline of number of unpaired spins. On the other hand, if Scheme II is applicable, then the number of bipolarons will increase linearly as the doping level increases. Therefore, in **Figure 7-7a**, both Scheme I and II should reach a certain number of spins correlated to the ratio of polaron pairs to bipolarons at a doping level of 100%.

In **Figure 7-7b-f**, we tested TANI powders with a variety of dopants and doping levels. The EPR spectra can be fit to a sum of Lorentzian and Gaussian components (**Figure S7-2a-e**), but here we focus only on the total signals. The number of spins per molecule for TANI in the EB state is less than 1 spin per 1000 molecules. Note that for $HClO_4$ doped TANI at a 100% doping level (**Figure 7-7c**), the EPR signal count agrees with what was reported in a previous study by Javadi *et al.*,[35] who observed the presence of around 2 localized spins per 100 tetramers. (Note that bipolarons can be statistically thermally excited to form polaron pairs.) Although the distributions may appear more like Scheme I, the signal intensities are much lower than 1 spin

per molecule. Considering the intensities of around 0.2 spins per molecule, *i.e.* 2 spins per 10 TANI molecules, for PTSA, HCl, CSA, and $HNO_3$ at a doping level of ~50%, even ignoring the thermally contributed polarons, less than 2 molecules would be singly-doped, but the other 8 molecules would be 50% doubly-doped and 50% undoped. A more reasonable explanation based on the spectra is that the doping mechanism mainly follows Scheme II, where only a very few dopants create singly-doped TANI. The singly-doped TANIs and thermally excited bipolarons both contribute to the total signal detected, while the few singly-doped TANI molecules make the distributions similar to Scheme I. These few singly-doped TANI molecules should give the highest number of spins at a doping level of 50% as mentioned above, and will eventually form bipolarons as the doping level increases. Note that the maximum of the number of spins per molecules for HCl, PTSA, and $HNO_3$ are slightly off from the doping level of 50%; while, the reason is not clear, it is likely due to the different acidities of acids and the evaporation of acid during the drying process.

According to our experiments, the second dopant tends to combine with the first dopant in order to form a bipolaron by sharing a phonon instead of creating two singly-doped TANI molecules. Theoretically, the lowering in energy of the whole system determines the location of the second dopant, the comparison here is different from the protonation mechanism of polyaniline where previous researchers compared two polarons to one bipolaron both on the same chain. Hence, with the same chain length and defect-free polyaniline, we expect to observe the same phenomena as with TANI not only for the initial doping step, but also predict that bipolarons will be the unit formed on subsequent doping.

## CONCLUSIONS

This work sheds light on a fundamental question as to how do dopants occupy available sites in the initial steps of doping polyaniline. By using aniline tetramers, for which the number of doping sites can be quantified, and adding in a precise number of dopants, we performed experiments in both the liquid and solid states. Optical results and PXRD spectra clearly show a transition from the EB state to the ES state for TANI at different doping levels, indicating that the partially doped materials are physical mixtures of TANI in the EB and the ES states. Our results also confirm that a doubly-charged bipolaron is the predominant unit created on doping aniline tetramers.

## EXPERIMENTAL SECTION

### Synthesis of TANI

All chemicals were purchased from Sigma-Aldrich and used without further purification. A mixture of N-phenyl-1,4-phenylenediamine, $Pd(dba)_2$, *rac*-BINAP, 1,4-dibromobenzene, sodium *tert*-butoxide, and anhydrous toluene were placed in a round bottom flask connected to a Schlenk line and reacted at 110 ℃ under argon for 24 hours. Similar to a previous report,[49] phenylhydrazine was then added and the solvent was removed from the Schlenk line after the reaction flask was cooled down to room temperature. The remaining solid was stirred with ethanol until the solid appeared light gray in color and the supernatant turned light blue. The solid was then dried via dynamic pumping overnight. The powder, in the leucoemeraldine oxidation state, was dissolved in DMF, and a solution of ammonium persulfate in hydrochloric acid was added drop-wise. After stirring for 30 min, deionized water was added and the solution stirred for another 15 min. The final product was collected via centrifugation after drying

overnight via dynamic pumping. The purity of the synthesized TANI as characterized by MALDI-TOF and $^{1}$H NMR, as seen in **Figures S7-3, S7-4**.

**Preparation of EPR samples**

4 mg samples of undoped phenyl-capped aniline tetramer powder were put into 20 ml glass vials with aliquots of 0.01 M acid and 2 ml of ethanol each for studying the different doping levels. The vials were put into a fume hood with the sash shut making sure that no volatile acidic or basic chemicals were present. The solutions were air-dried in the fume hood for around two days and the powders were then scraped down from the sides of the vials using a disposable plastic spatula. After weighing the powders with a microbalance (Mettler Toledo), the powders were carefully transferred into 4 mm thin wall quartz EPR sample tubes (250 mm in length from Wilmad Lab-Glass).

**Characterization**

The synthesized phenyl-capped aniline tetramer powders were characterized using an Applied Biosystems Voyager-DE-STR Matrix-Assisted Laser/Ionization-Time-of-Flight (MALDI-TOF) spectrometer with 2,5-dihydroxybenzoic acid (DHB) as the matrix. NMR spectroscopy was conducted on a Bruker AV 400. The UV-vis spectra were taken on a Shimadzu UV-3101 PC UV-vis-NIR Scanning Spectrophotometer with quartz cuvettes. Pure ethanol was used as the reference. The optical images were taken with a Zeiss Axiotech Materials Microscope. Powder XRD spectra were collected on a Bruker D8 X-ray powder diffractometer using Cu Kα radiation with a wavelength of 0.15418 nm. The EPR signals were detected using a Bruker EMX X-band EPR spectrometer operating at 9.76 GHz at room temperature. The number of spins per molecule

were determined by integrating the area under the absorption peaks and then correlating that area to a precise number of spins by using 4-Hydroxy-TEMPO as a standard.

**ACKNOWLEDGMENTS**

The authors thank Dr. Kan Wang for help with synthesis, Dr. Xin Cong for assistance with MALDI-TOF, Dr. Robert Taylor for help with quantitative EPR, and Dr. Jessica (Yue) Wang for helpful discussions. We thank the LA Sustainability grant for financial support.

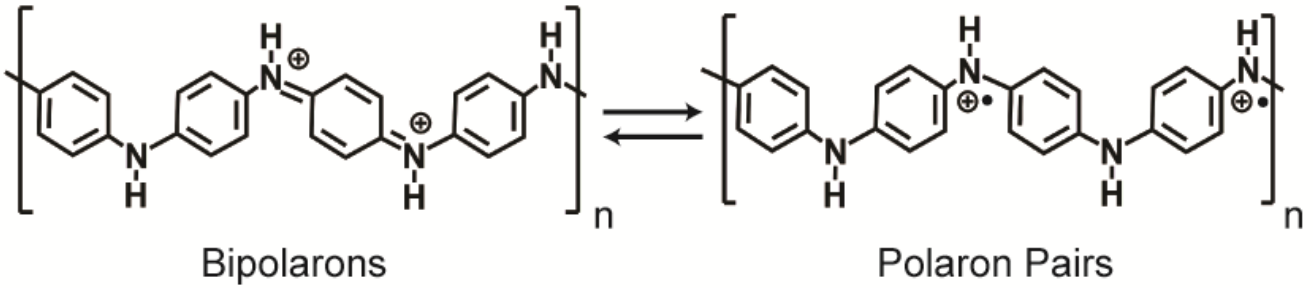


**Figure 7-1.** Upon doping, polyaniline can form bipolarons (left) and/or polaron pairs (right).

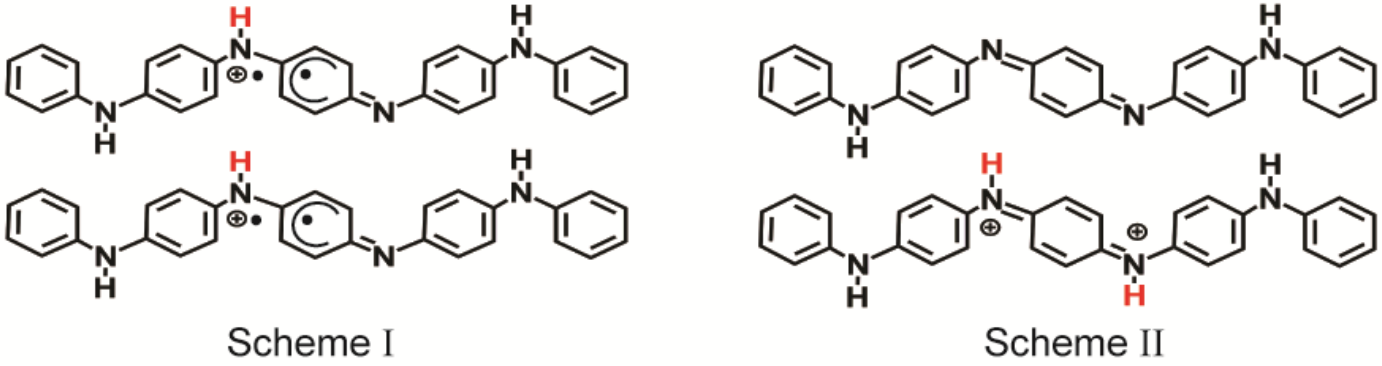


**Figure 7-2.** Doping of tetraaniline (TANI) with insufficient dopants can lead to: singly-doped TANIs (Scheme I) or doubly-doped TANI along with undoped TANI (Scheme II).

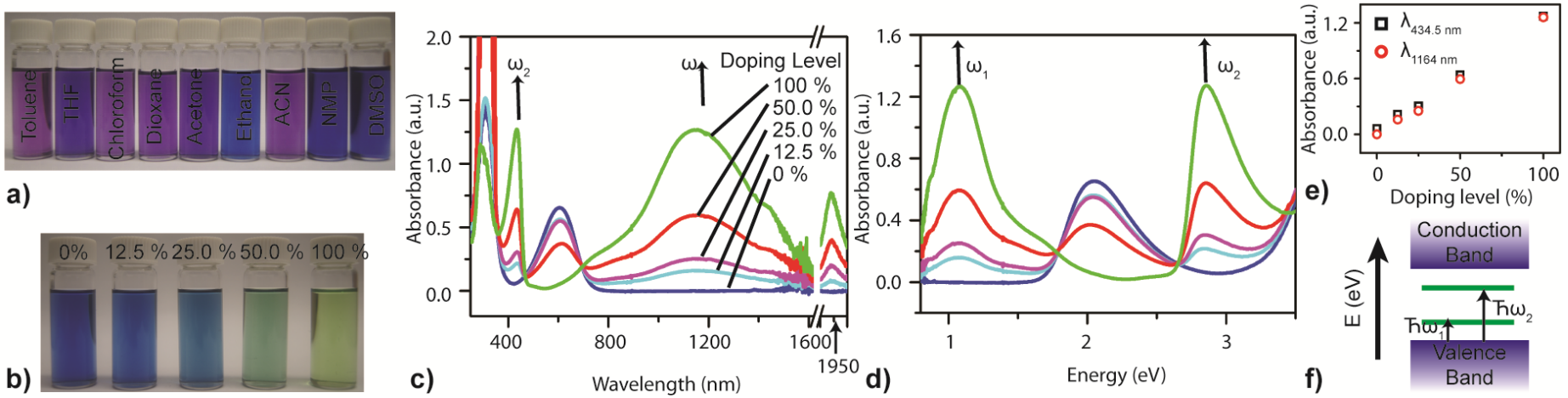


**Figure 7-3.** The doping states of TANI can be distinguished visually. (a) Photo showing emeraldine base TANI dispersed in different solvents. (b) Photo of TANI in ethanol at doping levels of 0, 12.5, 25.0, 50.0 and 100%. The absorbance versus (c) wavelength and (d) energy from Figure 3(b) indicating the formation of bipolarons (up arrows) upon doping. (e) The absorbances at both 434.5 nm and 1164.0 nm show a linear relationship with the doping level, confirming the presence of doubly-doped and undoped TANI. (f) The energy level diagram for the bipolaron state showing the allowed optical transitions responsible for the two absorption peaks, $\omega_1$ and $\omega_2$.

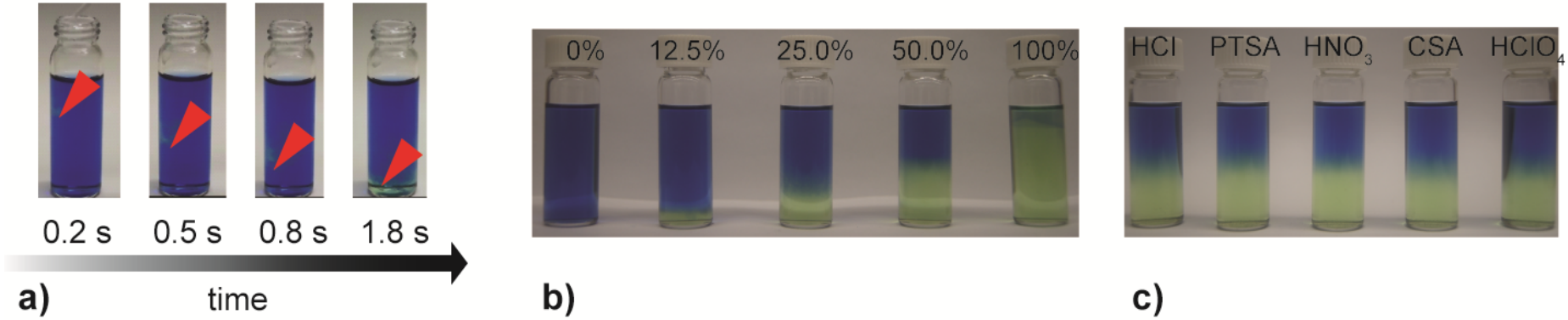


**Figure 7-4.** (a) Snapshots showing the progression of TANI emeraldine base in ethanol being doped by a drop of acid without shaking. (b) Photo showing TANI in ethanol being doped by HCl at doping levels of 0, 12.5, 25.0, 50.0 and 100% under static conditions. (c) The separation phenomena can also be achieved with the acids HCl, PTSA, $HNO_3$, CSA and $HClO_4$.

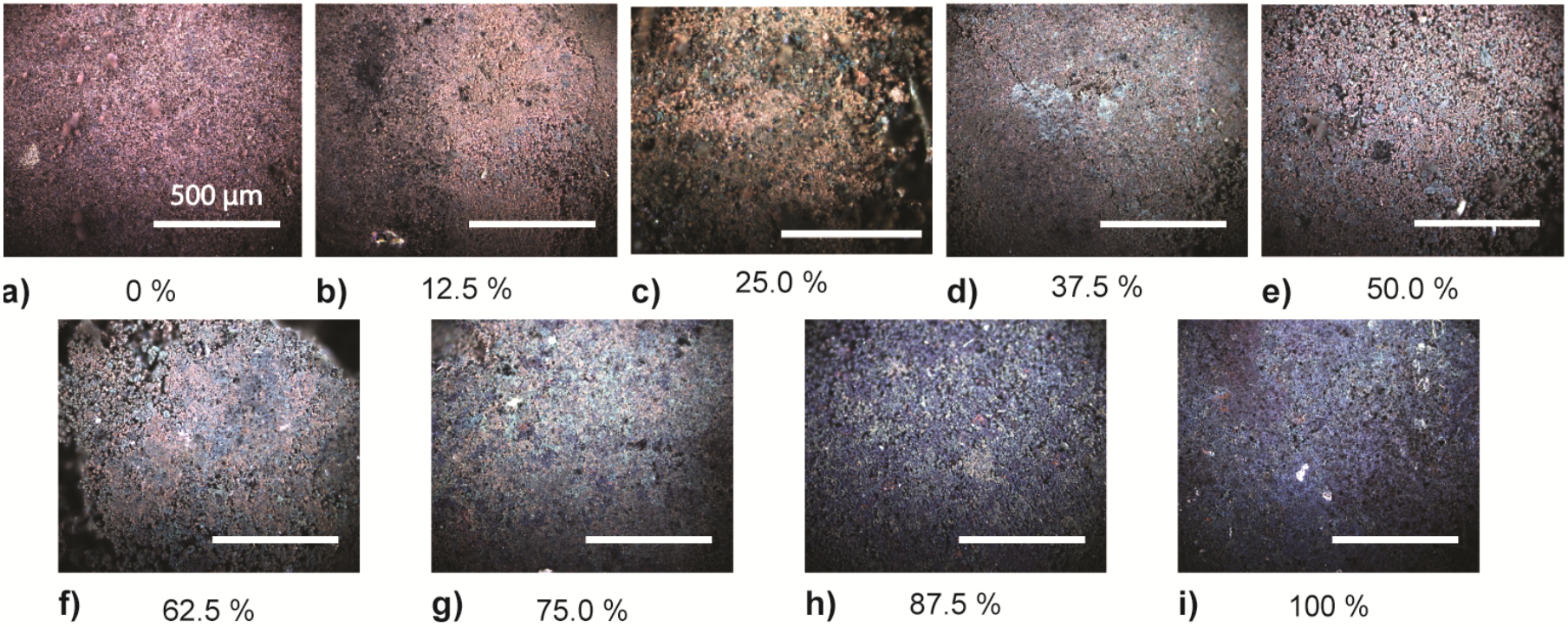


**Figure 7-5.** (a-i) Optical images of TANI powders with HCl doping levels of 0, 12.5, 25.0, 37.5, 50.0, 62.5, 75.0, 87.5 and 100%.

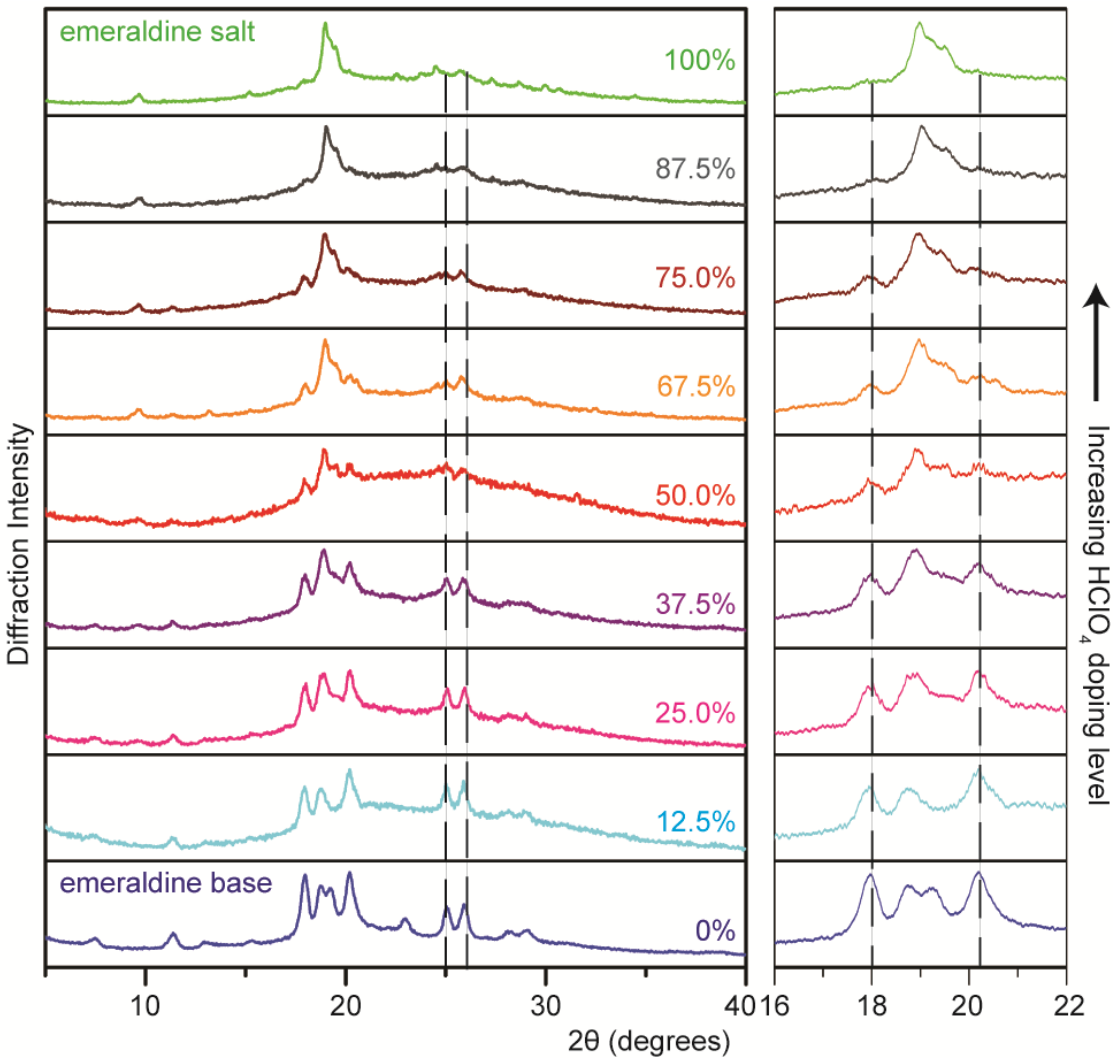


**Figure 7-6.** PXRD spectra of TANI powders doped with $HClO_4$ at levels of 0, 12.5, 25.0, 37.5, 50.0, 62.5, 75.0, 87.5 and 100%. Note the presence of two distinct crystalline species, *i.e.* emeraldine base and emeraldine salt for each level of partially doped TANI.

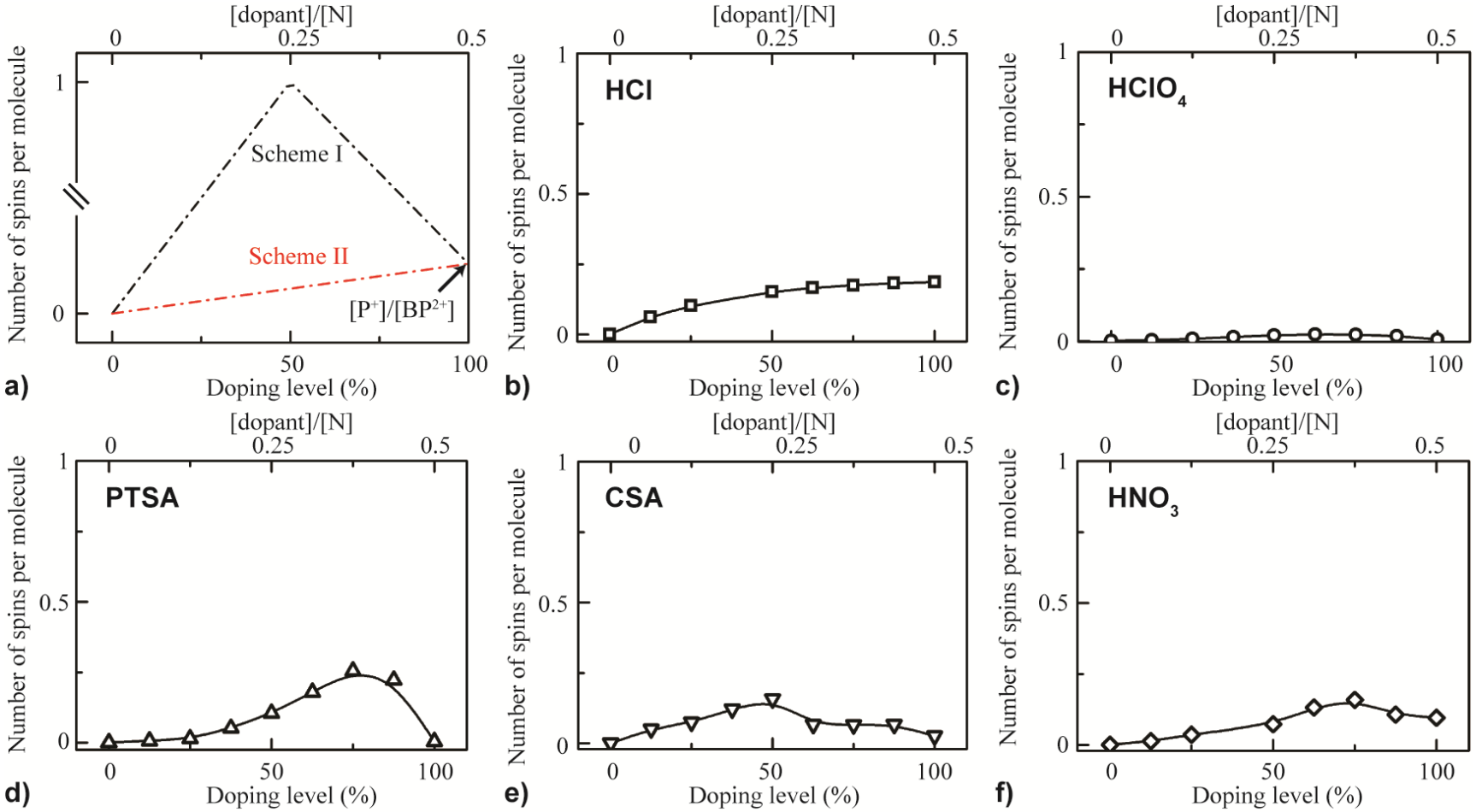


**Figure 7-7.** (a) The EPR signal, *i.e.* the number of spins as a function of doping level for Scheme I and Scheme II as proposed in Figure 2. (b-f) The EPR signals obtained from TANI powders with the acids HCl, $HClO_4$, PTSA, CSA and $HNO_3$ plotted at doping levels of 0, 12.5, 25.0, 37.5, 50.0, 62.5, 75.0, 87.5 and 100%.

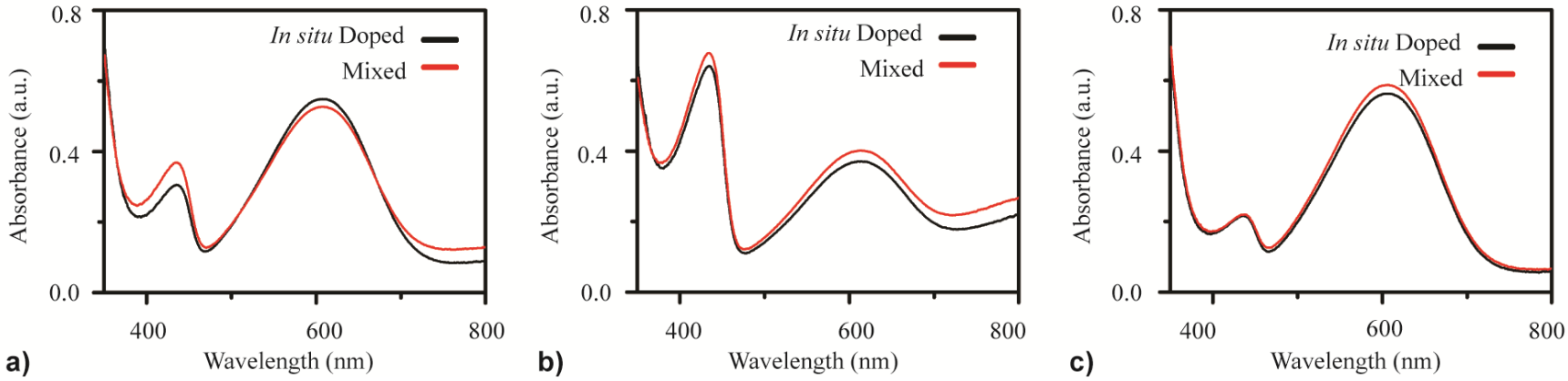


**Figure S7-1.** The uniformity of UV-vis spectra between two different methods: *in situ* acid doping and proportional mixing of the emeraldine base (EB) and the emeraldine salt (ES) solutions. Comparions between UV-vis spectra for different doping levels: (a) 12.5%, (b) 25.0%, (c) 50.0%.

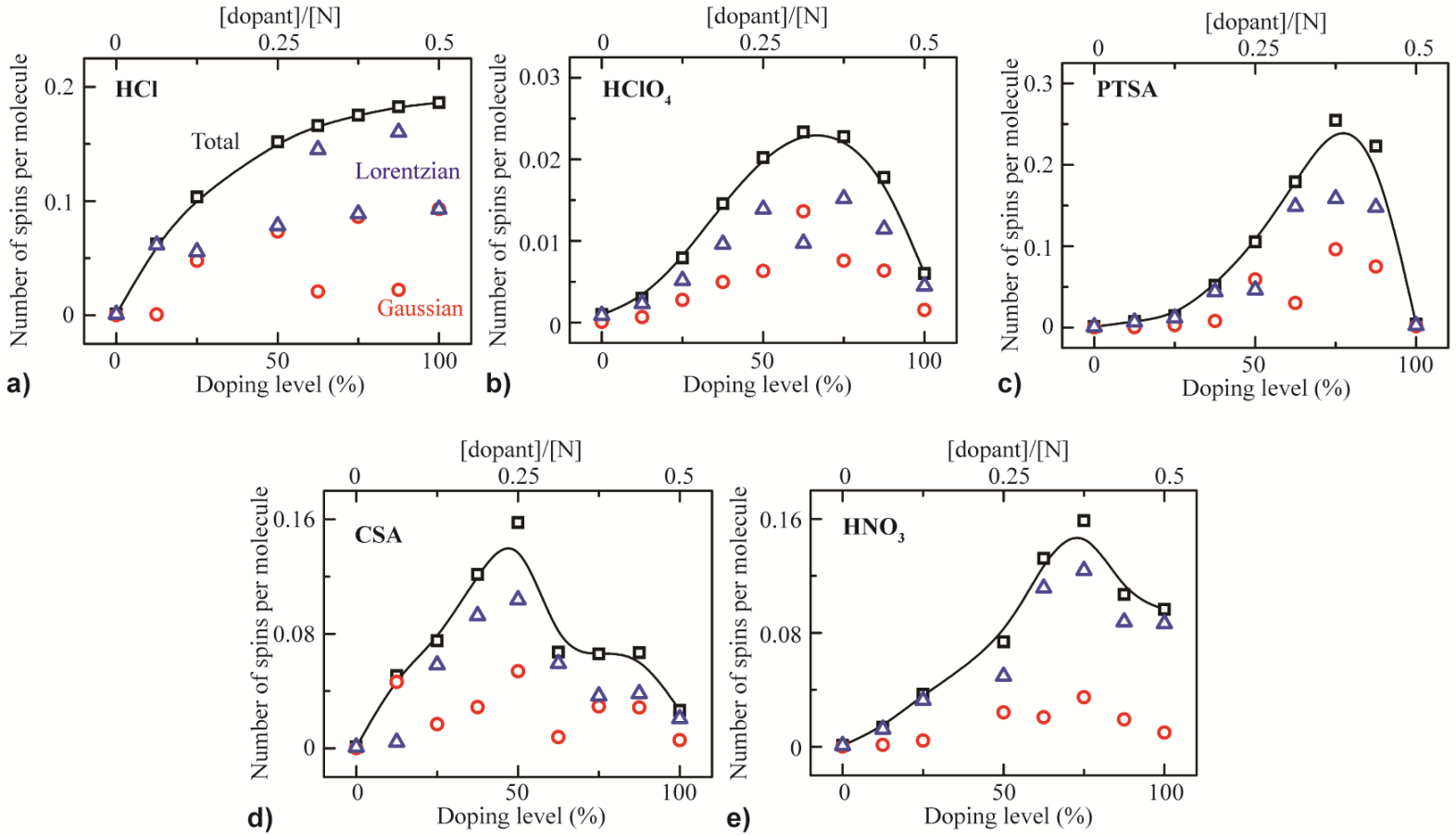


**Figure S7-2.** The EPR signals fit to Gaussian and Lorentzian distributions as obtained from TANI powders doped with the acids: (a) HCl, (b) $HClO_4$, (c) PTSA, (d) CSA, and (e) $HNO_3$.

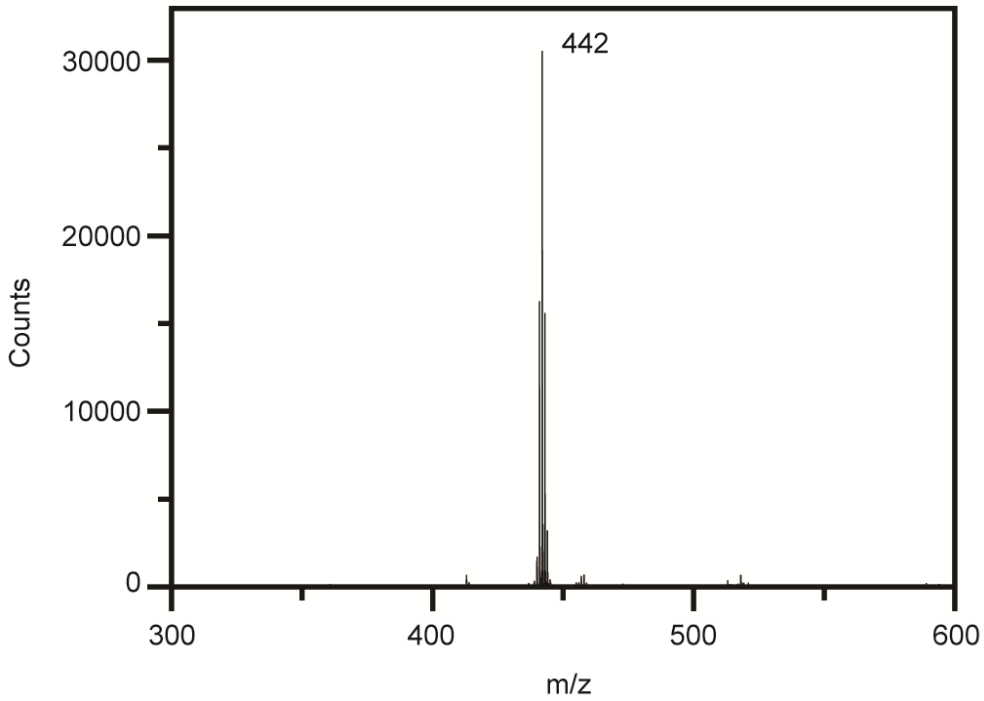


**Figure S7-3.** MALDI-TOF spectrum showing the molar mass of synthesized TANI with 2,5-dihydroxybenzoic acid (DHB) as the matrix. The calculated molar mass for TANI, $C_{30}N_4H_{26}$ is 442.21.

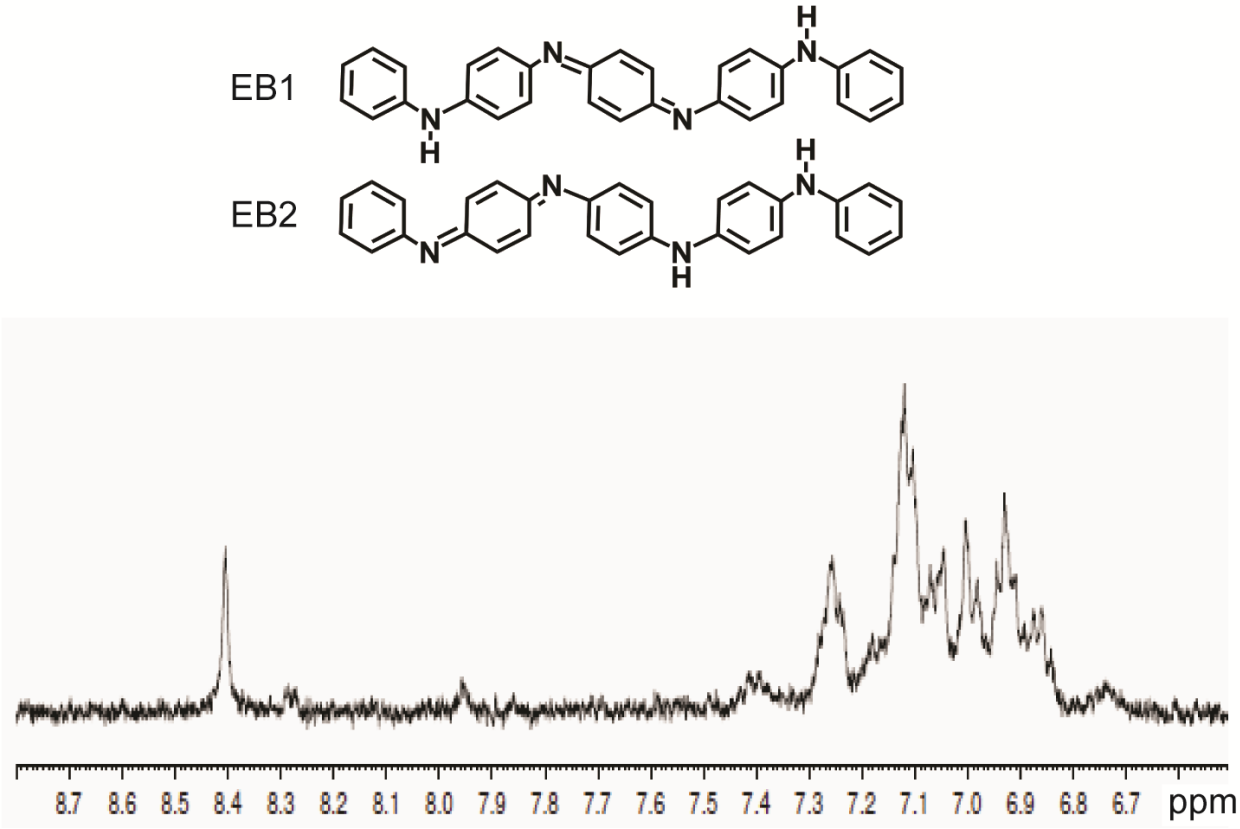


**Figure S7-4.** $^{1}$H NMR spectrum of TANI in the EB state in deuterated DMSO. The peak at 8.405 ppm is attributed to the isomer EB1. The two minor peaks at 8.286 and 7.957 are attributed to another isomer, EB2.[50] The characteristic peaks at 7.74 and 7.58 for leucoemeraldine base TANI are very low, indicating almost all the product is in the emeraldine base state and not the leucoemeraldine state.

## REFERENCES


1. Heeger, A. J. Semiconducting and Metallic Polymers: The Fourth Generation of Polymeric Materials (Nobel Lecture). *Angewandte Chemie International Edition* **2001,** 40 (14), 2591-2611 DOI: 10.1002/1521-3773(20010716)40:14<2591::AID-ANIE2591>3.0.CO;2-0.

2. MacDiarmid, A. G. "Synthetic Metals": A Novel Role for Organic Polymers (Nobel Lecture). *Angewandte Chemie International Edition* **2001,** 40 (14), 2581-2590 DOI: 10.1002/1521-3773(20010716)40:14<2581::AID-ANIE2581>3.0.CO;2-2.

3. Shirakawa, H. The Discovery of Polyacetylene Film: The Dawning of an Era of Conducting Polymers (Nobel Lecture). *Angewandte Chemie International Edition* **2001,** 40 (14), 2574-2580 DOI: 10.1002/1521-3773(20010716)40:14<2574::AID-ANIE2574>3.0.CO;2-N.

4. Huang, J.; Virji, S.; Weiller, B. H.; Kaner, R. B. Polyaniline Nanofibers: Facile Synthesis and Chemical Sensors. *Journal of the American Chemical Society* **2003,** 125 (2), 314-315 DOI: 10.1021/ja028371y.

5. Janata, J.; Josowicz, M. Conducting polymers in electronic chemical sensors. *Nat Mater* **2003,** 2 (1), 19-24.

6. Baughman, R. H. Conducting polymer artificial muscles. *Synthetic Metals* **1996,** 78 (3), 339-353 DOI: http://dx.doi.org/10.1016/0379-6779(96)80158-5.

7. Baker, C. O.; Shedd, B.; Innis, P. C.; Whitten, P. G.; Spinks, G. M.; Wallace, G. G.; Kaner, R. B. Monolithic Actuators from Flash-Welded Polyaniline Nanofibers. *Advanced Materials* **2008,** 20 (1), 155-158 DOI: 10.1002/adma.200602864.

8. Wu, Q.; Xu, Y.; Yao, Z.; Liu, A.; Shi, G. Supercapacitors Based on Flexible Graphene/Polyaniline Nanofiber Composite Films. *ACS Nano* **2010,** 4 (4), 1963-1970 DOI: 10.1021/nn1000035.

9. Liu, T.; Finn, L.; Yu, M.; Wang, H.; Zhai, T.; Lu, X.; Tong, Y.; Li, Y. Polyaniline and Polypyrrole Pseudocapacitor Electrodes with Excellent Cycling Stability. *Nano Letters* **2014,** 14 (5), 2522-2527 DOI: 10.1021/nl500255v.

10. Guimard, N. K.; Gomez, N.; Schmidt, C. E. Conducting polymers in biomedical engineering. *Progress in Polymer Science* **2007,** 32 (8–9), 876-921 DOI: http://dx.doi.org/10.1016/j.progpolymsci.2007.05.012.

11. Sapp, S. A.; Sotzing, G. A.; Reynolds, J. R. High Contrast Ratio and Fast-Switching Dual Polymer Electrochromic Devices. *Chemistry of Materials* **1998,** 10 (8), 2101-2108 DOI: 10.1021/cm9801237.

12. Ma, Y.; Zhang, J.; Zhang, G.; He, H. Polyaniline Nanowires on Si Surfaces Fabricated with DNA Templates. *Journal of the American Chemical Society* **2004,** 126 (22), 7097-7101 DOI: 10.1021/ja039621t.

13. Wessling, B. Passivation of metals by coating with polyaniline: Corrosion potential shift and morphological changes. *Advanced Materials* **1994,** 6 (3), 226-228 DOI: 10.1002/adma.19940060309.

14. Li, D.; Huang, J.; Kaner, R. B. Polyaniline Nanofibers: A Unique Polymer Nanostructure for Versatile Applications. *Accounts of Chemical Research* **2009,** 42 (1), 135-145 DOI: 10.1021/ar800080n.

15. Chiou, N.-R.; Lu, C.; Guan, J.; Lee, L. J.; Epstein, A. J. Growth and alignment of polyaniline nanofibres with superhydrophobic, superhydrophilic and other properties. *Nat Nano* **2007,** 2 (6), 354-357 DOI: http://www.nature.com/nnano/journal/v2/n6/suppinfo/nnano.2007.147_S1.html.

16. Varela-Álvarez, A.; Sordo, J. A.; Scuseria, G. E. Doping of Polyaniline by Acid−Base Chemistry: Density Functional Calculations with Periodic Boundary Conditions. *Journal of the American Chemical Society* **2005,** 127 (32), 11318-11327 DOI: 10.1021/ja051012t.

17. Lee, K.; Cho, S.; Heum Park, S.; Heeger, A. J.; Lee, C.-W.; Lee, S.-H. Metallic transport in polyaniline. *Nature* **2006,** 441 (7089), 65-68.

18. Wang, Y.; Tran, H. D.; Liao, L.; Duan, X.; Kaner, R. B. Nanoscale Morphology, Dimensional Control, and Electrical Properties of Oligoanilines. *Journal of the American Chemical Society* **2010,** 132 (30), 10365-10373 DOI: 10.1021/ja1014184.

19. Wang, Y.; Liu, J.; Tran, H. D.; Mecklenburg, M.; Guan, X. N.; Stieg, A. Z.; Regan, B. C.; Martin, D. C.; Kaner, R. B. Morphological and Dimensional Control via Hierarchical Assembly of Doped Oligoaniline Single Crystals. *Journal of the American Chemical Society* **2012,** 134 (22), 9251-9262 DOI: 10.1021/ja301061a.

20. Dane, T. G.; Cresswell, P. T.; Bikondoa, O.; Newby, G. E.; Arnold, T.; Faul, C. F. J.; Briscoe, W. H. Structured oligo(aniline) nanofilms via ionic self-assembly. *Soft Matter* **2012,** 8 (10), 2824-2832 DOI: 10.1039/C2SM06492H.

21. Faul, C. F. J. Ionic Self-Assembly for Functional Hierarchical Nanostructured Materials. *Accounts of Chemical Research* **2014,** 47 (12), 3428-3438 DOI: 10.1021/ar500162a.

22. Ford, W. E.; Gao, D.; Scholz, F.; Nelles, G.; von Wrochem, F. Conductance Modulation in Tetraaniline Monolayers by HCl-Doping and by Field-Enhanced Dissociation of H2O. *ACS Nano* **2013,** 7 (3), 1943-1951 DOI: 10.1021/nn3050769.

23. Yan, J.; Yang, L.; Cui, M.; Wang, X.; Chee, K. J.; Nguyen, V. C.; Kumar, V.; Sumboja, A.; Wang, M.; Lee, P. S. Aniline Tetramer-Graphene Oxide Composites for High Performance Supercapacitors. *Advanced Energy Materials* **2014,** 4 (18), n/a-n/a DOI: 10.1002/aenm.201400781.

24. Bell, O. A.; Wu, G.; Haataja, J. S.; Brömmel, F.; Fey, N.; Seddon, A. M.; Harniman, R. L.; Richardson, R. M.; Ikkala, O.; Zhang, X.; Faul, C. F. J. Self-Assembly of a Functional

Oligo(Aniline)-Based Amphiphile into Helical Conductive Nanowires. *Journal of the American Chemical Society* **2015,** 137 (45), 14288-14294 DOI: 10.1021/jacs.5b06892.

25. Guo, B.; Finne-Wistrand, A.; Albertsson, A.-C. Electroactive Hydrophilic Polylactide Surface by Covalent Modification with Tetraaniline. *Macromolecules* **2012,** 45 (2), 652-659 DOI: 10.1021/ma202508h.

26. MacDiarmid, A. G.; Zhou, Y.; Feng, J. Oligomers and isomers: new horizons in poly-anilines. *Synthetic Metals* **1999,** 100 (1), 131-140 DOI: http://dx.doi.org/10.1016/S0379-6779(98)00164-7.

27. Bredas, J. L.; Street, G. B. Polarons, bipolarons, and solitons in conducting polymers. *Accounts of Chemical Research* **1985,** 18 (10), 309-315 DOI: 10.1021/ar00118a005.

28. Stafström, S.; Brédas, J. L.; Epstein, A. J.; Woo, H. S.; Tanner, D. B.; Huang, W. S.; MacDiarmid, A. G. Polaron lattice in highly conducting polyaniline: Theoretical and optical studies. *Physical Review Letters* **1987,** 59 (13), 1464-1467.

29. McCall, R. P.; Ginder, J. M.; Leng, J. M.; Ye, H. J.; Manohar, S. K.; Masters, J. G.; Asturias, G. E.; MacDiarmid, A. G.; Epstein, A. J. Spectroscopy and defect states in polyaniline. *Physical Review B* **1990,** 41 (8), 5202-5213.

30. Pouget, J. P.; Jozefowicz, M. E.; Epstein, A. J.; Tang, X.; MacDiarmid, A. G. X-ray structure of polyaniline. *Macromolecules* **1991,** 24 (3), 779-789 DOI: 10.1021/ma00003a022.

31. Nowak, M.; Rughooputh, S. D. D. V.; Hotta, S.; Heeger, A. J. Polarons and bipolarons on a conducting polymer in solution. *Macromolecules* **1987,** 20 (5), 965-968 DOI: 10.1021/ma00171a013.

32. Canales, M.; Torras, J.; Fabregat, G.; Meneguzzi, A.; Alemán, C. Polyaniline Emeraldine Salt in the Amorphous Solid State: Polaron versus Bipolaron. *The Journal of Physical Chemistry B* **2014,** 118 (39), 11552-11562 DOI: 10.1021/jp5067583.

33. Petrova, J.; Romanova, J.; Madjarova, G.; Ivanova, A.; Tadjer, A. Absorption Spectra of Model Single Chains of Conducting Polyaniline. *The Journal of Physical Chemistry B* **2012,** 116 (22), 6543-6552 DOI: 10.1021/jp301814u.

34. Shacklette, L. W.; Wolf, J. F.; Gould, S.; Baughman, R. H. Structure and properties of polyaniline as modeled by single-crystal oligomers. *The Journal of Chemical Physics* **1988,** 88 (6), 3955-3961 DOI: 10.1063/1.453844.

35. Javadi, H. H. S.; Treat, S. P.; Ginder, J. M.; Wolf, J. F.; Epstein, A. J. Aniline tetramers: Comparison with aniline octamer and polyaniline. *Journal of Physics and Chemistry of Solids* **1990,** 51 (2), 107-112 DOI: http://dx.doi.org/10.1016/0022-3697(90)90080-Y.

36. Petrova, J. N.; Romanova, J. R.; Madjarova, G. K.; Ivanova, A. N.; Tadjer, A. V. Fully Doped Oligomers of Emeraldine Salt: Polaronic versus Bipolaronic Configuration. *The Journal of Physical Chemistry B* **2011,** 115 (14), 3765-3776 DOI: 10.1021/jp111914n.

37. Sjögren, B.; Stafström, S. Electronic excitations in polyaniline: An INDO/S-CI study. *The Journal of Chemical Physics* **1988,** 88 (6), 3840-3847 DOI: 10.1063/1.453885.

38. Wienk, M. M.; Janssen, R. A. J. Stable Triplet-State Di(Cation Radicals) of a Meta−Para Aniline Oligomer by "Acid Doping". *Journal of the American Chemical Society* **1996,** 118 (43), 10626-10628 DOI: 10.1021/ja9616591.

39. González, S. R.; Ie, Y.; Aso, Y.; López Navarrete, J. T.; Casado, J. The Frontiers of Quinoidal Stability in Long Oligothiophenes: Raman Spectra of Dicationic Polaron Pairs. *Journal of the American Chemical Society* **2011,** 133 (41), 16350-16353 DOI: 10.1021/ja2061903.

40. Liptay, W. Elektrochromie – Solvatochromie. *Angewandte Chemie* **1969,** 81 (6), 195-206 DOI: 10.1002/ange.19690810602.

41. Cao, Y.; Li, S.; Xue, Z.; Guo, D. Spectroscopic and electrical characterization of some aniline oligomers and polyaniline. *Synthetic Metals* **1986,** 16 (3), 305-315 DOI: http://dx.doi.org/10.1016/0379-6779(86)90167-0.

42. Kwon, O.; McKee, M. L. Calculations of Band Gaps in Polyaniline from Theoretical Studies of Oligomers. *The Journal of Physical Chemistry B* **2000,** 104 (8), 1686-1694 DOI: 10.1021/jp9910946.

43. Epstein, A. J.; Ginder, J. M.; Zuo, F.; Bigelow, R. W.; Woo, H. S.; Tanner, D. B.; Richter, A. F.; Huang, W. S.; MacDiarmid, A. G. Insulator-to-metal transition in polyaniline. *Synthetic Metals* **1987,** 18 (1), 303-309 DOI: http://dx.doi.org/10.1016/0379-6779(87)90896-4.

44. Beer. Bestimmung der Absorption des rothen Lichts in farbigen Flüssigkeiten. *Annalen der Physik* **1852,** 162 (5), 78-88 DOI: 10.1002/andp.18521620505.

45. Wang, C. L.; Su, Z. B.; Martino, F. Bipolaron dynamics in nearly degenerate quasi-one-dimensional polymers. *Physical Review B* **1986,** 33 (2), 1512-1515.

46. Kramers, H. A. Brownian motion in a field of force and the diffusion model of chemical reactions. *Physica* **1940,** 7 (4), 284-304 DOI: http://dx.doi.org/10.1016/S0031-8914(40)90098-2.

47. Zhou, Y.; Geng, J.; Li, G.; Zhou, E.; Chen, L.; Zhang, W. Crystal structure and morphology of phenyl-capped tetraaniline in the leucoemeraldine oxidation state. *Journal of Polymer Science Part B: Polymer Physics* **2006,** 44 (4), 764-769 DOI: 10.1002/polb.20700.

48. Wang, Y.; Torres, J. A.; Stieg, A. Z.; Jiang, S.; Yeung, M. T.; Rubin, Y.; Chaudhuri, S.; Duan, X.; Kaner, R. B. Graphene-Assisted Solution Growth of Vertically Oriented Organic Semiconducting Single Crystals. *ACS Nano* **2015,** 9 (10), 9486-9496 DOI: 10.1021/acsnano.5b03465.

49. Shao, Z.; Rannou, P.; Sadki, S.; Fey, N.; Lindsay, D. M.; Faul, C. F. J. Delineating Poly(Aniline) Redox Chemistry by Using Tailored Oligo(Aryleneamine)s: Towards Oligo(Aniline)-Based Organic Semiconductors with Tunable Optoelectronic Properties. *Chemistry – A European Journal* **2011,** 17 (44), 12512-12521 DOI: 10.1002/chem.201101697.

50. E. Rebourt, J.A. Joule, A.P. Monkman, *Synthetic Metals*, **1997**, 84, 65-66.

# CHAPTER 8. CATALYTIC EFFECTS OF ANILINE POLYMERIZATION ASSISTED BY OLIGOMERS


## ABSTRACT

Polyaniline was first confirmed as a dark green precipitate on an electrode during the electrochemical polymerization of aniline in 1862. Since then, scientists have been studying the kinetics and growth mechanisms of polyaniline through the electrochemical approach. Studies have shown that p-phenylenediamine, p-aminodiphenylamine, and other aromatic small molecules may serve as initiators for accelerating the polymerization reaction due to the autocatalytic effect of polyaniline. However, little research has been focused on the catalytic effects of introducing the oligoanilines. In this paper, quantitative rate constants for the electrochemical polymerization of aniline in both HCl and acetonitrile/HCl solutions with 0.5 mol% of added oligoanilines including diphenylamine, N-phenyl-p-phenylenediamine, 1,4-phenylenediamine, N,N'-diphenyl-1,4-phenylenediamine, 4,4'-diaminodiphneylamine, and tetraaniline in both emeraldine and leucoemeraldine states are reported. Among all the rate constants, N-phenyl-p-phenylenediamine, 1,4-phenylenediamine, and 4,4'-diaminodiphneylamine are shown to be the most effective catalysts for aniline polymerization. Tetraaniline is likely the intermediate species where the polymerization process starts to slow down, while diphenylamine and N,N'-diphenyl-1,4-phenylenediamine decelerate the reaction. Additionally, adding in oligothiophenes is confirmed to reduce the reaction rate. It is also shown for the first time that the rate constants measured are consistent with two other methods: 1. monitoring the open-circuit potential and 2. measuring temperature of the solution. These methods were used previously to qualitatively compare the speed of the polymerization reactions.

Additionally, the existence of both agglomerated and nanofibrillar polymer morphologies for reactions with slow rate constants are revealed.

## INTRODUCTION

Polyaniline, one of the most studied conducting polymers, was first discovered by Ferdinand Runge as a blue dye from coal tar in 1834.[1,2] Years later, an English chemist, Henry Letheby, conducted the first electrochemical reaction of aniline, and confirmed the dark green precipitate on the electrode as polyaniline.[2,3] Although some research were carried out on polyaniline during the early twentieth century, it was not until the 1970's when MacDiarmid, Heeger and Shirakawa's discovery of its electrical conducting properties did extensive research on it burgeon.[4–7] In order to investigate the growth mechanism and kinetics of the aniline polymerization process, electrochemical polymerization in aqueous inorganic acid solutions has been widely conducted.[8–10] This work indicated that the anodic current is directly proportional to the amount of the dark green precipitate deposited on the electrode.[11–14] Hence, scientists were able to quantify the rate of aniline polymerization, which has been found to be an autocatalytic reaction.[15–18]

A reaction can be considered as autocatalytic when one of the products is either a catalyst or reactant; therefore, the rate of the whole reaction should be non-linear.[19] In 1962, Mohilner *et al.* reported that the electrochemical polymerization rate of p-aminodiphenylamine (aniline dimer) is faster than that of aniline monomer. This indicates that forming aniline dimers should be the rate-determining step during aniline polymerization, while also implying autocatalysis for the polymerization of aniline.[11] Later in 1990, Wei *et al.* first introduced small amount of aromatic additives, including p-phenylenediamine, benzidine, p-aminodiphenylamine, N,N'-diphenylhydrazine, p-phenoxyaniline, hydroquinone, and N,N-diphenylamine, into the aniline

polymerization system to avoid the slow step, *i.e.* the formation of aniline dimer. By fitting the variations of the anodic peak current up to 16 mA, rate constants for each additive under various concentrations were able to be quantified.[12] Other ways to qualitatively evaluate the rate of aniline polymerization reported by Wei *et al.* include monitoring the open-circuit potential (OCP) and the temperature versus time during the chemical oxidation reaction of aniline by adding ammonium persulfate. The time duration for the chemical potential and the temperature to reach their maximum readings due to the consumption of ammonium persulfate was found to be inversely proportional to the rate of polymerization.[20]

However, kinetic studies on incorporating additives into the aniline polymerization system have dwindled as a great deal of research has turned to the field of morphology, owing to the discovery of nanofibers in 2003.[21,22] In 2004, Li and Wang reported enhancing chirality of polyaniline nanofibers with the assist of aniline oligomers.[23] Tran, thereafter, stated the intimate relationship between the rate of polymerization and the nanofibrilar morphology, and expanded the concept to different conjugated systems including polypyrrole and polythiophene.[24] However, no research to our knowledge has yet discussed the kinetics of introducing oligoanilines with longer chains into the aniline polymerization reaction. As the oxidizing potential is known to be lower for more units of oligoanilines,[25–28] the catalytic effect should not only take the oxidizing potential, *i.e.* the ease of generating radicals, into consideration, but also the factor of the probability of radical transfer.[29]

In this study, we performed thorough electrochemical polymerizations of aniline in the presence of a variety of linear aniline oligomers in both HCl and acetonitrile/HCl solutions. By fitting to the change of anodic peak current over time with higher order of polynomial equations, catalytic effects of each additive under different ranges of potential sweep were quantified.

Additionally, variations of temperature and the open-circuit potential (OCP) of solutions over time are compared to the quantified numbers of rate constant, demonstrating the consistency and practical feasibility of these two methods for measuring reaction rates. Furthermore, the kinetics of placing thiophene oligomers into the aniline system are investigated. Insights associated with the catalytic phenomena and polymer morphologies, along with the characteristics of additives, are also addressed in the following sections.

## RESULTS AND DISCUSSION

*Aniline Polymerization in HCl solutions.* In order to meticulously investigate the influence of additives, the following oligoanilines we used: aniline, N,N-diphenylamine, p-aminodiphenylamine, p-phenylenediamine, N,N'-diphenyl-1,4-phenylenediamine, 4,4'-diaminodiphenylamine, and tetraaniline in both emeraldine and leucoemeraldine states, denoted as 1A, 1′A, 2A, 2′A, 2″A, 3′A, 4A(EB), and 4A(LEB), respectively, where the first number stands for the numbers of nitrogens, the single prime represents the amino-ended molecules, and the double prime indicates the phenyl-capped molecules (**Figure 8-1**). Electrochemical polymerization conditions similar to the previous report, 0.2 M of aniline monomer and 1.0 mM additives in a 30 mL 1.0 M HCl solution, were carried out for comparisons. Potential sweeps ranging from -0.2 V to 0.8 V, 0.9 V, and 1.0 V versus Ag/AgCl were tested at a scan rate of 25 mV/s.[12]

In a typical cyclic voltammetry of the electrochemical polymerization of aniline, it is known that there are two oxidizing peaks and two reducing peaks, which correspond to the transitions from the reduced state (leucoemeraldine) to emeraldine, and emeraldine to the oxidized state (pernigraniline), and vice versa.[9] In this study, the first anodic peak current was

targeted since previous reports confirmed its linear relationship with the amount of polyaniline deposited on the platinum working electrode during the electrochemical polymerizations of aniline. The first anodic (oxidizing) peak was reported to be located at ~0.17 V versus the saturated calomel electrode (SCE), which is at ~0.215 V against the Ag/AgCl reference electrode.[9,30] In **Figure 8-2a**, the first anodic peaks are at ~0.215 V vs. Ag/AgCl and gradually increase with more scans as the potential is swept from -0.2 V to 0.8 V. Likewise, the cyclic voltammetry with a potential sweep range from -0.2 V to 0.9 V (**Figure 8-2b**) shows an increasing anodic peak current with increasing numbers of scans. However, the first anodic peaks increase as the oxidizing potentials shift to higher voltages. This phenomenon is known because of the thick layer of the polyaniline film deposited on the electrode.[12] As the polyaniline layer grows thicker on the electrode, the resistance, *i.e.* the iR drop, of the polyaniline film increases, hence, higher voltages for oxidations and lower potentials for reductions are needed for further precipitation. By observing the anodic peak current readings of the last ($40^{th}$) scan in both Figure 8-2a and 8-2b, the extremely low current for Figure 8-2a indicates that polyaniline does not tend to polymerize under the potential range of -0.2 V to 0.8 V (against Ag/AgCl), which is in agreement with previous studies; therefore, no iR drop nor shifts in potential are observed. Experimentally, little precipitate was found on the electrode with the potential sweep ranging from -0.2 V to 0.8 V, while thick cakes of deposition were observed for electrodes operated between -0.2 V to 0.9 V and -0.2 V to 1.0 V.

According to reports published around 1990, the rate of aniline electrochemical polymerization can be expressed as

$$R = k[M]i^n \qquad (8\text{-}1)$$

where i is the anodic peak current at ~0.17 V; R can be obtained from the derivatives of the anodic peak current versus scan, *i.e.* di/dt; k is the rate constant; [M] is the concentration of monomer; and n was determined empirically as 0.5.[12,18] As cyclic voltammetry curves of aniline electrochemical polymerization with and without oligoanilines were recorded under potential sweeps from -0.2 V to 0.8 V (**Figure S8-1**), -0.2 V to 0.9 V (**Figure S8-2**), and -0.2 V to 1.0 V (**Figure S8-3**), the relationships between the anodic peak current, i, and the number of scans can be plotted and fit with higher order polynomial equations in order to have every coefficient of determination greater than 0.999 (**Figure S8-4, S8-5, S8-6**). **Figure 8-3a** shows plots of i against the number of scans, for aniline electrochemical polymerization with and without aniline oligomers, with the potential swept from -0.2 V to 0.9 V. By simply taking derivatives of the equations fit in Figure S8-5, the rate of polymerization, R, can be plotted against the number of scans (**Figure 8-3b**) and the anodic peak current (**Figure 8-3c**). It is evident that each polymerization reaction reaches its own maximum rate at different numbers of scans and anodic peak current, indicating distinct catalytic effects caused by the additive. Since decelerations are likely due to the thick layers of polyaniline formed on the electrode, it would be much more meaningful for us to focus on data points before reaching the polymerization rate maxima. Note that all reactions reach their rate maximum at anodic peak currents equal or greater than ~50 mA, which is consistent with the range of anodic peak currents reported previously.[12]

By truncating the parts after the polymerization rate maxima, the anodic peak currents of aniline polymerization with the sweep range between -0.2 V and 0.9 V against the number of scans are plotted in **Figure 8-4a**. Intuitively, based on the plot of rate versus number of scans (**Figure 8-4b**), the rate of polymerization can be considered to follow the order: 3′A > 2A ≈ 2′A > 4A(LEB) > 4A(EB) ≈ 1A > 1″A > 2″A. In **Figure 8-4c**, we found that the plots of rate versus

the anodic peak current fit well with Equation 1 as multiples of k and [M] alter the amplitude of those curves, showing different levels of catalysis. Similar plots for the potential sweep range between -0.2 V to 0.8 V, and -0.2 V to 1.0 V can be found in **Figures S8-7** and **S8-8**. In order to carefully examine the rate constant, plots of rate versus the square root of the anodic peak current are plotted. Based on Equation 1, the slope of the plot should be a multiple of the rate constant, k, and the concentration of aniline, [M]. As shown in **Figure 8-5**, two slopes were fit for i < 9 mA, and i > 9 mA for better fittings, indicating that two mechanisms likely exist for the electrochemical polymerization of aniline with the potential sweep range from -0.2 V to 0.9 V. However, only a single polymerization kinetics seems to apply based on the existence of one certain slope for each curve in the graphs of rate versus the anodic peak current for -0.2 V to 0.8 V and -0.2 V to 1.0 V. The reason may be attributed to the electrochemical polymerization processes that tend not to occur when the potential is swept between -0.2 V to 0.8 V. Hence the anodic peak readings are small. Applying a high voltage, *i.e.* 1.0 V, shortens the time duration to reach a high value of anodic current (**Figure S8-9, S8-10**).

The rate constants, with the unit of $mA^{1/2}\ M^{-1}\ scan^{-1}$, are plotted in **Figure 8-6**. The rate constants reveal that the electrochemical polymerization of aniline does not tend to form polyaniline when the potential applied is less than 0.8 V against Ag/AgCl as the rate constants at 0.8 V are significantly lower than that at 0.9 V and 1.0 V. A higher potential directly leads to a higher rate constant, except for 1″A where the rate constant for 1.0 V is even lower than that for 0.9 V. Based on the rate constants at 0.8 V, it is evident that 2A, 2′A, 3′A, 4AEB, and 4ALEB can catalyze the polymerization as the second rate constant, $k_2$, from -0.2 V to 0.9 V and the rate constant, $k_2$, from -0.2 V to 1.0 V, only 2A, 2′A, and 3′A show conspicuous enhancements. Both 4A(EB) and 4A(LEB) show significantly higher rate constants for 0.8 V compared to the system

without additives, which may be attributed to the conductive nature of tetraaniline itself,[31,32] but no apparent improvement is observed for 0.9 V and 1.0 V compared to the polymerization of aniline without additives. Therefore, we speculate that the polymerization reaction accelerates before the formation of tetramer, which might be the intermediate step during aniline polymerization where the rate begins to decline. It is noteworthy that the first rate constant, $k_1$, at 0.9 V is much greater than the second rate constant, $k_2$, for 2A, 2′A, and 3′A, indicating that the catalytic effect initiates a sharp acceleration at the very beginning of the polymerization reaction, followed by a comparatively slower mechanism.

All rate constants and oxidation potentials for each material are listed in **Table 8-1**. The general order of the polymerization rate may be concluded as follow: 3′A > 2′A > 2A > 4A(LEB) ≈ 4A(EB) ≈ no additives > 2″A > 1″A. This order is consistent with what Wei *et al.* reported where only 2′A, 2A, and 1′A were investigated.[12] In order to increase the polymerization rate of aniline, Wei *et al.* concluded that the additives must have a lower oxidation potential than aniline, and at least one sterically accessible amino group should be present. The relatively high oxidation potential for 1″A and its phenyl-capped structure should therefore cause extremely low rate constants. However, 2″A with the phenyl-capped structure seems not to decelerate the polymerization reaction very much. The reason may be because of the low dispersity of 2″A in a1.0 M HCl solution. As molecules of 2″A tend to stay at the interface between the aqueous solution and air, 2″A tends to show little influence on the rate constants. In a later section, where a mixture of half acetonitrile and half HCl solution is used, the decrease of the rate constant for 2″A can be readily observed. Also, the measured rate constants, k, are not proportional to the oxidation potentials, meaning that oligoanilines with longer chains are not guaranteed to speed

up the polymerization reaction as the oxidation potential of oligoanilines is known to decrease with longer chain lengths.

For further elucidation, we first compare 3′A and 2A, where the rate constants for 3′A are greater than for 2A. The oxidation potentials for 3′A and 2A are 0.574 V and 0.588 V, respectively, as listed in Table 8-1. The huge differences in rate constants should not be solely attributed to the tiny oxidation potential difference (0.014 V). In terms of molecular structures, 3′A possesses two amine groups at both ends of the molecule, while 2A only has one accessible amine group. Likewise, the rate constants of 2′A are higher than that of 2A, but the oxidation potential of 2′A (0.670 V) is higher than 2A (0.588 V). Based on the two abovementioned cases, we realize that a lower oxidation potential compared to that of aniline is essential for accelerating the reaction, but the structure of the molecule, *i.e.* phenyl or amino groups, can dramatically affect the rate constant when the oxidation potential of such a molecule is lower than that of aniline.

Another way to compare the rate of electrochemical polymerization of aniline reported is to measure the temperature of the reaction solution over time.[20] This method is based on the exothermic oxidation expected during aniline polymerization with a fixed amount of oxidizing agent, ammonium persulfate in this case. Theoretically, the slower the reaction is, the slower the oxidizing agent will be consumed, therefore it takes more time for the solution to reach its maximum temperature. In **Figure 8-7**, profiles of temperature versus time with and without additives are shown. Instead of just focusing on the time to reach the temperature maximum, we also define the time for the reaction's temperature to start increasing as $t_1$, and the time duration between the temperature starts to rise and the peak of temperature as $t_2$. Therefore, the time duration $t_1$ indicates when the oxidation reaction starts, and $t_1 + t_2$ is the time for oxidation

reactions to end. In **Figure 8-8**, $t_1$ is found to be linearly proportional to $t_1 + t_2$, indicating that the earlier the reactants are being oxidized, the faster the reaction is to be terminated. Since the amount of additives is almost negligible compared to the concentration of aniline, *i.e.* the heat released by oxidizing additives is not likely be the reason to cause the rise of temperature, we postulate that $t_1$ reflects the generation of radicals on monomers and just about to start polymerize, which is affected by the additives added in. For example, a relatively small $t_1$ caused by the introduction of an initiator, meaning that the radicals are easier to generate and propagate for further polymerization, hence, the polymerization should have a higher rate constant.

The third method proposed by Wei is to monitor the OCP versus time.[20] The chemical potential of the oxidizing agent, ammonium persulfate, in a solution can be simply measured through a two electrode setup. Similar to the abovementioned temperature measurement, the ammonium persulfate would be consumed sooner if the polymerization reaction is faster. Therefore, the time durations for the OCP starts to decline, t, would be an indicator for evaluating the rate of polymerization. In **Figure 8-9**, it is clear that 1″A has the slowest rate of polymerization while 3′A has the fastest. By comparing the time, t, for OCP and $t_1 + t_2$ for temperature measurement, a linear relationship is found (**Figure 8-10**), showing that these two methods are coherent. In order to examine whether these two methods can be well related to the rates of polymerization comparatively, contour mappings with rate constants at 0.8 V (**Figure 8-11a**), 0.9 V (**Figure 8-11b** for $k_1$, and **Figure 8-11c** for $k_2$), and 1.0 V (**Figure 8-11d**) were applied. Based on those colored mappings, we confirm that the OCP and temperature measurements are directly related to the rate constants measured. Note that the OCP measurement tends to be more intimate correlated, which may be due to the human errors and time gaps, 15 seconds, between each readings from using conventional thermometers.

In this system, oligothiophenes and pyrrole monomers were also introduced. By applying same measurements under identical conditions (**Figure S8-12-17**), rate constants under different voltages applied can be obtained, as shown in **Table 8-2**. Note that the solutions with pyrrole monomers added in do not tend to polymerize, *i.e.* no precipitate was observed. For oligothiophenes, both temperature and OCP measurements show slower reaction rates than the aniline without additives, except for terthiophene (3T) (**Figure S8-18**). In **Figure S8-19**, the contour mappings show consistencies among the temperature, OCP measurements, and rate constants. The reasons for the slow reaction rates for oligothiophenes can be attributed to the high oxidation potentials for thiophene monomers and bithiophenes, and low probabilities for radicals to transfer for terthiophenes and sexithiophenes.[29]

*Chemical Polymerizations and Morphologies.* The morphology of polyaniline is known to be associated with its mode of nucleation during polymerization.[36] Heterogeneous nucleation would tend to result in bulk and granular morphologies while homogeneous nucleation would facilitate the formation of nanofibers. Low temperature, oxidizing agents with low oxidizing potentials, and the gradual addition of oxidizing agents would favor the heterogeneous nucleation, *i.e.* enhance the secondary growth, resulting in granular features. Agitation, rapid mixing, and adding initiators to promote rate of polymerization are believed to suppress the secondary growth of polyaniline, hence, nanofribrillar morphologies are likely to be generated.[24,37–39] As shown **Figure 8-12**, aniline polymerized with additives including 2A, 2′A, 3′A, and 4A(EB) forms fiber-like morphologies with thin widths, which is in agreement with the mechanism abovementioned. On the other hand, morphologies of 1″A, 2″A, and 4A(LEB) are more similar to that of pure polyaniline.

For aniline polymerization with pyrrole monomers as the additive, no precipitate was observed. Therefore, suspension of the reaction is shown in **Figure 8-13a**, which should be granular polypyrrole as pyrrole monomers tend to be oxidized first but radicals did not tend to transfer onto aniline monomers. Interestingly, SEM images of aniline with oligothiophenes (**Figure 8-13b-e**) show a coral-like morphology. The rates for polymerization of aniline with oligothiophenes possess similar or smaller rate constants than additive-free aniline polymerization but greater than that of 1″A, which is counter-intuitive for the fibrillar morphology of 1″A, and the coral-like morphologies of oligothiophenes. Therefore, we speculate that the formations of those non-granular morphologies for slower polymerization rates are because of the high oxidation potential of ammonium persulfate (2.1 eV) and the alike steric structures, *i.e.* $\pi - \pi$ stackings. As the measured rate constants increase with increasing voltage applied, the strong oxidizing agent, ammonium persulfate, may tend to offer fast polymerization rates, which favors homogeneous nucleation. The slower rates for oligothiophenes indicate that the secondary growth were not suppressed, therefore, with 5 seconds of rapid shaking during the synthesis, a coral-like morphology associated with both homogeneous and heterogeneous nucleation was formed.[36] On the other hand, the explanation for 1″A with a much slower rate constant but still maintains a more fibrillar morphology may be attributed to the π—π stackings. Based on previous studies, morphology of polyaniline and crystallizations of oligoanilines are known to be intimately associated with the strong π—π stacking force between molecules.[32,40–42] The similar molecular structures between 1″A and polyaniline may make 1″A serve as a directional template for growing nanofibers.

*Aniline Polymerization in Acetonitrile/HCl solutions.* During the electrochemical polymerization, it is noteworthy that some additives, for example, 1″A, 2″A, and oligothiophenes

are not well dispersible in the 1.0 M HCl solution even they were pre-dissolved in a trace amount of acetonitrile. Therefore, in order to have all the materials dispersed well in solutions, also with proton resources, we perform each electrochemical polymerization experiment abovementioned in a solution of 15 mL 1.0 M HCl and 15 mL of acetonitrile with the sweep range between -0.2 V and 1.0 V (referenced to Ag/AgCl). Note that the relationship between the anodic peak current and the amount of polyaniline deposited on the electrode should be different than that in the 1.0 M HCl solution, but here we still follow the same rules simply for comparisons. The graphs of anodic peak current versus number of scans, rate versus number of scans, rate versus the anodic peak current, and the fittings between the rate and the square root of the anodic peak current are plotted in **Figure S8-20, S8-21**. Different from the aqueous solution, there's merely one voltage range tested, also two rate constants are found to fit the curves with the cutoff at i = 3 mA, instead of 9 mA for the aqueous ones.

The rate constants are listed in **Table S8-1**, and plotted in **Figure 8-14**. The trends between each additive are similar with that in the aqueous solutions (Figure 8-6). The much higher rate constants $k_1$ are attributed to the fitting range of the anodic peak current which is below 3 mA. Base on the second rate constant, $k_2$, 2A, 2′A, 3′A, 4A(EB) and 4A(LEB) are eligible to catalyze the polymerization reactions. It is possible that the conducting 4A(EB) and 4A(LEB) (after oxidation) contribute lots to the current readings as they both dissolved pretty well in such solutions. The rate constants for the acetonitrile/HCl system is much smaller than that in the pure aqueous system at 1.0 V, but more close to the rate constants at 0.9 V, the reasons for causing this phenomena could possibly be the shift of the reference potential due to different solvents used, and, most likely, the acetonitrile dissolute the polyaniline deposited on the electrode more efficient than 1.0 M HCl so that it takes much more scans for the anodic peak

current to reach a certain number, *i.e.* faster depositions for the HCl system. By plotting the rate constants for this acetonitrile/HCl system and the OCP and temperature over time tested in the pure 1.0 M HCl system, it is clear that values of $k_1$ do not consist with the OCP and temperature monitoring, while values of $k_2$ are closer to the trends measured in the 1.0 M HCl system, except for the rate constant of 2″A is lower.

## CONCLUSIONS

In this study, we have confirmed the autocatalytic effect of polyaniline, and the catalytic effect of introducing oligoanilines including 2A, 2′A, and 3′A into the system of aniline polymerization by fitting curves with the established empirical equation up to the maximum values of the polymerization rate. Aniline with and without additives does not tend to polymerize with an applied potential lower than 0.8 V against Ag/AgCl, but possesses higher rate constants as applied potential increases. Tetraaniline in both emeraldine (4AEB) and leucoemeraldine (4ALEB) states does not tend to accelerate reactions, hence, the formation of tetraaniline might be the intermediate step during the polymerization of aniline when the rate of polymerization begins to slow down. On the other hand, 1″A and 2″A can decelerate reactions as their rate constants are smaller than that of additive-free aniline polymerization, owing to the high oxidation potential and the phenyl-capped structures. Pyrrole monomer, as an additive, inhibits the polymerization of aniline, while oligothophenes do not facilitate the aniline polymerization. By comparing between the rate constants measured and the time durations $t_1 + t_2$ for temperature and the time duration t for OCP of solutions, we verify the feasibility of these two qualitative methods for evaluating the speed of aniline polymerization.

### Experimental Section

*Materials and Instrumentation*. All chemicals were used as received. Aniline (ACS reagent >99.5%), diphenylamine (1″A), N-phenyl-p-phenylenediamine (2A), 2,2'-bithiophene (2T), 2,2':5',2''-terthiophene (3T), α-sexithiophene (6T), and phenylhydrazine (97%) were purchased from Sigma Aldrich. Ammonium persulfate (98+%), thiophene (99+%), and anhydrous acetonitrile (99.9%, Extra Dry AcroSeal, 1 L) were purchased from ACROS. N,N'-diphenyl-1,4-phenylenediamine (2″A) and 4,4'-diaminodiphneylamine sulfate hydrate (3′A) were acquired from Tokyo Chemical Industry. 1,4-phenylenediamine (2′A) was purchased from Fluka. Pyrrole (98+%) and platinum foils (99.9%, 0.025 mm thickness, metal basis) for the working and counter electrodes were obtained from Alfa Aesar. Tetraaniline (4A) in both emeraldine and leucoemeraldine states were synthesized as previously reported.[43] The reference electrode (Ag/AgCl, MR-5275) for aqueous electrolytes was obtained from BASi. SEM images were taken with a JEOL JSM-6700 Field Emission scanning electron miscroscope. All electrochemical data were collected with a Biologic VMP3 workstation. All reactions were performed in air at room temperature.

*Electrochemical Polymerization.* The setup for electrochemical reactions is shown in **Figure S8-23**. Platinum foils were used as the working and counter electrodes with an area of ~1.0 cm x 1.0 cm and 1.0 cm x 2.0 cm, each. The extended electrodes were attached with copper foil and sealed with Kapton tape. A suitable electrolyte, monomers, additives and a tiny magnetic stirring bar were placed in a 50 mL beaker. All reactions were stirred at 500 rpm. For the aqueous electrochemical polymerization of aniline, an additive (1.0 mM) was pre-dissolved with ~200 to 400 μL of acetonitrile in a 7 mL glass vial, then pipetted to a 50 mL beaker, which contained aniline monomers (0.2 M) and 1.0 M hydrochloric acid (30 mL). The cyclic potential was swept from -0.2 V to 0.8 V, 0.9 V and 1.0 V (referenced against Ag/AgCl) at a scan rate of

25 mV/s for 40 cycles. For polymerization of aniline in acetonitrile and hydrochloric acid, the electrolyte contained 15 mL of acetonitrile and 15 mL of 1.0 M hydrochloric acid.

*Open-Circuit Voltage Measurements.* The aniline system was measured in an aqueous environment. First, 20 mL of 1.0 M hydrochloric acid, aniline monomer (1.5 mmol) and an additive (0.03 mmol) pre-dissolved in a small amount of acetonitrile were placed in a 50 mL beaker. In a 20 mL glass vial, 342 mg of ammonium persulfate was dissolved in 10 mL of 1.0 M hydrochloric acid. The electrode setup is the same as described above. The real-time voltage versus an Ag/AgCl reference electrode was recorded about 3 seconds after one-time pipetting the ammonium persulfate solution into the beaker.

*Temperature Monitoring.* An additive (0.03 mmol) pre-dissolved in a small amount of acetonitrile was mixed with 20 mL of 1.0 M hydrochloric acid and aniline monomer (1.5 mmol) in a 150 mL glass jar. The jar was placed in a fume hood, and a conventional thermometer was mounted on the rack in order to read the temperature of the solution. After the thermometer reading reached equilibrium, a 10 mL solution of 1.0 M hydrochloric acid with pre-dissolved ammonium persulfate (342 mg) was poured into the jar. Temperature readings were recorded every 15 seconds.

*Chemical Polymerization.* Aniline monomer (0.8 mmol) was added into a 20 mL of 1.0 M hydrochloric acid solution. An appropriate additive (0.02 mmol) was first dissolved in a trace amount of acetonitrile in a 7 mL glass vial, and then transferred to the solution. Reactions were shaken for 5 seconds after adding in 45 mg of ammonium persulfate and left to stand for 24 hours with caps sealed. The products were left in a vacuum chamber and collected after centrifugation followed by washing with a copious amount of deionized water.

*Cyclic Voltammetry of Materials.* Cyclic Voltammetry of 1″A, 2A, 2′A, 2″A, 3′A and 4A were characterized by adding a 10 mM of material into 30 mL of 1.0 M hydrochloric acid solution and swept between -0.2 V and 1.0 V, referenced against an Ag/AgCl electrode, at a scan rate of 25 mV/s.

## ACKNOWLEDGMENTS

The authors thank Dr. Dandan Zhang and Prof. Chong Liu for lending us reference electrodes. C.-W.L. thanks Dr. Jeong Hoon Ko for useful discussions, and the support from the UCLA Dissertation Year Fellowship. W.H.M. and S.A. would like to acknowledge their UCLA Eugene V. Cota-Robles Fellowships, and R.B.K. would like to acknowledge the support from Dr. Myung Ki Hong Endowed Chair in Materials Innovation at UCLA.

**Table 8-1.** The Aniline Electrochemical Polymerization Rate Constant k[a]

| additive | k at 0.8 V | $k_1$ at 0.9 V | $k_2$ at 0.9 V | k at 1.0 V | $E_{ox}$ [b] |
|---|---|---|---|---|---|
| none | 0.307 | 3.90 | 3.62 | 13.4 | 0.785[33,34] |
| 1"A | 0.0317 | 2.61 | 3.15 | 2.64 | 0.840 |
| 2A | 2.32 | 14.2 | 6.01 | 16.0 | 0.588 |
| 2'A | 2.11 | 14.8 | 5.52 | 20.5 | 0.670 |
| 2"A | 0.343 | 4.19 | 3.23 | 8.45 | 0.617 |
| 3'A | 3.12 | 35.0 | 9.15 | 24.1 | 0.574 |
| 4A(EB) | 3.41 | 5.32 | 3.94 | 8.05 | 0.637 |
| 4A(LEB) | 0.853 | 4.01 | 4.60 | 13.6 | 0.347 |

a: k is given in units of $mA^{1/2}\ M^{-1}\ scan^{-1}$ with and without additives under the potential sweeps of -0.2 V to 0.8 V, -0.2 V to 0.9 V, and -0.2 V to 1.0 V (vs. Ag/AgCl). The concentration of aniline monomer and additives are 0.2 M and 1.0 mM, respectively. The electrochemical polymerization experiments were carried out with a 30 mL 1.0 M HCl solution at a scan rate of 25 mV/s.

b: The oxidation potential ($E_{ox}$) for each material was measured by dispersing 10 mM of materials into a 30 mL 1.0 M HCl solution with a potential swept between -0.2 V and 1.0 V versus Ag/AgCl, at a scan rate of 25 mV/s. Cyclic voltammograms of each material are shown in **Figure S8-11**.

**Table 8-2.** Electrochemical Polymerization Rate Constant k[a]

| additive | k at 0.8 V | $k_1$ at 0.9 V | $k_2$ at 0.9V | k at 1.0 V | $E_{ox}$ |
|---|---|---|---|---|---|
| none | 0.307 | 3.90 | 3.62 | 13.4 | 0.800 |
| 1T | 0.283 | 4.68 | 4.28 | 9.14 | 1.76[35] |
| 2T | 0.307 | 2.85 | 2.36 | 8.14 | 1.00[35] |
| 3T | 0.317 | 4.81 | 4.23 | 11.2 | 0.740[35] |
| 6T | 0.326 | 7.17 | 3.82 | 9.71 | 0.600[35] |

a: k is given in units of $mA^{1/2}$ $M^{-1}$ $scan^{-1}$ with and without oligothiophene additives under the potential sweeps of -0.2 V to 0.8 V, -0.2 V to 0.9 V, and -0.2 V to 1.0 V (vs. Ag/AgCl). The concentration of aniline monomer and oligothiophene additives are 0.2 M and 1.0 mM, respectively. The electrochemical polymerization experiments were carried out with a 30 mL 1.0 M HCl solution at a scan rate of 25 mV/s.

**Table S1.** The electrochemical polymerization rate constant k ($mA^{1/2}$ $M^{-1}$ $scan^{-1}$) with and without oligothiophenes and oligoanilines with the potential sweep from -0.2 V to 1.0 V (vs. Ag/AgCl). The concentration of aniline monomer and additives are 0.2 M and 1.0 mM, respectively. The electrochemical polymerization experiments were carried out with a 15 mL 1.0 M HCl and 15 mL acetonitrile solution at a scan rate of 25 mV/s.

| additive | $k_1$ at 1.0 V | $k_2$ at 1.0 V |
|---|---|---|
| none | 4.39 | 2.23 |
| 1"A | 0.983 | 1.42 |
| 2A | 4.05 | 3.81 |
| 2'A | 3.39 | 2.83 |
| 2"A | 2.16 | 1.86 |
| 3'A | 4.72 | 2.92 |
| 4A(EB) | 1.91 | 2.07 |
| 4A(LEB) | 6.65 | 2.90 |
| 1T | 1.63 | 1.76 |
| 2T | 1.14 | 1.44 |
| 3T | 4.35 | 2.10 |
| 6T | 5.36 | 2.17 |

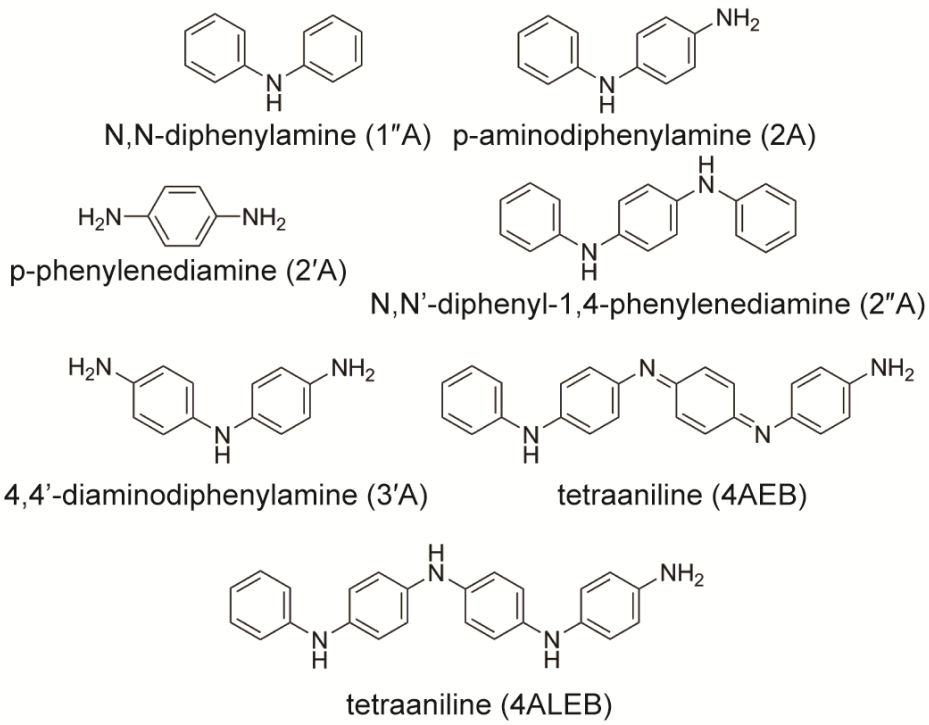


**Figure 8-1.** Molecular structures of aniline additives and their abbreviations.

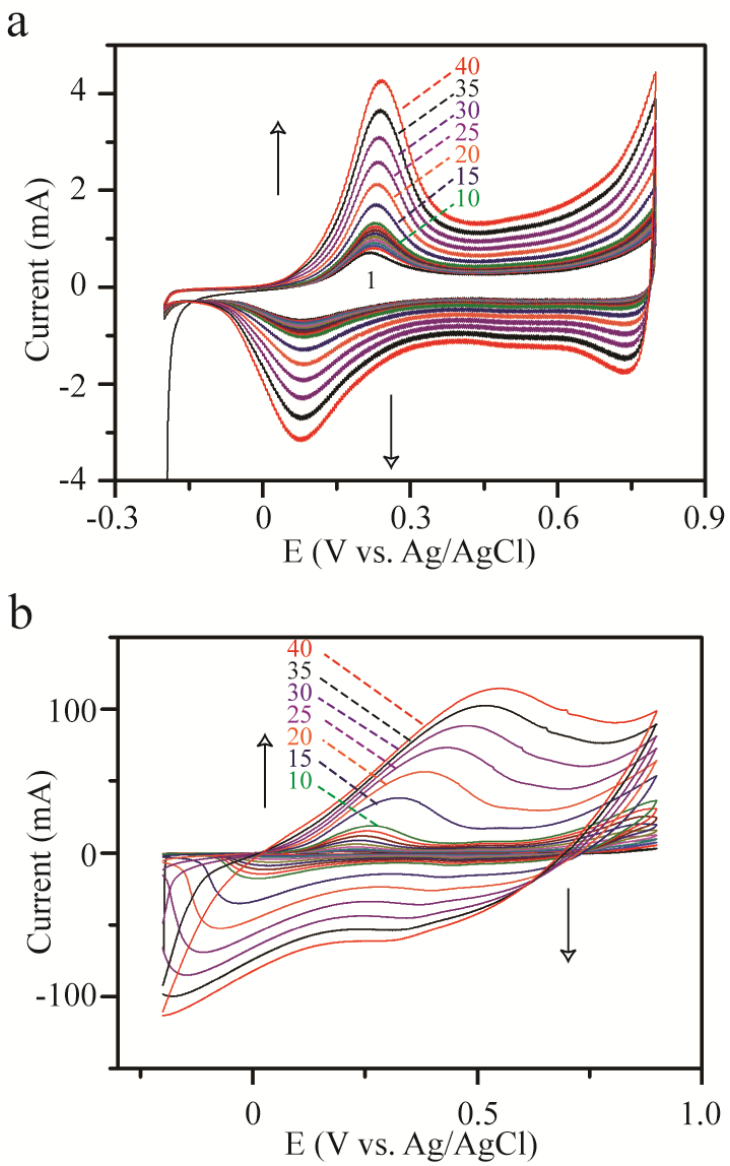


**Figure 8-2.** Cyclic voltammograms of electrochemical polymerization of 0.2 M aniline in a 1.0 M HCl solution on a platinum electrode from -0.2 V to (a) 0.8 V and (b) 0.9 V versus Ag/AgCl at a scan rate of 25 mV/s. The number of scan from 1 to 10, and at 15, 20, 25, 30, 35, 40 are indicated.

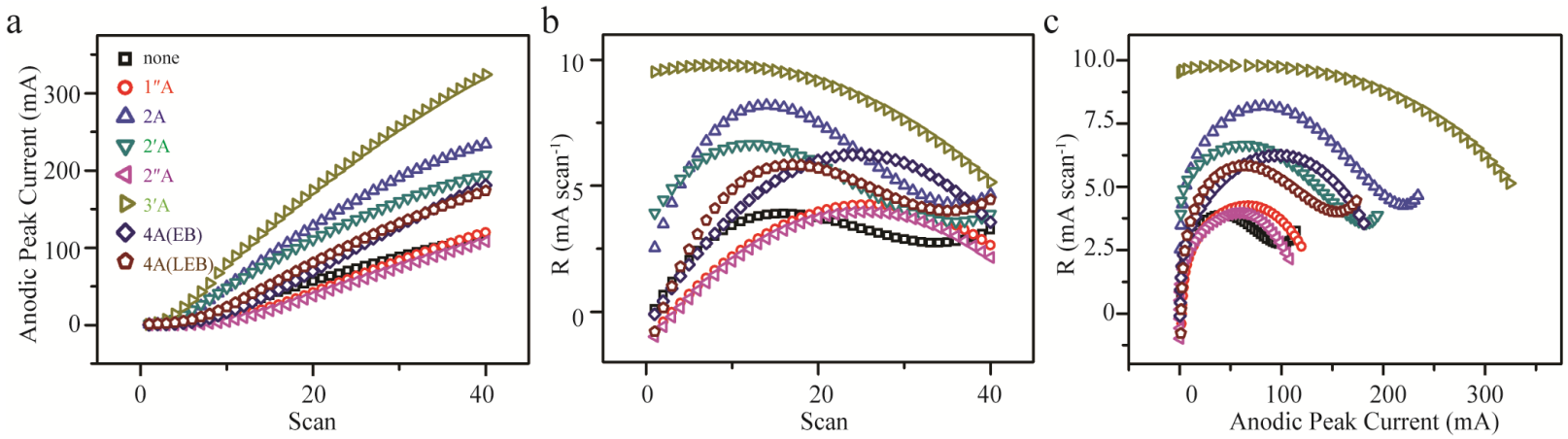


**Figure 8-3.** Full graphs of (a) anodic peak current versus number of scans, (b) polymerization rate versus the number of scans, and (c) polymerization rate versus the anodic peak current, for aniline electrochemical polymerization with and without oligoanilines. The reactions contain 0.2 M of aniline and 1.0 mM of additives−30 mL of a 1.0 M HCl solution, with the potential sweep ranges from -0.2 V to 0.9 V (against Ag/AgCl) at a scan rate of 25 mV/s.

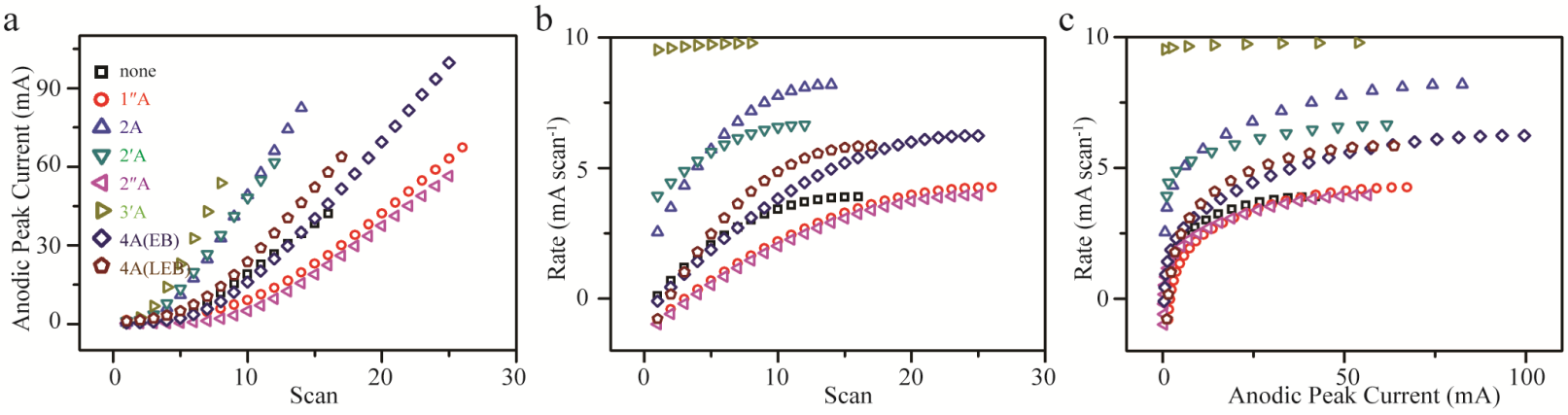


**Figure 8-4.** Graphs of (a) anodic peak current versus number of scans, (b) polymerization rate versus the number of scans, and (c) polymerization rate versus the anodic peak current, for aniline electrochemical polymerization with and without oligoanilines to reach their maximum rates of electrochemical polymerization. The reactions contain 0.2 M of aniline and 1.0 mM of additives− 30 mL of a 1.0 M HCl solution, with the potential sweep ranges from -0.2 V to 0.9 V (against Ag/AgCl) at a scan rate of 25 mV/s.

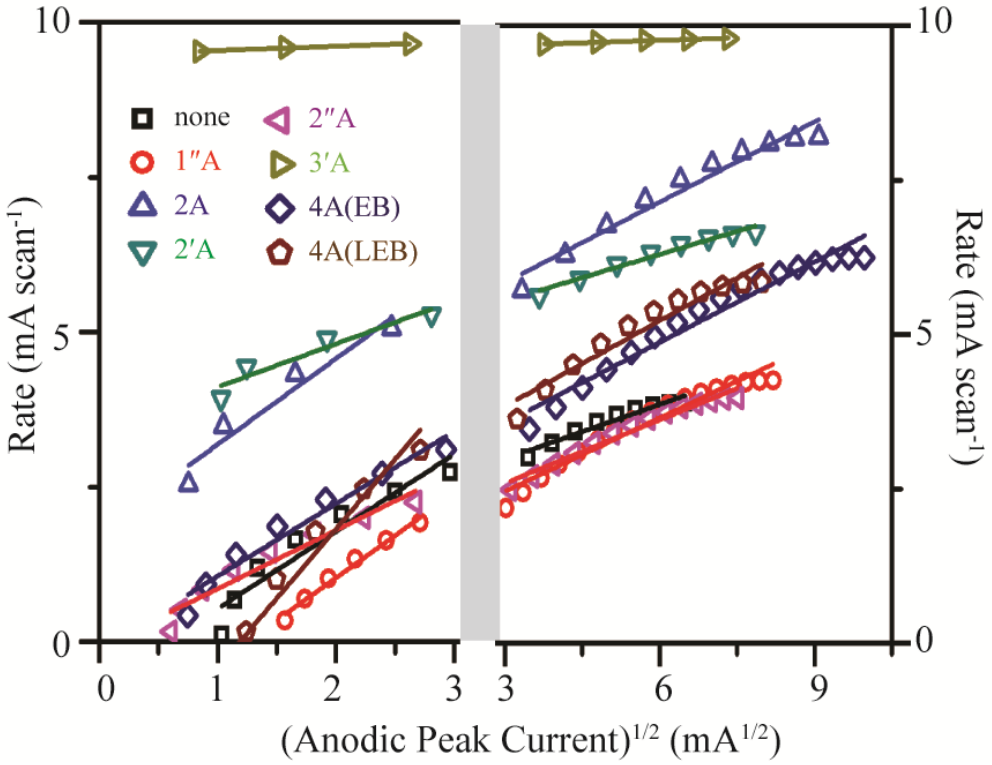


**Figure 8-5.** The linear relationships of the rate of electrochemical polymerization of aniline with the square root of the anodic peak current. Potential sweep range: -0.2 V to 0.9 V (versus Ag/AgCl). Scan rate: 25 mV/s.

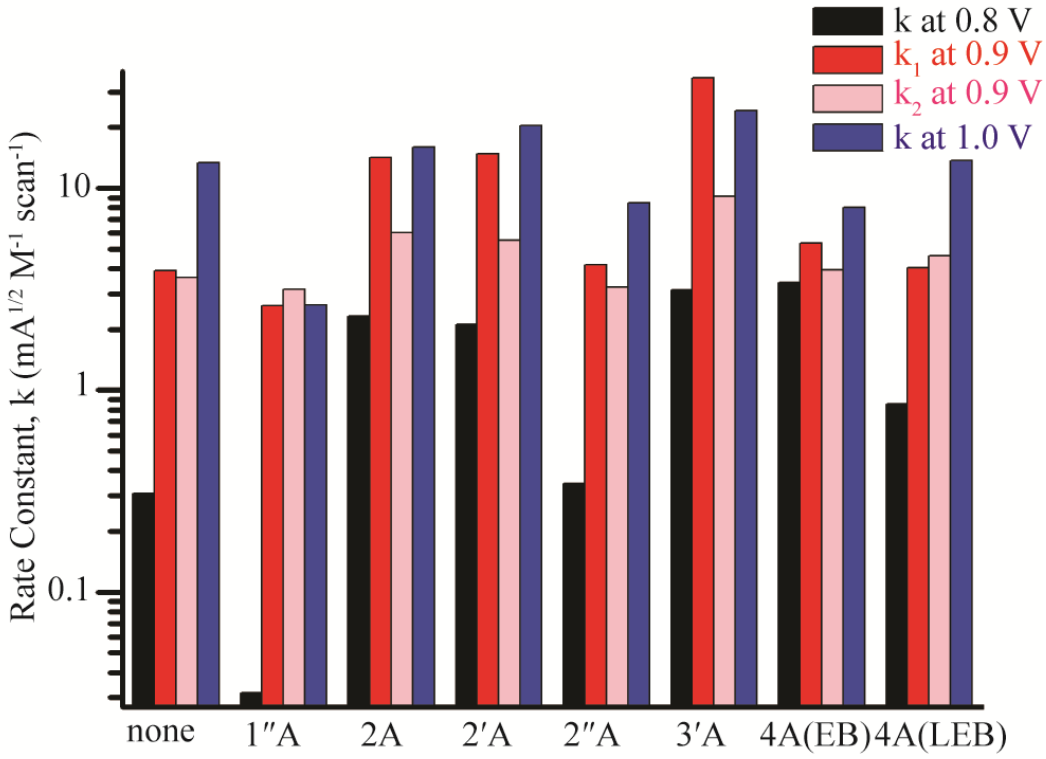


**Figure 8-6.** Rate constant, k, for the electrochemical polymerization of aniline with and without oligoanilines in a 1.0 M HCl solutsion, with potential sweeps from -0.2 V to 0.8 V, 0.9 V, and 1.0 V.

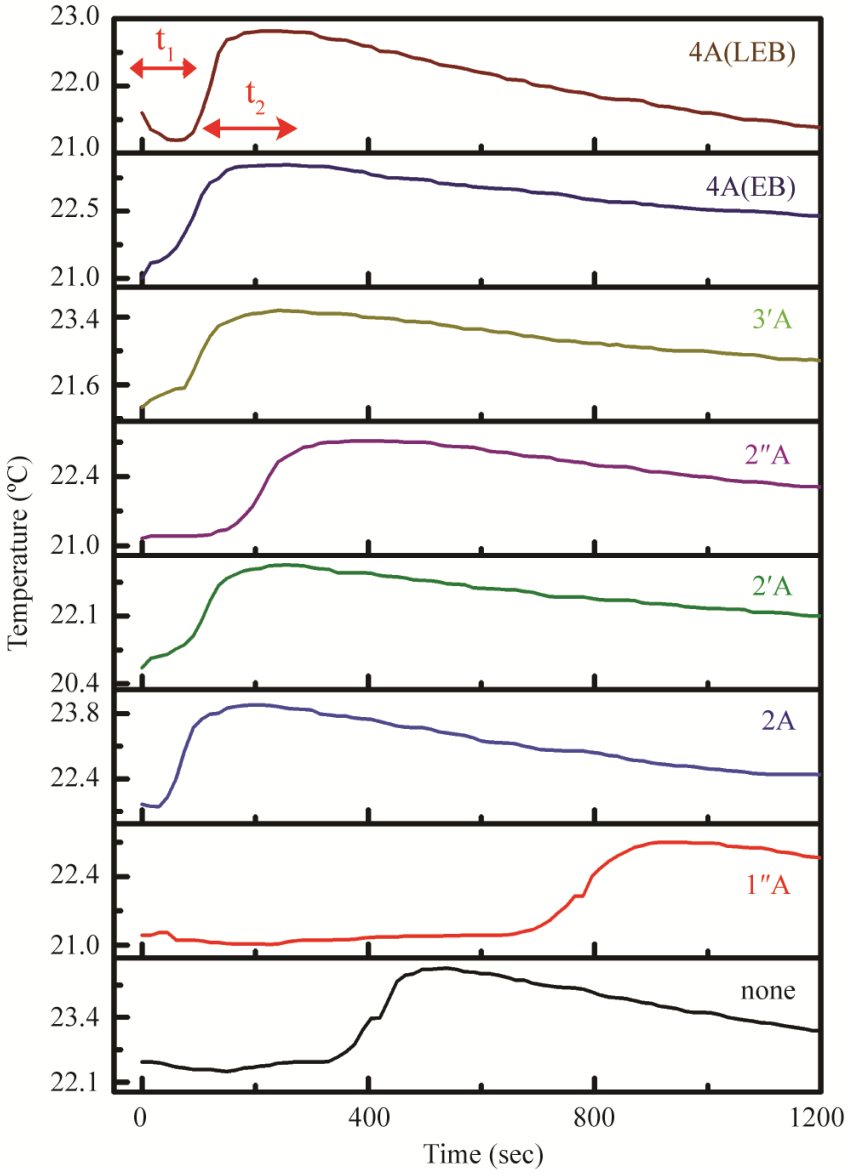


**Figure 8-7.** Profiles of time versus temperature of a 1.0 M HCl solution containing 0.2 M of aniline, 1.0 mM of oligoanilines, and 45 mg of ammonium persulfate.

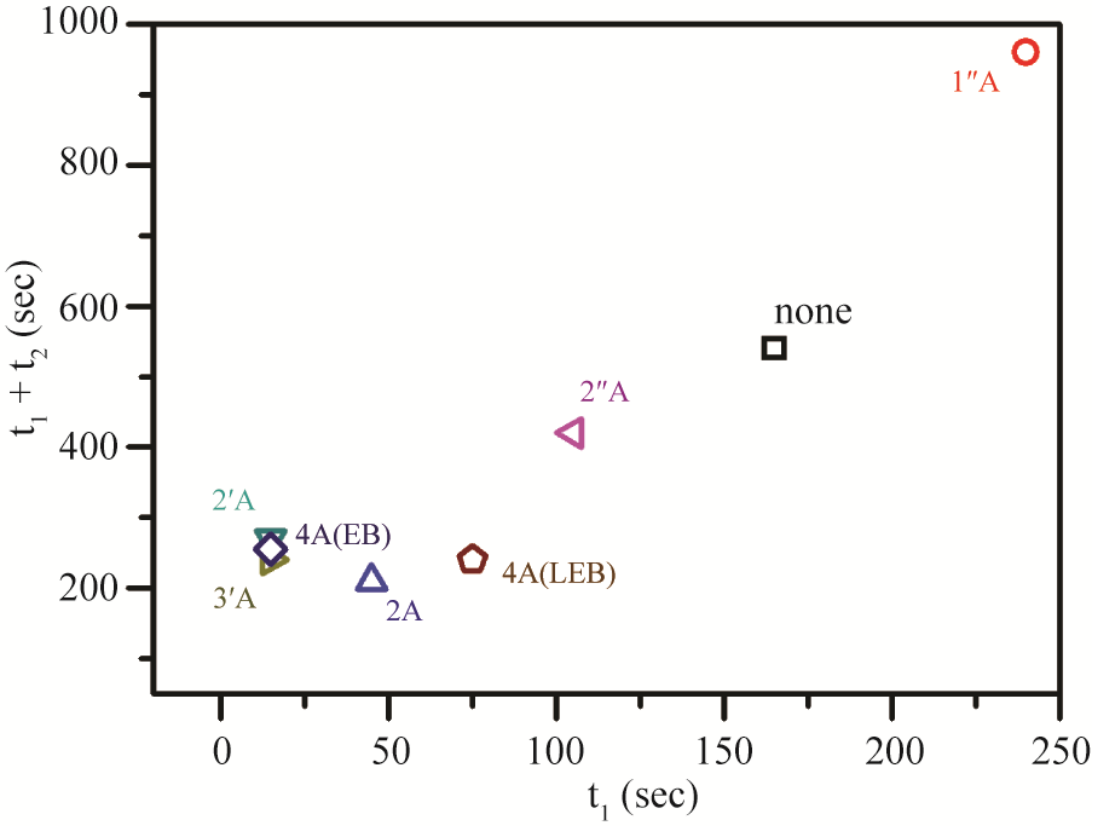


**Figure 8-8.** Plot of temperature $t_1$ versus temperature $t_1 + t_2$ for oligoanilines in chemical polymerizations of aniline with ammonium persulfate as the oxidizing agent in a 1.0 M HCl solution.

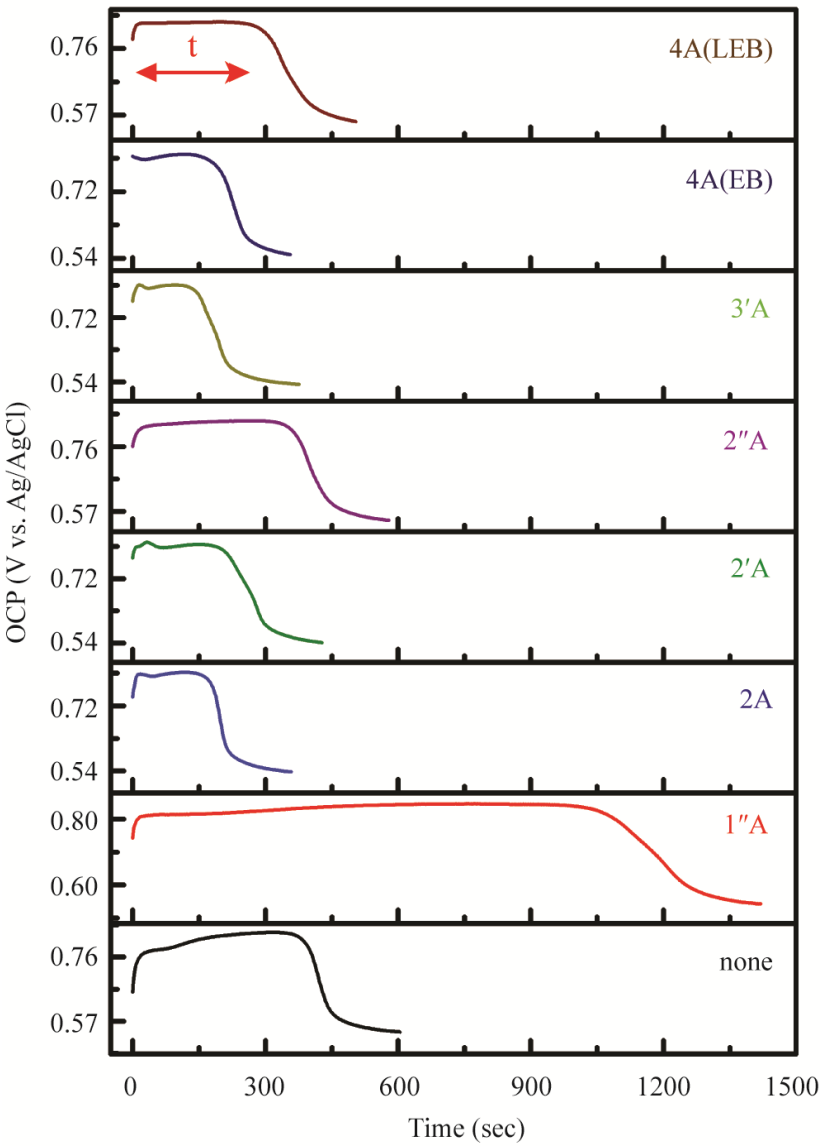


**Figure 8-9.** Profiles of time versus the open-circuit voltage of a 1.0 M HCl solution containing 0.2 M of aniline, 1.0 mM of oligoanilines, and 45 mg of ammonium persulfate.

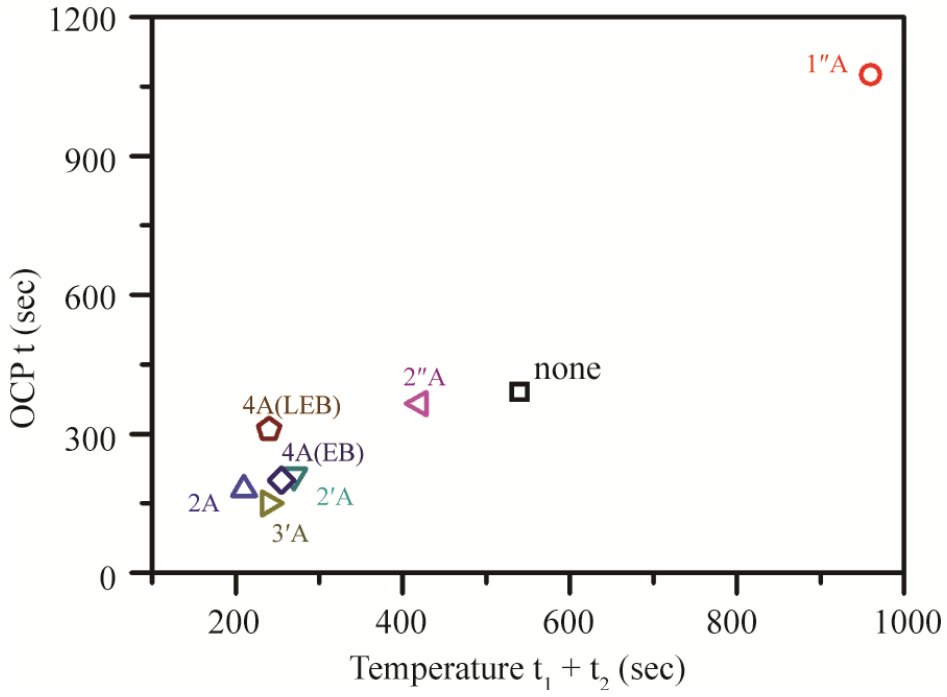


**Figure 8-10.** Plot of open-circuit potential t versus temperature $t_1 + t_2$ for oligoanilines in chemical polymerizations of aniline with ammonium persulfate as the oxidizing agent in a 1.0 M HCl solution.

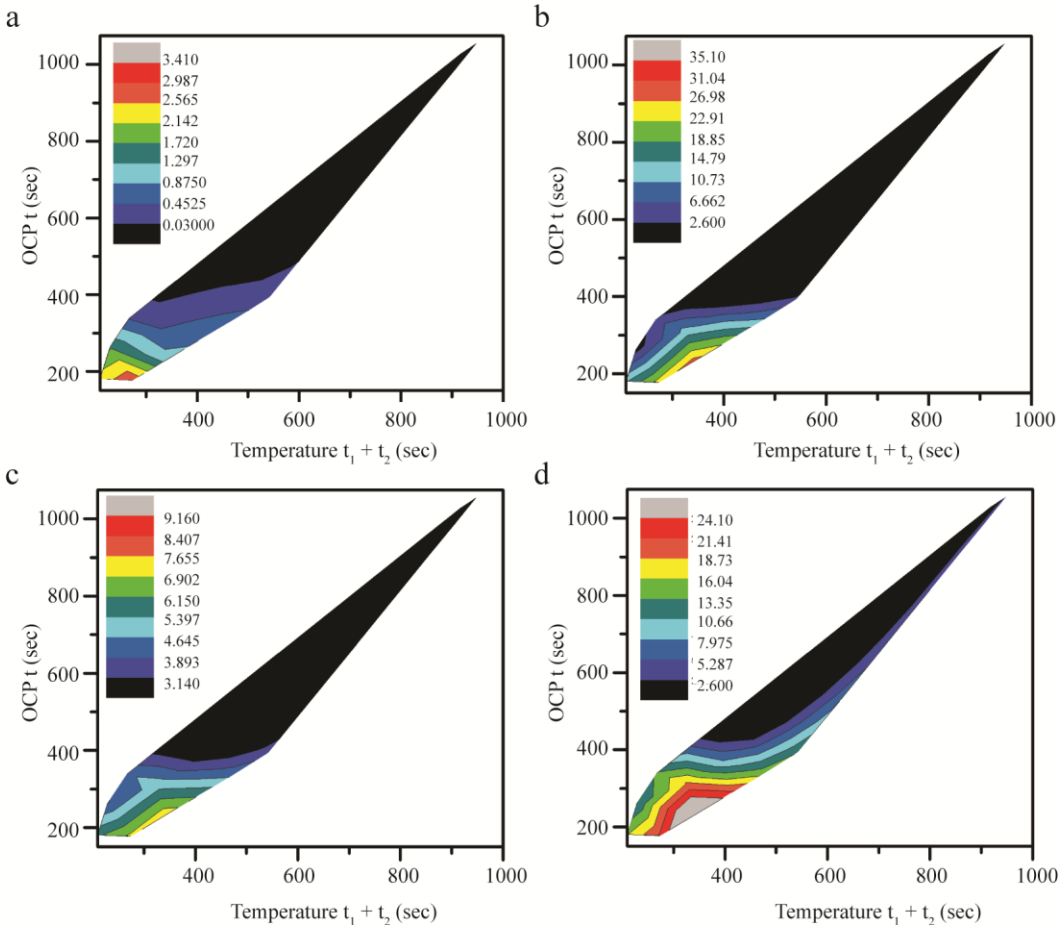


**Figure 8-11.** Contour plots of t for the open-circuit potential versus the $t_1 + t_2$ duration for temperature profiles, with color mappings for (a) rate constants at 0.8 V, (b) first rate constant, $k_1$, at 0.9 V, (c) second rate constant, $k_2$, at 0.9 V, and (d) rate constant at 1.0 V, for introducing oligoanilines into the chemical polymerization of aniline in a 1.0 M HCl solution.

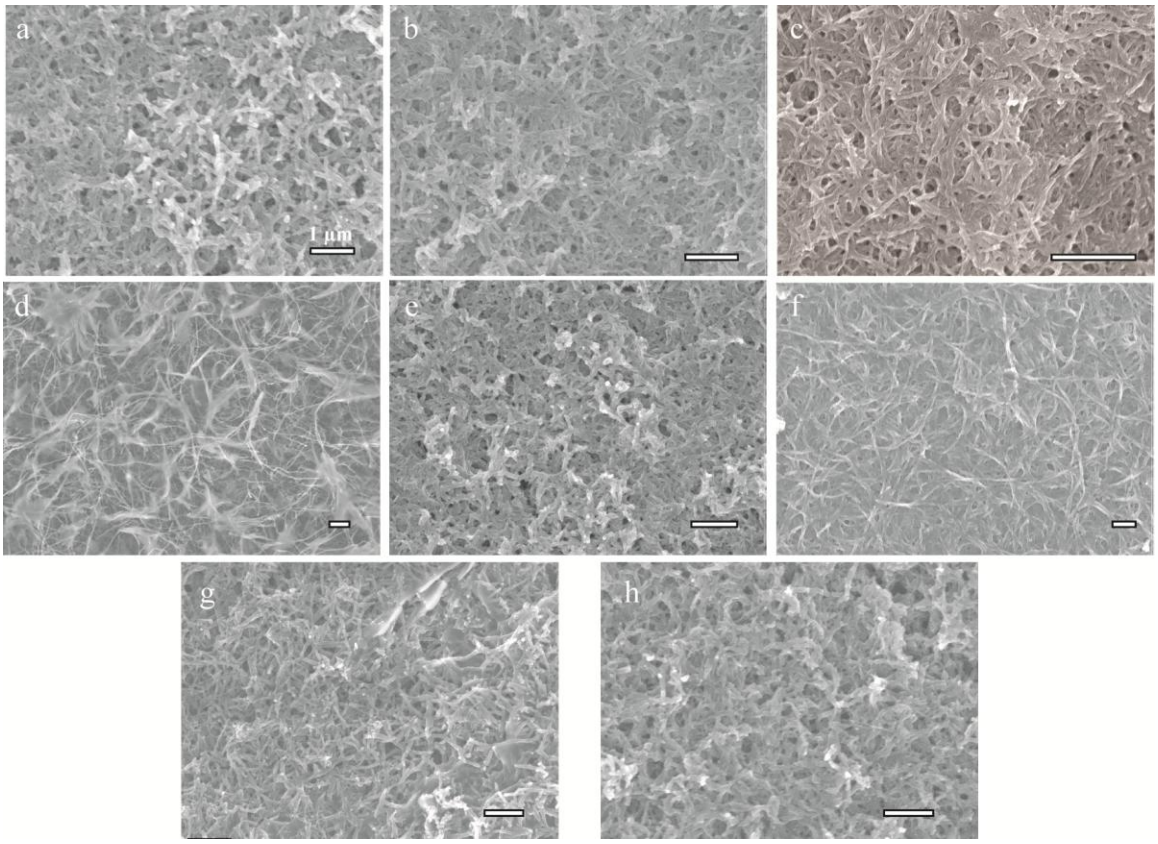


**Figure 8-12.** Scanning electron microscope images of the chemical polymerization of aniline with (a) no additives, (b) 1″A, (c) 2A, (d) 2′A, (e) 2″A, (f) 3′A, (g) 4A(EB), and (h) 4A(LEB), in a 1.0 M HCl solution.

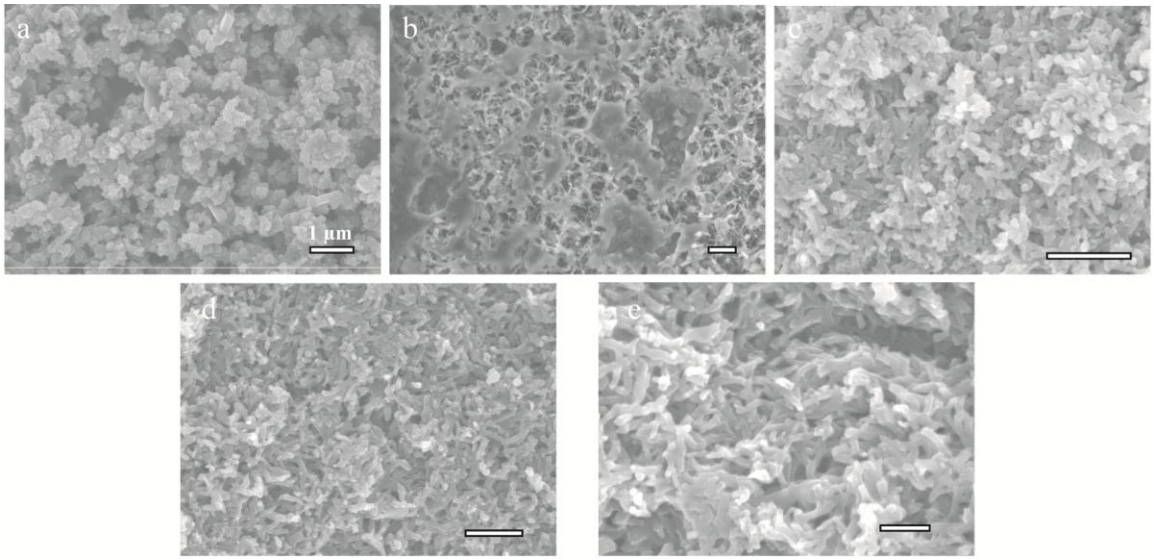


**Figure 8-13.** Scanning electron microscope images of the chemical polymerization of aniline with (a) pyrrole monomers, (b) 1T, (c) 2T, (d) 3T, (e) 6T, in a 1.0 M HCl solution.

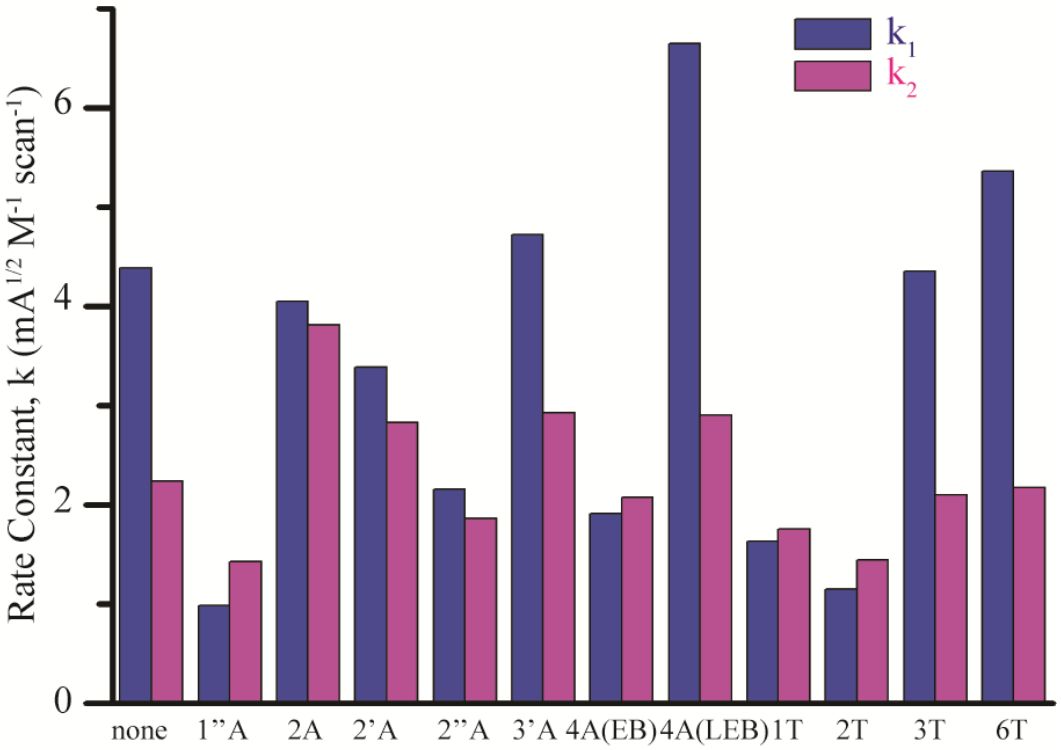


**Figure 8-14.** Plot showing the first and second rate constants for the electrochemical polymerization of aniline in an acetonitrile/HCl solution, with the potential sweep from -0.2 V to 1.0 V, against Ag/AgCl. The scan rate is 25 mV/s.

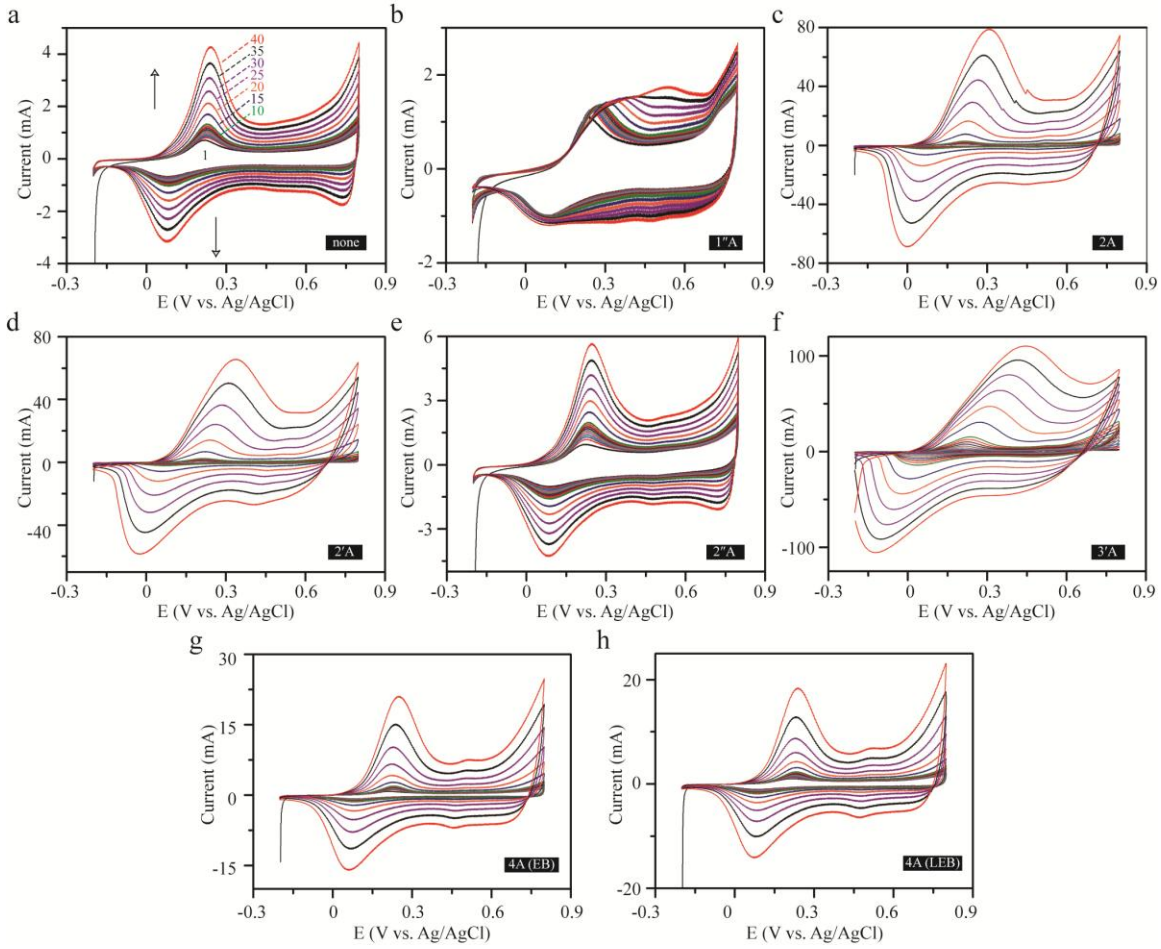


**Figure S8-1.** Cyclic voltammograms of electrochemical polymerization of aniline in a 1.0 M HCl solution with (a) no additives, (b) 1″A, (c) 2A, (d) 2′A, (e) 2″A, (f) 3′A, (g) 4A(EB), and (h) 4A(LEB). The reactions contain 0.2 M of aniline and 1.0 mM of additives, with the potential sweep from -0.2 V to 0.8 V (against Ag/AgCl) at a scan rate of 25 mV/s.

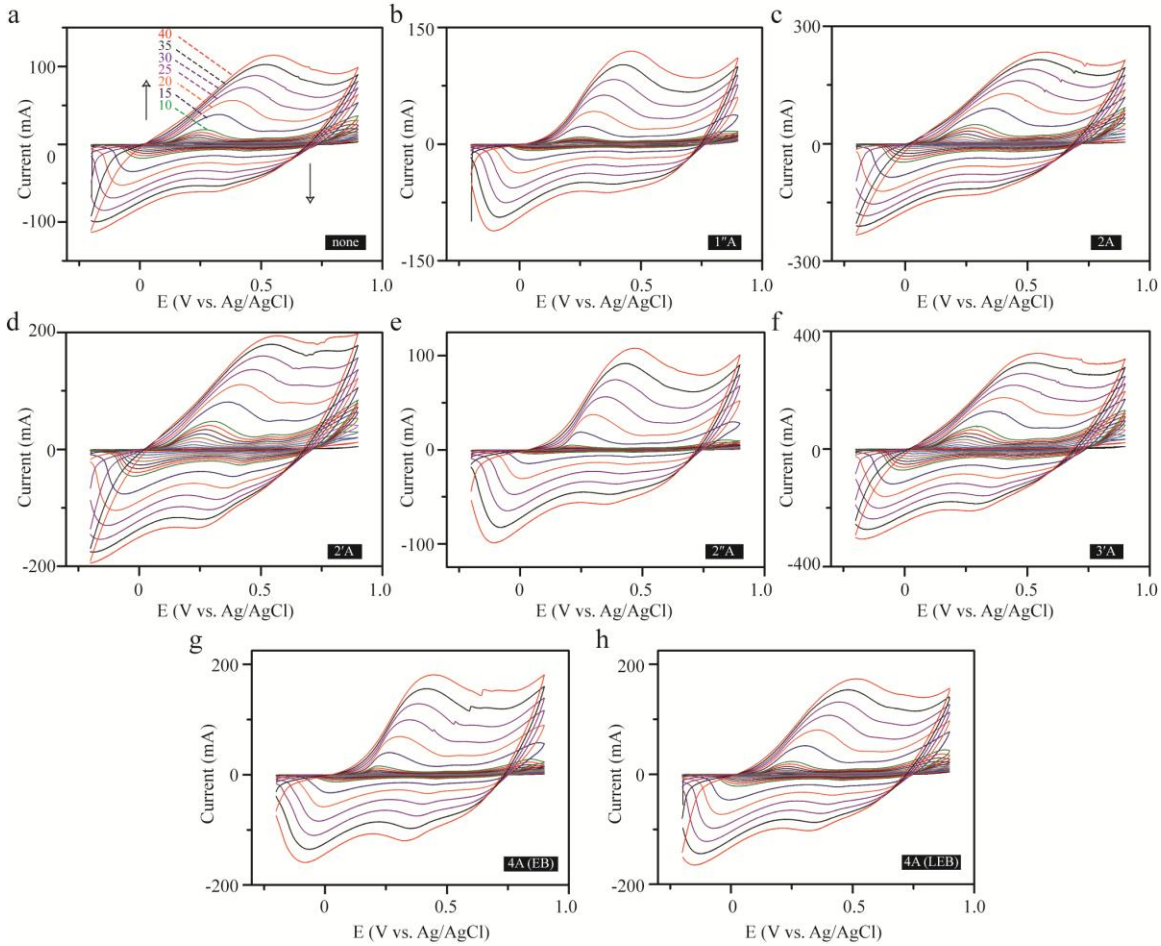


**Figure S8-2.** Cyclic voltammograms of electrochemical polymerization of aniline in a 1.0 M HCl solution with (a) no additives, (b) 1″A, (c) 2A, (d) 2′A, (e) 2″A, (f) 3′A, (g) 4A(EB), and (h) 4A(LEB). The reactions contain 0.2 M of aniline and 1.0 mM of additives, with the potential sweep from -0.2 V to 0.9 V (against Ag/AgCl) at a scan rate of 25 mV/s.

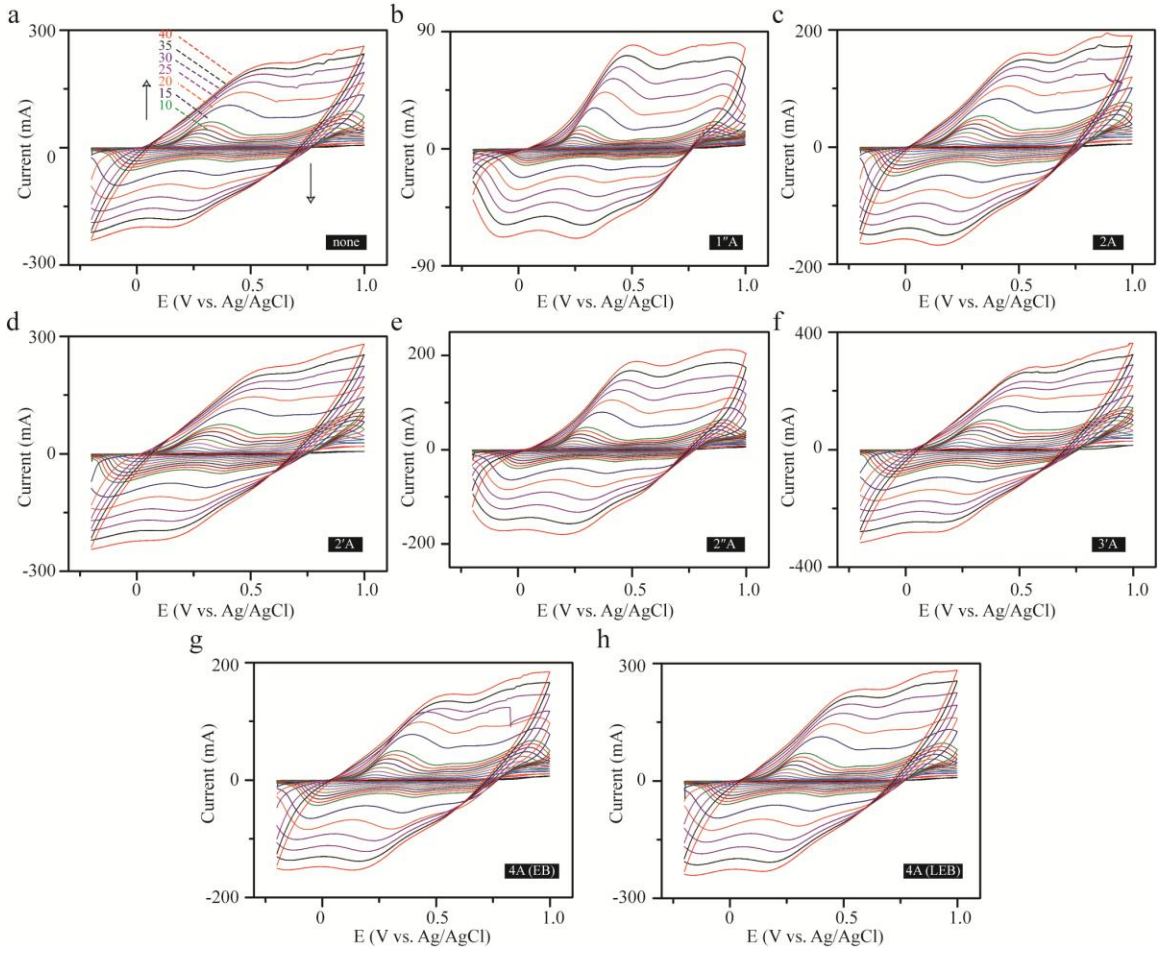


**Figure S8-3.** Cyclic voltammograms of electrochemical polymerization of aniline in a 1.0 M HCl solution with (a) no additives, (b) 1″A, (c) 2A, (d) 2′A, (e) 2″A, (f) 3′A, (g) 4A(EB), and (h) 4A(LEB). The reactions contain 0.2 M of aniline and 1.0 mM of additives, with the potential sweep from -0.2 V to 1.0 V (against Ag/AgCl) at a scan rate of 25 mV/s.

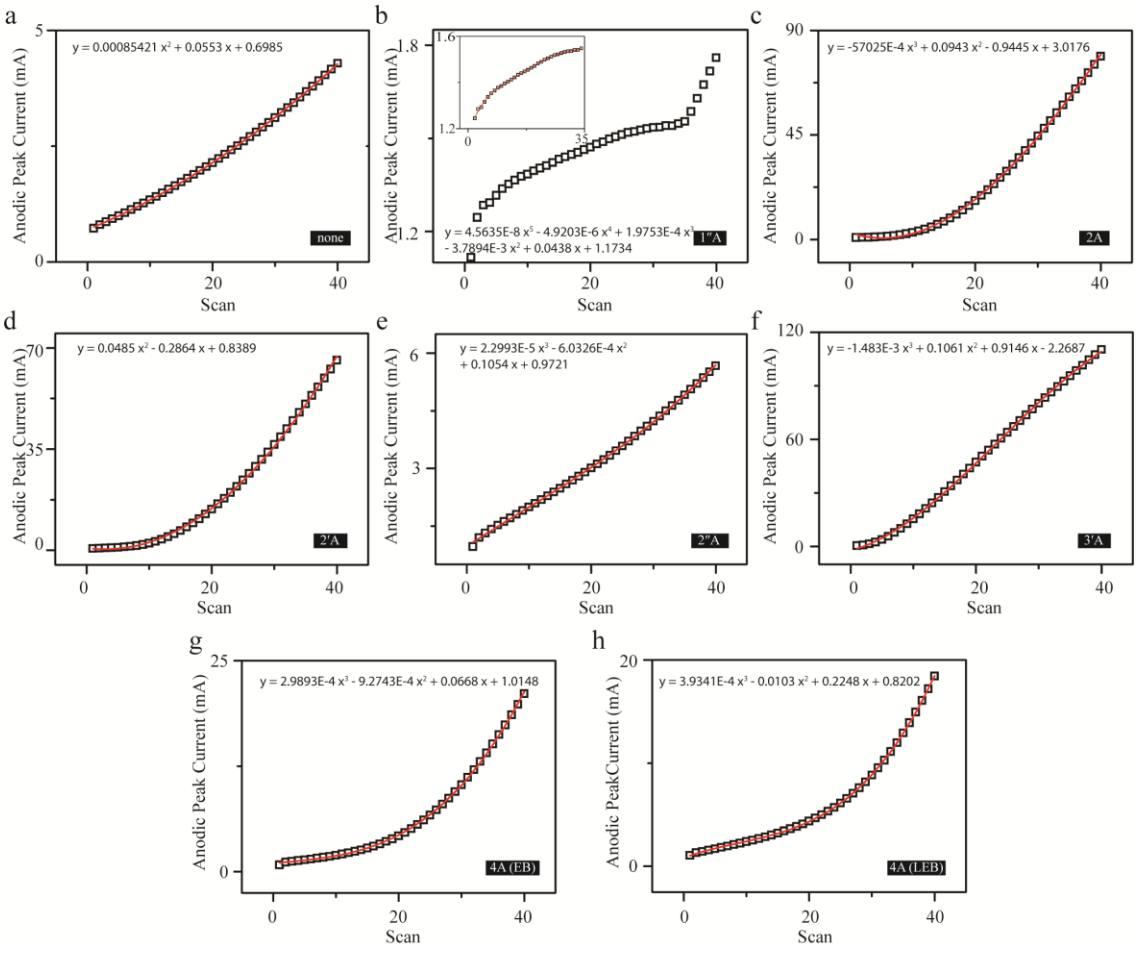


**Figure S8-4.** Graphs and polynomial fittings of the anodic peak current versus number of scans for electrochemical polymerization of aniline in a 1.0 M HCl solution with (a) no additives, (b) 1″A, (c) 2A, (d) 2′A, (e) 2″A, (f) 3′A, (g) 4A(EB), and (h) 4A(LEB). The reactions contain 0.2 M of aniline and 1.0 mM of additives, with the potential sweep from -0.2 V to 0.8 V (against Ag/AgCl) at a scan rate of 25 mV/s.

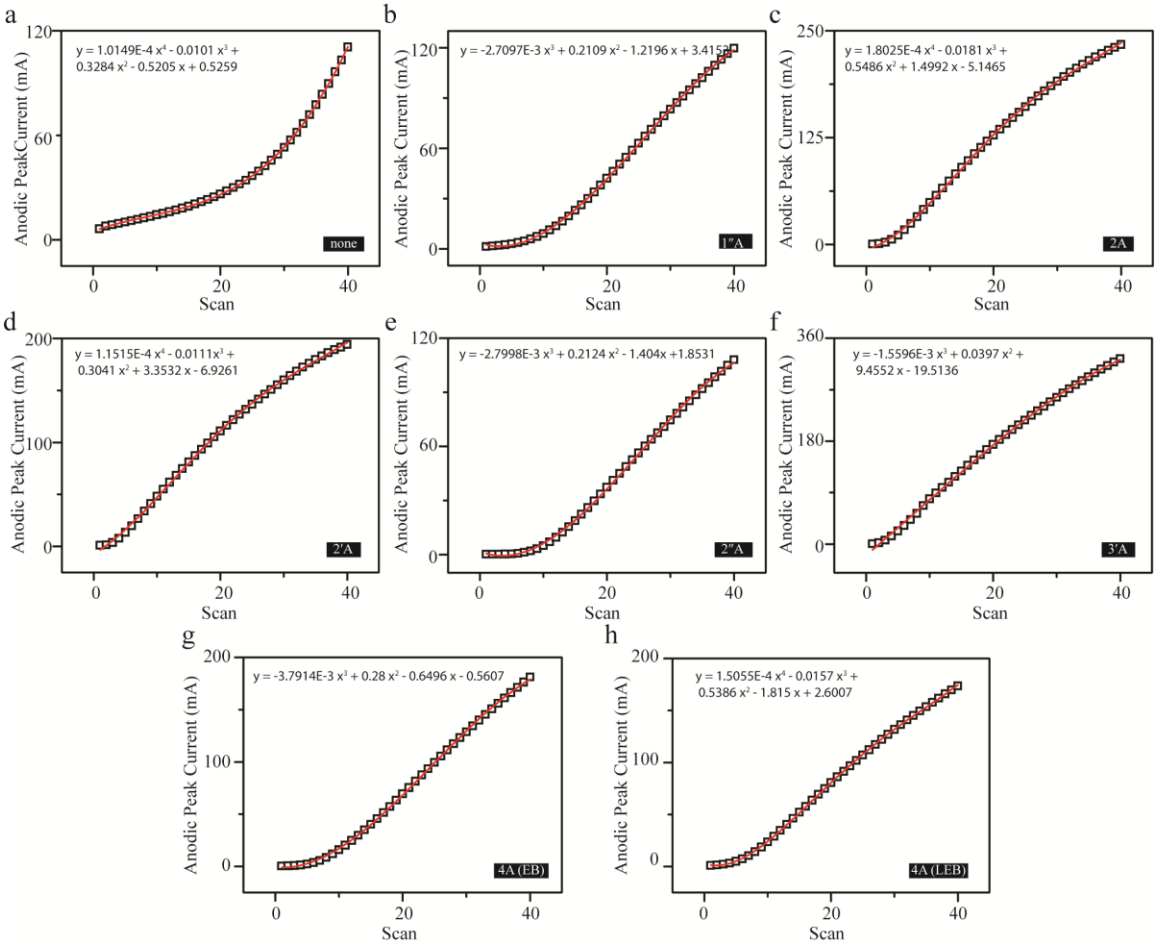


**Figure S8-5.** Graphs and polynomial fittings of the anodic peak current versus number of scans for electrochemical polymerization of aniline in a 1.0 M HCl solution with (a) no additives, (b) 1″A, (c) 2A, (d) 2′A, (e) 2″A, (f) 3′A, (g) 4A(EB), and (h) 4A(LEB). The reactions contain 0.2 M of aniline and 1.0 mM of additives, with the potential sweep from -0.2 V to 0.9 V (against Ag/AgCl) at a scan rate of 25 mV/s.

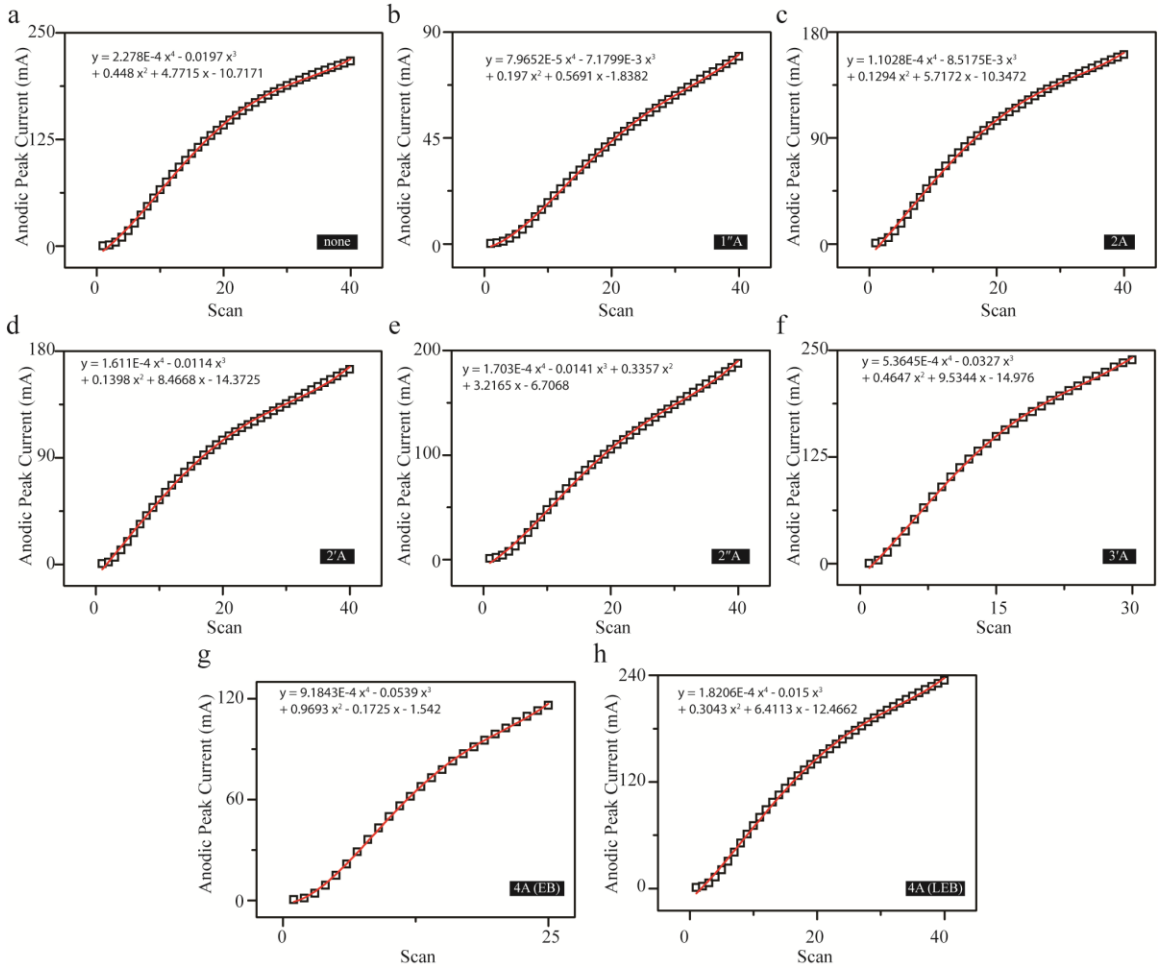


**Figure S8-6.** Graphs and polynomial fittings of the anodic peak current versus number of scans for electrochemical polymerization of aniline in a 1.0 M HCl solution with (a) no additives, (b) 1″A, (c) 2A, (d) 2′A, (e) 2″A, (f) 3′A, (g) 4A(EB), and (h) 4A(LEB). The reactions contain 0.2 M of aniline and 1.0 mM of additives, with the potential sweep from -0.2 V to 1.0 V (against Ag/AgCl) at a scan rate of 25 mV/s.

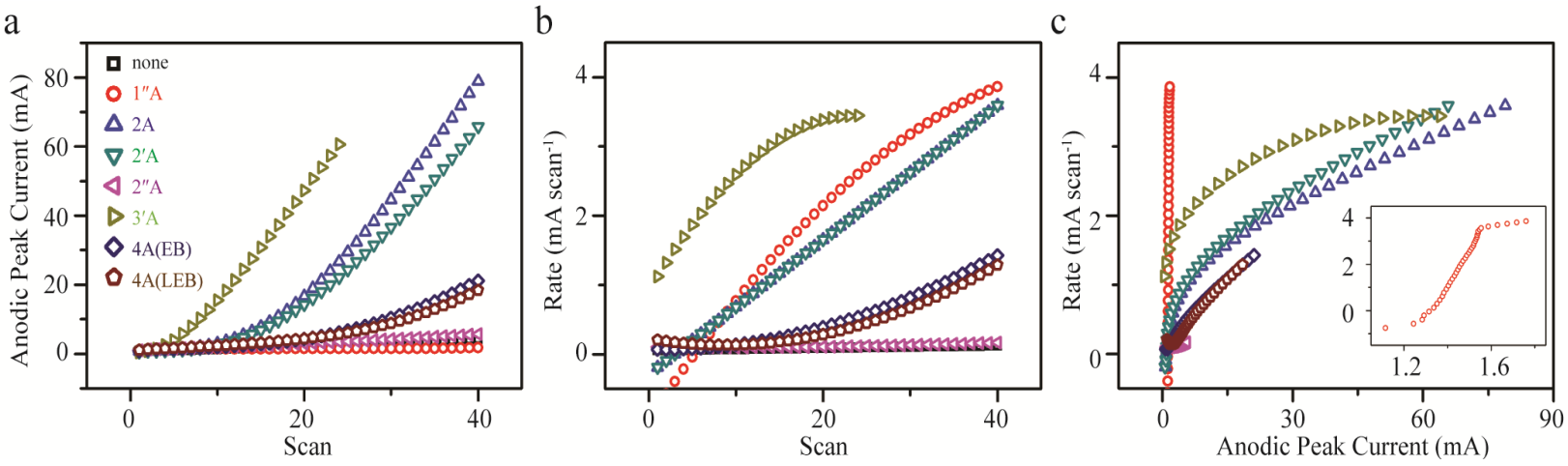


**Figure S8-7.** Full graphs of (a) anodic peak current versus number of scans, (b) polymerization rate versus the number of scans, and (c) polymerization rate versus the anodic peak current, for aniline electrochemical polymerization with and without oligoanilines. The reactions contain 0.2 M of aniline and 1.0 mM of additives in a 30 mL 1.0 M HCl solution, with the potential sweep from -0.2 V to 0.8 V (against Ag/AgCl) at a scan rate of 25 mV/s.

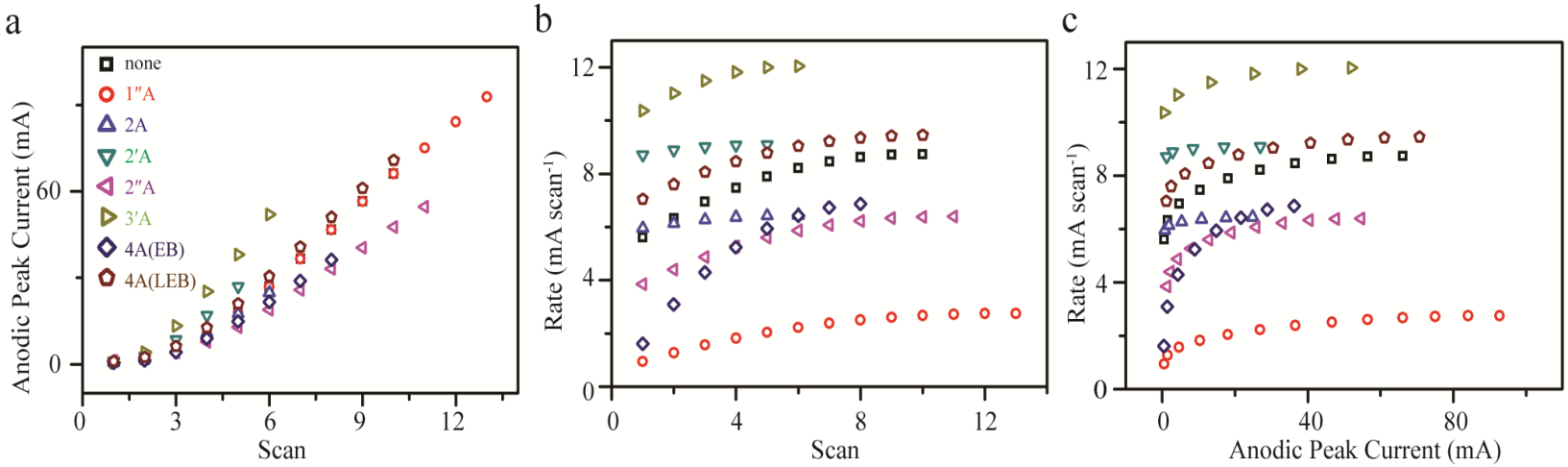


**Figure S8-8.** Graphs of (a) anodic peak current versus number of scans, (b) polymerization rate versus the number of scans, and (c) polymerization rate versus the anodic peak current, for aniline electrochemical polymerization with and without oligoanilines. The reactions contain 0.2 M of aniline and 1.0 mM of additives in a 30 mL 1.0 M HCl solution, with the potential sweep from -0.2 V to 1.0 V (against Ag/AgCl) at a scan rate of 25 mV/s.

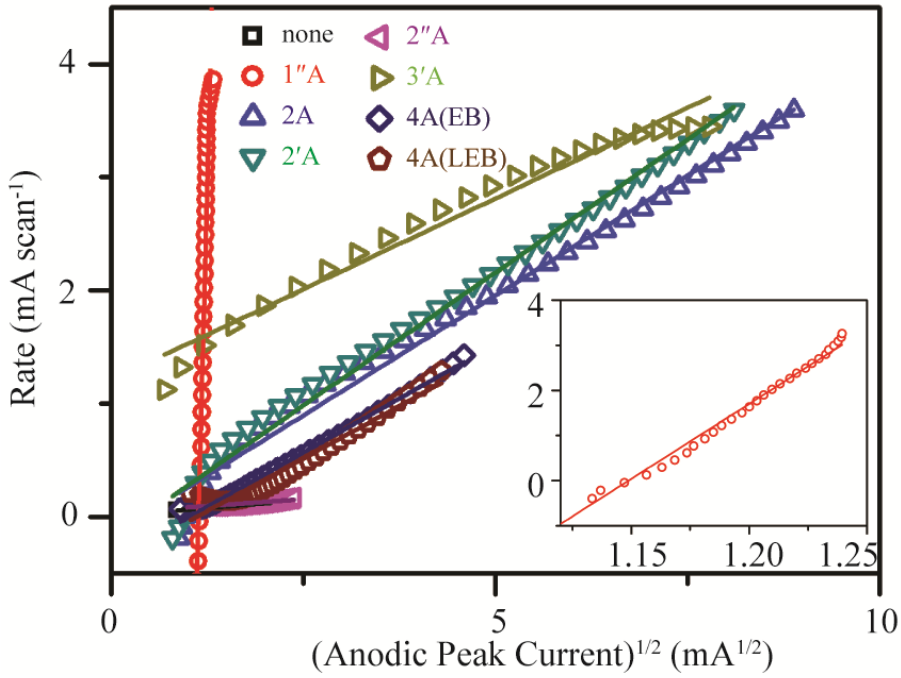


**Figure S8-9.** The linear relationship of the rate of electrochemical polymerization of aniline with square root of the anodic peak current. Potential sweep range: -0.2 V to 0.8 V (versus Ag/AgCl). Scan rate: 25 mV/s.

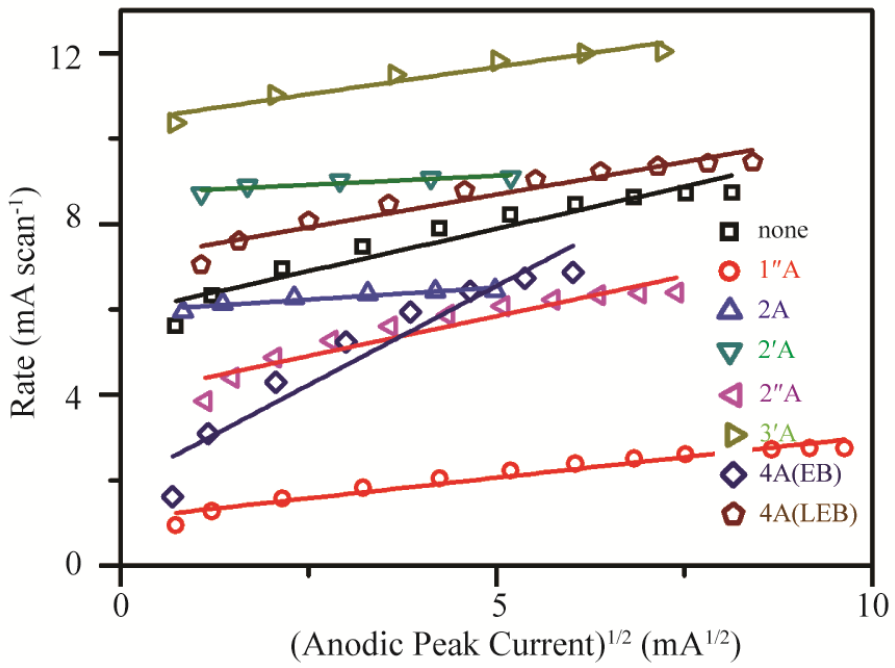


**Figure S8-10.** The linear relationship of the rate of electrochemical polymerization of aniline with square root of the anodic peak current. Potential sweep range: -0.2 V to 1.0 V (versus Ag/AgCl). Scan rate: 25 mV/s.

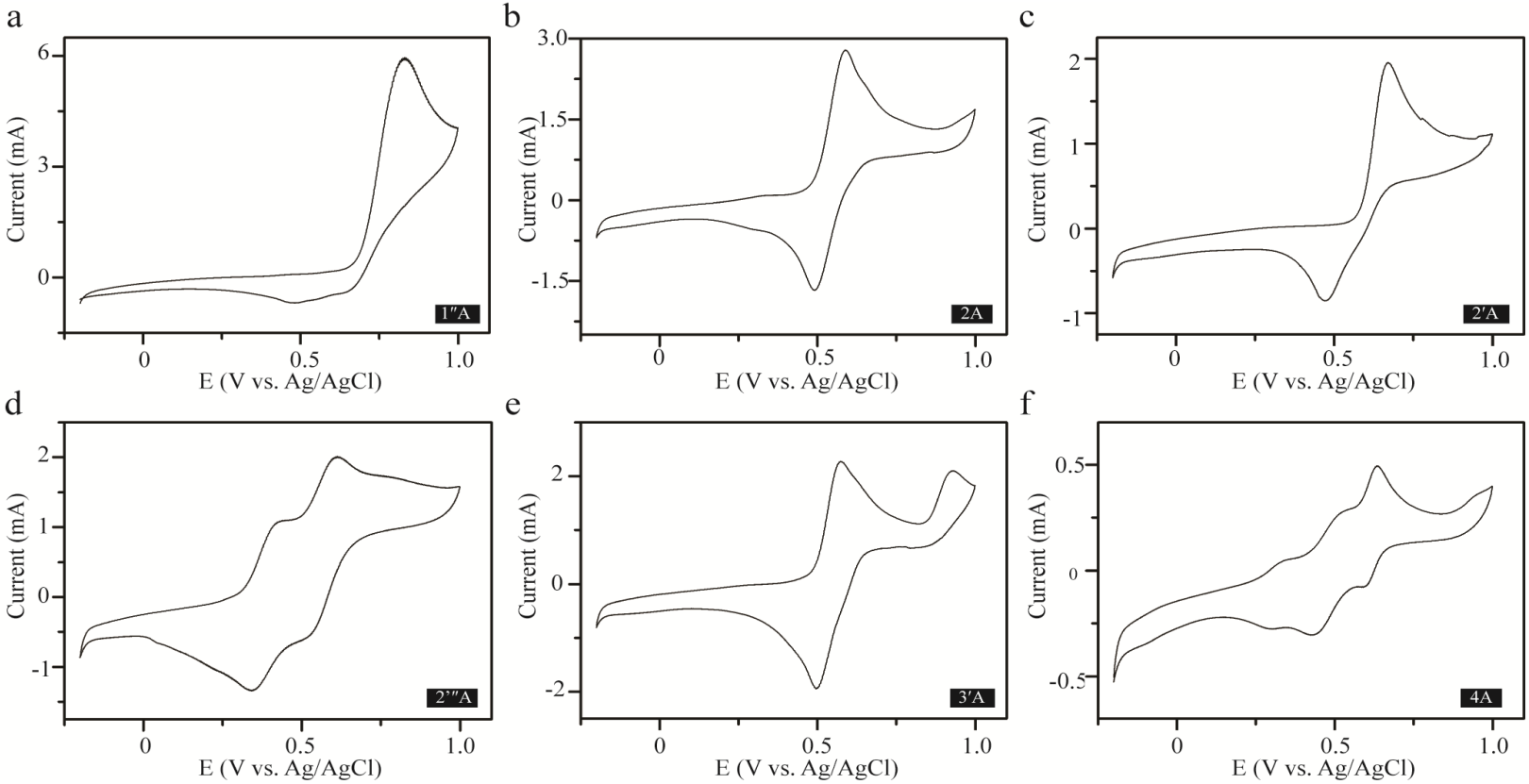


**Figure S8-11.** Cyclic voltammograms of 10 mM of (a) 1″A, (b) 2A, (c) 2′A, (d) 2″A, (e) 3′A, and (f) 4A in a 30 mL 1.0 M HCl solution between -0.2 V to 1.0 V (referenced against Ag/AgCl), at a scan rate of 25 mV/s.

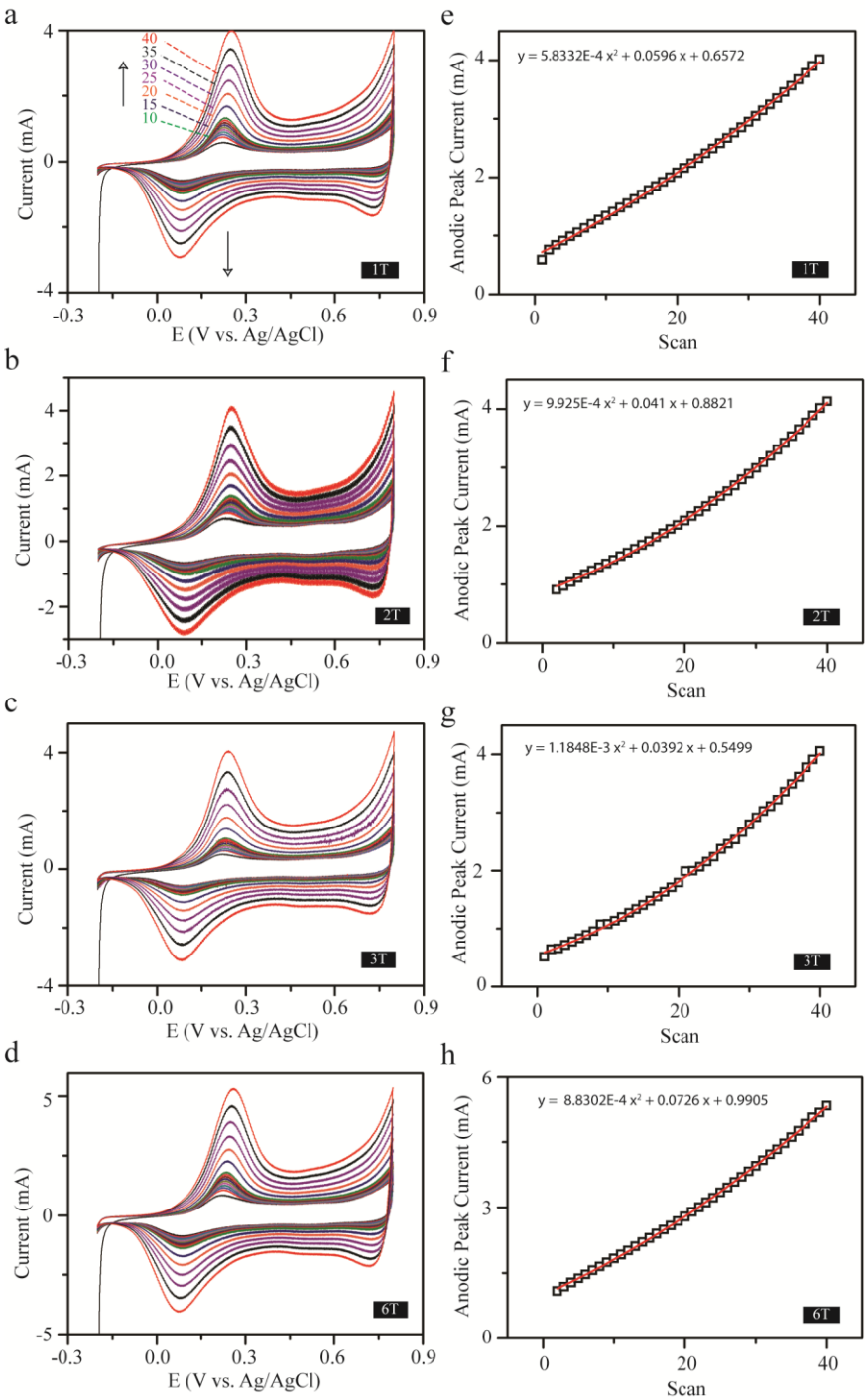


**Figure S8-12.** Graphs showing the cyclic voltammograms and the fittings for anodic peak current against number of scans for additives of (a, b) 1T, (c, d) 2T, (e, f) 3T, (g, h) 6T in the electrochemical polymerization of aniline in a 30 mL 1.0 M HCl solution. Sweep range: -0.2 V to 0.8 V (against Ag/AgCl). Scan rate: 25 mV/s.

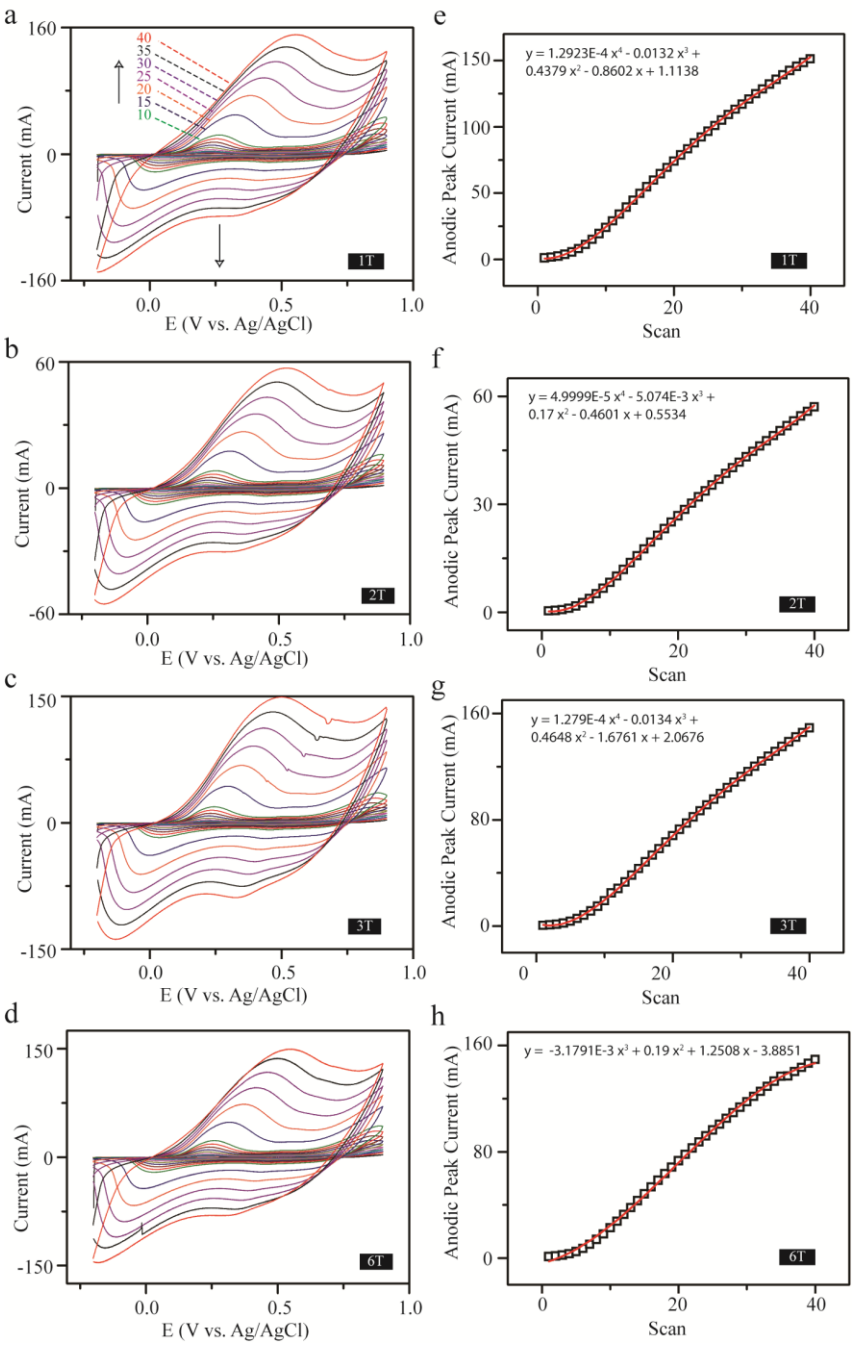


**Figure S8-13.** Graphs showing the cyclic voltammograms and the fittings for anodic peak current against number of scans for additives of (a, b) 1T, (c, d) 2T, (e, f) 3T, (g, h) 6T in the electrochemical polymerization of aniline in a 30 mL 1.0 M HCl solution. Sweep range: -0.2 V to 0.9 V (against Ag/AgCl). Scan rate: 25 mV/s.

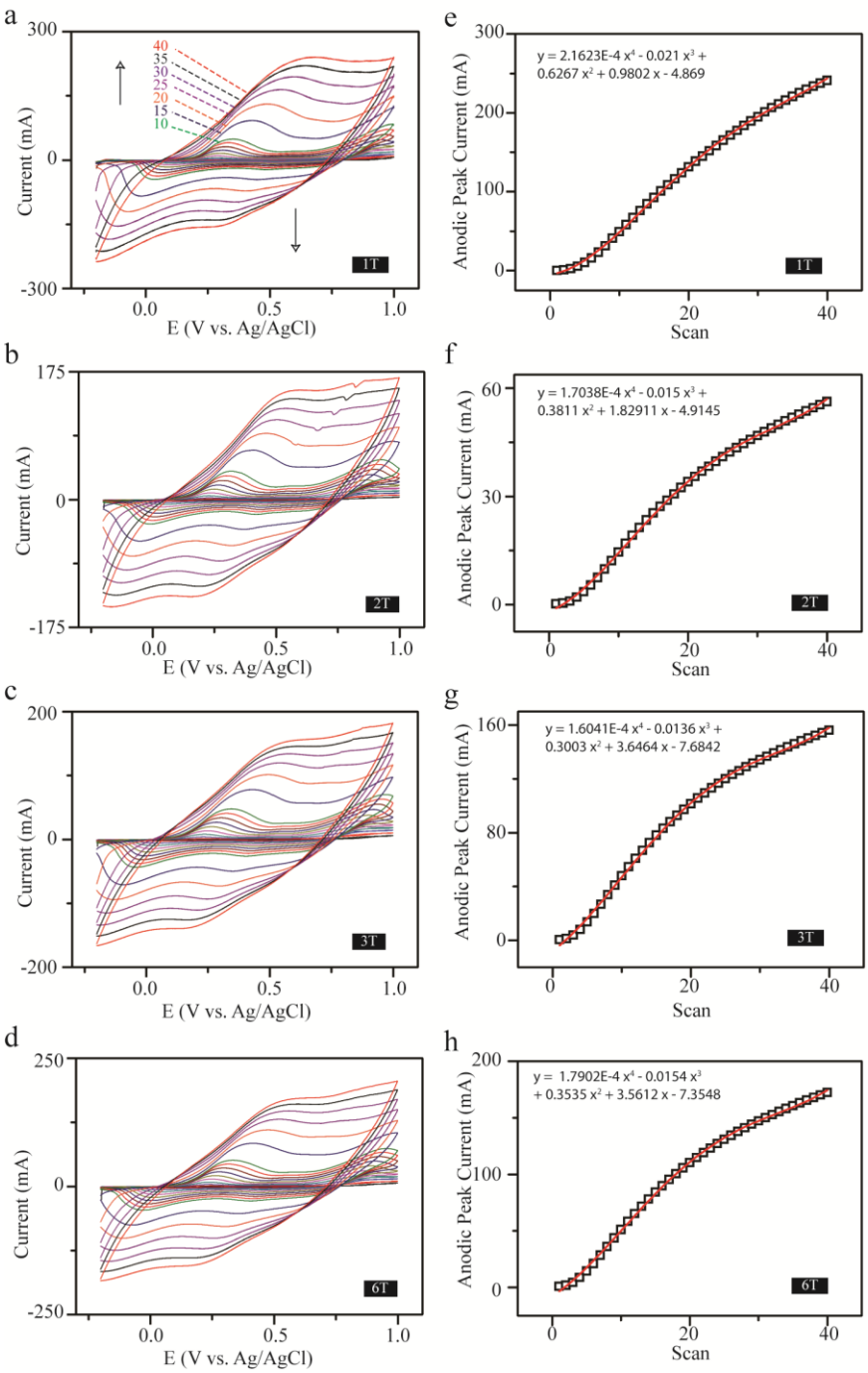


**Figure S8-14.** Graphs showing the cyclic voltammograms and the fittings for anodic peak current against number of scans for additives of (a, b) 1T, (c, d) 2T, (e, f) 3T, (g, h) 6T in the electrochemical polymerization of aniline in a 30 mL 1.0 M HCl solution. Sweep range: -0.2 V to 1.0 V (against Ag/AgCl). Scan rate: 25 mV/s.

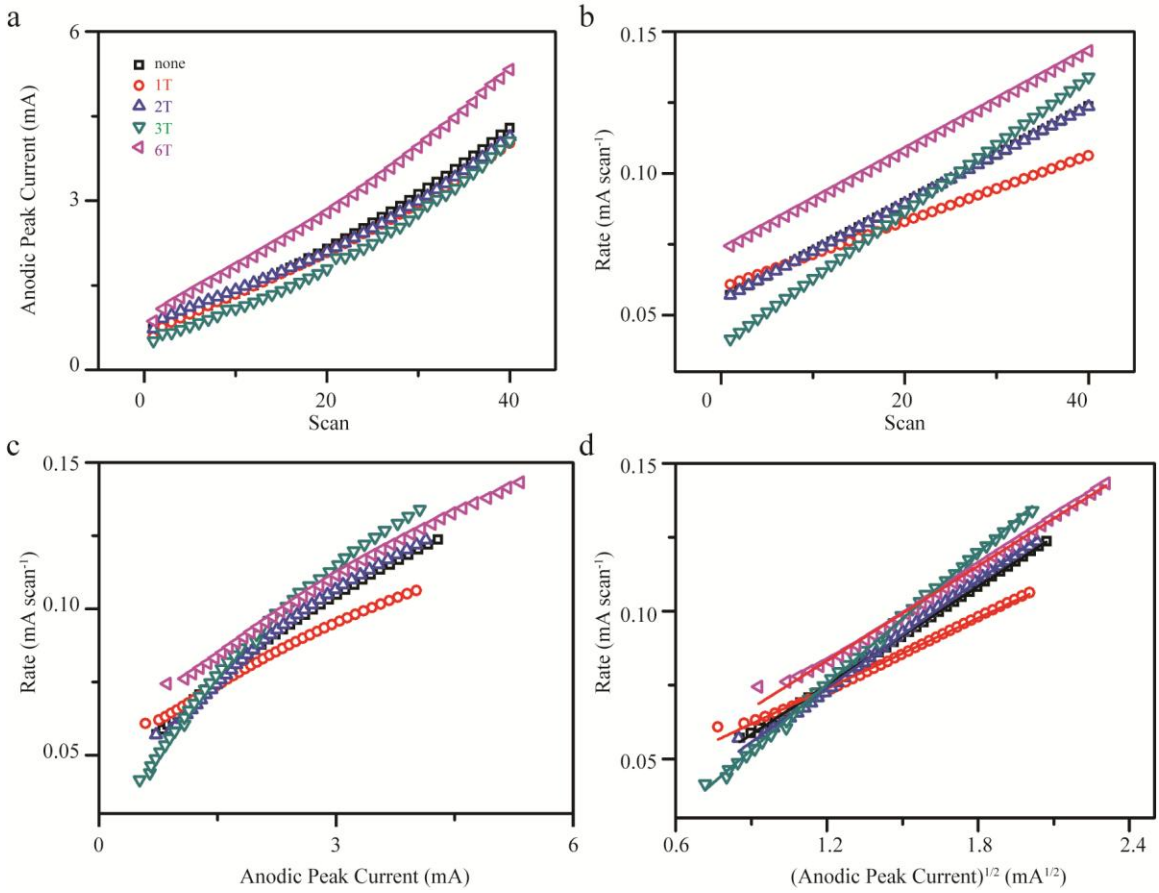


**Figure S8-15.** Graphs of (a) anodic peak current versus number of scans, (b) polymerization rate versus the number of scans, (c) polymerization rate versus the anodic peak current, and (d) the fittings for rate versus the square root of anodic peak current, for aniline electrochemical polymerization with and without oligothiophenes. The reactions contain 0.2 M of aniline and 1.0 mM of additives in a 30 mL 1.0 M HCl solution, with the potential sweep from -0.2 V to 0.8 V (against Ag/AgCl) at a scan rate of 25 mV/s.

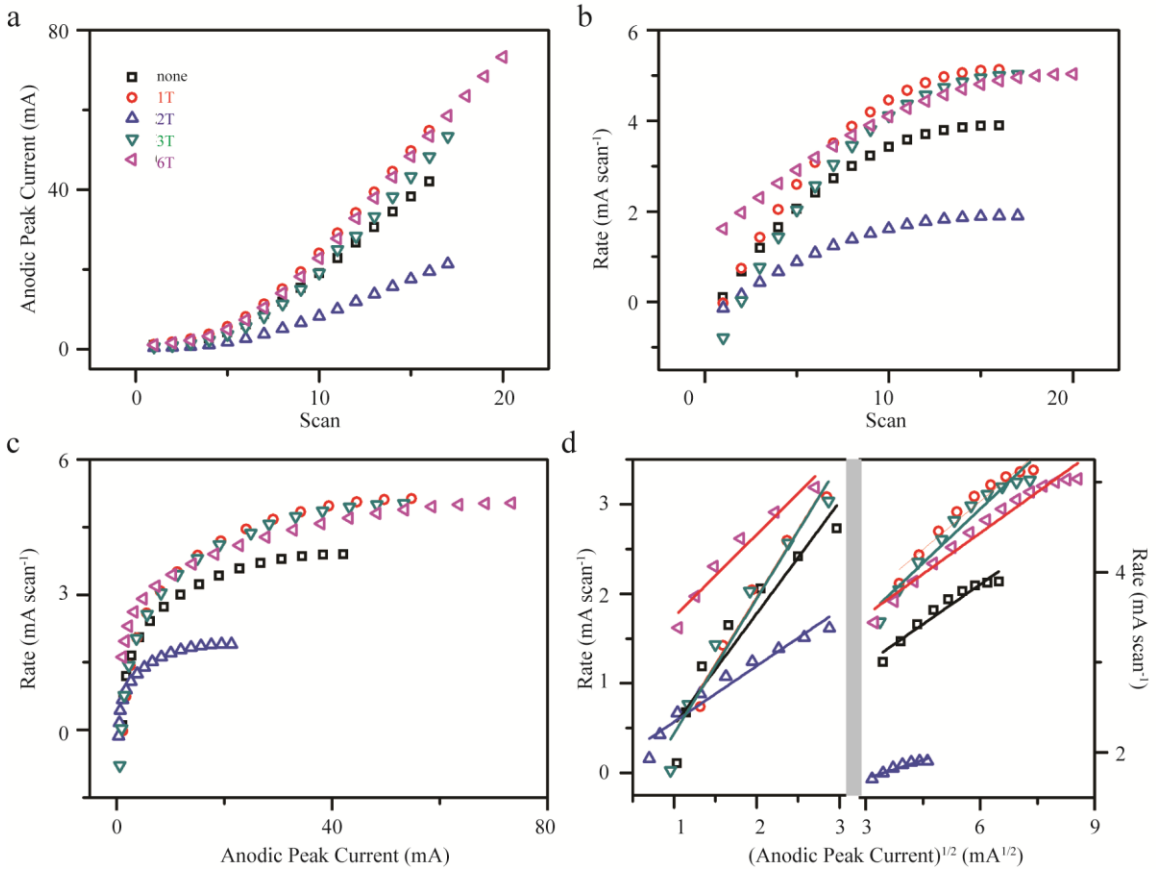


**Figure S8-16.** Graphs of (a) anodic peak current versus number of scans, (b) polymerization rate versus the number of scans, (c) polymerization rate versus the anodic peak current, and (d) the fittings for rate versus the square root of anodic peak current, for aniline electrochemical polymerization with and without oligothiophenes. The reactions contain 0.2 M of aniline and 1.0 mM of additives in a 30 mL 1.0 M HCl solution, with the potential sweep from -0.2 V to 0.9 V (against Ag/AgCl) at a scan rate of 25 mV/s.

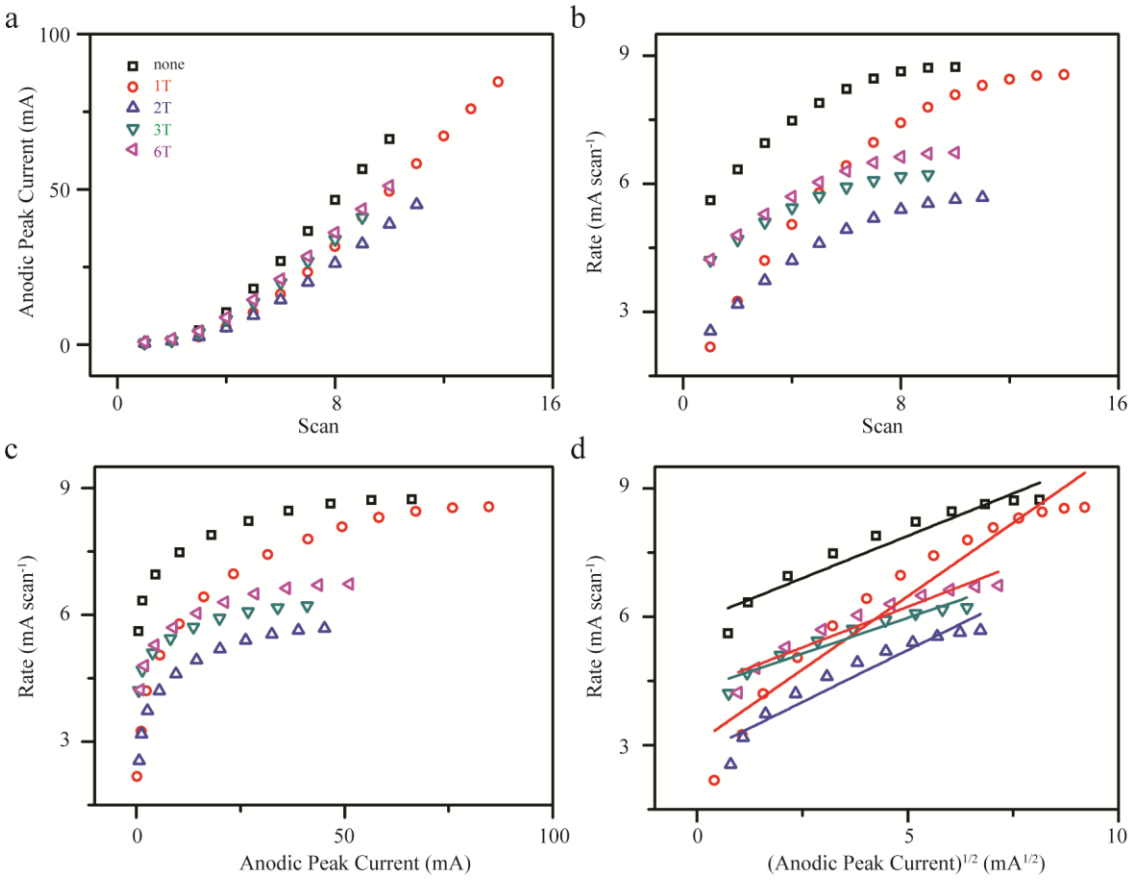


**Figure S8-17.** Graphs of (a) anodic peak current versus number of scans, (b) polymerization rate versus the number of scans, (c) polymerization rate versus the anodic peak current, and (d) the fittings for rate versus the square root of anodic peak current, for aniline electrochemical polymerization with and without oligothiophenes. The reactions contain 0.2 M of aniline and 1.0 mM of additives in a 30 mL 1.0 M HCl solution, with the potential sweep from -0.2 V to 1.0 V (against Ag/AgCl) at a scan rate of 25 mV/s.

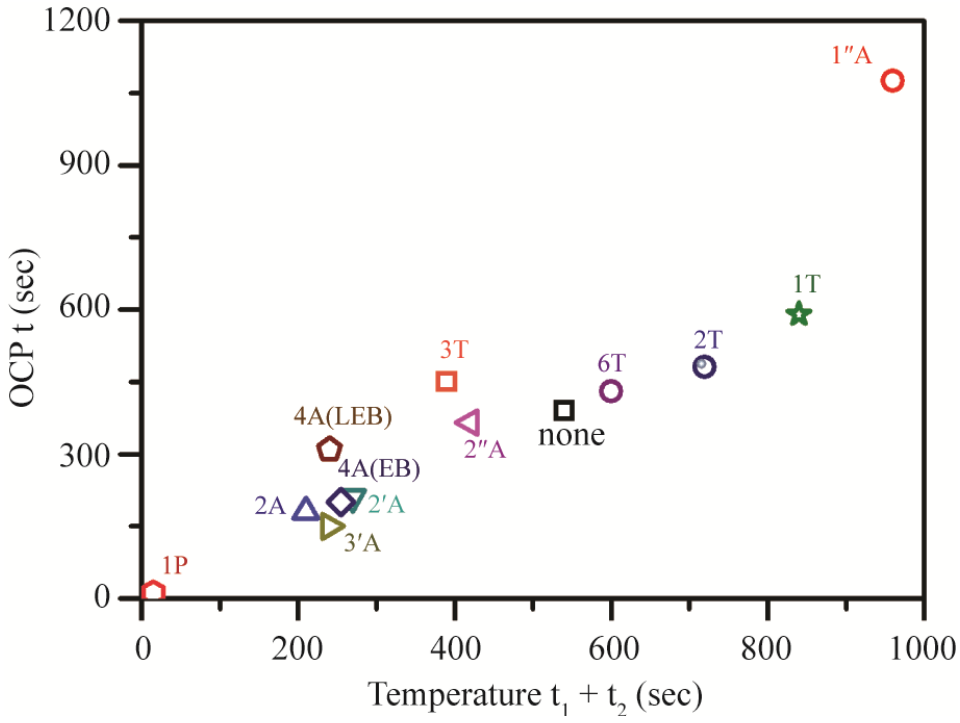


**Figure S8-18.** Plot showing t in terms of the open-circuit potential versus $t_1 + t_2$ in terms of temperature for all additives in 1.0 M HCl solutions of chemical polymerization of aniline with ammonium persulfate as the oxidizing agent.

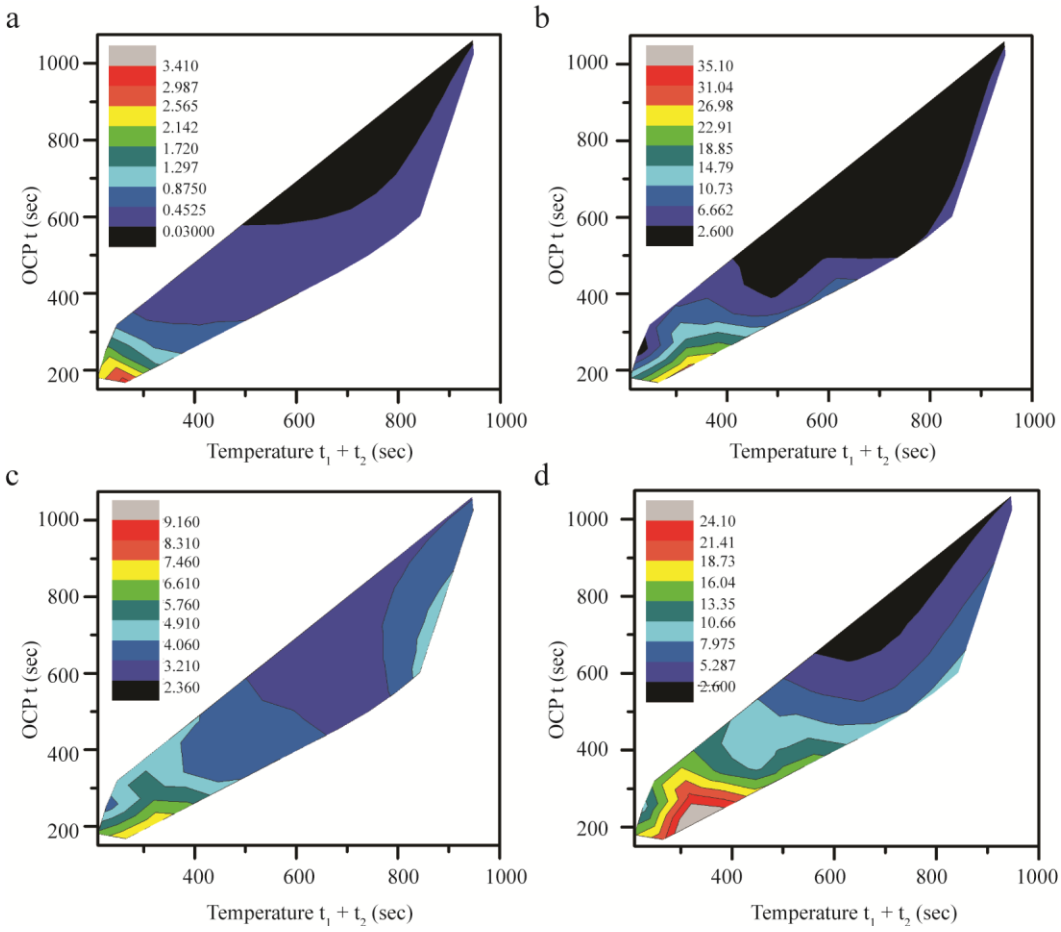


**Figure S8-19.** Contour plots of t for the open-circuit potential profiles versus the $t_1 + t_2$ duration for temperature profiles, with color mappings for (a) rate constants at 0.8 V, (b) first rate constant, $k_1$, at 0.9 V, (c) second rate constant, $k_2$, at 0.9 V, and (d) rate constant at 1.0 V, for introducing oligoanilines and oligothiophenes into chemical polymerization of aniline in a 1.0 M HCl solution.

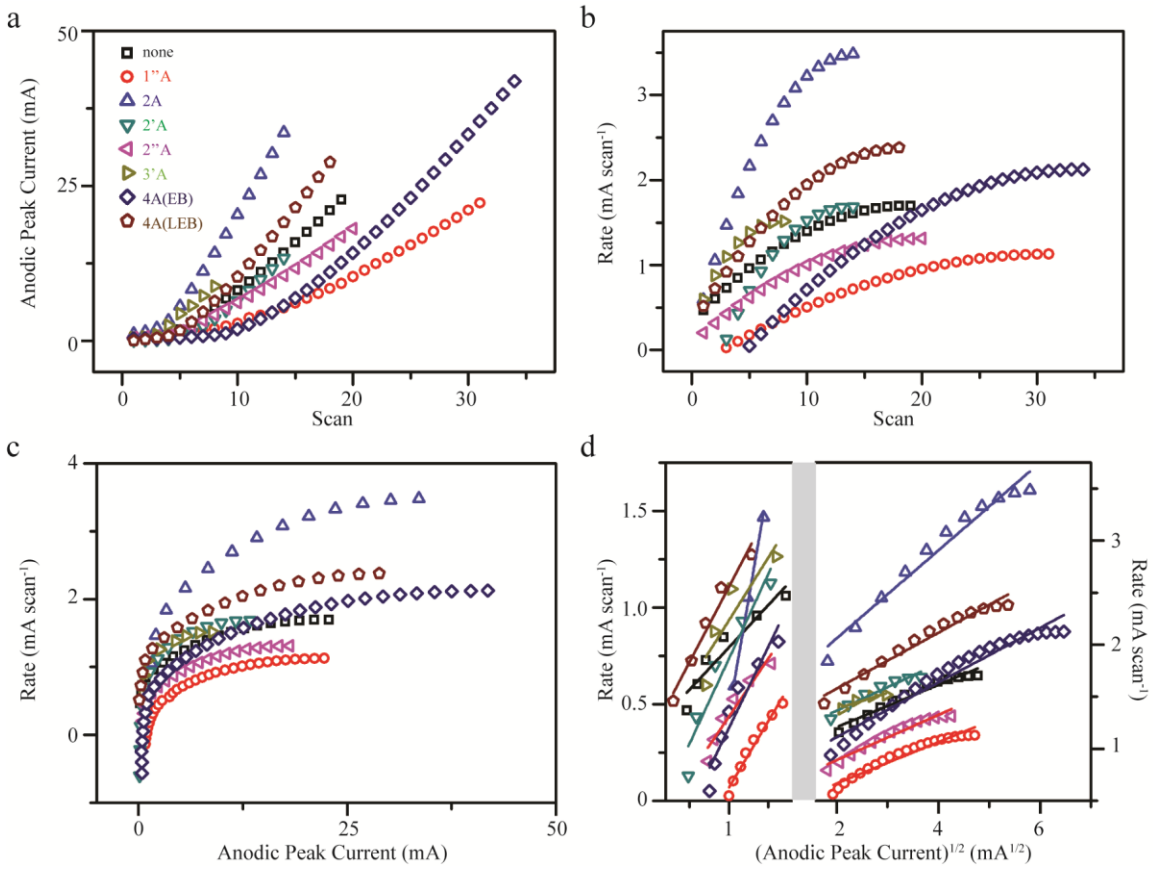


**Figure S8-20.** Graphs of (a) anodic peak current versus number of scans, (b) polymerization rate versus the number of scans, (c) polymerization rate versus the anodic peak current, (d) polymerization rate versus the square root of anodic peak current, for aniline electrochemical polymerization with and without oligoanilines to reach their maximum rates of electrochemical polymerization. The reactions contain 0.2 M of aniline and 1.0 mM of additives in a 15 mL 1.0 M HCl and 15 mL of acetonitrile solution, with the potential sweep from -0.2 V to 1.0 V (against Ag/AgCl) at a scan rate of 25 mV/s.

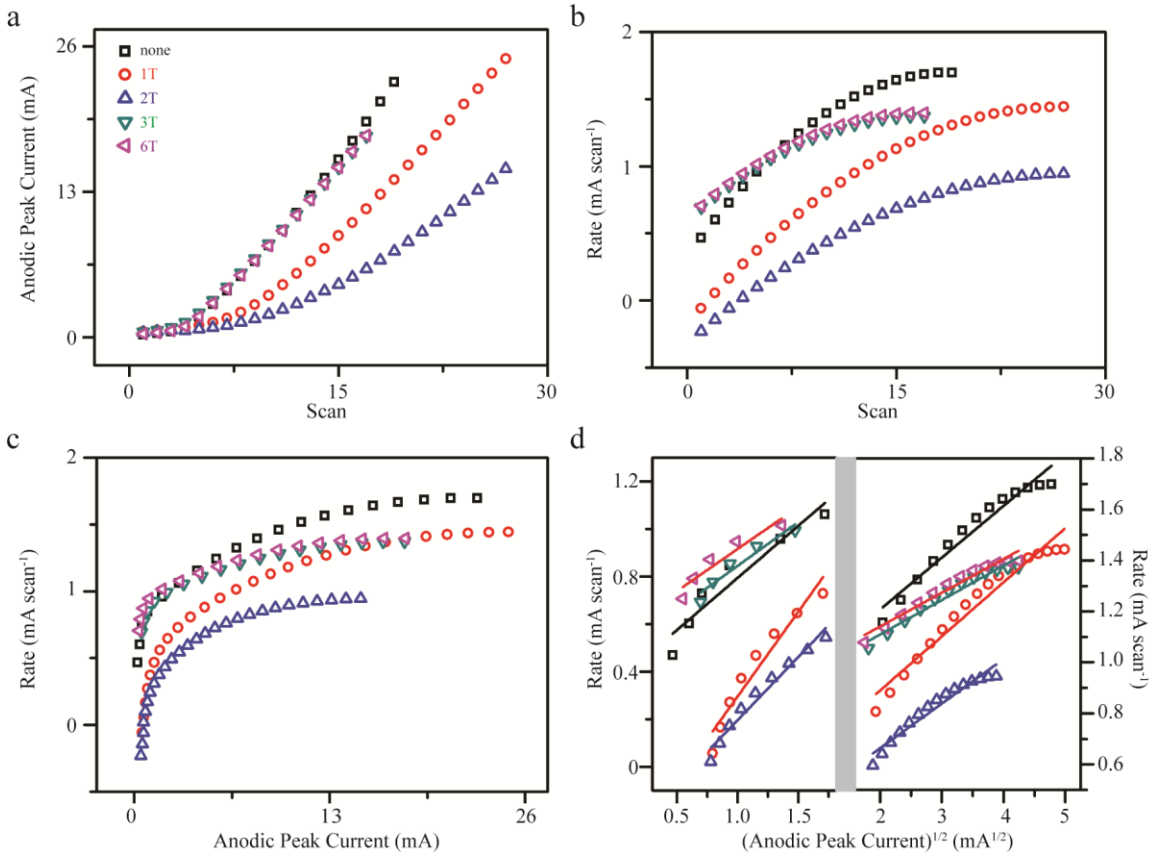


**Figure S8-21.** Graphs of (a) anodic peak current versus number of scans, (b) polymerization rate versus the number of scans, (c) polymerization rate versus the anodic peak current, (d) polymerization rate versus the square root of anodic peak current, for aniline electrochemical polymerization with and without oligothiophenes to reach their maximum rates of electrochemical polymerization. The reactions contain 0.2 M of aniline and 1.0 mM of additives in a 15 mL 1.0 M HCl an 15 mL of acetonitrile solution, with the potential sweep from -0.2 V to 1.0 V (against Ag/AgCl) at a scan rate of 25 mV/s.

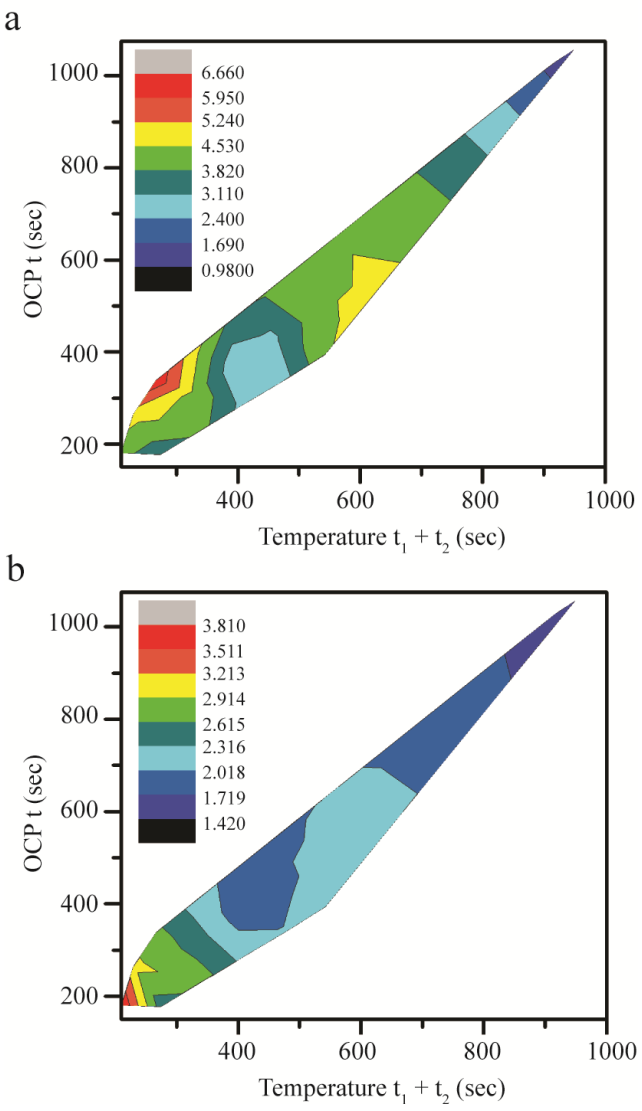


**Figure S8-22.** Contour plots of t for the open-circuit potential versus the $t_1$ + $t_2$ duration for temperature profiles, with color mappings for (b) first rate constant, $k_1$, at 1.0 V, and (c) second rate constant, $k_2$, at 1.0 V, for introducing oligoanilines into chemical polymerization of aniline in a 1.0 M HCl/acetonitrile solution.

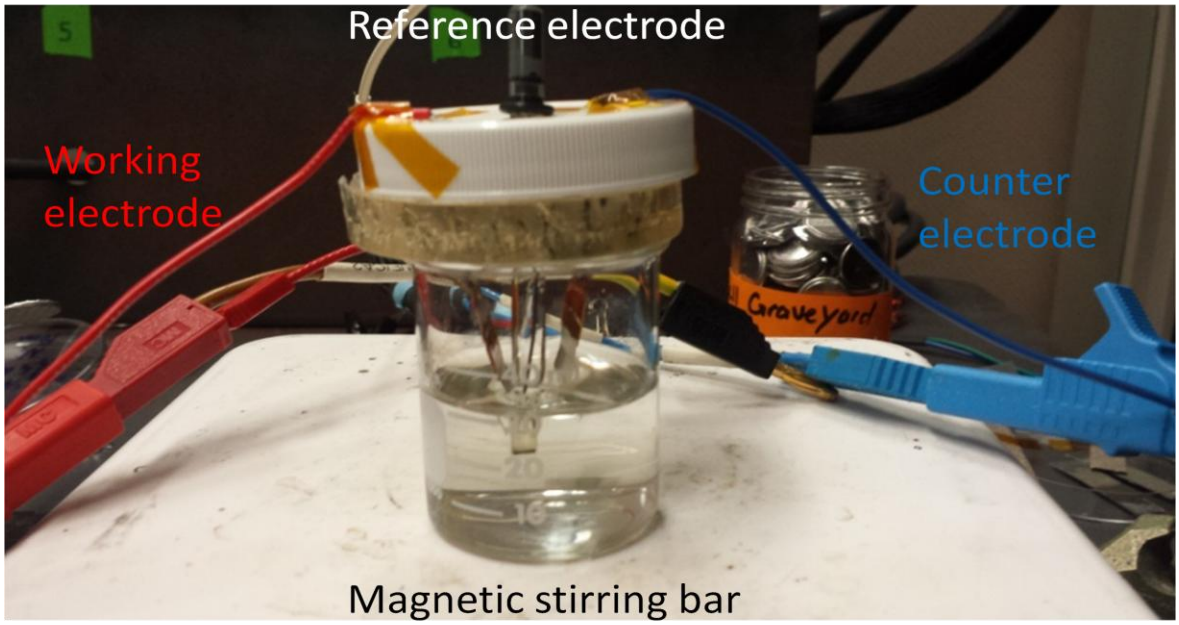


**Figure S8-23.** Picture showing the setup for electrochemical reactions.

## REFERENCES


(1) Runge, F. F.Ueber Einige Produkte Der Steinkohlendestillation. *Ann. der Phys. und Chemie* **1834**, 65–78.

(2) Rasmussen, S. C.The Early History of Polyaniline: Discovery and Origins. *Substantia* **2017**, *1* (2 SE-Historical Articles).

(3) Letheby, H.XXIX.—On the Production of a Blue Substance by the Electrolysis of Sulphate of Aniline. *J. Chem. Soc.* **1862**, *15* (0), 161–163.

(4) Macdiarmid, A. G."Synthetic Metals": A Novel Role for Organic Polymers ( Nobel Lecture )**. *Angew. Chemie Int. Ed.* **2001**, *40*, 2581–2590.

(5) Heeger, A. J.Semiconducting and Metallic Polymers: The Fourth Generation of Polymeric Materials ( Nobel Lecture )**. *Angew. Chemie Int. Ed.* **2001**, *40*, 2591–2611.

(6) Shirakawa, H.The Discovery of Polyacetylene Film: The Dawning of an Era of Conducting Polymers (Nobel Lecture)**. *Angew. Chemie Int. Ed.* **2000**, *40*, 2574–2580.

(7) Chiang, J.-C.; MacDiarmid, A. G.'Polyaniline': Protonic Acid Doping of the Emeraldine Form to the Metallic Regime. *Synth. Met.* **1986**, *13* (1), 193–205.

(8) Diaz, A. F.; Logan, J. A.Electroactive Polyaniline Films. *J. Electroanal. Chem. Interfacial Electrochem.* **1980**, *111* (1), 111–114.

(9) Huang, W.-S.; Humphrey, B. D.; MacDiarmid, A. G.Polyaniline, a Novel Conducting Polymer. Morphology and Chemistry of Its Oxidation and Reduction in Aqueous Electrolytes. *J. Chem. Soc. Faraday Trans. 1 Phys. Chem. Condens. Phases* **1986**, *82* (8),

2385–2400.

(10) Tzou, K.; Gregory, R.V.Kinetic Study of the Chemical Polymerization of Aniline in Aqueous Solutions. *Synth. Met.* **1992**, *47* (3), 267–277.

(11) Mohilner, D. M.; Adams, R. N.; Argersinger, W. J.Investigation of the Kinetics and Mechanism of the Anodic Oxidation of Aniline in Aqueous Sulfuric Acid Solution at a Platinum Electrode. *J. Am. Chem. Soc.* **1962**, *84* (19), 3618–3622.

(12) Wei, Y.; Jang, G. W.; Chan, C. C.; Hsueh, K. F.; Hariharan, R.; Patel, S. A.; Whitecar, C. K.Polymerization of Aniline and Alkyl Ring-Substituted Anilines in the Presence of Aromatic Additives. *J. Phys. Chem.* **1990**, *94* (19), 7716–7721.

(13) Orata, D.; Buttry, D. A.Determination of Ion Populations and Solvent Content as Functions of Redox State and PH in Polyaniline. *J. Am. Chem. Soc.* **1987**, *109* (12), 3574–3581.

(14) Zotti, G.; Cattarin, S.; Comisso, N.Cyclic Potential Sweep Electropolymerization of Aniline: The Role of Anions in the Polymerization Mechanism. *J. Electroanal. Chem. Interfacial Electrochem.* **1988**, *239* (1), 387–396.

(15) Sasaki, K.; Kaya, M.; Yano, J.; Kitani, A.; Kunai, A.Growth Mechanism in the Electropolymerization of Aniline and P-Aminodiphenylamine. *J. Electroanal. Chem. Interfacial Electrochem.* **1986**, *215* (1), 401–407.

(16) Kitani, A.; Yano, J.; Kunai, A.; Sasaki, K.A Conducting Polymer Derived from Para-Aminodiphenylamine. *J. Electroanal. Chem. Interfacial Electrochem.* **1987**, *221* (1), 69–82.

(17) Shim, Y. B.; Park, S. M.Electrochemistry of Conductive Polymers VII. Autocatalytic Rate Constant for Polyaniline Growth. *Synth. Met.* **1989**, *29* (1), 169–174.

(18) Wei, Y.; Sun, Y.; Tang, X.Autoacceleration and Kinetics of Electrochemical Polymerization of Aniline. *J. Phys. Chem.* **1989**, *93* (12), 4878–4881.

(19) Farmer, J. D.; Kauffman, S. A.; Packard, N. H.Autocatalytic Replication of Polymers. *Phys. D Nonlinear Phenom.* **1986**, *22* (1), 50–67.

(20) Wei, Y.; Hsueh, K. F.; Jang, G. W.Monitoring the Chemical Polymerization of Aniline by Open-Circuit-Potential Measurements. *Polymer (Guildf).* **1994**, *35* (16), 3572–3575.

(21) Huang, J.; Virji, S.; Weiller, B. H.; Kaner, R. B.Polyaniline Nanofibers : Facile Synthesis and Chemical Sensors. *J. Am. Chem. Soc.* **2003**, *125*, 314–315.

(22) Baker, B. C. O.; Shedd, B.; Innis, P. C.; Whitten, P. G.; Spinks, G. M.; Wallace, G. G.; Kaner, R. B.Monolithic Actuators from Flash-Welded Polyaniline Nanofibers. *Adv. Mater.* **2008**, *20*, 155–158.

(23) Li, W.; Wang, H. L.Oligomer-Assisted Synthesis of Chiral Polyaniline Nanofibers. *J. Am. Chem. Soc.* **2004**, *126* (8), 2278–2279.

(24) Tran, H. D.; Wang, Y.; D'Arcy, J. M.; Kaner, R. B.Toward an Understanding of the Formation of Conducting Polymer Nanofibers. *ACS Nano* **2008**, *2* (9), 1841–1848.

(25) Cao, Y.; Li, S.; Xue, Z.; Guo, D.Spectroscopic and Electrical Characterization of Some Aniline Oligomers and Polyaniline. *Synth. Met.* **1986**, *16* (3), 305–315.

(26) Kwon, O.; McKee, M. L.Calculations of Band Gaps in Polyaniline from Theoretical

Studies of Oligomers. *J. Phys. Chem. B* **2000**, *104* (8), 1686–1694.

(27) Zade, S. S.; Zamoshchik, N.; Bendikov, M.From Short Conjugated Oligomers to Conjugated Polymers. Lessons from Studies on Long Conjugated Oligomers. *Acc. Chem. Res.* **2011**, *44* (1), 14–24.

(28) D'Aprano, G.; Leclerc, M.; Zotti, G.Electrochemistry of Phenyl-N-Capped Aniline Oligomers. Evaluation of Optical and Electrochemical Properties of Ideal Polyaniline. *Synth. Met.* **1996**, *82* (1), 59–61.

(29) Wei, Y.; Chan, C. C.; Tian, J.; Jang, G. W.; Hsueh, K. F.Electrochemical Polymerization of Thiophenes in the Presence of Bithiophene or Terthiophene: Kinetics and Mechanism of the Polymerization. *Chem. Mater.* **1991**, *3* (5), 888–897.

(30) Focke, W. W.; Wnek, G. E.; Wei, Y.Influence of Oxidation State, PH, and Counterion on the Conductivity of Polyaniline. *J. Phys. Chem.* **1987**, *91* (22), 5813–5818.

(31) Javadi, H. H. S.; Treat, S. P.; Ginder, J. M.; Wolf, J. F.; Epstein, A. J.Aniline Tetramers: Comparison with Aniline Octamer and Polyaniline. *J. Phys. Chem. Solids* **1990**, *51* (2), 107–112.

(32) Wang, Y.; Torres, J. A.; Stieg, A. Z.; Jiang, S.; Yeung, M. T.; Rubin, Y.; Chaudhuri, S.; Duan, X.; Kaner, R. B.Graphene-Assisted Solution Growth of Vertically Oriented Organic Semiconducting Single Crystals. *ACS Nano* **2015**, *9* (10), 9486–9496.

(33) Jonsson, M.; Wayner, D. D. M.; Lusztyk, J.Redox and Acidity Properties of Alkyl- and Arylamine Radical Cations and the Corresponding Aminyl Radicals. *J. Phys. Chem.* **1996**, *100* (44), 17539–17543.

(34) Sapurina, I. Y.; Stejskal, J.Oxidation of Aniline with Strong and Weak Oxidants. *Russ. J. Gen. Chem.* **2012**, *82* (2), 256–275.

(35) Zotti, G.; Zecchin, S.; Vercelli, B.; Pasini, M.; Destri, S.; Bertini, F.; Berlin, A.Electrochemical, Magnetic, and Electrical Properties of α,ω-Capped Sexithiophene Films. 2. Conduction in Sexithiophenes with α,ω-Aryl-Extended Conjugation. *Chem. Mater.* **2006**, *18* (13), 3151–3161.

(36) Li, D.; Kaner, R. B.Shape and Aggregation Control of Nanoparticles: Not Shaken, Not Stirred. *J. Am. Chem. Soc.* **2006**, *128* (3), 968–975.

(37) Li, D.; Huang, J.; Kaner, R. B.Polyaniline Nanofibers : A Unique Polymer. *Acc. Chem. Res.* **2009**, *42* (1), 135–145.

(38) Li, D.; Kaner, R. B.How Nucleation Affects the Aggregation of Nanoparticles. *J. Mater. Chem.* **2007**, *17* (22), 2279–2282.

(39) Huang, J.; Kaner, R. B.A General Chemical Route to Polyaniline Nanofibers. *J. Am. Chem. Soc.* **2004**, *126*, 851–855.

(40) Zhang, X.; Goux, W. J.; Manohar, S. K.Synthesis of Polyaniline Nanofibers by "Nanofiber Seeding." *J. Am. Chem. Soc.* **2004**, *126* (14), 4502–4503.

(41) Wang, Y.; Tran, H. D.; Liao, L.; Duan, X.; Kaner, R. B.Nanoscale Morphology, Dimensional Control, and Electrical Properties of Oligoanilines. *J. Am. Chem. Soc.* **2010**, *132* (30), 10365–10373.

(42) Leng, W.; Chen, M.; Zhou, S.; Wu, L.Facile Synthesis of Water-Based Aniline Oligomer Nanowires and Their Uses in Low-Cost Fabrication of Oxide Nanotubes in Aqueous

Phase. *Chem. Commun.* **2013**, *49* (65), 7225–7227.

(43) Shao, Z.; Rannou, P.; Sadki, S.; Fey, N.; Lindsay, D. M.; Faul, C. F. J.Delineating Poly(Aniline) Redox Chemistry by Using Tailored Oligo(Aryleneamine)s: Towards Oligo(Aniline)-Based Organic Semiconductors with Tunable Optoelectronic Properties. *Chem. Eur. J.* **2011**, *17*, 12512–12521.